Mechanochemical Alteration of the Mineralogical Structure and Chemical Composition of Lunar and Martian Analogues

Page Number: 170

Master of Science by Research (M.Sc.)

Nadia Laila Butt

Dr. Jonathan Tandy

October 2023

School of Chemistry and Forensic Science

Materials for Energy and Electronics

University of Kent

Acknowledgements

First and foremost, I would like to thank and acknowledge the University of Kent for not only providing me with the apparatus and environment I required during my research, but for the divisional and general support I have constantly received since 2019. The past four years at Kent have been the most memorable and enriching of my life, helping me to develop not just my academic skills but also myself as a person, and I have grown a lot. The relationships I have formed here will be with me forevermore.

I would like to thank my research supervisors Dr. Jonathan Tandy and Professor Donna Arnold. Jon has been the best supervisor and mentor any research student could ask for, and not only provided me with constant support and encouragement during our weekly meetings, but whenever I needed it, and never failed to motivate me to be the best researcher, and person, I could be. As I embark on my future academic journey and leave Kent, Jon remains the primary reason I have gained a newfound confidence in my ability as a scientist, and his advice will forever stay with me. Jon, thank you for always listening to my silly little rambles, encouraging my tea and biscuits addiction, and reminding me (with great patience) to look after myself, I will miss our meetings. Professor Mark Green, you have been a great mentor to me the past few years, I will always appreciate and remember all of your advice, continuous support and cups of tea. I would also like to thank Dr. Alex Wright, who has been a great mentor and always believed in me, from marking my lab reports till now as a researcher.

I am and always will be extremely grateful to my mum and dad, you have always been there for me, and shown how proud you are especially when I needed it most. Thank you, I love you and you mean everything to me. Mum, you are my rock throughout everything in my life. Luke, thank you for always being there for me, I love you with all my heart and I always will. You are my best friend and no one knows me like you do. Your support and encouragement means so much to me, and you are my happiest and most precious memory of my University years. Lastly I would like to thank my friends from Kent and London for always being there for me.

Thank you to Larry, our 127 lab mascot who I have now adopted as my little Moon.

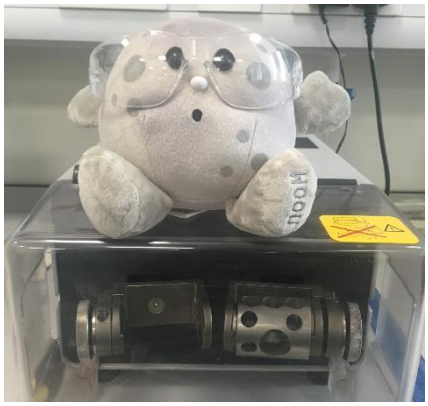

Abstract

The chemical and mineralogical composition of the Lunar and Martian surface, for instance the presence of inorganics (SiO_2, TiO_2, CaO, MgO, Na_2O, Al_2O_3 and Fe_2O_3), water ice (within Lunar cold traps and Martian polar regions) and trace organic compounds (e.g. chlorinated hydrocarbons within Gale Crater on Mars), has been previously studied in detail. However, the specific chemical changes occurring within regolith due to wind-driven and impact processes has only recently been explored. The research presented in this thesis illustrates the novel use of the planetary analogues JSC-Lunar, LHS-1, JSC-Martian and MGS-1 to assess mechanochemical-induced alterations in their chemistry, physical and mineralogical properties through ball milling techniques. This research sought to utilise ball milling techniques upon the named simulants to simulate potential chemical changes due to the collisional impact processing during regolith transport occurring on the Moon and Mars.

Milling experiments within the laboratory have been complemented with a variety of analytical techniques, namely XRD to analyse potential mechanochemical-induced modifications in mineralogy, ATR-FTIR to assess induced chemistry, TGA to observe thermal activation effects and loss of volatiles, and SEM to record alterations in physical properties such as grain size distribution, surface texture and grain morphology. Water ice was also incorporated into milling experiments, and subsequent analogous analyses conducted to assess the effects of collisional processes on regolith-ice mixtures and water ice-driven reactions on the Lunar and Martian surfaces. However, such reactions were more probably driven by water in its liquid state due to a combination of partial melting during the crushing of ice prior to milling and slight increases in temperature within the internal reaction system during the grinding process.

The results in this thesis indicate significant mechanochemical-induced alterations in the properties of planetary analogues, and an increase in mineral surface reactivity. XRD results showed noticeable modifications in relative peak intensities and potentially indicate corresponding mineralogical variations. ATR-FTIR spectroscopy displayed consistent increases in absorbance for the Si-O-M^+ (M^+ = metal cation) vibrational band after milling. These findings are invaluable when considering the effect of collisional impact processes on planetary surfaces and the transport of their regolith, for instance the dehydroxylation of mechanically activated mineral surfaces through meteoritic impacts on the Lunar surface resulting in H_2O_2 production, as indicated by toxic moon dust. TGA results in conjunction with infrared spectroscopy have shown the CO_2 sequestration ability of the planetary analogues, which is of great significance to the Martian atmosphere and uptake of CO_2. The potential formation of hydrated minerals (for instance hydrated silicates) due to water ice experiments, has been suggested through XRD and infrared spectroscopy, which is of relevance when considering areas on the Lunar and Martian surface which contain water ice, or studying the historical hydrological cycle on Mars. Milling experiments also displayed considerable abrasion-induced alterations in physical properties, for

instance agglomeration of grains observed for the LHS-1 and MGS-1 simulants indicating potential triboelectrification. This is of high relevance to the future exploration and exploitation of the Lunar and Martian surfaces, due to granular electrification observed through environmental processes such as sandstorms, meteoritic bombardment (and thus regolith transport) and UV irradiation. The experimental analyses of planetary analogues on Earth will assist not only understanding of the Lunar and Martian surface and its regolith composition, but also the manner in which it evolves over time due to environmental processes, thus complementing interpretation from current and future space missions.

Keywords

Regolith, analogues, simulants, mechanochemistry, Earth-based, synthetic, Moon, Mars, Lunar surface, Martian surface, mineralogy, chemical composition, abrasion, weathering, meteoritic bombardment, collisional impacts, ball milling, environmental conditions.

Table of Contents

Chapter 1: Introduction

1.1 The Essential Role of Planetary Analogues

The utilisation of analogue materials within the laboratory enables processes and environments to be simulated due to the materials' comparable physical and/or chemical properties to the area of interest. In particular, specific geographical regions may be challenging to study directly due to numerous factors, for instance remote locations, hazardous conditions, time and financial restrains (research budgets) or an extraterrestrial and in general inaccessible body. Mechanical alteration processes and other geochemical environmental cycles such as hydrothermalism, weathering and metamorphism can thus be potentially explained through the usage of such analogues [1]. Foucher *et al*. reports that whilst the exact scientific definition of an 'analogue material' may vary depending on what is being investigated, in general it is known as a geographical site and material on Earth which possesses similar properties including chemical composition to the genuine material being studied [1]. Simulants, otherwise known as synthetic materials, are a viable alternative due to the fact that genuine samples returned from space missions are costly and difficult to obtain. Additionally, samples returned to Earth would not be in large enough quantities for thorough and constant analysis during experiments within the laboratory [1,2]. Thus materials already present on Earth (whether they are found naturally on the Earth's crust or synthesised within the laboratory) are inevitably more sustainable and less limited. *In situ* experimental analyses conduced within space are without a doubt restricted in comparison to experiments executed on Earth due to space probe limitations, restricting sensitivity, precision and resolution of data collections, and therefore is space-mission dependent (concerning factors such as mission budget, timeframe and accessible apparatus) [1].

Despite this, planetary analogues present inevitable limitations and restrains also. Analogues and analogue sites will always have a degree of variation to the materials and environments they simulate due to the ever-changing physical, chemical and mineralogical properties of natural materials [1,3]. Natural materials are potentially more heterogeneous in mineralogical composition due to varied elemental abundances at the microscopic scale (in comparison to the macroscale). It is therefore essential to analyse relevant and specific properties, for instance chemical composition. Great variation in mineralogical composition of the Earth's surface in comparison to that of extraterrestrial bodies has already been discovered. For example, Foucher *et al.* discusses the high abundance of anorthosite found on the Lunar surface in comparison to the almost negligible amounts found on the Earth's crust and reports several limitations when drawing comparisons between the Earth's surface and environmental conditions and those found on extraterrestrial

bodies. They emphasise the fact that the rocks seen as analogues on Earth have already been subjected to geochemical processes, including oxidation and fluvial or aqueous weathering. This is not solely relevant to the present state of the analogue site, but also formation processes that were required to achieve the current mineralogy. These processes would be vividly different from those occurring on an extraterrestrial body such as the Moon or Mars, for example processes causing higher iron abundances within Martian surface basalt in comparison to those found on Earth [1].

1.1.2 Earth based and Synthetic Analogues

On Earth, various companies and research groups, such as ExoLith Laboratory based at the University of Central Florida (UCF), are involved with the production of planetary analogues through synthesis in the laboratory, for example the MGS-1 and LHS-1 [4]. The planning of processes and mechanisms for the production of such materials is based on data collected from on-board instrumentation during space missions. Grain textures and grain size distributions are often accurately matched to those found and measured on the planetary body's surface. The production frequently involves the incorporation of mineral and rock constituents to match the surface/subsurface texture which varies across a planetary surface. This therefore suggests that analogues synthesised in the laboratory are more specific to a particular process or chemical property due to more controlled formation processes [1,4].

Planetary analogues may also be excavated naturally from the Earth's surface, whereby regolith (weathered, unconsolidated material which lies above bedrock [5]) discovered has comparable (analogous) physical, chemical and mineralogical properties to the authentic material being analysed. A prominent example of a geographical area on Earth with known planetary analogue materials is Antarctica [3]. Investigating areas on Earth can be considered a preliminary characterisation in order to comprehend (to an extent) the nature of planetary surfaces. Extreme environments such as the South Pole are a fitting demonstration for the harsh and hostile conditions experienced on the Lunar and Martian surface [3,6,7] with its immensely cold and dry climate, highly penetrating radiation, high salt concentrations and low attainable water [3]. Such analogous conditions thus mean the formation and evolution of regolith material within the area will have comparable properties to some extraterrestrial surfaces.

1.1.3 PFAs (Planetary Field Analogues)

An Antarctic environment will have comparable properties to that found on the Lunar and Martian surface [3]. For instance, the Lunar surface and its constituent regolith is exposed to harsh celestial radiation and frequent meteoritic impacts due to the lack of an atmospheric barrier [8]. The Martian atmosphere is highly oxidising due to the regolith's reactive oxygen species (ROS) components such as hydrogen peroxide formed by dehydroxylation of mineral surfaces (for example quartz) [6,9,10].

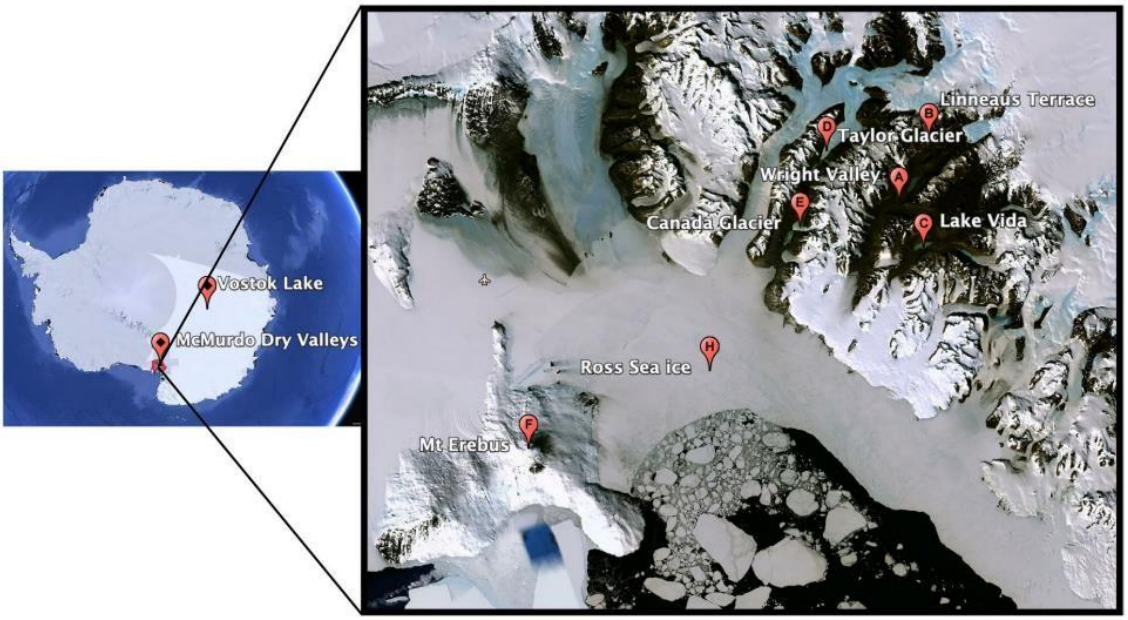

Figure 1. Mapped PFAs within Antarctica for analysing Mars and Icy moons. Image credit: Google Earth/PGC/NASA/U.S. (Geological Survey/Landsat/Copernicus) [3].

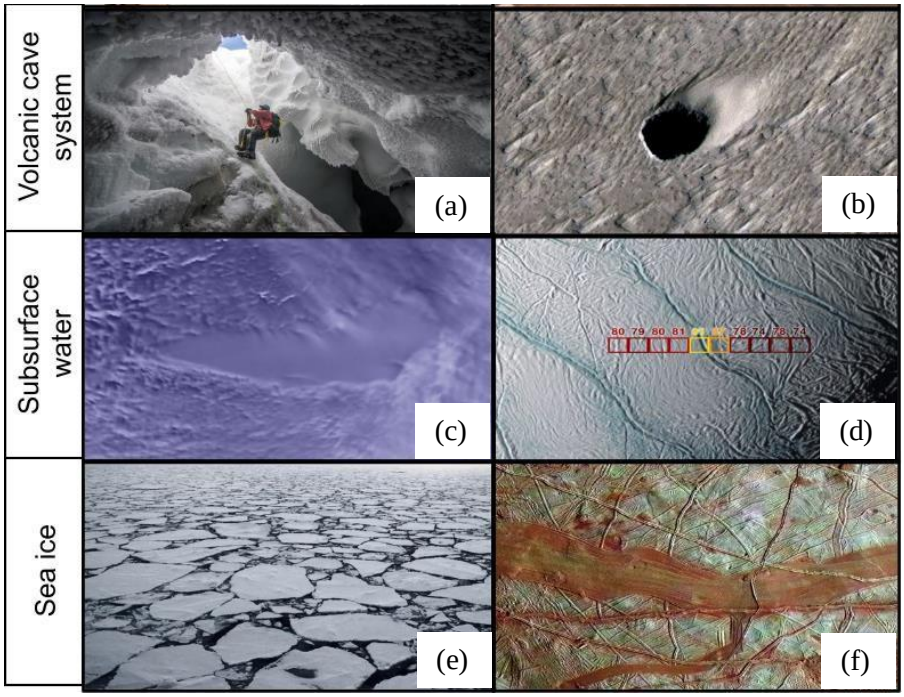

Figure 2. Comparing PFAs found on Antarctica (left) to hypothetical planetary environments (right) (a) Ice cave surrounding Mt Erebus volcano (image credit: Alasdair Turner/National Geographic Traveller Photo Contest); (b) Pit crater surrounding Arsia Mons Volcano on the Martian surface (image credit: NASA/JPL-Caltech/University of Arizona); (c) Subglacial Lake Vostok (image credit: NASA/Goddard Space Flight Center Scientific Visualisation Studio/Canadian Space Agency/RADARSAT International Inc.); (d) Surface ice fracturing on Enceladus, Saturn's moon (image credit: NASA/JPL/GSFC/Space Science Institute); (e) Antarctic Ross Sea's floating ice (image credit: John B. Weller/The Pew Charitable Trusts); (f) Water ice with incorporated hydrated salt minerals on the surface of Europa (image credit: NASA/JPL-Caltech/SETI Institute) [3].

Geographical locations such as the Antarctic are often referred to as Planetary Field Analogues (PFAs) due to their analogous characteristics and environmental properties to extraterrestrial bodies. Such areas and their properties assist planetary exploration through ongoing interpretations simultaneous to space missions. Figure 1 illustrates the PFA areas and their abundance within Antarctica which are studied to investigate Martian and icy moon environments. Areas of Antarctic land without ice, otherwise known as Dry Valleys, possess a cold, desert-like climate and are therefore regarded suitable and the most accurate Martian analogues due to comparable hydrological cycles including aqueous alteration processes such as sublimation. Cassaro reports that the icy Dry Valleys may be analogous to the once icy lakes thought to have been present on the Martian surface [3]. Glacier-carved valley landscapes consist of glacial meltpods, ice-cemented soils, icy lakes and short-lived meltwater stream features. The presence of icy caves within Antarctica provide a good training site for future astronauts who will be monitoring the exploration

of planetary caves through robotic instrumentation. Such caves are investigated for habitable conditions due to the protection they provide from harsh environmental conditions such as extremely low temperatures. Both the Lunar Reconnaissance Orbiter Camera (LROC) and Mars Reconnaissance Orbiter's on-board High Resolution Imaging Experiment (HiRISE) instrumentation were used to detect cave entrances on both the Lunar and Martian surface. Figure 2 demonstrates some of these similarities, with images (a) showing an icy cave around an Antarctic volcano and comparing its geological formation to (b), a pit crater on Mars [3]. However, a more fitting planetary geological comparison to (c) would be the subglacial lake formations present on the Martian surface's polar cap [3].

Through the employment of planetary analogues, environmental processes which affect the physical and chemical properties of regolith (such as weathering) can be simulated on a smaller scale within the laboratory through experimental techniques such as ball milling. These experiments assist understanding of the Lunar and Martian surfaces and how surface and subsurface-level geochemical and environmental processes and reactions occur. The focus of the research outlined in this thesis is based on environmental weathering and abrasion, so it is important to note that because silicate minerals (e.g. plagioclase feldspars) are the main component of the majority of rock fragments on Earth, most analogues will be silicate-based [1], including the Lunar and Martian simulants utilised within this research.

1.1.4 Lunar and Martian Analogues[1]

As discussed previously, planetary analogues can be naturally sourced from the Earth's surface, or synthesised within the laboratory. An essential and novel area of research discussed within this thesis is the difference in behaviour between Earth-based and synthetic analogues when subjected to identical experimental conditions within the laboratory. Earth-based simulants may be more geochemically complex than synthetic materials due to prior alteration through environmental processes, therefore scientists have more control over synthesised simulants where individual minerals have been blended together (e.g. through ball milling).

The two Lunar analogues utilised within this research were the Earth-based JSC-Lunar (NASA Johnson Space Center) and synthesised LHS-1 (Lunar Highlands Simulant). The JSC-Lunar simulant originates from a volcanic field in San Francisco, close to Flagstaff, Arizona. Land composing of pyroclastic basalt was utilised for the excavation of the simulant, making it a glass-rich basaltic material. The sourced material was mined in a cinder quarry in Merriam Crater and

[1] Specific compositions of the regolith analogues are shown in chapter 2.

further broken down by means of milling by employing an impact mill. Milled ash was left to dry, reducing the average water abundance to 2.7 wt. %. Typical Lunar samples contain no traces of water and volatile oxide phases [11].

The synthesised LHS-1 simulant has been developed by the Exolith Laboratory Facility to simulate the properties of the highland regions of the Moon, which consist of ancient soil most exposed to meteoritic bombardment. X-Ray Fluorescence (XRF) spectroscopy was employed to assess the composition of constituent minerals and rock fragments and X-Ray Diffraction (XRD) to assess mineralogical structures and individual phases. These experiments were run in attempts to match data collected from the extracted Apollo and Lunar mission samples. Individual minerals and rock fragments, primarily anorthosite (rock), were crushed together to obtain desired angular morphologies and grain size distributions (analysed through sieving procedures), matched to those identified during Apollo landing site missions [12].

The two Martian analogues utilised were the Earth-based JSC-Martian (Johnson Space Center) and synthesised MGS-1 (Martian Global Simulant). The JSC-Martian simulant was excavated from a palagonitic tephra within the Pu'u Nene cinder cone in Hawaii, and was found to be primarily amorphous palagonite with crystalline components of magnetite and plagioclase. This simulant was designed to be analogous to Martian dust deposits, and was therefore a spectral simulant whereby the nanophase iron oxide components were comparable to VNIR (visible/near-infrared) spectral results collected by orbiters for instance Opportunity. The JSC-Martian simulant is abundant in carbon-containing species and is very hygroscopic at room temperature [2].

The synthesised MGS-1 simulant is considered a standardised composition of the Martian surface, as it is based on the Rocknest windblown regolith situated at Gale crater. Rocknest windblown soil provides an average composition of the Martian surface, and therefore the MGS-1 simulant can be utilised as a standard reference due to its baseline physical, chemical and mineralogical properties. Individual minerals in their appropriate quantities were blended together by means of ball milling by Exolith. Rocknest windblown soil and its mineralogical composition was analysed by the CheMin instrumentation on-board Curiosity through means of XRD. Whilst crystalline carbonate compounds were not detected, there was an observed release of gaseous products indicating other carbonate materials being present. Despite previous Martian simulants lacking in glass abundance, glass spherule formations have been found in regolith in Curiosity landing sites, and thus Cannon *et al*. reports the increased awareness of the requirement for an increased glass incorporation within synthesis. To truly simulate the formation processes of regolith on Mars as closely as possible, rather than dry milling individual mineral powders, polymineralic fused solid cobbles were produced (through the combining of individual minerals such as olivine with water and a sodium metasilicate pentahydrate binding agent which forms a strong polymer network material upon

heating) before ball milling, thus resulting in a more accurate grain size distribution and general texture. The resulting concoction was dehydrated and the cobbles ball milled with secondary minerals such as hydrated silica [2].

1.2 Environmental Weathering Processes

Weathering of any surface material, no matter the body in question, is where surface rocks are broken down into smaller fragments, creating a layer known as regolith [5, 13]. A key, novel area of this research was to analyse the induced chemical reactions caused by collisional impact processes through regolith transport on the Lunar and Martian surfaces, but also the transport of regolith with ice and the minerals it contains. As reported by Bazilevskaya *et al*., the rate at which regolith weathers will affect its depth, whereby fast weathering yields thinner regolith compared to slow weathering [5]. Consequently, depending on wind speeds experienced on Mars, some recovered regolith may differ in depth compared to other collected samples, potentially affecting the mineralogy and chemical properties due to different reaction rates and efficiency of diffusion pathways [5].

On the Lunar surface, dust clouds have been identified by the Surveyor and Apollo 17 missions due to the interaction between emitted electrons from the exposed regolith surface and the areas unaffected by ultraviolet (UV) radiation. The free electrons which reside on these areas produce a net negative charge, therefore causing both positively and negatively charged particles to coexist. Forward *et al.* reports that due to these findings, Lunar dust clouds are present due to electrostatic charging [13]. The triboelectric effect, defined by Forward *et al.* as contact between charged grains resulting in electrostatic charging, is also experienced on the Moon's surface. As J.P. Merrison reports, environmental processes associated with triboelectric effects include dust devils and sandstorms, which are processes known to occur on the Martian surface, but not on the Moon [14]. Nonetheless, the Lunar surface is frequently subjected to meteoritic impacts which subsequently causes the transport of regolith, and thus could in fact cause electrostatic charging through granular contact [13, 14]. On the Martian surface, granular electrification effects can be the driving force behind environmental scenarios such as sandstorms and speculated increased volcanic activity in the history of the Martian environment, however, microscopically (for instance studying planetary analogues), the physical properties of the material (e.g. cohesion) can be partially controlled by triboelectric effects during processes such as ball milling and thus abrasion. Despite the majority of experimental studies suggesting more efficient transport of regolith due to electrostatic charging, studies by Holstein-Rathlou have indicated that this may not always be the case, with the hindrance of Aeolian transport in some cases, such as in insulating environments [14]. Previous work has been conducted on tumbling experiments and granular electrification at Aarhus University. Bregnhøj *et*

al. reports that through tumbling of quartz in a $CO_{2\,(g)}$ experimental atmosphere, triboelectric effects are observed due to grain surface contact, which in turn has been recorded to drive $CO_{2\,(g)}$ sequestration [15].

1.3 The Lunar Surface

Considering the lack of an atmosphere, the surface of the Moon is subjected to harsh radiation and meteoritic bombardments and is not exposed to wind-driven processes for instance erosion (unlike the surface of Mars) [7,8]. The Lunar highlands are composed of ancient soil in comparison to the mare regions, and have been subjected to more frequent meteorite impacts [12] as shown in Figure 3 below displaying a range of differently sized impact craters [16]. Whilst the highland regions are composed primarily of anorthosite [12], the mare regions are thought to have been landscaped by basaltic lava flows from the subsurface [8]. Unlike on Mars, the surface of the Moon is not subjected to wind-driven weathering processes, however, its regolith is 'gardened' over time, whereby impact events such as meteoritic bombardment causes the excavation of material and its turnover [7]. The majority of the Lunar surface is composed of anorthosite and glass-rich basalt, with inorganic oxides such as silicates, Al_2O_3, TiO_2, MgO, Cr_2O_3 and Fe_2O_3 [7,8]. The dehydroxylation of these minerals through mechanochemical pulverization has led to H_2O_2 being produced, causing reactive and toxic dust on the Moon's surface [6].

Figure 3. Photograph taken of regolith and its combination of Moon dust, impact craters and rocks at Station 1 during the Apollo 17 mission. Image credit: Hasselblad photo AS17-1342048 [16].

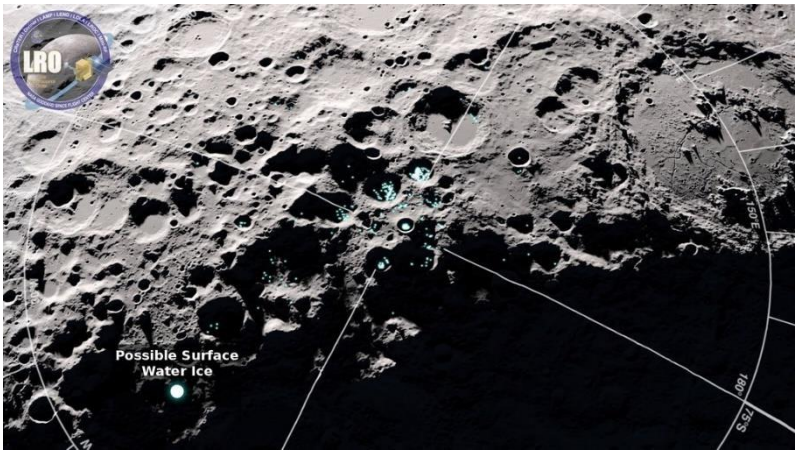

Figure 4. Photograph illustrating cold traps on the surface of the Moon. Image credit: NASA/Goddard Space Flight Center [17].

Previous studies have shown the existence of water ice on the Lunar surface, situated within permanently shadowed crater formations located on unlit regions of the Moon, otherwise known as cold traps as seen in Figure 4 above [17]. Such landscape formations are pits on the Moon which consist of much lower temperatures and can therefore sustain water and CO_2 ice. Due to the Moon's natural slight tilting of its rotational axis, topographic depressions such as the aforementioned cold traps are thus shielded from the sun permanently, causing these areas to have much lower temperatures and harsher climatic conditions [18]. Minerals found within these areas will be interlocked with water ice , and thus the incorporation of ice could potentially alter the regolith's chemistry. Despite findings from the Moon Mineralogy Mapper (M^3) instrumentation which consisted of near-infrared spectroscopic absorption features of water ice, Li *et al*. reported that the water ice present within the cold traps at the Lunar poles cannot be distinguished with confidence from water ice exposed on the surface [18]. However, studies conducted by Shifeng J. *et al*. have suggested the presence of water ice at higher latitudes on the Moon's surface than previously suspected, meaning it is exposed to higher temperatures. The increased thermal stability of such water ice indicates that on the Lunar surface, numerous forms of ice may exist. Research conducted by the Beijing National Laboratory for Condensed Matter Physics has identified the presence of a new hydrous mineral $(NH_4)\ MgCl_3.6H_2O$, ULM-1 with an analogous composition (determined by XRD, IR and Raman analyses) to novograblenovite, a fumarole mineral found on Earth, and with a water abundance of 41.7 wt. %, indicating the survival of thermal attacks [19].

1.4 The Martian Surface

The Martian surface and its atmosphere has evolved significantly over time. Although its inorganic components within the regolith are known, the contributions from organic compounds such as carbonates and thiophenes are still a relatively novel area of research. The Martian surface primarily

consists of silicate minerals, more specifically basaltic compounds, with investigations conducted by, for example, the Mars Global Surveyor, Mars Odyssey and Viking Landers all observing the high abundance of basaltic minerals [20]. The majority of the silicate minerals are plagioclase feldspar, olivine and pyroxene, as identified by a Thermal Emission Spectrometer onboard the Mars Global Surveyor mission. A process known as rubification is additionally thought to occur within Martian soil due to its reddish hue, whereby primary minerals release iron, thus yielding free iron oxide materials which can coat the soil with a red layer [21].

Regolith transport on the Martian atmosphere can occur over long distances, for example from one geographical plain to another for several kilometres, or within more confined areas such as craters. The primary mode of transport investigated in this research is saltation as illustrated in Figure 5, a wind-driven abrasion mechanism whereby saltating sand grains of size > 10 µm are ascended into the atmosphere and upon descent, inevitably collide with the remaining surface and its constituent material [6]. This collisional impact subsequently causes the fracturing of the remaining regolith material, yielding in more reactive minerals and increasing their surface reactivity, altering the chemistry and mineralogical structure, for instance through the production of secondary minerals and generating Reactive Oxygen Species (ROS) [6]. Edgar *et al.* reports the production of ROS through experiments conducted on abraded silicate-based minerals, including quartz. Research conducted at Newcastle University has involved the simulation of aforementioned saltation occurring on the Martian surface by means of tumbling experiments utilising temperature-controlled quartz ampoules. Such experiments have shown the production of ROS such as H_2O_2 through water-driven reactions with abraded silicates, with detection of H_2O_2 executed through Cu^{2+} reduction through reactions with 2,9-dimethyl-1,10-phenanthroline, forming $Cu(DMP)^{2+}$. Edgar *et al.* discusses the generation of ROS through aeolian-driven processes other than saltation on the Martian surface and their triboelectrification effects due to environmental events such as dust storms, which cause the segregation of atmospheric CO_2 and H_2O, thus forming ROS such as H_2O_2. Understanding the production of reactive chemicals on the Martian surface will assist in analysing the potential degradation of organics such as perchlorates, and what this entails for potential habitability [22].

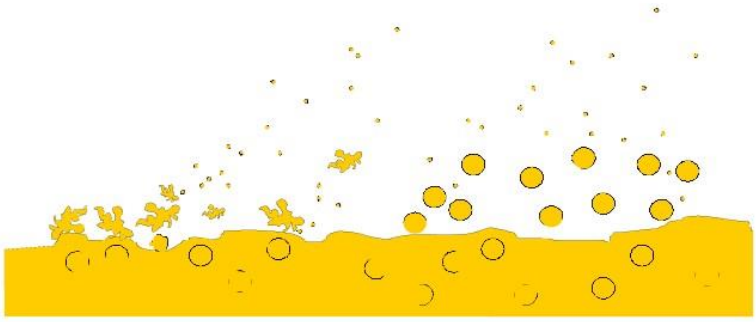

Figure 5. Illustration demonstrating the separation of sand grains and subsequent wind-driven saltation on the Martian surface. Fine dust aggregates shown on the left represents wind-induced detachment, whereas the right displays saltation of larger grains [14].

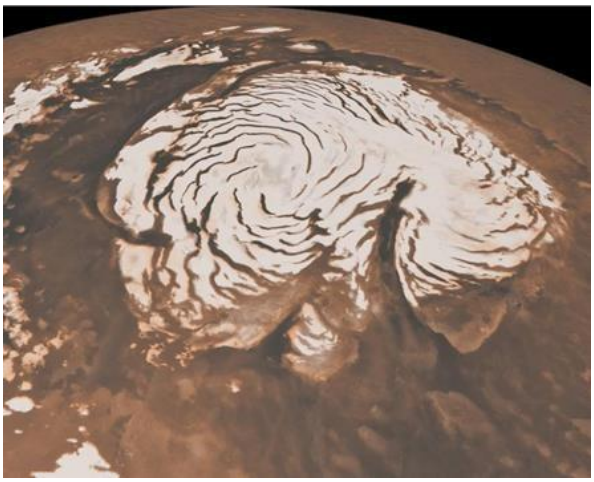

Figure 6. Photograph illustrating the Martian ice polar caps. Image credit: NASA/JPL-Caltech/MSSS [23].

As illustrated in Figure 6 above [23], the presence of water ice on Mars is clearly evident. The Martian polar caps are abundant in water ice, which is also interlocked with minerals within regolith at much lower latitudes. Due to the landscape formations and carvings of the Martian surface in some geographical plains, there is evidence of a historically different Martian environment, abundant in water existing in numerous hydrological forms. Water is thought to have once been present on the surface of Mars in a similar manner to that of Earth, with the existence of lakes, rivers, pools and even larger volumes of water such as seas [20]. Hydrated and clay minerals have been observed on other areas on Mars, such as at Gale Crater by Curiosity rover [24]. Minerals such as sulfates, carbonates and hydrated silicates have also been detected by Curiosity within the large impact basin due to historic groundwater present ~ 3.7 billion years ago, eventually forming a lake structure [24]. Jezero Crater has been studied by Perseverance rover, which identified hydrated minerals and lacustrine carbonates (related to lake formations) [25].

Therefore, being able to simulate abrasion on a smaller scale within the laboratory will inevitably assist in the interpretation of these planetary surface processes in terms of their surface properties and composition, therefore giving an insight into potential habitable environments and safety hazards on the Moon and Mars and the history/evolution of their formation.

1.5 Mechanochemical Techniques

Environmental processes such as weathering can be experimentally simulated on a small scale within the laboratory. Procedures such as ball milling can be executed to replicate granular abrasion experienced on planetary surfaces such as the Moon and Mars due to the transport of regolith. Simulating such mechanochemical processes which occur during modes of transportation, for instance saltation, allows the effect on the regolith material's physical, chemical and mineralogical properties to be examined and monitored as experimental conditions are altered. Depending on the type of ball mill being utilised, varying collisional processes can be simulated, therefore assisting in the interpretation of the properties of regolith samples recovered from plains (where it may have been transported over several km) and smaller, confined areas such as craters (constraining and localising abrasion). The type and amount of energy provided within the reaction system can have varying effects on the induced alterations in chemistry, due to modifications in frequency and energy of ball bearing impacts upon the material. Some more advanced ball mill apparatus (for instance with a built-in Raman spectrometer) provided by suppliers such as Fritsch can be employed to analyse *in situ* simultaneous alterations in chemistry in real time as the material is being abraded within the milling reaction system, which would prove to be invaluable when comparing interpretations to those being gathered during space missions. Another example is the CryoMill supplied by Retsch which allows cryogenic milling at a systematic temperature of -196°C, and can be used for dry or wet milling [26]. This would be particularly useful when simulating extremely cold climatic conditions potentially experienced on the Lunar (cold traps) and Martian (polar caps) surfaces.

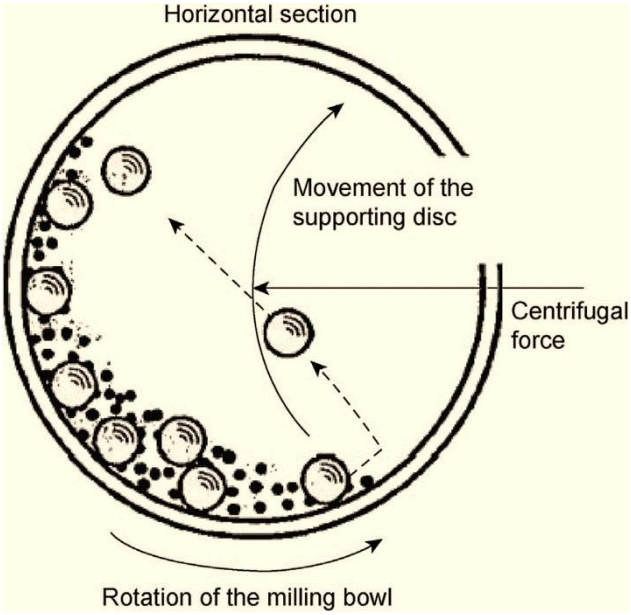

Figure 7. Schematic illustrating the interior mechanics of a ball mill, where ball bearings are represented by larger drawn circles, and material being milled by small black granular structures [27].

The theory of ball milling and its experimental set-up is relatively simple, however the numerous potentially induced reactions occurring within the reaction vessel for materials such as planetary analogues is extremely complicated, and requires further extensive analysis to be understood with greater confidence and reliability. Depending on the specific properties required, for instance corrosion resistance, chemical inertness and durability, varying apparatus materials can be employed, including stainless steel, hardened steel and agate. Ball bearings are transferred to the reaction vessel to provide the abrasion mechanism through collisional impacts. Various milling conditions can be alternated, including apparatus material, number and size of ball bearings (mm), milling times, milling frequencies, and the incorporation of lubricant materials if necessary. The milling vial is either rotated, or oscillates horizontally or vertically. Some ball mills, such as a planetary ball mill, provides simultaneous elliptical and vertical motions. Figure 7 above illustrates a typical schematic diagram for the internal motion of a planetary ball mill vessel in conjunction with ball bearings [27]. The collisional impacts from the ball bearings causes the intended abrasion and shearing of the material.

Mechanochemistry techniques can be employed to purposefully cause the breakdown of materials in a controlled manner and environment, and such is the novelty of this research. Solid state reactions and processes occurring within the reaction system include the shearing of crystalline layers, weakening the intermolecular forces between them within the lattice network. Mechanochemical activation can trigger

different reaction pathways, and increase the reactivity of mineral surfaces. Ball milling studies have given insights into the processes occurring within the milling vessel [28].

The ignition of self-sustaining reactions within ball mill systems involves many reaction steps prior to reaching such processes. During the initial activation stage within the reaction system, processes including grain size reduction, blending and the formation of defect sites occurs. Once a critical/ignition state has been achieved and rate of reaction increases, a mechanically induced self-propagating stage (MSR) is achieved if an exothermic powder is being milled, where the powdered material is propelled through the reaction system by means of combustion. A typical general schematic is illustrated in Figure 8. The number of surface defects increases with a reduction in grain size, and thus increase in surface area. Ball milling is therefore known and utilised for increasing reactivity due to a greater number of active sites. Through the mechanism of physical shearing forces, intermolecular bonding between layers within a material (such as Van der Waal's interactions) are weakened, lowering the activation energy required for certain chemical reactions to proceed. Chemical activation of mineral surfaces will thus increase their reactivity, and their interactions with other mineral compounds within the material [28]. Mechanochemical activation and the production of chemically activated grain surfaces can also subsequently cause mineral alteration, for example the production of secondary minerals from primary minerals and oxidation. Additionally, dust grains can be formed due to fracturing and abrasion of grains [13,18]. Mechanochemistry and its techniques such as ball milling cause the deformation of a material and fracturing of chemical bonds, thus generating charged species and photons. Such deformation of a crystalline lattice can cause dislocations, leading to the presence of surface radicals which lower the activation energy for chemical processes such as adsorption [29]. There are a range of analytical techniques which can be employed to assess such activation of mineral surfaces and increase in chemically active sites, and how resistant to abrasion they may be. Some of these techniques most relevant to the research within this thesis are outlined below.

Figure 8. Schematic illustrating the mechanochemical processes which lead to a self-sustaining reaction within a milling reaction system.

1.6 Analytical Experimental Techniques

1.6.2 X-Ray Diffraction (XRD)

X-ray diffraction techniques are utilised to analyse and identify the mineralogical structure and composition of a material. As shown in Figure 9, an x-ray beam of a specific wavelength (incident ray) is incident on the surface of a material interacting with surface and inner depth atoms, which

subsequently reflect the x-ray beam. The theory of x-ray diffraction as reported by R. Chang [30] relies on Bragg's law and the associated Bragg equation:

$$2d\ \sin\theta = n\lambda, \text{ where } n = 1,2, \ldots$$

Considering $n = 1$ (1st order diffraction):

$$2d\ \sin\theta = \lambda$$

where d = interatomic planar distance (Å), $\sin\theta$ = angle of diffraction (°) and λ = x-ray wavelength (Å).

This law demonstrates that the path length between two wave phases equates to $2d\ \sin\theta$. For constructive interference between the reflected rays from varying planes within the crystal lattice structure, as illustrated in Figure 9, Bragg's law must be satisfied [30].

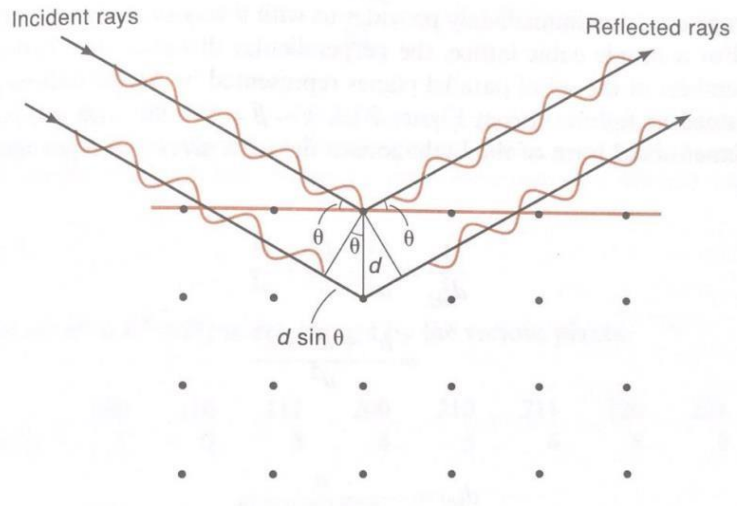

Figure 9. Diagram illustrating the constructive interference of x-rays between planes within a crystalline lattice [30].

XRD techniques can be employed to assess potential mineralogical structures within Lunar and Martian simulants being modified. This includes understanding both the amorphous and crystalline content, but also how this may be altered due to abrasion through ball milling. The mechanochemical-induced production of secondary minerals from primary minerals, the increase in oxocarbon compounds and any other alterations in mineralogy as a result of milling can be inferred from XRD analysis. However, there are a few limitations to this approach. Due to the complex nature of the materials being analysed and their constituent minerals, simple classification and identification of crystalline phases are typically only tentative suggestions. Thus due to the geochemically-innate properties of the samples run using XRD, standard reference data was often not readily available.

1.6.3 ATR-FTIR Spectroscopy

ATR-FTIR spectroscopy utilises the reflectance of infrared light off the surface of a crystal, which is subsequently monitored by the FTIR detector system. The depth at which the infrared radiation is absorbed depends on its angle of radiation and its wavelength [30]. FTIR spectroscopy often uses a focal plane array detector rather than a single element detector, which collects the resulting spectra. A penetration depth of ~ 0.5 µm – 5 µm is usually utilised from the internal reflection element's surface which is usually composed of diamond, ZnSe, Si or Ge. Infrared radiation comes into contact with the sample layer which is situated upon the internal reflection element surface as illustrated by the diagram in Figure 10 [31].

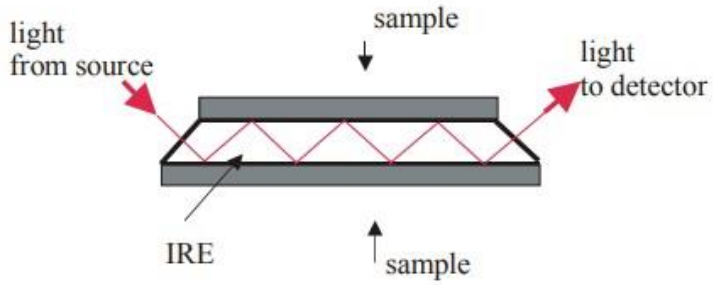

Figure 10. Diagram illustrating the absorption of infrared light and its pathway from source to detector [31].

FTIR is non-destructive, typically more economical in comparison to Raman spectroscopy (due to Raman spectroscopy requiring highly powered laser apparatus) and has the ability to detect organic mineral inclusions [33]. However, given the high inorganic content of the regolith analogues, Raman spectroscopy would often be a more reliable and useful analytical technique due to reduced interference, in particular regarding regolith-ice mixtures due to water displaying weak scattering [32,33]. Additionally, Raman spectroscopic methods can also identify specific metal-ligand complex feature such as Si-O-M^+ bonds, whereas some of these may have only very low/almost negligible absorption bands in an infrared spectrum [32]. However, due to obscuring of data from fluorescence, previous and current research at the University of Kent has shown that Raman measurements of Lunar and Mars analogues are experimentally challenging, in particular for the Earth-based JSC-Lunar simulant.

1.6.4 Scanning Electron Microscopy-Energy Dispersive Spectroscopy (SEM-EDS)

SEM analysis relies on electron bombardment. The sample is observed under vacuum and scanned with a beam of electrons which have been accelerated down a column within the SEM apparatus as illustrated by Figure 11, and focused using various apertures and lenses onto the sample. The electron and surface atom interaction electrons (backscattered and secondary) are collected and measured to produce images. [34]. EDS mapping is a complementary technique whereby x-ray spectroscopy is utilised for elemental

characterisation and identification. This process involves collecting x-rays generated by the electron beam interactions with the sample. If collected over an entire frame, these can be combined to generate an elemental map of the surface [34,35] (refer to Figure 12 below for an example of elemental mapping).

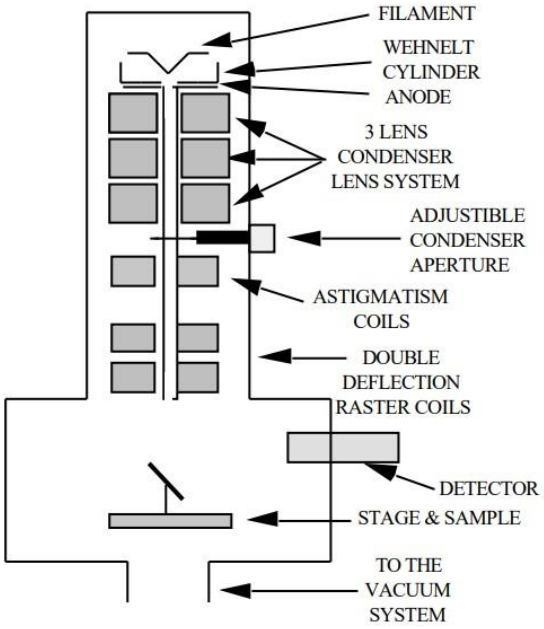

Figure 11. Diagram illustrating components of a SEM [34].

SEM methods can show great detail when observing the topographies of grains, their size uniformity and morphologies. Given the complex nature of the mineralogies and elemental abundances within the regolith samples, EDS mapping is not straightforward due to large variations within the area being examined. The high quality imaging of individual grains provides ideal complementary data to XRD analyses, although samples must be carefully prepared to avoid the introduction of artefacts [34].

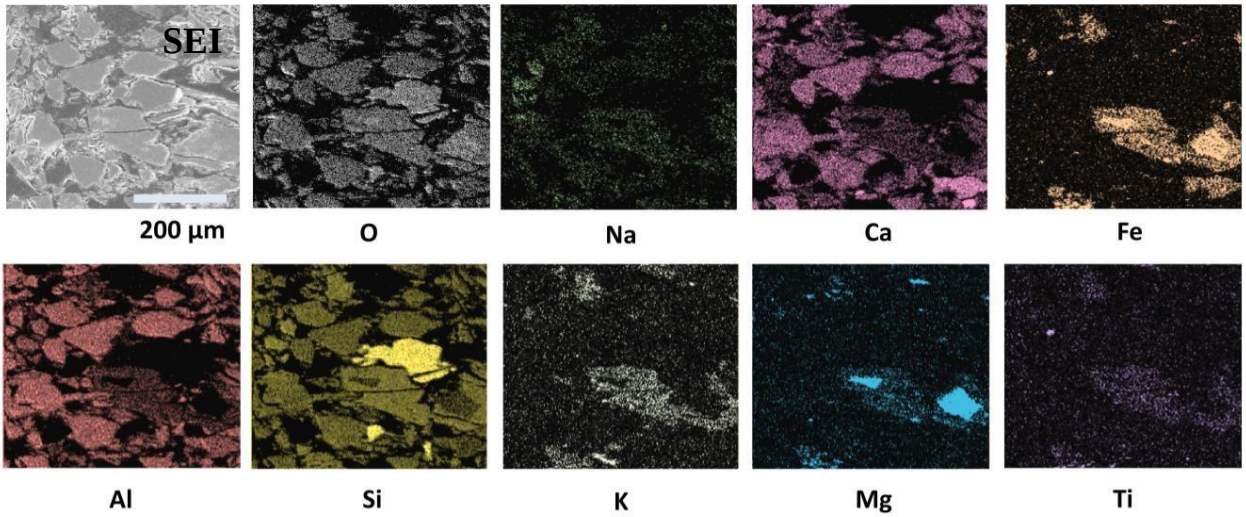

Figure 12. EDS mapping of the LHS-1 planetary analogue, displaying individual maps labelled based on the element they represent [12].

1.6.5 Thermogravitational Analysis (TGA)

Thermogravitational analysis relies on the constant weighing of a small sample (within a crucible as seen in Figure 13) whilst heating at a constant rate to a predefined, maximum temperature. Whilst heating, an inert gas (e.g. N_2) is introduced into the system. Changes in mass (an increase and/or decrease depending on liberation and/or uptake of species), are typically due to loss of water and liberation of volatile species. Structural phase transitions may also simultaneously/solely occur at certain temperatures [36]. Other processes that may lead to the change in mass include oxidation, decomposition, decarboxylation and pyrolysis [36,37].

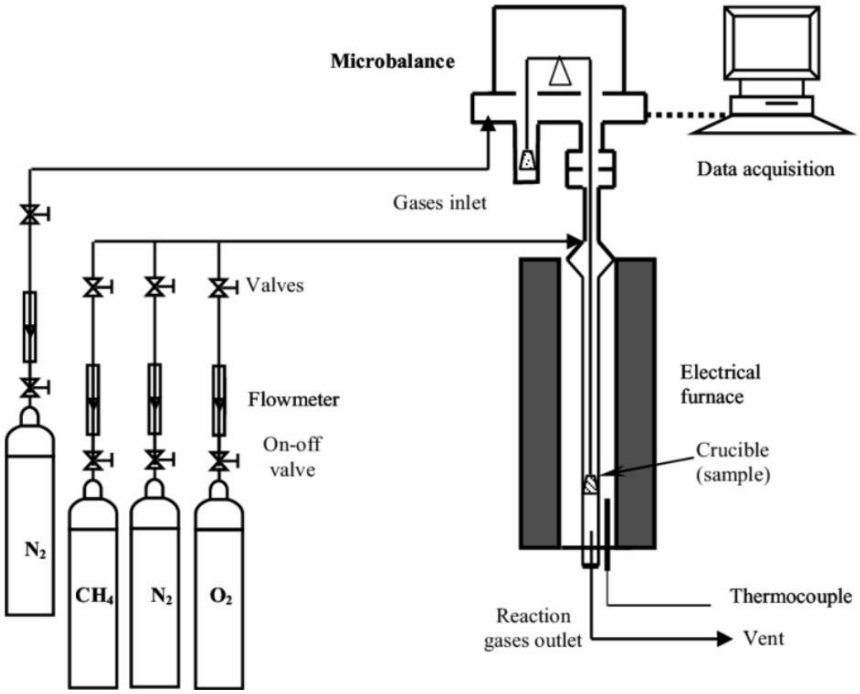

Figure 13. Diagram illustrating a typical TGA apparatus setup of a sample being heated within a crucible under a constant flow of nitrogen gas within the reaction system [38].

Whilst thermal degradation of materials such as the Lunar and Martian regolith analogues can provide vital information on the thermal effects on mineral surfaces and their pores at the microscopic scale, due to their complicated geochemical properties, the exact reasons for mass loss/gain may be difficult to unambiguously obtain. In order to gain a better understanding of the changes occurring, TGA is ideally used in conjunction with XRD and ATR-FTIR techniques, in order to increase confidence in findings. Heating of the regolith samples following milling indirectly allows an analysis of the effect of abrasion on the chemistry of such materials to be assessed. Subjecting the materials to high temperatures will also simulate on a small scale the effects of the harsh climatic conditions experienced by the surface soil.

Research conducted on the Lunar and Martian planetary analogues and their preliminary characterisation as presented within this thesis has included not solely an understanding of their physical and chemical properties, but also a direct comparison between the Earth-based and synthetic materials. The primary scientific aims within research were to employ ball milling techniques to simulate the potential induced chemistry and abrasion-induced mineralogical alterations occurring on the Lunar and Martian surface due to regolith transport. Assessing the induced chemistry from regolith transport and mixing with ices and thus collisional impact processes by simulating abrasion through ball milling is a novel area of research as space exploration continues and develops. Therefore, this is extremely critical as we aim to explore these planetary surfaces with greater detail and more advanced on-board instrumentation.

Overall, the experiments conducted within this research to assess the mechanochemical-induced alterations in chemistry and mineralogy as an effect of regolith transport are novel, yet extremely important. Through concluding which planetary analogues are most suitable for assisting data interpretations gathered from space exploration, more accurate conclusions can be drawn, thus allowing the development of improved analogue materials on Earth.

Chapter 2: Experimental Methods

Preliminary characterisation of the Lunar and Martian simulants utilised was first conducted to provide a standardised baseline for subsequent comparative analyses to be made when assessing the effect of ball milling and thus mechanochemical-induced alterations on mineralogical structure, chemical composition and bonding. Each of the simulants being analysed, whether they be Earth-based or synthesised within the laboratory, were composed of varying minerals and abundances. These mineral substances were already blended together, either by means of natural weathering processes occurring on Earth for an unknown prolonged period of time, or mechanically within the laboratory, therefore yielding reactive mineral products. In order to identify specific minerals and mineralogical structures present within the raw and milled simulants, the pure, raw Earth minerals of relevance were also characterised utilising identical analytical techniques to obtain preliminary data. Such results could then be utilised when analysing the raw analogue materials, and how their mineralogical composition varied upon milling.

A second, key element of experimental work was the simulation of environmental icy conditions and H_2O ice-driven geochemical reaction processes occurring on the Lunar and Martian surface (refer to chapter 5) through the incorporation of H_2O ice by means of ball milling. As discussed subsequently within this chapter (refer to subsection 3.7), differently treated water ice, namely deionised, distilled and tap, was combined with regolith samples prior to milling due to the varying minerals present depending on the water's origin and treatment.

The entire preliminary characterisation and further analyses conducted employed a varied range of analytical techniques and apparatus, as discussed subsequently within this chapter. Sifting of the pure, raw Earth minerals and regolith analogues by means of sieving was conducted to collect grain size distribution data. Optical microscopy and SEM were utilised to observe physical properties, for instance, surface textures and grain morphologies/geometries of pure, raw Earth minerals and regolith analogues. Shearing of any potential crystalline layers within the material structures and any potential alterations to their amorphous content caused by milling were thus recorded through visual observations. XRD techniques were utilised to characterise crystalline phases and oxide components within the structures observed. ATR-FTIR was employed as a spectroscopic technique to analyse chemical composition and mode of bonding, including alterations due to mechanochemical activation effects. TGA was utilised to analyse the effect of heating on crystalline phases and chemical composition on the pure, raw Earth minerals and simulants.

2.1 Preliminary Characterisation of the Pure, Raw Earth Minerals and Regolith Analogues

Materials utilised within this research as seen in Figures 14 and 15 (the pure, raw Earth minerals and simulants, LHS-1, and MGS-1) were acquired from ExoLith laboratories, University of Central Florida [4]. JSC-1A Lunar and JSC-1 Mars simulants were acquired from existing stock within the Center for Astrophysics and Planetary Science impact laboratory. Gathering preliminary composition and abundance data of the pure, raw Earth minerals allowed direct comparisons to be made to simulant materials after milling. Identifying the constituent elemental components and interpreting the varying reaction pathways and processes occurring within the raw materials, innately enhanced analysis of the regolith analogues when assessing the alterations in mineralogy and chemical composition upon milling.

It was originally intended that the individual constituents within each Earth mineral sample would be ascertained by X-Ray Fluorescence (XRF) analyses, however, due to apparatus system failure this was not possible, thus charactertisation relied solely on XRD and ATR-FTIR techniques to assess oxide phases and chemical composition and bonding/structural integrity.

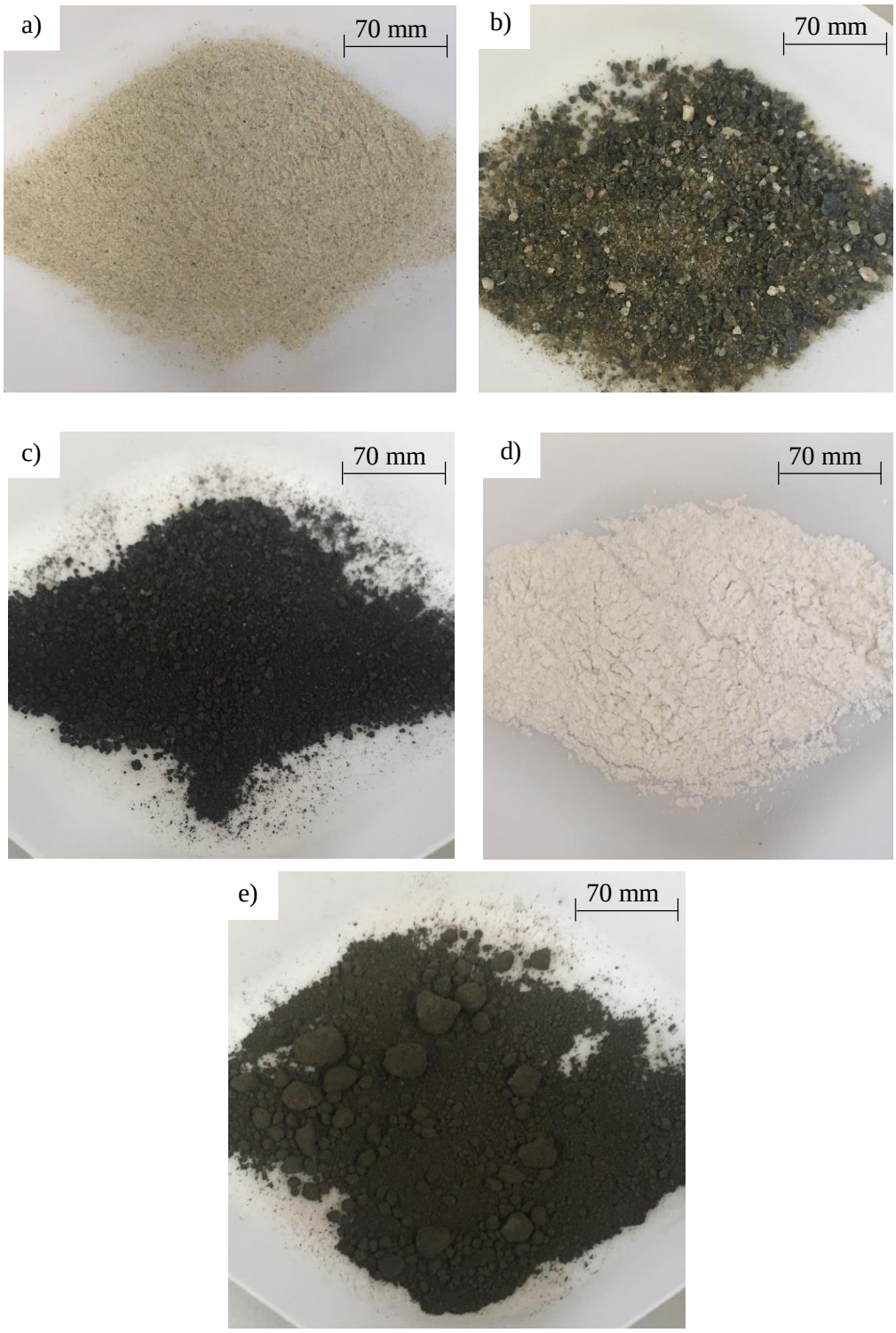

Figure 14. Photographs taken of the pure, raw Earth rock and mineral samples a) olivine; b) bronzite (pyroxene); c) lava rock basalt; d) anorthosite rock; e) ilmenite.

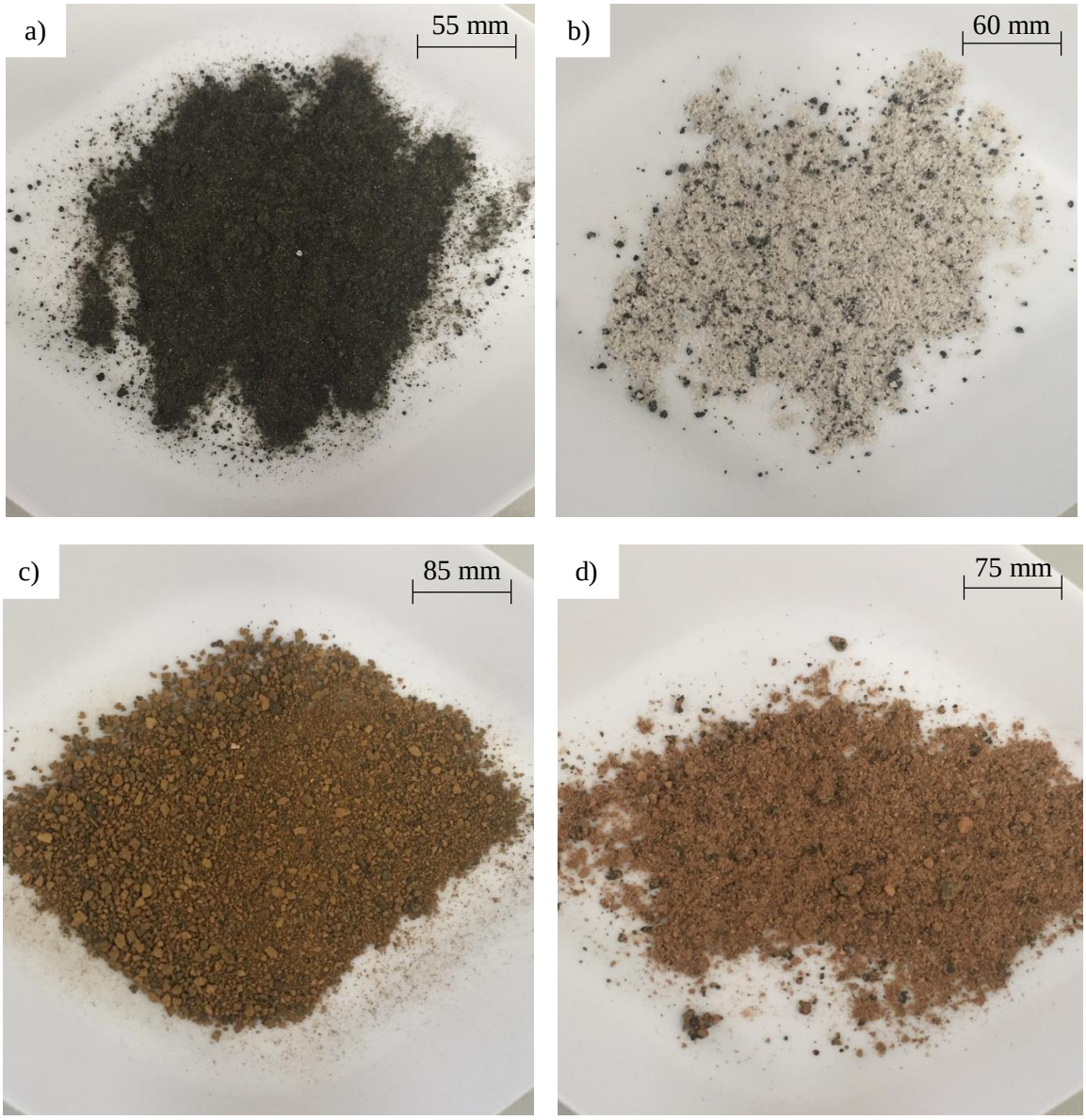

Figure 15. Photographs taken of the raw planetary analogue samples a) JSC-Lunar; b) LHS-1; c) JSC-Martian; d) MGS-1.

2.2 Mechanochemical Activation by means of Ball Milling

The sole mechanochemistry technique utilised within the research was ball milling. Three different types of ball mill were employed: The Retsch MM301 mixer mill, the Fritsch P23 mini mixer mill and the Fritsch P7 planetary micromill (as shown in Figure 16). All apparatus (reaction vessels and ball bearings) was composed of stainless steel or hardened steel (regarding the Fritsch P23 mini mixer mill), as seen in Figure 17. Any lubricant materials were omitted from reactions to prevent/reduce chemical contamination and thus misinterpretation of results.

Figure 16. Photographs taken of a) Retsch MM301 mixer mill; b) Fritsch P23 mini mixer mill; c) Fritsch P7 planetary micromill.

a)

b)

Figure 17. Photographs taken of empty stainless steel reaction vessels and ball bearings for a) Retsch MM301 mixer mill; b) Fritsch P23 mini mixer mill; c) Fritsch P7 planetary micromill.

2.2.2 Retsch MM301 Mixer Mill

The University of Kent's Retsch MM301 mixer mill was employed to experimentally replicate modes of geographically longer-distance regolith transport occurring on the Lunar and Martian surfaces, for instance through short range saltation and abrasion within dust devils. Secondary collisional impacts, perhaps due to meteoroidal impact ejecta striking the Lunar and Martian surface can also be simulated by this milling type. Mechanically, the mixer mill oscillates horizontally, and a stainless steel vessel (15 mL) containing the milled material is held by compression of two metal plates either end of the vessel. Stainless steel ball bearings (3 x 5 mm) were placed in the vessel combined with ~ 5 g of simulant. A maximum of ~ 1/3 of the vessel is filled to prevent an over-pressurised reaction system and thus excess gaseous accumulation but also to ensure efficient grinding and sufficient collisional contact between the regolith material and ball bearings. Apparatus conditions were continuously controlled (temperature being approximately monitored through simply assessing the surface temperature of the interior of the reaction vessel and the ball bearings through touching the surface – an increase in the system's temperature is inevitable due to collisional heating) and the milling frequency maintained at

10 Hz. Milling times of 2, 4, 6, 8 and 10 minutes were carried out to observe changes in not solely just physical properties such as grain size distribution, but also effects on mineralogical structure and chemical composition. Minor amounts of Fe and Fe_2O_3 may potentially be generated during the milling process due to ball bearings impacting with each other (not solely grinding the material), and therefore rust residue may be observed (as demonstrated in Figure 17a). Any potential contamination was minimised by utilising a relatively small number and size of ball bearings and thoroughly cleaning both the milling vial and ball bearings after each use. Despite this inevitable possibility, this by-product was not predicted to influence the overall composition of the constituent minerals due to the relatively high abundance of iron oxide components already present within the analogue samples (for instance the JSC-Lunar simulant has an Fe_2O_3 abundance of 11.4 wt %).

2.2.3 Fritsch P23 Mini Mixer Mill

A Fritsch P23 mini mixer mill was utilised in conjunction with the Retsch MM301 mixer mill to provide a direct comparison between horizontal and vertical collisional impacts, with both simulating longer-distance transport across a bedrock surface. Secondary collisional impacts for instance due to meteoritic bombardment can also be simulated, in a similar manner to the Retsch MM301 mixer mill. A significantly smaller hardened steel vessel (5 mL) of oval shape and hardened steel ball bearings (8 x 3 mm) were used (as shown in Figure 17b), with ~ 2 g of simulant (ensuring a maximum of ~ 1/3 of the vessel is filled). The milling frequency was maintained at 30 Hz and grinding times of 2 and 10 minutes were conducted, omitting intermediate times after initial experimentation with the Retsch MM301 mixer mill. Lubricant material to reduce frictional forces was omitted to prevent chemical contamination through incorporation into the samples. Iron and iron oxide residue was not as noticeable as expected in comparison to the Retsch MM301 mixer mill, despite a greater volume of ball bearings. Despite a greater frequency of collisions occurring between the ball bearings, a plausible explanation is the more durable hardened steel of the P23 vial and ball bearings is better suited to resist collision-induced corrosion than the stainless steel of the MM301 apparatus.

2.2.4 Fritsch P7 Planetary Micromill

The University of Kent's Fritsch P7 Planetary micromill operates by grinding the material both vertical and elliptically simultaneously (refer to Figure 18 below [37]), replicating weathering caused by processes such as localised gardening of regolith, whereby material is oscillated or transported across a surface contained within a small, confined area such as a crater. Samples (~5 g of each simulant was used, ensuring a maximum of ~ 1/3 of the vessel is filled) were run in batches of two, and hardened stainless steel reaction vessels (12 mL) and ball bearings (50 x 3 mm) were utilised (as seen in Figure 17c). Milling times of 2 and 10 minutes were employed, with a frequency of 400 rpm.

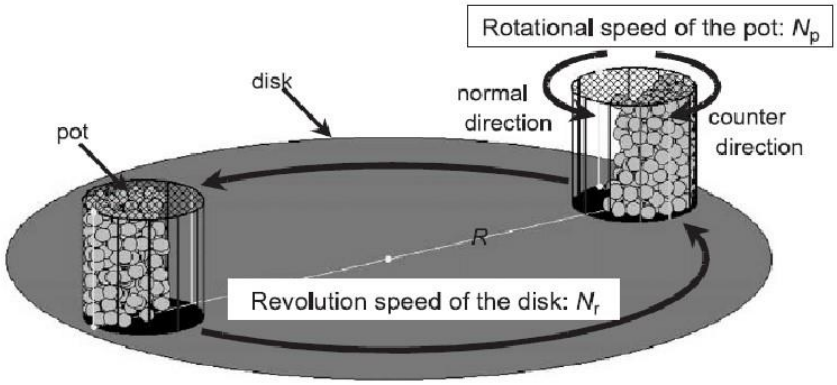

Figure 18. Schematic diagram illustrating the mechanical operations regarding a planetary ball mill [39].

2.3 Grain Size Distributions and Morphologies

Initial grain size distributions of the pure, raw Earth minerals and regolith analogues were measured by means of sifting through utilising a set of sieve trays, ranging from numbers 40 to > 250 as seen in Figure 19 (refer to Table 1 for tray number to pore size conversion [40]). The effect of milling on sample homogeneity was subsequently assessed again through repeated sifting measurements, with the mass sifted through (mass remaining) at each corresponding sieve pore size recorded. All regolith samples milled for 0, 2, 4, 6, 8 and 10 minutes were sieved to assess the effect of increased abrasion on grain size distribution and thus sample homogeneity.

Optical microscopic methods were employed to observe the physical appearance of the pure, raw Earth minerals and the raw, un-milled regolith analogues, assessing the samples' surface textures and general appearances. Magnification was kept constant at 0.2 mm.

The University of Kent's Hitachi High Technologies S-3400H SEM apparatus was employed to observe granular morphologies and grain textures (and topography). Magnification varied depending on the sample being analysed, and an accelerating voltage of 10 kV was utilised on the SE (secondary electron) setting rather than BSE (back scattering electron) as it analyses the surface topographical properties such as texture.

Table 1. Sieve pore size (µm) corresponding to sieve tray number [40].

Sieve Tray Number	**Sieve Pore Diameter (µm)**
40	420
60	250
80	177
100	149
120	125
250	~ 63 – 53
> 250	< 53

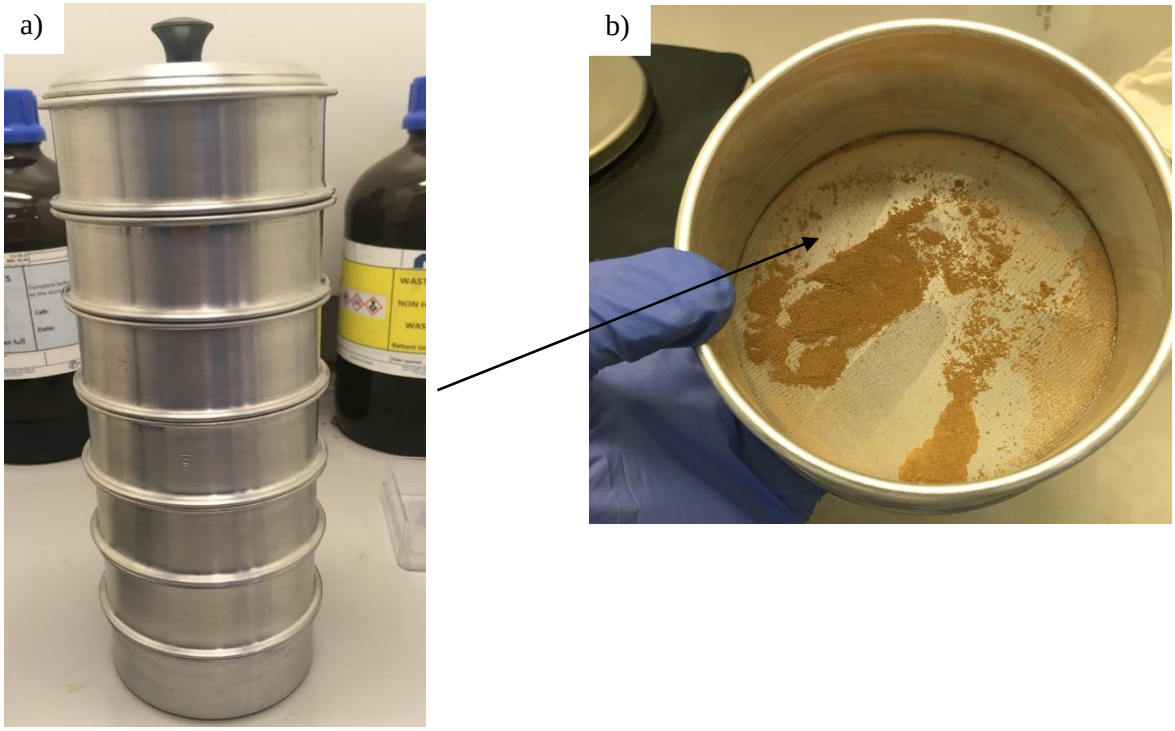

Figure 19. Photographs taken of a) Set of sieve trays of sizes 40 to > 250 (mesh pore diameters of 420 µm to < 53 µm [40]); b) Example of interior of sieve tray with mesh pore size µm showing mass of MGS-1 simulant collected (upon 6 minutes of milling).

2.4 X-Ray Diffraction Assignment Techniques to Assess Mineralogy and Mineralogical Structures

The University of Kent's Rigaku MiniFlex 600 was employed (utilising Cu Kα radiation) to assess the effect of milling on mineralogy and mineralogical structures and any potential crystalline phases. Silica-based XRD glass sample plate holders (0.2 mm in depth) were used for loading the materials.

The pure, raw Earth minerals and regolith samples were run for a scan time of ~ 3 hours (scan speed of 0.3° min^{-1}) at an angle range of 10°-70° (steps of 0.02°) and set to spin in order to allow an evenly distributed proportion of the sample to be penetrated by the active x-ray radiation and thus prevent preferred orientation. The x-ray tube voltage was 40 kV, and current 15 mA. The attached condenser system had a constant water flow rate of 4.6 L min^{-1}. The PHA baseline was 39 div, and PHA window 15 div.

All XRD data analysis and characterisation was conducted using the PANalytical software Highscore [40] within the laboratory. Subsequent formatting and further analyses were conducted using the CrystalDiffract (CrystalMaker Software Ltd.) for presentation of finalised data and assigning diffraction angle values. Such methods were employed due to literature searches and online databases (namely ICSD) yielding few useful references regarding the relevant minerals and their constituent elemental oxides and crystalline phases.

2.5 Spectroscopic Experimental Work on Pure, Raw Earth Materials and Regolith Analogues

The University of Kent's Shimadzu IRAffinity-1S ATR-FTIR spectrophotometer was utilised to analyse the effect of milling on the chemical composition and structural bonding. The pure, raw Earth materials and regolith samples in their raw form and those milled for 2 and 10 minutes were analysed within a wavenumber range of 4000 cm^{-1} to 500 cm^{-1}. A spectral resolution of 4 cm^{-1} was set, with a scan speed of 2.8 $cm^{-1}s^{-1}$ and an aperture delay of 10 s.

2.6 Thermogravitational Analysis

The University of Kent's Netzsch 409 PG/PC TGA Thermogravimetric Analyser was utilised to assess the potential changes in relative mass upon heating, and therefore potential liberation of water and/or volatiles. All samples were heated in an alumina crucible (weight 161.6 mg) from room temperature (25 °C) to 1000 ℃ at a heating rate of 20 K min^{-1} under a constant flow of $N_{2\,(g)}$ at a flow rate of 30 mL min^{-1}. A high temperature was utilised due to substantial silica abundance, and therefore stable Si-O-Si intramolecular (in between crystalline layers) and intermolecular (strong covalent and ionic bonding within a tetrahedral geometric structure) bonding throughout the crystalline structural network within all the Earth minerals and analogues (elemental silica exists in a stable form and is naturally relatively inert). The samples' physical appearance was observed and photographically recorded, noting down changes in colour upon heating and the effect of milling time.

2.7 Incorporation of Ice

Water ice was prepared using three different forms of water treatment; deionised, distilled and tap water, to analyse how the varying mineral content (refer to chapter 5) of each affected the regolith's mineralogy, mineralogical structure, and underlying chemistry. Whilst the ratio of ice to regolith material is clearly a critical parameter to induce these alterations, a constant ratio of 25 % ice to 75 % regolith material was employed. This ratio was selected as a compromise for these preliminary experiments, ensuring a sufficient quantity of ice to successfully measure its effect during the milling process, but also prevent sample analyses (e.g. FTIR and TGA) being dominated by water, leading to inconclusive results. Other proportions of regolith and ice may be considered to simulate different icy conditions on the Lunar and Martian surface and are discussed in the future work (chapter 6). The University of Kent's Retsch MM301 mixer ball mill was employed to mill the raw, unadulterated analogues with 25 % water ice. As previously conducted, ~ 1/3 of the vessel was filled to prevent an over-pressurised reaction system and thus excess gaseous accumulation, but also to ensure efficient grinding and sufficient collisional contact between the regolith material and ball bearings. A pestle and mortar were utilised to rapidly crush the ice cubes before transferring ~ 1.25 g to the stainless steel reaction vessel, before combining with the simulant material (3.75 g) in the milling vial. Milling times of 2 and 10 minutes at a frequency of 10 Hz were employed. Melting of the ices utilised during experiments was inevitable, primarily due to an uncontrollable temperature increase during milling within a closed system (through conversion of kinetic energy to heat due to mechanochemical-driven work). Distinguishable separation of layers for each regolith-ice sample was noted and recorded, as detailed in chapter 5.

Figure 20. Photograph taken of LHS-1 simulant milled with 25 % deionised water ice after milling for 10 minutes using the Retsch MM301 mixer mill.

2.7.2 Assessing Alterations in Mineralogy and Mineralogical Structure

Regolith-ice mixtures were dried in a desiccator (refer to Figure 21) (using sodium carbonate desiccant) for > 24 hours before being run on the University of Kent's Rigaku MiniFlex 600. Silica-based XRD sample holders were used for loading the materials. Ice mixtures milled for 2 and 10 minutes were analysed for scan times of ~ 3 hours and at an angle range of 10° - 70° and set to spin. A step angle of 0.02° and scan speed of 0.3° min^{-1} were utilised. Highscore software was employed to characterise mineral contributions and identify diffraction angle values and mixed phases [39].

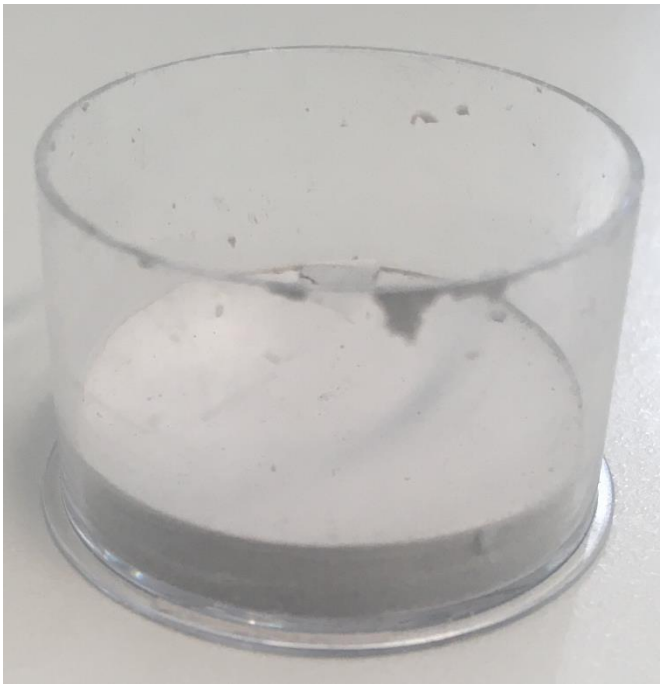

Figure 21. Photograph taken of LHS-1 simulant 25 % deionised H_2O ice mixture dried for > 24 hours.

2.7.3 Assessing Alterations in Chemical Composition and Mode of Bonding

The wet regolith-ice samples were run on the ATR-FTIR spectrometer within a wavenumber range of 4000 cm^{-1} – 500 cm^{-1}. Due to the emergence of distinct layers within each sample as seen in Figures 21 and 22, top and bottom layers were extracted and analysed to assess whether their chemical compositions differed.

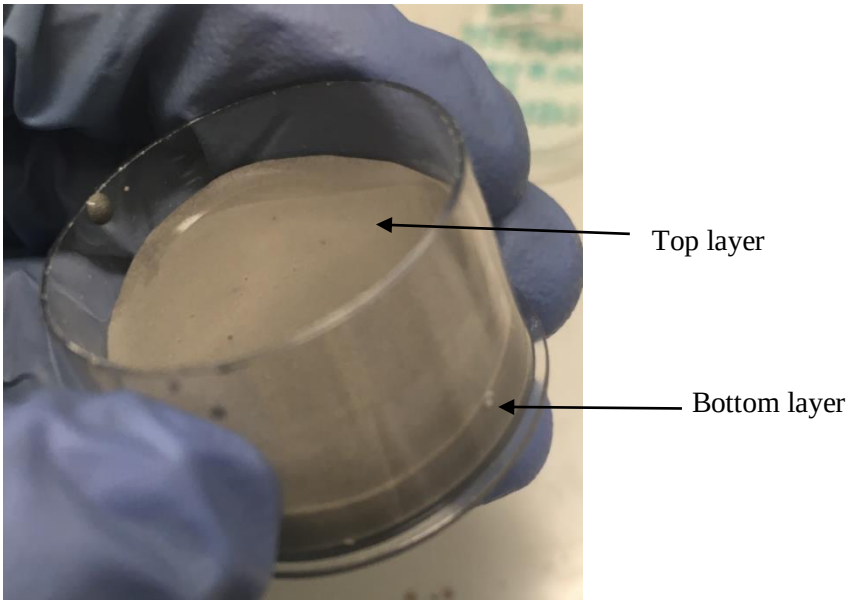

Figure 22. Photograph taken of LHS-1 simulant milled with 25 % tap water ice for 10 minutes using the Retsch MM301 mixer mill, demonstrating the two distinct layers collected in the sample vial.

2.7.4 Thermogravitational Analysis of Regolith-Ice Mixtures

Dried regolith-ice mixtures were run on the Thermogravitational Analyser and heated to 1000 ℃ to assess the potential effect of milling with water ice on thermodynamically-driven chemical reactions and possible phase transitions.

Chapter 3: Characterisation of the Raw Lunar and Martian Simulants and their Constituent Raw Earth Minerals

The analogue materials utilised during experimental work in the laboratory all consisted of constituent minerals present in varying abundances, and prior to milling, preliminary characterisation was conducted upon such minerals in their raw form, rather than blended with one another. The Earth materials olivine, ilmenite, basalt (lava rock), pyroxene (bronzite) and anorthosite rock were obtained from ExoLith laboratory, central Florida. The pure minerals handled by ExoLith were compared against analysed data from collected Lunar soil samples during the Apollo missions, therefore have analogous grain textures and size distributions [4].

The simulants being analysed, whether Earth-based or synthesised within the laboratory, all possessed varying initial grain size distributions which were crucial physical properties to take into consideration before assessing the effects of ball milling on sample homogeneity. During the milling process, one predicted factor affecting collisional impacts between grains was their diameters and thus surface areas, influencing the surface's exposure to mechanochemical impacts and rate of mechanochemical reactions occurring within the closed reaction system. The Earth-based simulants (JSC-Lunar and JSC-Martian) being purposefully manipulated were naturally weathered for years prior to sampling during fieldwork, and therefore their initial grain size distributions were already altered and natural variation expected [2, 11]. As discussed later on during this chapter, this was observed prior to milling with the initial grain appearance of the Earth-based simulants being finer and somewhat more powdered compared to the synthesised simulants also being analysed. A direct comparison between the Earth-based simulants against those synthesised within the laboratory was one of the key areas of analysis. Therefore, preliminary characterisation of these simulants (before purposefully shearing their crystalline layers/the materials' structural layers to assess any potential (and predicted) alterations in mineralogy and chemical composition) was essential to comprehend whether utilising a particular form of analogue is more advantageous than another during experiments (refer to chapter 1). Whether of Earth origin or synthesised in the laboratory, it was essential to examine the individual minerals before milling, therefore enabling the effect of grinding to be thoroughly understood. The physical properties of individual mineral components for each simulant were required including which mineral group they were classified under, their crystal structure and chemical properties. Prior to ball milling, individual minerals within the simulants were already interconnected and blended together, either naturally (environmental weathering over hundreds if not thousands of years) or synthetically (through controlled and purposeful blending of reactants, producing such simulants through milling itself). A combination of the constituent chemical components and elemental abundances within each mineral therefore affects the physical and chemical properties of the simulants.

A general hypothesis was gathered on the effect of milling on sample homogeneity and therefore grain size distribution. It was predicted that as the milling time increased, simulants' grain size distributions would become narrower and thus more uniform. This is due to the activation stage of the milling reaction; whereby size reduction occurs due to the mechanochemical breakdown of material into smaller fragments [28].

3.1 Elemental and Oxide Abundances

A literature search yielded little data concerning the chemical composition and abundances of the specified minerals analysed within this research other than that of olivine, therefore XRF (X-Ray Fluorescence) analyses were scheduled to be utilised to collect local experimental data on the constituent oxides within the pure, raw mineral samples. However, instrument error caused delays in such measurements, therefore this data cannot be presented. Data gathered in such a manner allowed for natural variability of mineral abundances within each simulant to be accounted for, as this is affected by the origin of each analogue material. Earth-based simulants and their constituent minerals will have been weathered and eroded gradually for a considerable number of years, and therefore compounds such as prominent oxides will be present in varying abundances and the number of ionic sites and active M^+ surface cations within the material will differ to those synthesised within the laboratory. Environmental and geochemical conditions are geological factors affecting the formation of such minerals, and therefore their potential oxide abundances. Another variable affecting the mineralogical composition would inevitably be which geographical area the analogue is imitating, for instance JSC-Lunar simulant is analogous to the average surface of the Moon, whereas LHS-1 simulant is specific to the highland, higher altitude regions which are composed of more fragmented soil than that of the mare regions due to being more heavily bombarded by meteoritic impacts, forcing material from beneath the surface upwards [12].

Olivine, a magnesium iron silicate, of general chemical formula $(Mg, Fe)_2SiO_4$, is naturally occurring across the Earth's surface, however, the majority is mined in Norway and naturally exists in igneous rocks and granite [42]. Depending on composition, it can be of a green appearance (pure Forsterite) or brown (pure Fayalite) with dark inclusions not observed with the naked eye, and has a fine, dust-like granular texture. It is of orthorhombic-dipyramidal crystal structure [42]. Work by Kleiv et al has already suggested the increase in mineral surface activity upon mechanical activation through increasing adsorption kinetics, mineral synthesis rates and catalysis [43]. This study reported the noticeable decrease in surface area after a certain amount of milling, which they discuss is a frequent consequence of milling under dry conditions, and this process of agglomeration after grain size reduction is commonly observed within experiments [43].

Table 2. XRF data for elemental and oxide abundances found in pure, raw olivine (Forsterite) [44].

Element	Abundance (wt %)	Oxide	Abundance (wt %)
Mg	25.37	MgO	42.06
Fe	14.57	FeO	18.75
Si	18.32	SiO_2	39.19
O	41.47	-	-

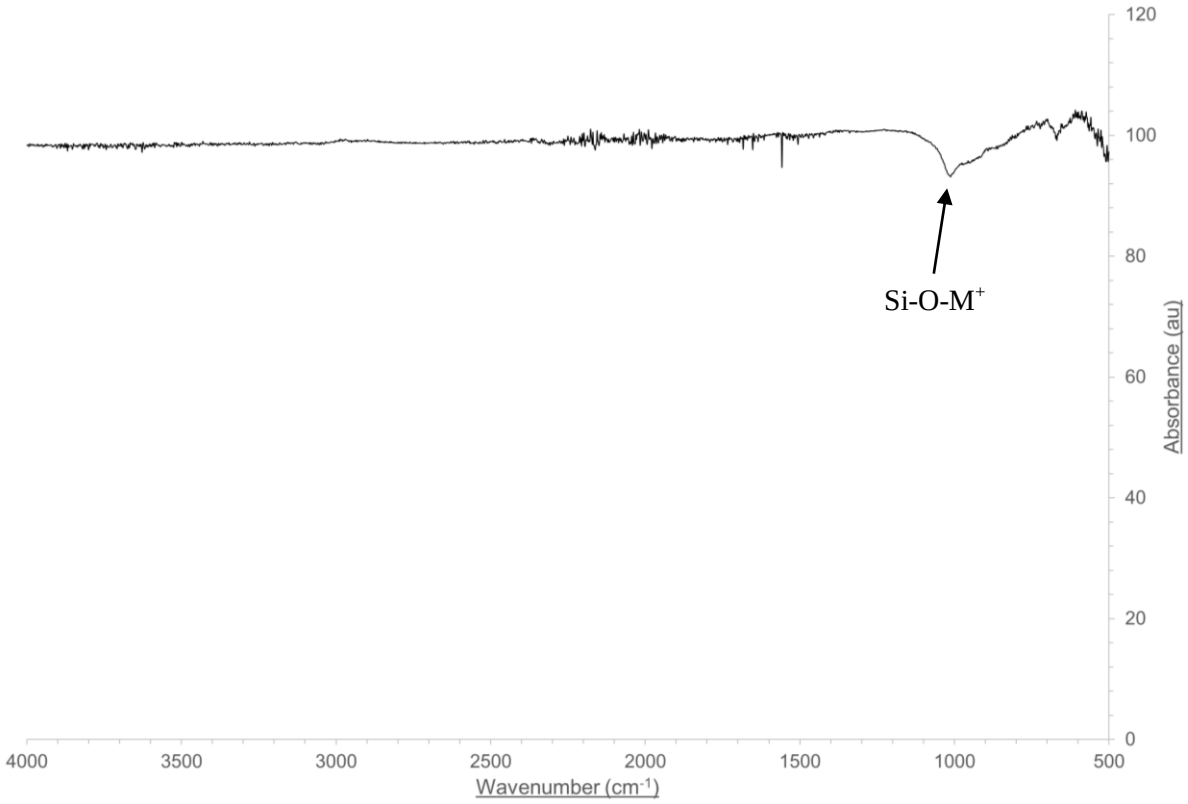

Figure 23. Infrared spectrum for the pure, raw olivine sample with a wavenumber range of 4000 cm^{-1} - 500 cm^{-1}. The absorption band at ~ 1000 cm^{-1} suggests the presence of Si-O-M^+ bonding.

As illustrated in Figure 23 above, the characteristic sharp peak at ~ 3750 cm^{-1} and band at ~ 1200 cm^{-1} for olivine was not observed [45], however, the most noticeable absorption band at ~ 1000 cm^{-1} suggested the presence of a Si-O-M^+ (M^+ = metal cation) bond within the mineral's structure. Due to the known abundances of Mg and Fe within olivine, this was as expected. The slight sharp peak at ~ 1500 cm^{-1} was not successfully characterised, potentially due to instrumental artefacts. Table 2 shown above displays the chemical composition of olivine, which is predominantly composed of MgO [44]. Additional analysis of olivine by means of XRD as discussed further on within this chapter proved to be of great use in comprehending olivine's mineralogical structure. It should be noted that the majority

IR analysis was conducted with characterisation based on literature from Launer e*t al.* [46] for all silica-based spectral bands. Due to the complexity of the simulants and their constituent materials, all analysis and characterisation should not be taken as confirmations, but rather as potential compositions and chemistry.As mentioned in chapter 2, all XRD characterisation and analysis was conducted by employing the PANalytical software Highscore [41] within the laboratory.

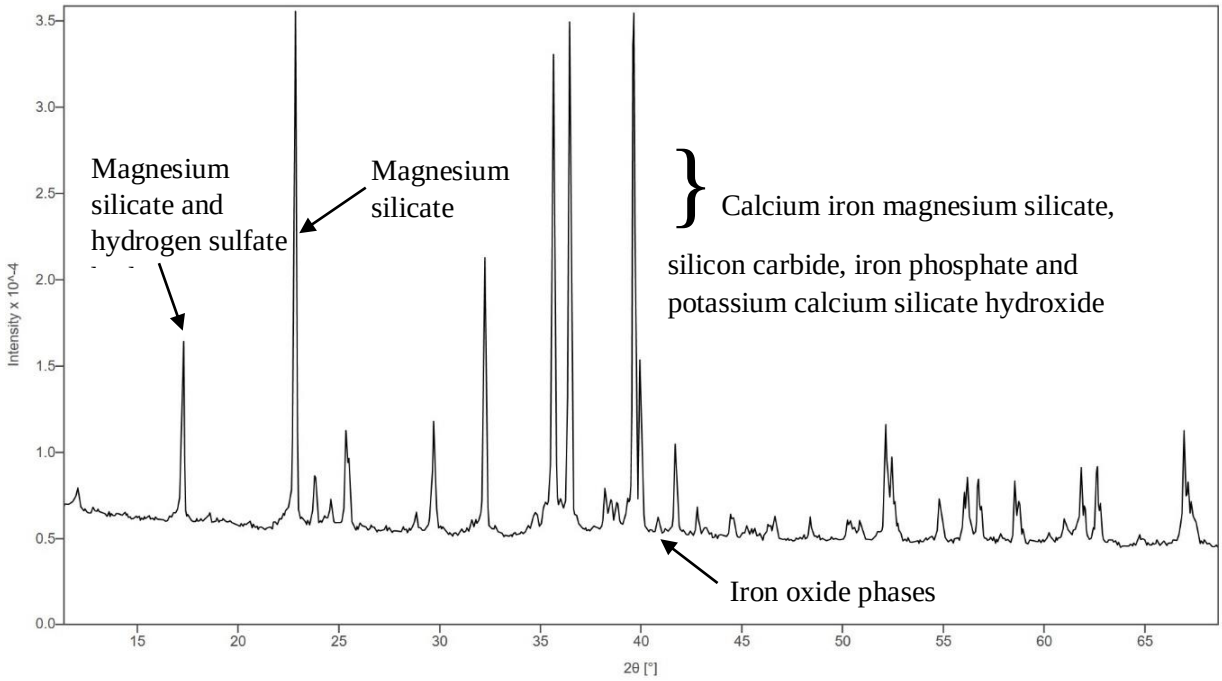

Figure 24. XRD diffractogram of the pure, un-milled olivine between 15°-65° and a scan time of 3 hours.

In contrast to the other pure, raw minerals analysed, un-milled olivine had the sharpest and clearest XRD diffractogram, with the highest SNR (signal to noise ratio) achieved, as seen in Figure 24. The first peak between 15° - 20° was potentially identified as a combination of magnesium silicate and hydrogen sulfate hydrate, indicating the integration of water within the crystalline structure and thus the introduction of hydrated mineral phases The vast majority of the intense peaks throughout olivine's diffractogram are due to the contribution (or partial contribution) of magnesium and magnesium-containing compounds, with a high abundance of magnesium silicate minerals. The most intense, sharp peak at ~ 22.8° was found to be due to magnesium silicate, with slight broadening observed potentially on account of SiO_2 and magnesium hydrogen sulfate. The other three most significant peaks (35.6°, 36.4° and 39.7°) following data characterised at ~ 22.8° suggested potential contributions from magnesium iron silicate, calcium iron magnesium silicate, silicon carbide, iron silicate hydroxide, iron phosphate, potassium calcium silicate hydroxide and magnesium silicate hydroxide. Once more illustrating the high abundance of magnesium and calcium-rich minerals present within the pure, raw olivine. Some few iron and iron oxide phases were observed, with less intense peaks characterised at ~ 41.7°. The suggested increase in reactivity upon milling due to the mechanochemical activation of

olivine may be due to structural disordering of the mineral surface, as similar XRD results were obtained by Kleiv et al, however agglomeration effects reported by researchers is counterintuitive regarding effective surface area [43].

Pyroxenes are a collective group of ferromagnesian silicate minerals with generic formula XYZ_2O_6 whereby X could exist as Na^+, Ca^{2+}, Mn^{2+}, Fe^{2+}, Mg^{2+} or Li^+; Y may exist as Mn^{2+}, Fe^{2+}, Mg^{2+}, Fe^{3+}, Al^{3+}, Cr^{3+} or Ti^{4+}; and Z could exist as Si^{4+} or Al^{3+} [47]. Such minerals are sourced in most igneous rocks, similarly to olivine, with significant abundances of calcium, magnesium and iron-oxides within their crystal structures. It is of orthorhombic and monoclinic crystal structure formations [47]. The pyroxene variety provided by ExoLith, bronzite, is mainly of composition $(Mg, Fe)_2Si_2O_6$, with Mn^{2+} and Ca^{2+} sites [4]. Sourced in various geographical locations, such as Finland and South Africa, bronzite is found in metamorphic rocks, and is naturally synthesised under high temperature and pressure environmental conditions, by means of recrystallisation of already present rocks within the given area of land (metamorphism) [47]. Bronzite's crystallographic structure is of monoclinic arrangement and is of a silicate tetrahedral chain [48].

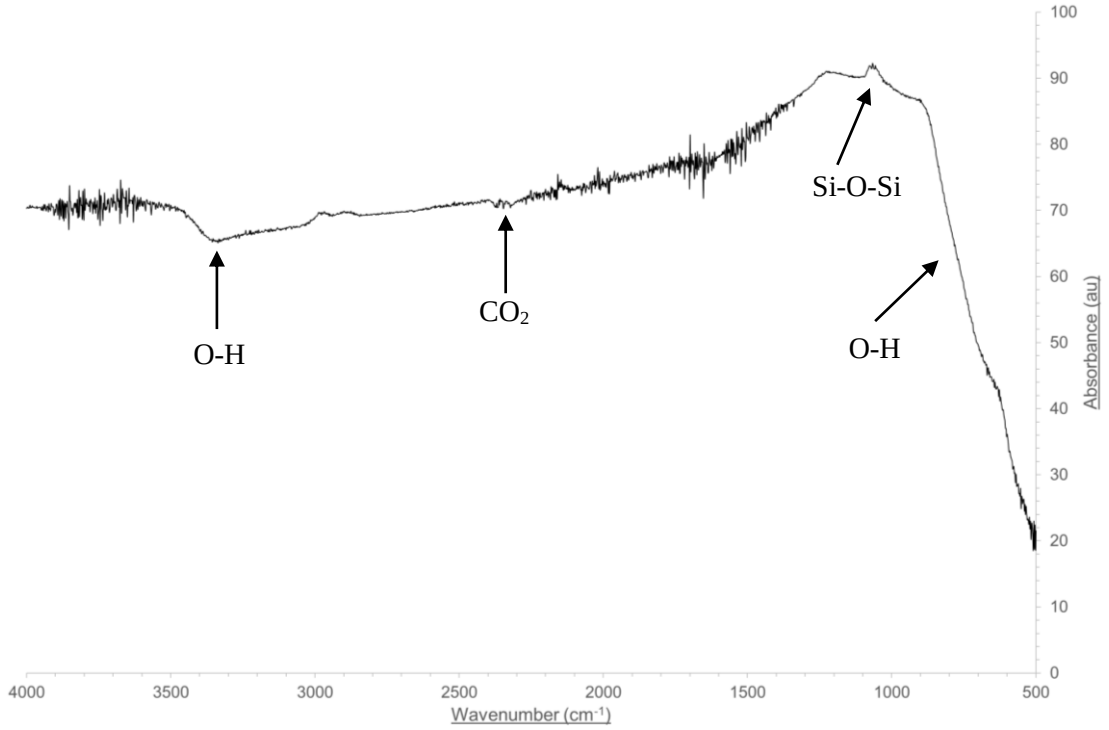

Figure 25. Infrared spectrum for the pure, raw bronzite sample with a wavenumber range of 4000 cm^{-1} -500 cm^{-1}. The absorption bands at ~ 3350 and < 800 cm^{-1} indicate the presence of water.

The infrared spectrum of raw bronzite (Figure 25) showed an extremely small CO_2 band at ~ 2400 cm^{-1}. The subtle yet broad peak at ~ 3350 cm^{-1} and < 800 cm^{-1} indicated contributions from H_2O due to adsorption which has been reported previously in literature for various hygroscopic materials such as hydrolysed calcium chloride [49]. A small transmittance band at ~ 1000 cm^{-1} can be observed, suggesting Si-O-Si contributions.

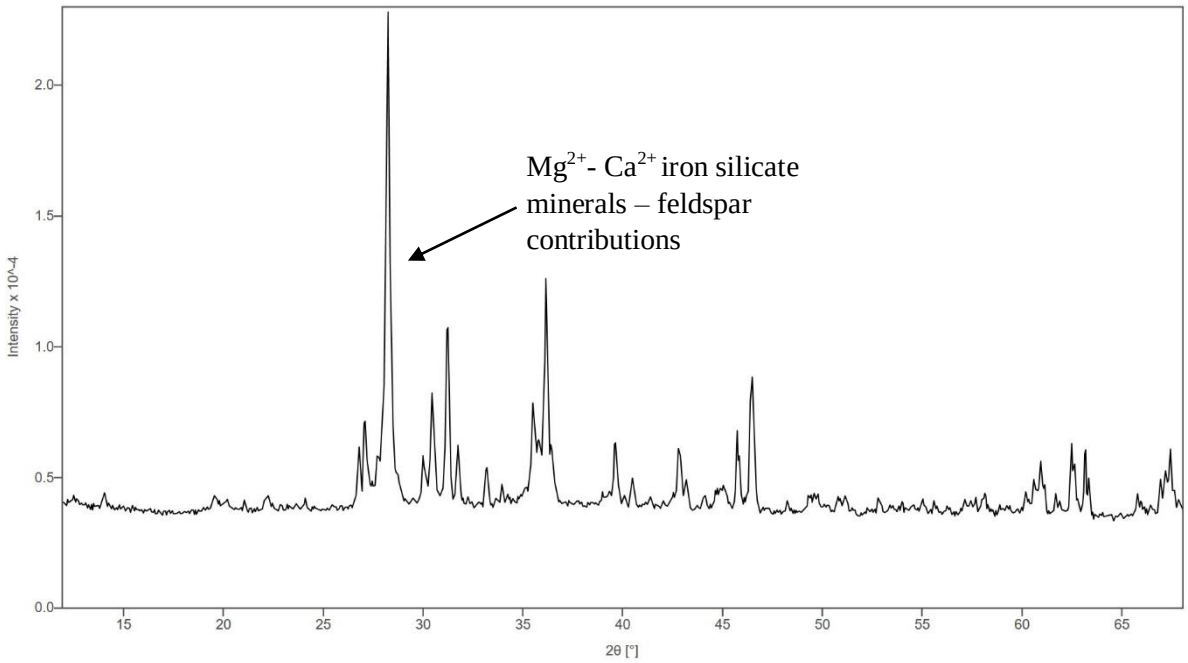

Figure 26. XRD diffractogram of the pure, un-milled pyroxene (bronzite) between 15°-65° and a scan time of 3 hours.

Characterisation of pure, raw bronzite by means of X-ray diffraction analysis (refer to Figure 26) showed a similar, characteristic, sharp intense peak at 28.3°, indicating a silica-based compound, namely Mg^{2+}- Ca^{2+} iron silicate minerals, with some manganese contributions as expected based on literature [47]. Additional peaks characteristic for this ferromagnesian silicate-based mineral suggesting the presence of magnesium iron silicates were observed at angle values of 30.4°, 36.1° and 46.4°, alongside other less noticeable peaks. The relatively intense peak at 31.2° suggests the presence of calcium phosphide, with other insignificant peaks indicating P^{3-} contributions within other anionic sites within the crystalline network, however, current literature does not discuss the integration of phosphates within pyroxenes. The preliminary characterisation of pyroxenes was most important for experimental work conducted on the MGS-1 simulant as the sample provided by ExoLith had the highest pyroxene abundance of 13.7 wt. % compared against the remaining simulants. Exolith specified that the general formula for this Pyroxene variety is $(Mg, Fe)_3SiO_3$ [4]. Nonetheless, Papike et al reports the Mg-rich nature of bronzite found within Lunar soil, contributing to regolith a coarse granular texture [7]. It is noted that the mare regions are more abundant in Fe-rich pyroxenes in comparison to Mg-rich varieties, whilst the opposite is true of the highlands [7].

Anorthosite, which is predominately composed of Ca^{2+} - plagioclase feldspar, is an igneous rock. It is found more commonly on the Lunar surface compared to the Earth's crust [50]. The highland regions of the Moon primarily consist of anorthosite with high crystallinity [12]. Plagioclase is a feldspar mineral of significant abundance on the Earth's crust, and is composed of $NaAlSi_3O_8$ (albite) and $CaAl_2Si_2O_8$ (anorthite) [50].

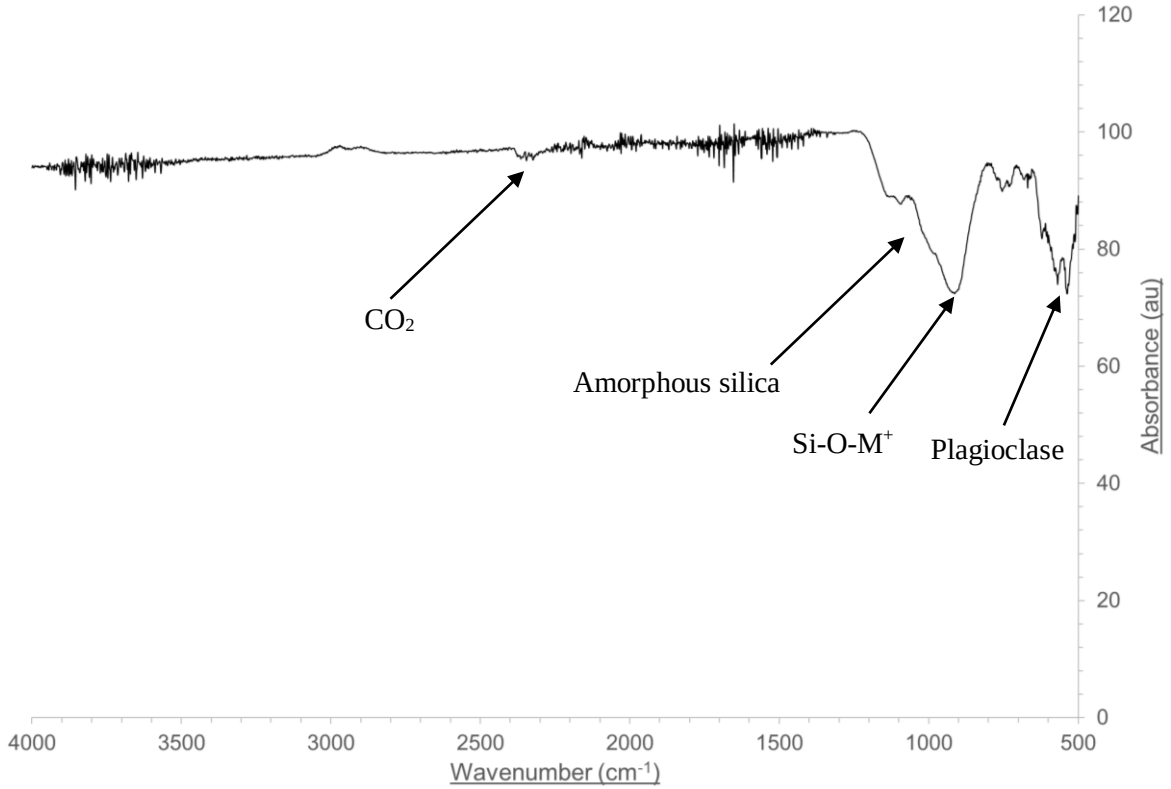

Figure 27. Infrared spectrum for the pure, raw anorthosite sample with a wavenumber range of 4000 cm^{-1} -500 cm^{-1}. The absorption band at ~ 1150 cm^{-1} suggests amorphous silica contributions [45].

As shown in Figure 27 above, the IR spectrum of the pure, raw anorthosite sample indicated amorphous silica contributions due to the presence of the broad shoulder band at ~ 1150 cm^{-1}, with a broad peak adjacent at ~ 900 cm^{-1} [45]. As with all of the Earth minerals provided, the characteristic Si-O-M^+ peak was observed at ~ 1000 cm^{-1} - 900 cm^{-1}. Literature indicates that the observed absorbance bands are predominately due to plagioclase, in regards to the shouldered peak at ~ 900 cm^{-1} and the doublet at ~ 580 cm^{-1} [51]. A very slight absorbance band was observed at ~ 2400 cm^{-1}, indicating the presence of CO_2 within the sample, suggesting the gas being trapped within the mineralogical structure possibly due to adsorption [29].

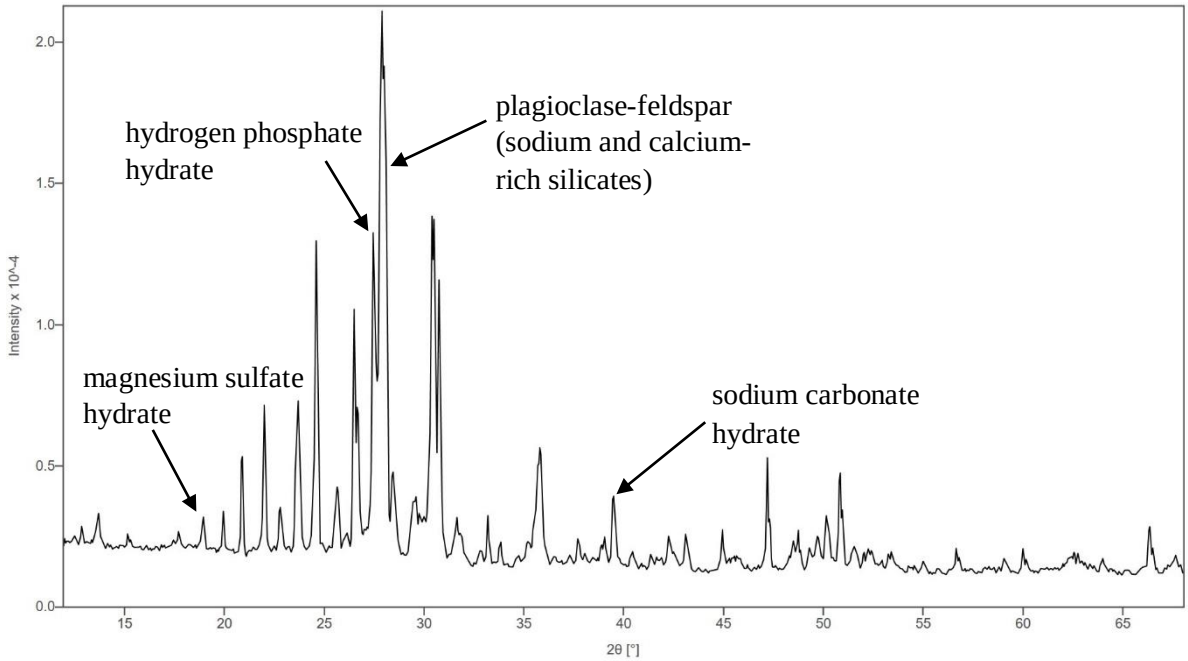

Figure 28. XRD diffractogram of the pure, un-milled anorthosite between 15°-65° and a scan time of 3 hours.

As demonstrated in Figure 28, characterisation of pure, raw anorthosite by means of XRD analysis demonstrated a large number of intense peaks, particularly within the range of ~ 22° - 30°. The most intense, sharp peak at ~ 27.9° indicates the presence of plagioclase-feldspar minerals within anorthosite itself, with this diffraction value being assigned to sodium and calcium-rich silicates, alongside Al^{3+} present within a few sites in the crystalline network. This sharp peak is of great significance with regard to characterising silicates, as it a diagnostic feature for any silica-based/containing material [52]. The peak's shoulder at ~ 28.4° is due to iron magnesium silicate contributions, suggesting a mixed phase present within the mineral. Certain peaks indicating hydrated minerals within anorthosite are present, with diffraction angle values of ~18.8°, 27.4°, 39.0° and 34.7°. These indicate contributions from magnesium sulfate hydrate, hydrogen phosphate hydrate, and sodium carbonate hydrate respectively. Anorthosite is generally accepted as a Ca^{2+}-plagioclase feldspar mineral, therefore the diffractogram in Figure 28 is as expected with evidence of Ca^{2+} and Na^{2+} contributions. XRD analysis suggested the presence of phosphate ions which was not anticipated. However, sample composition may vary depending on where material is extracted from, and introduction of impurities is always possible

Ilmenite, of chemical formula $FeTiO_3$, is most commonly sourced in igneous rocks and formed through gradual cooling within magma chambers. Depending on the sample and its origin, varying abundances of Mg and Mn are observed. Apollo missions have discovered geographical locations on the Lunar surface abundant in ilmenite, with rocks within the regolith layer consisting of > 10 % TiO_2 [53].

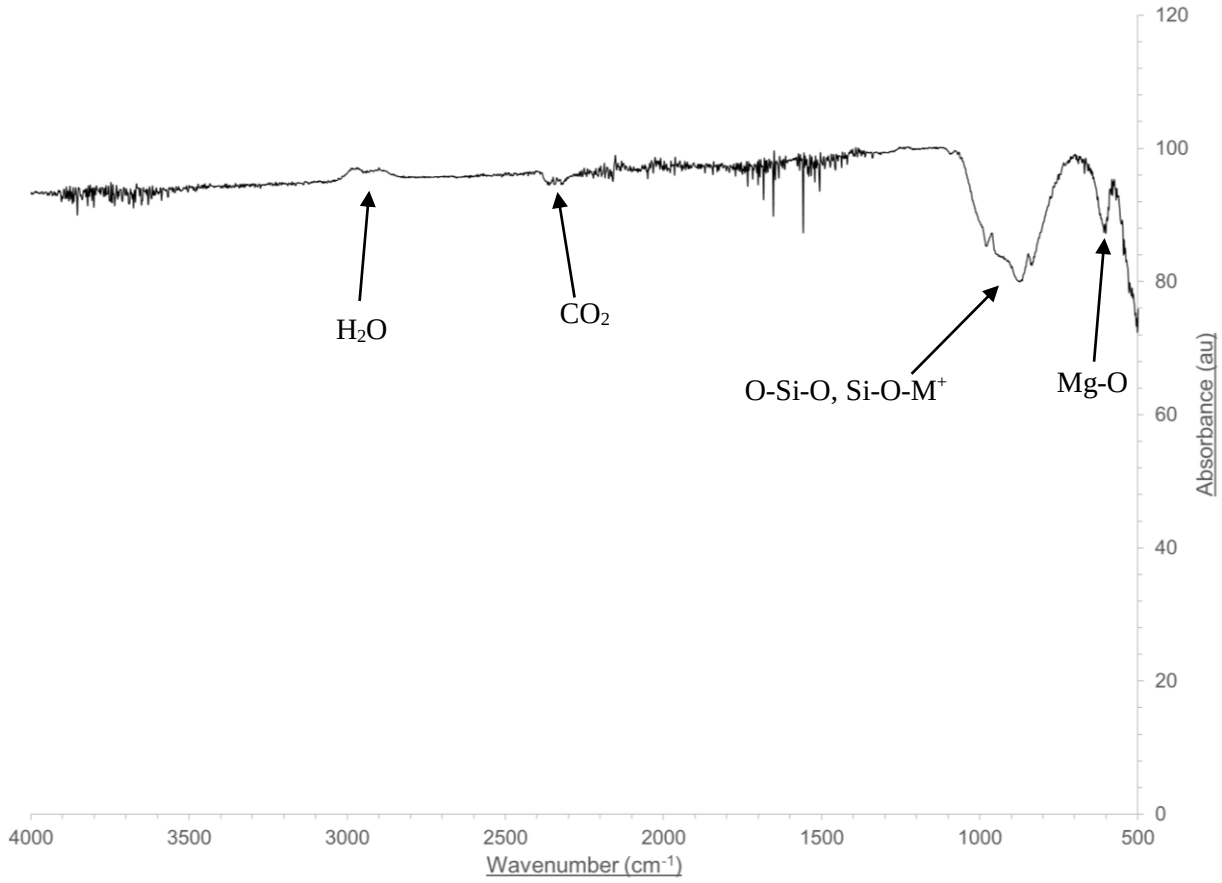

Figure 29. Infrared spectrum for the pure, raw ilmenite sample with a wavenumber range of 4000 cm^{-1} -500 cm^{-1}. The absorption band at ~ 600 cm^{-1} suggests Mg-O contributions [55].

The IR spectrum seen in Figure 29 of the raw ilmenite sample demonstrates the presence of $CO_{2\,(g)}$ by the very slight broad peak at ~ 2400 cm^{-1}. Research conducted by Hipólito *et al.* has suggested the photocatalytic properties through using solar light energy to manipulate its CO_2 sequestration properties [54]. A similar characteristic silica/silicate peak at ~ 1000 cm^{-1} indicated the presence of O-Si-O and Si-O-M^+ bonding within the structure. The sharp band at ~ 600 cm^{-1} suggests Mg-O contributions [55]. The broad band at ~ 3000 cm^{-1} indicates contributions from water.

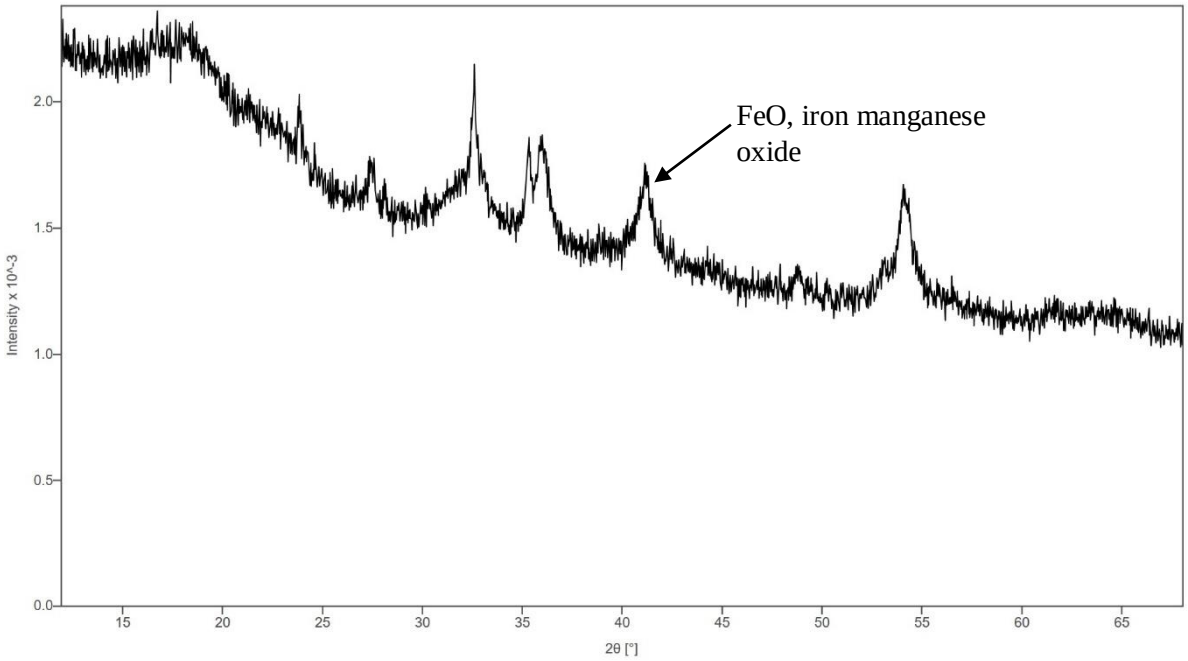

Figure 30. XRD pattern of the pure, un-milled ilmenite between 15°-65° and a scan time of 3 hours.

The XRD of pure, raw ilmenite clearly indicates the composition $FeTiO_3$, with a significant abundance of iron (~ 30 % - 70 % TiO_2) [52], as demonstrated in Figure 30, showing considerable fluorescence and noise, caused by iron oxide and other iron phases within the mineral. Upon exposure to Cu Kα radiation, a low signal to noise ratio (SNR) is observed, with a high background signal due to the effect of fluorescence. The natural ore of ilmenite is known for being composed of a range of elements, for instance carbon, iron and manganese, and thus possesses a more complex lattice structure [54].

Although difficulties arose when analysing X-ray diffraction data collected for ilmenite, with the possibility of incorrect phase identification, certain peaks as shown above in Figure 30 were identified. As predicted with its significant iron oxide abundance, peak angle values at 39.6° and 41.2° indicated the presence of FeO, alongside other oxide phases, including iron manganese oxide, as expected due to the varying incorporation of Mn^{2+} cations into vacant sites within the crystal lattice structure. As discussed in subsection 1.1, Mg^{2+} cations may also be incorporated within the mineral, as demonstrated by the peak observed at 41.2°, due to manganese magnesium oxide contributions. There was some uncertainty with the assignment of some of the other observed peaks due to difficulties during sample loading (ilmenite's natural clumpy texture makes it challenging to handle).

Lava rock basalt is an igneous rock and is present across the Earth's crust, including dry land and beneath the seabed. Basalt is formed through the process of molten lava cooling and solidifying, with its major constituent minerals being pyroxene, olivine and plagioclase feldspar. Contrary to the other minerals discussed within this chapter, basalt is not highly abundant in silica/silicate minerals (~ 45 wt % SiO_2), however, Mg and Fe-rich [56]. Structures and landscapes formed by basaltic lava flows are present on both the Lunar and Martian surfaces [57].

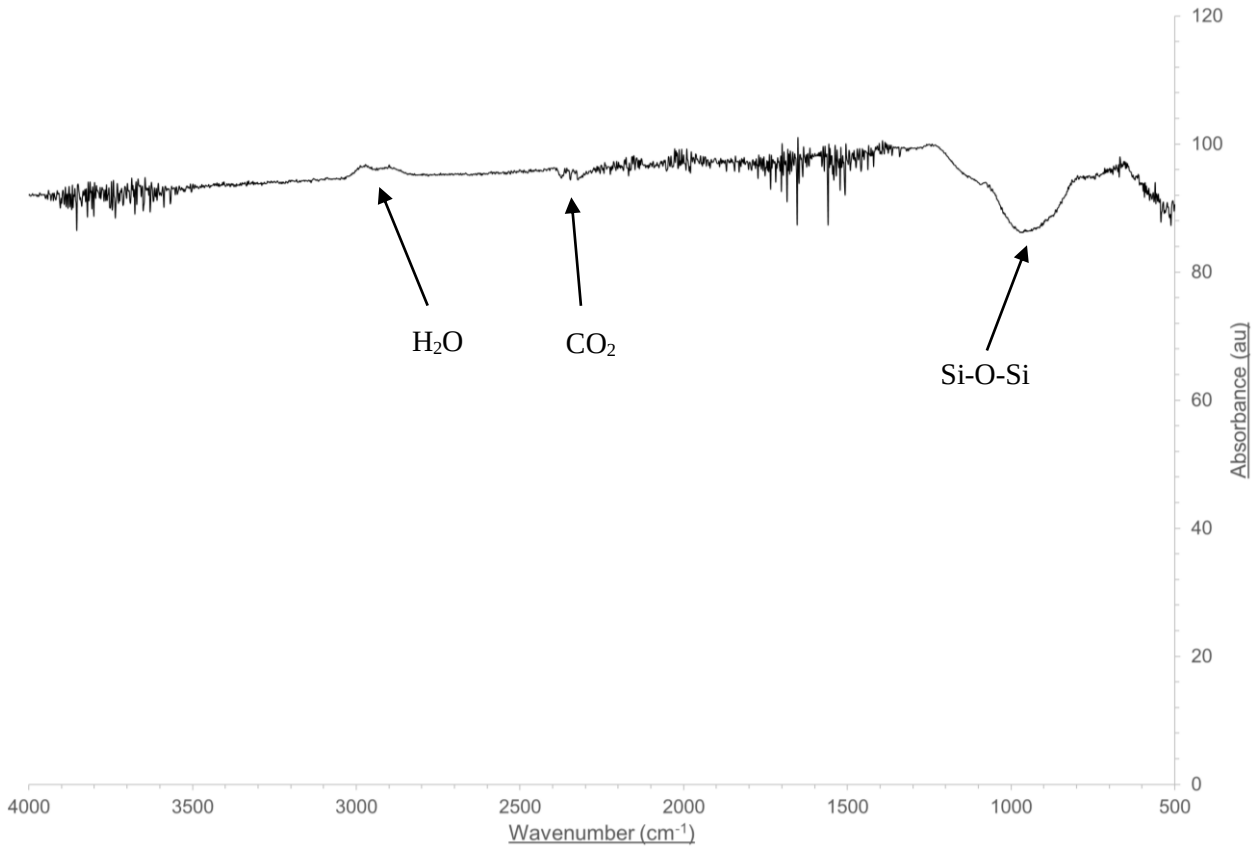

Figure 31. Infrared spectrum for the pure, raw lava rock (basalt) sample with a wavenumber range of 4000 cm^{-1} -500 cm^{-1}. The transmittance band at ~ 2900 cm^{-1} is likely due to adsorbed water from the atmosphere.

As illustrated in figure 31 above the characteristic CO_2 peak at ~ 2400 cm^{-1} was identified by a very slight peak. The slightly broad silica peak at ~ 1000 cm^{-1} is characteristic of basalt, indicating possible Si-O-Si contributions. The same shouldered hump (but of different intensities) at ~ 2900 cm^{-1} was observed for each of the pure, raw Earth minerals. This was assumed to be due to trapped moisture, either due to the minerals themselves, sample loading or the atmospheric conditions.

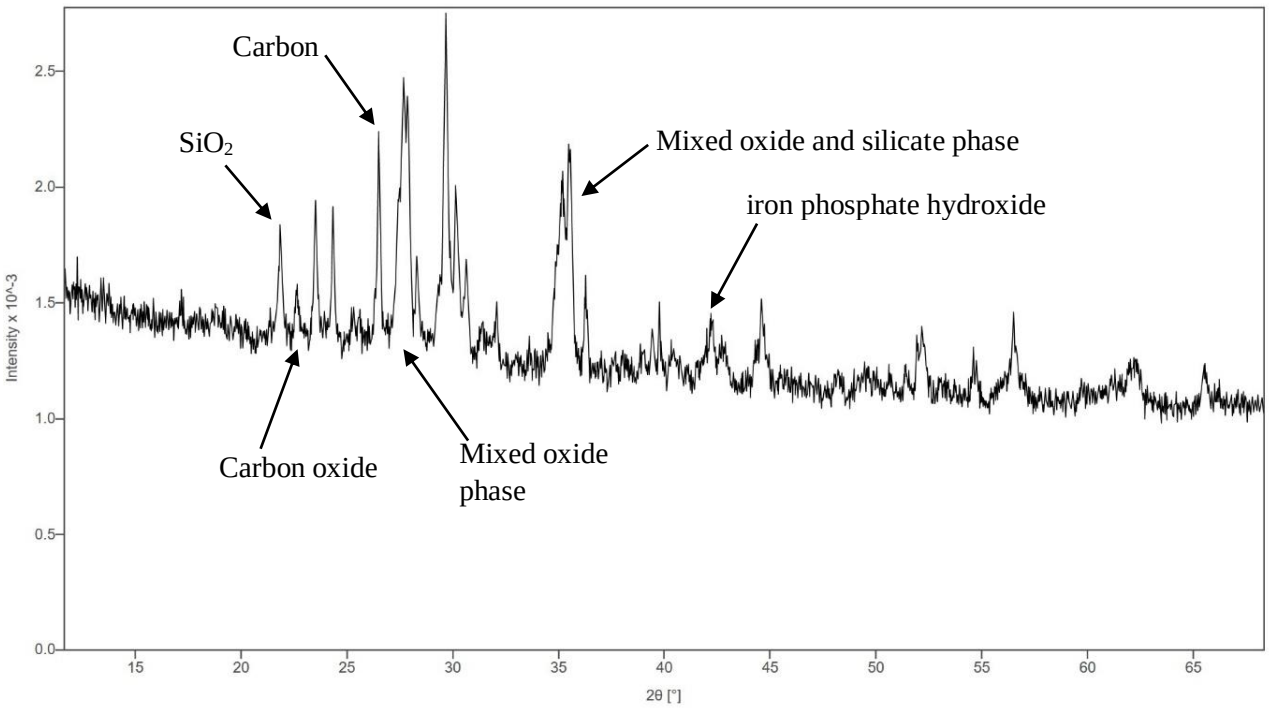

Figure 32. XRD diffractogram of the pure, un-milled basalt (lava rock) between 15°-65° and a scan time of 3 hours.

Characterisation of the pure, raw lava rock basalt by means of XRD analysis demonstrated evidence for oxocarbon compounds such as carbon oxide and additional carbon-containing phases within the mineral. The sharp, intense peak seen in Figure 32 at ~ 26.5° indicated the contribution of carbon within the mineral sample, alongside less noticeable contributions at ~ 22.7° and ~ 44.6° indicating oxocarbon compounds carbon oxide and a mixed phase composed of carbon, iron and iron phosphate hydroxide. SiO_2 was identified at ~ 21.9° as a sharp, noticeable peak despite lava rock basalt not being highly abundant in silica/silicate minerals [56]. The peak at ~ 26.7° was possibly due to the presence of a great variety of oxides, those being silicon oxide, potassium chromium oxide, aluminium oxide, titanium oxide and carbon oxide. The neighbouring intense peak at 29.7° was characterised to be carbon sulfide. Additionally, other phases were perhaps present, including sodium, potassium chromium oxide, manganese phosphate and calcium manganese silicate. An unexpected peak, perhaps due to sampling error and/or impurities, was at ~ 23.5°, and according to the computational software utilised, caused by the presence of lithium phosphate. There is a degree of uncertainty within this assignment and this would have to be analysed further. The shouldered peak at ~ 35.5° was implied to be due to another mix of phases within the crystalline network, those being chromium manganese oxide, iron oxide, calcium manganese silicate and calcium iron oxide. Compared with the other pure, raw minerals characterised, lava rock basalt had the greatest amount of mixed oxide phases within the sample, which could be due to numerous factors, one being geographical location of sampling.

A high level of background noise was recorded similarly to ilmenite, although to a lesser extent. This result was not unexpected, due to the high abundance of iron and iron oxide phases within the basalt provided, yielding similar fluorescence effects on the diffractogram.

Prior to milling, preliminary characterisation of the analogues in their raw form was conducted, utilising pre-collected data (results gathered from space missions for instance onboard Curiosity, the CheMin instrument measured a sub-equal proportion of crystalline and amorphous content within Martian regolith [2]) by ExoLith on the mineralogical structure and chemical composition as shown within subsection 1.1. As the relative composition and abundances of the mineral components were already known, certain 'signature' peaks/bands were expected during preliminary characterisation by XRD and ATR-FTIR. Preliminary data gathered was utilised as a baseline for comparisons between the raw, un-milled analogues against those ball milled for 2 and 10 minutes. Obtaining raw, preliminary data was thus essential in analysing any differences in mineralogy and crystalline structure, but also chemical bonding (alterations made by mechanochemical activation of reaction pathways during ball milling). All analogues analysed were silica-based, and therefore the characteristic silicate peak at ~ 27° was predicted to be significant in the XRD data collected from generic reported literature of silica-containing minerals.

To analyse any potential alterations in chemical bonding and composition, for instance bonding strength and elements involved, ATR-FTIR was utilised within the laboratory in addition to XRD for preliminary characterisation of the planetary analogues. With oxide phases known for the synthetic analogues from data provided by Exolith, infrared spectroscopy allowed the structure and mode of bonding within the crystalline network to be identified (see chapter 2). Raman spectroscopy proved to be a challenging experimental analytical technique for the compounds being identified due to considerable fluorescence from the samples (refer to chapter 1), and therefore ATR-FTIR, despite its limitations for inorganic compounds, was the chosen solution for identifying molecular structures and exploring relative band intensities between Earth-based and synthesised simulants.

Table 2. Mineralogical and chemical composition and abundance (wt. %) of JSC-Lunar simulant. Highlighted cells represent major abundances [11].

Mineral	**Abundance (wt. %)**	**Oxide**	**Abundance (wt. %)**
Glass	49.3	SiO_2	47.4
Plagioclase	37.1	TiO_2	1.56
Olivine	9.0	Al_2O_3	16.1
Cr-spinel	1.1	Fe_2O_3	11.4
Ti-magnetite	0.4	MnO	0.18
K-silicate	1.4	MgO	7.72
Sulfide	1.0	CaO	10.5
Albite	0.3	Na_2O	2.94
Quartz	0.2	K_2O	0.80
Chlorite	0.1	P_2O_5	0.59
Apatite	< 0.1	Cr_2O_3	0.03

Table 2 shows the compositional data for of JSC-Lunar simulant with the major abundances of greatest focus for analysis highlighted [11]. JSC-Lunar's mineralogical structure and composition is significantly composed of glass, plagioclase and olivine (olivine is of noticeably low abundance in comparison to other constituent minerals found in the regolith analogue). Its oxide composition is primarily SiO_2, with Al^{3+}, Fe^{3+}, Mg^{2+} and Ca^{2+} oxide phases simultaneously present in cationic sites within the crystalline structure [11]. The minerals and chemical compounds of noticeably lower abundance in comparison to other components, for instance chlorite, were hypothesised to still contribute in XRD data of the milled JSC-Lunar simulant, potentially due to varying reactions occurring between minerals and the mechanochemical activation of reaction pathways, and the mechanism of milling increasing the reactivity of mineral surfaces.

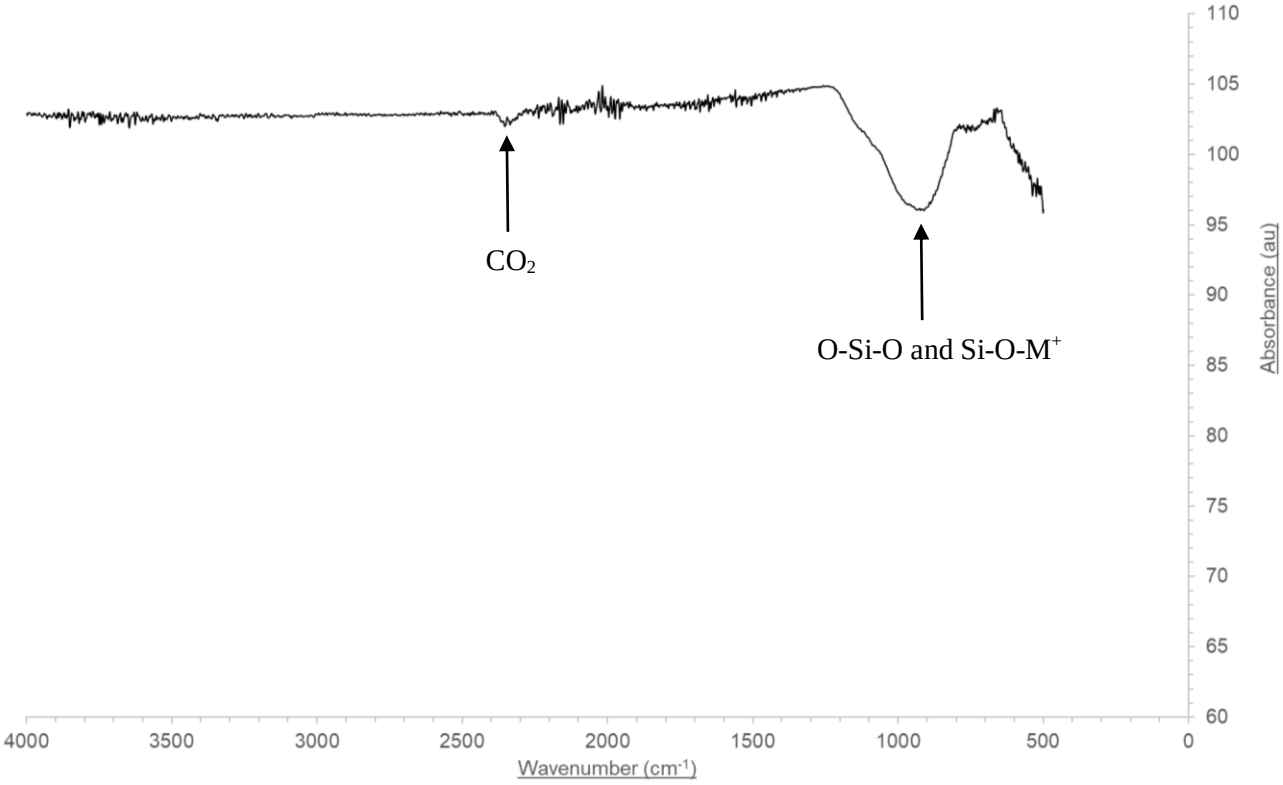

Figure 33. Infrared spectrum for the raw JSC-Lunar sample with a wavenumber range of 4000 cm^{-1} - 500 cm^{-1}. The absorption band at ~ 900 cm^{-1} suggests O-Si-O contributions.

As shown in Figure 33, infrared spectroscopy analysis of the raw JSC-Lunar simulant before milling demonstrated the presence of silica/silicate minerals by the intense, sharp absorbance peak at ~ 900 cm^{-1} indicating O-Si-O and Si-O-M^+ (M^+ being a metal cation). Considering the high abundance of SiO_2 within the JSC-Lunar simulant, this was predicted. Nonetheless, chemical oxide bonds such as Al_2O_3, Fe_2O_3, MgO and CaO were not clearly shown contrary to what might be expected. Additionally, certain minerals of high abundance, for instance glass and plagioclase, did not contribute observable bands in the infrared spectrum. It was hypothesised that subsequent mechanochemical activation by means of ball milling would increase reactivity and activate certain bonding within the simulants' structures, causing certain spectral bands to become more apparent through the activation of reaction pathways within the material. The noticeable shouldered peak at ~ 2400 cm^{-1} indicated CO_2 contributions, suggesting CO_2 is trapped within mineral grains and absorbed by surface pores through diffusion throughout the lattice interstitials [29].

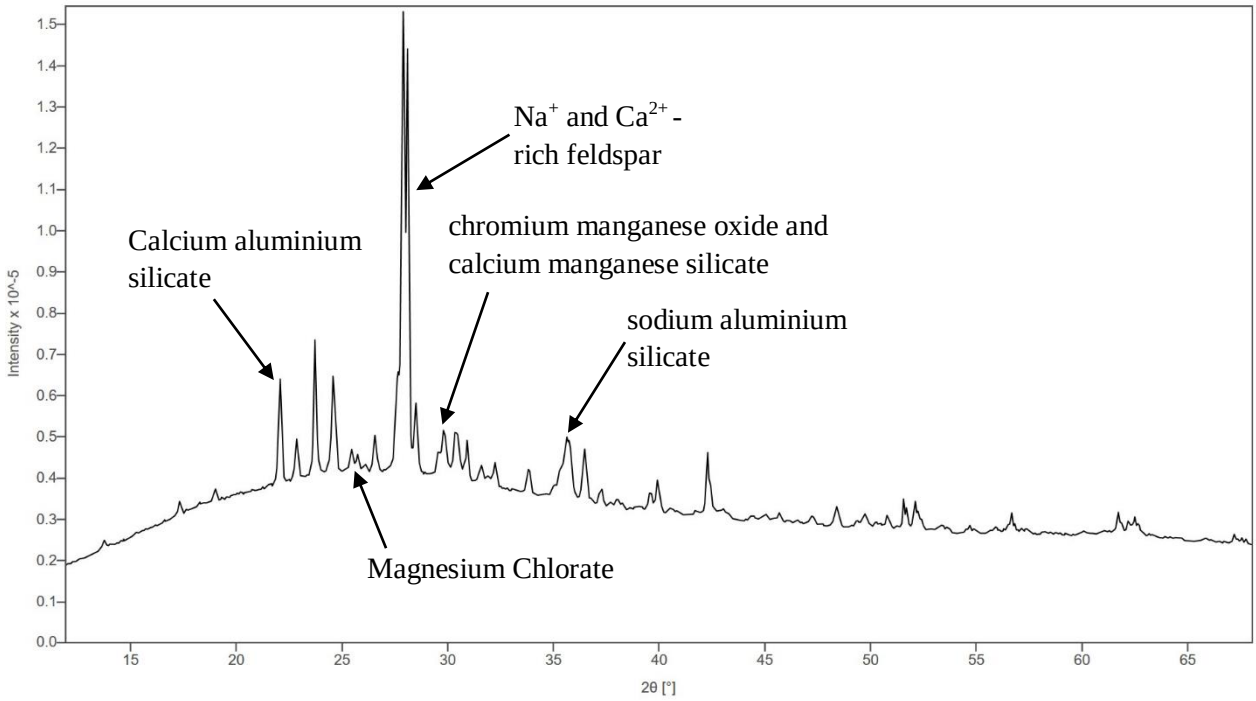

Figure 34. XRD diffractogram of the raw JSC-Lunar analogue between 15°-65° and a scan time of 3 hours.

Preliminary characterisation of the raw JSC-Lunar simulant by XRD as shown in Figure 34 demonstrated the high abundance of silica/silica-based minerals, illustrated by the intense, sharp peak at ~ 27.9° showing the Na^+ and Ca^{2+} - rich feldspar mineral contribution, with phases present being sodium potassium/calcium aluminium silicate and sodium aluminium silicate, also indicated by the shoulder present at the peak's base (characterised by calcium aluminium silicate). Additionally, contributions from aluminium phosphate and manganese phosphate oxide were also observed. This diffraction angle value was also due to oxocarbon compounds present within the raw JSC-Lunar simulant, perhaps due to trapped carbon within some of the constituent minerals. Organic inclusions are not uncommon in minerals, in particular silicate-based materials [29]. Gases such as CO_2 can become trapped in fluid inclusions. These small pores or cavities can contain trapped gas from its formation process. This is particularly observed for quartz and olivine minerals [58]. Feldspar contributions were also seen at angle values of ~ 22.1° and 35.7° due to the presence of calcium aluminium silicate and sodium aluminium silicate respectively. The shouldered peak at ~ 25.5° is due to magnesium chlorate, suggesting reactive processes occurring between the chlorite and magnesium oxide phases found within the JSC-Lunar simulant, as predicted. A mixed manganese phase of chromium manganese oxide and calcium manganese silicate was observed at ~ 29.8°, despite the JSC-Lunar's low abundance of Cr_2O_3 (0.03 wt. %). The amorphous nature of the JSC-Lunar simulant is illustrated in the slight hump present between ~ 0° - 23°.

Table 3. Mineralogical and chemical composition and abundance (wt. %) of LHS-1 simulant. Highlighted cells represent major abundances [4].

Mineral/Rock	Abundance (wt. %)	Oxide	Abundance (wt. %)
Anorthosite rock	74.4	SiO_2	48.7
*Glass-rich basalt	24.7	TiO_2	0.7
Ilmenite	0.4	Al_2O_3	25.6
Pyroxene	0.3	FeO	3.4
Olivine	0.2	MnO	0.1
-	-	MgO	2.5
-	-	CaO	16.6
-	-	Na_2O	0.7
-	-	K_2O_5	0.4
-	-	P_2O_5	0.9

*Basalt extracted from Merriam crater, cinder cone located in Humphreys Peak, Northern Arizona.

As shown in Table 3, LHS-1 is primarily comprised of anorthosite (74.4 wt. %), replicating the high abundance of anorthosite found on the Lunar highland regions [12]. Additionally, LHS-1 has a somewhat notable abundance of glass-rich basalt. Its chemical oxide composition is predominately SiO_2, Al_2O_3 and CaO, with SiO_2 being of the highest abundance, in the same manner as that of the Earth-based Lunar simulant, JSC-Lunar [4,11]. Comparing the two Lunar simulants utilised within the laboratory, the two notable contrasts are the lack of chromium within LHS-1, and its much lower iron abundance, as well as iron existing within a different oxidation state (Fe^{2+} instead of Fe^{3+}).

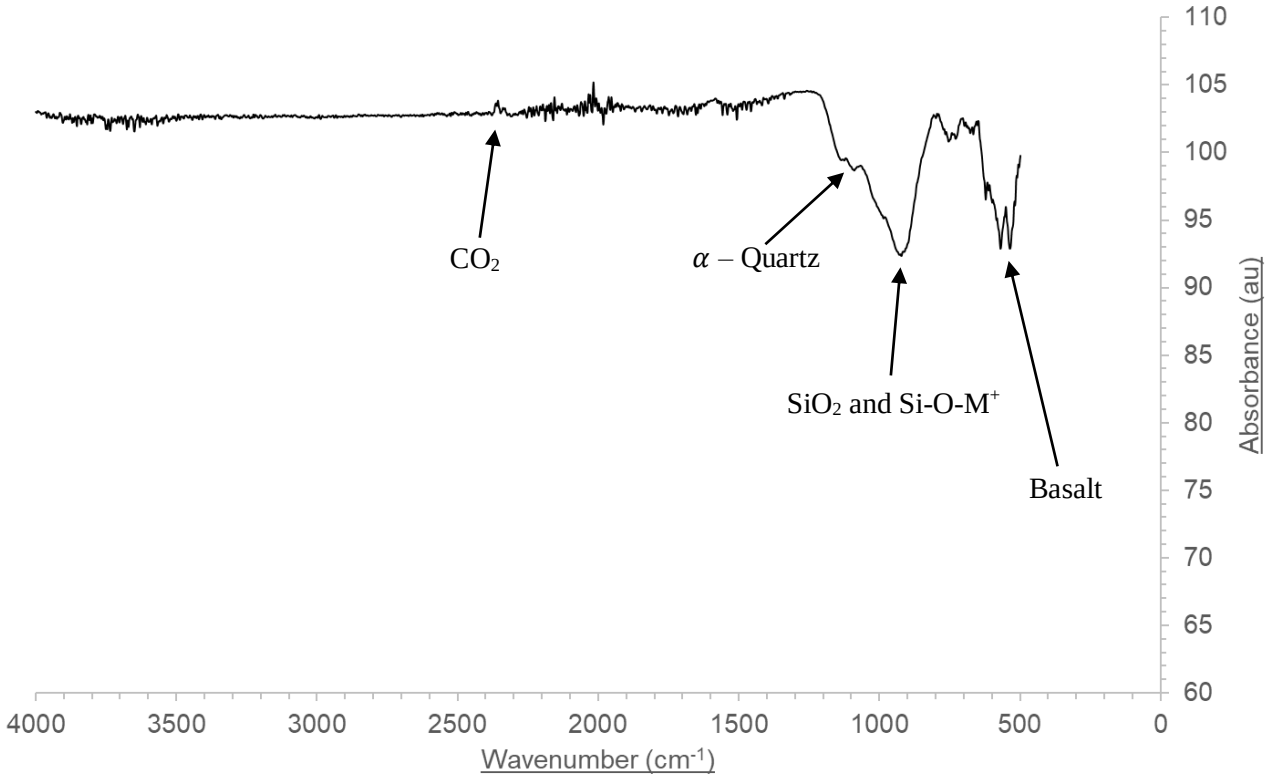

Figure 35. Infrared spectrum for the raw LHS-1 sample with a wavenumber range of 4000 cm^{-1} -500 cm^{-1}. The shouldered peak at ~ 1100 cm^{-1} is possibly due to α – Quartz [46].

The infrared spectrum of the LHS-1 simulant shown in Figure 35 has prominent differences in band width and additional peaks compared to that of the JSC-Lunar simulant. The same SiO_2/Si-O-M^+ characteristic peak at ~ 900 cm^{-1} was identified, with one noticeable difference being the small shoulder present at ~ 1100 cm^{-1}, possibly due to α – Quartz [46] or O-Si-O contributions within a different phase. An additional split peak at ~ 550 cm^{-1}, which was not present in the IR spectrum of the JSC-Lunar simulant indicated the presence of basalt, with the slight shoulder increasing confidence in this assignment. The less intense split peak at ~ 750 cm^{-1} is of higher absorbance than the corresponding peak observed for the JSC-Lunar simulant. This band could not be confidently assigned, however, one potential origin may be a sampling issue and/or impurity from sampling loading or the instrument apparatus. Similarly, to the IR spectrum of the JSC-Lunar simulant, a band at around 2400 cm^{-1} was observed suggesting the adsorption of CO_2, although this was measured as a positive band (i.e. an increased transmittance).

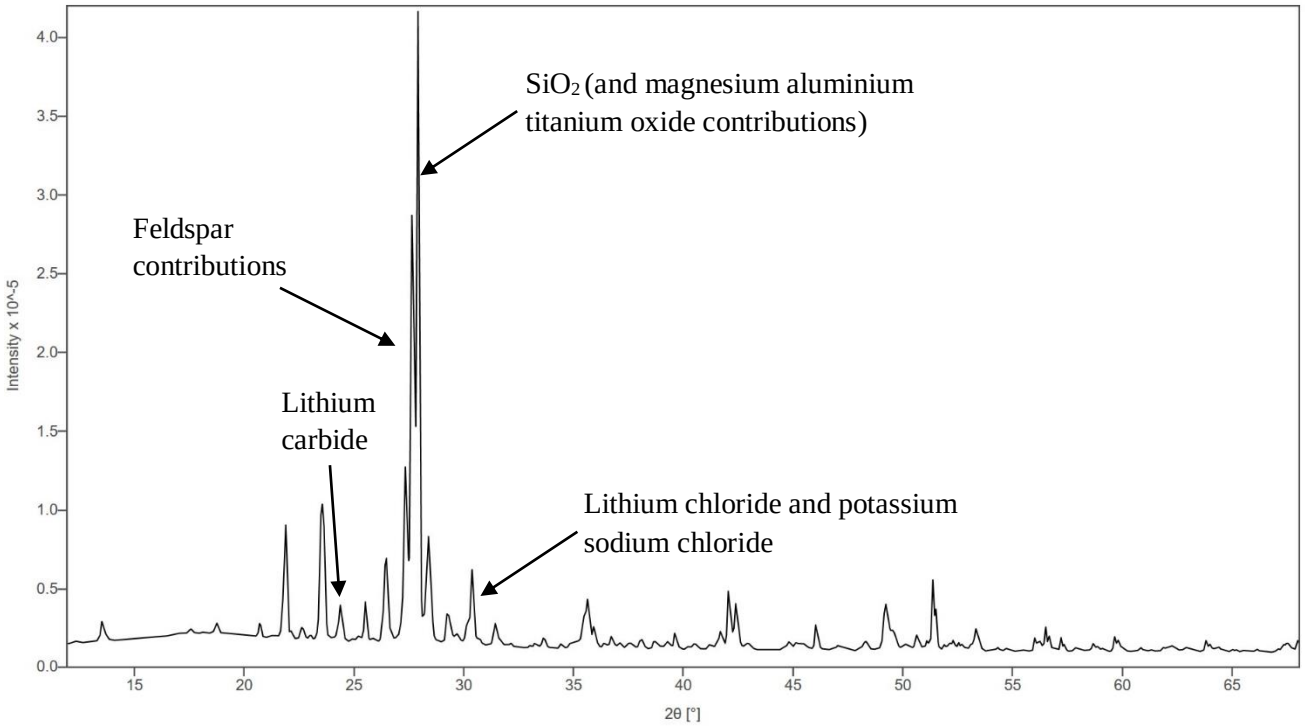

Figure 36. XRD diffractogram of the raw LHS-1 analogue between 15°-65° and a scan time of 3 hours.

XRD analysis of the LHS-1 simulant shown in Figure 36 demonstrated the high abundance of silica/silicate based minerals as expected, with the intense peak between 25° - 30°. SiO_2 was characterised by diffraction angle values of ~ 21.9°, 26.5° and most significantly, ~ 27.9°. The sharp, intense peak at ~ 27.9° indicated a mixed oxide phase of SiO_2 and magnesium aluminium titanium oxide, also shown at ~ 26.5°. Lithium compounds were additionally potentially identified, those being lithium carbide and lithium chloride, at diffraction angle values of ~ 24.4° and 30.4°. Lithium chloride and potassium sodium chloride were identified as a mixed chloride phase at ~ 30.4°. Despite the low pyroxene abundance (0.3 wt. %), depending on the type of pyroxene mineral, Li^+ may be present within the vacant cationic sites. XRD demonstrated the high degree of crystallinity of the LHS-1 simulant, illustrating its replication of the more glass-rich highland regions of the Moon [12].

Preliminary characterisation of LHS-1 immediately highlighted noticeable variations between the mineralogy and mineralogical structure of JSC-Lunar compared to the synthesised Lunar simulant. A direct comparison of XRD data acquired is shown in Figure 37 that demonstrates the higher peak intensity regarding LHS-1 relative to the JSC-Lunar simulant, in particular for the characteristic silicate mineral and oxocarbon band of diffraction angle between 25°-30°. The similarity in band width indicated little variation in crystal/grain diameter between the two Lunar simulants on average, however, more varied peak widths were observed for LHS-1 as predicted due to its wider initial grain size distribution. As there is an inversely proportional correlation between band width and crystal diameter (chapter 2), the fairly narrow band widths in diffractograms of the JSC-Lunar and LHS-1

simulants showed that on average, grain sizes were somewhat large in comparison to data collected for individual minerals. LHS-1 appeared to be of greater crystallinity than that of the JSC-Lunar simulant, which was expected due to LHS-1's composition being primarily anorthosite, representing the highly crystalline highland regions on the Moon. Additionally, LHS-1 appeared to be composed of a wider range of oxide phases than that of the JSC-Lunar simulant, despite LHS-1 only representing the Lunar highlands. The highlands are thought to have a more varied elemental and oxide composition due to the frequent meteoritic bombardments it is exposed to in comparison to the mare regions, resulting in more frequent 'gardening' [7,8,12]. Despite XRD data already pre-existing within literature for these Lunar simulants, the essential direct comparison of their mineralogies conducted has been relatively unexplored in depth, therefore understanding the differences in their initial mineralogical structure is essential prior to conducting experiments on them in the laboratory.

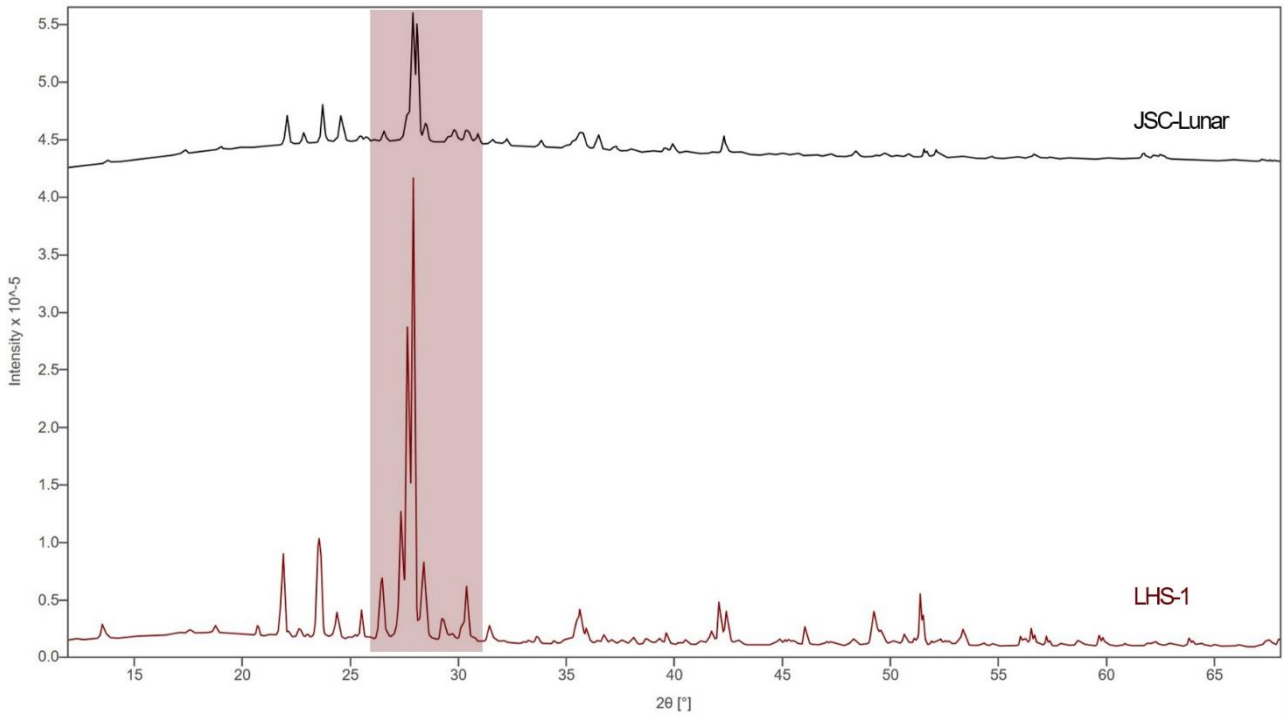

Figure 37. XRD diffractogram comparing the raw JSC-Lunar and LHS-1 analogues between 15°-65° and a scan time of 3 hours. The highlighted region illustrates the sharp relative increase in peak intensity for LHS-1 in comparison to the raw JSC-Lunar simulant.

Table 4. Mineralogical and chemical composition and abundance (wt. %) of JSC-Martian simulant. Highlighted cells represent major abundances [2].

Mineral	Abundance (wt. %)	Oxide	Abundance (wt. %)
Palagonite	Majority	SiO_2	43.48
Plagioclase	Tr	TiO_2	3.62
Magnetite	Tr	Al_2O_3	22.09
-	-	Cr_2O_3	0.03
-	-	Fe_2O_3	16.08
-	-	MnO	0.26
-	-	MgO	4.22
-	-	CaO	6.05
-	-	Na_2O	2.34
-	-	K_2O	0.70
-	-	P_2O_5	0.78
-	-	SO_3	0.31

As shown in Table 4 above, the Earth-based JSC-Martian simulant is primarily composed of palagonite, a volcanic mineral produced by means of aqueous alteration as a product of volcanic glass with analogous chemical properties to basalt reacting with water [59]. Palagonite's composition consists of zeolites, clay minerals, illite or kaolinites [60]. The majority of the JSC-Martian simulant's chemical composition is comprised of SiO_2, Al_2O_3, Fe_2O_3 and CaO [2]. Despite existing within the material's crystalline molecular structure in low abundances, the other constituents were predicted to provide minor contributions to the results, potentially due to activation of certain mineral surfaces. Subsequent ball milling was predicted to activate certain minerals and potentially increase their reactivity and thus contribution to the resulting composition and structural bonding.

Table 5. Mineralogical and chemical composition and abundance (wt. %) of MGS-1 simulant. Highlighted cells represent major abundances [4].

Mineral	Abundance (wt. %)	Oxide	Abundance (wt. %)
Anorthosite	27.1	SiO_2	42.9
Glass-rich basalt	22.9	TiO_2	0.6
Pyroxene	20.3	Al_2O_3	12.8
Olivine	13.7	FeO	11.2
Mg-sulfate	4.0	MnO	0.1
Ferrihydrite	3.5	MgO	14.6
Hydrated silica	3.0	CaO	7.4
Magnetite	1.9	Na_2O	1.5
Anhydrite	1.7	K_2O	0.6
Fe-carbonate	1.4	P_2O_5	0.1
Hematite	0.5	-	-

As shown in Table 5 above, the synthesised Martian simulant MGS-1 is primarily composed of anorthosite, basalt (glass-rich), pyroxene and olivine, thus showing the immense importance of preliminary characterisation analysis of the pure, raw Earth minerals for subsequent comparative analysis. Minerals such as hydrated silica were incorporated by ExoLith to simulate the occurrence of hydrated minerals thought to be present on the Martian surface, for instance within Gale Crater [2,4]. The high abundance of SiO_2 (42.9 %) was to be expected due to all the simulants provided being silica-based. The relatively high abundance of Al_2O_3, FeO and MgO oxides meant that corresponding peaks were expected to be of greater intensity than for other compounds, for instance CaO (7.4 wt. %).

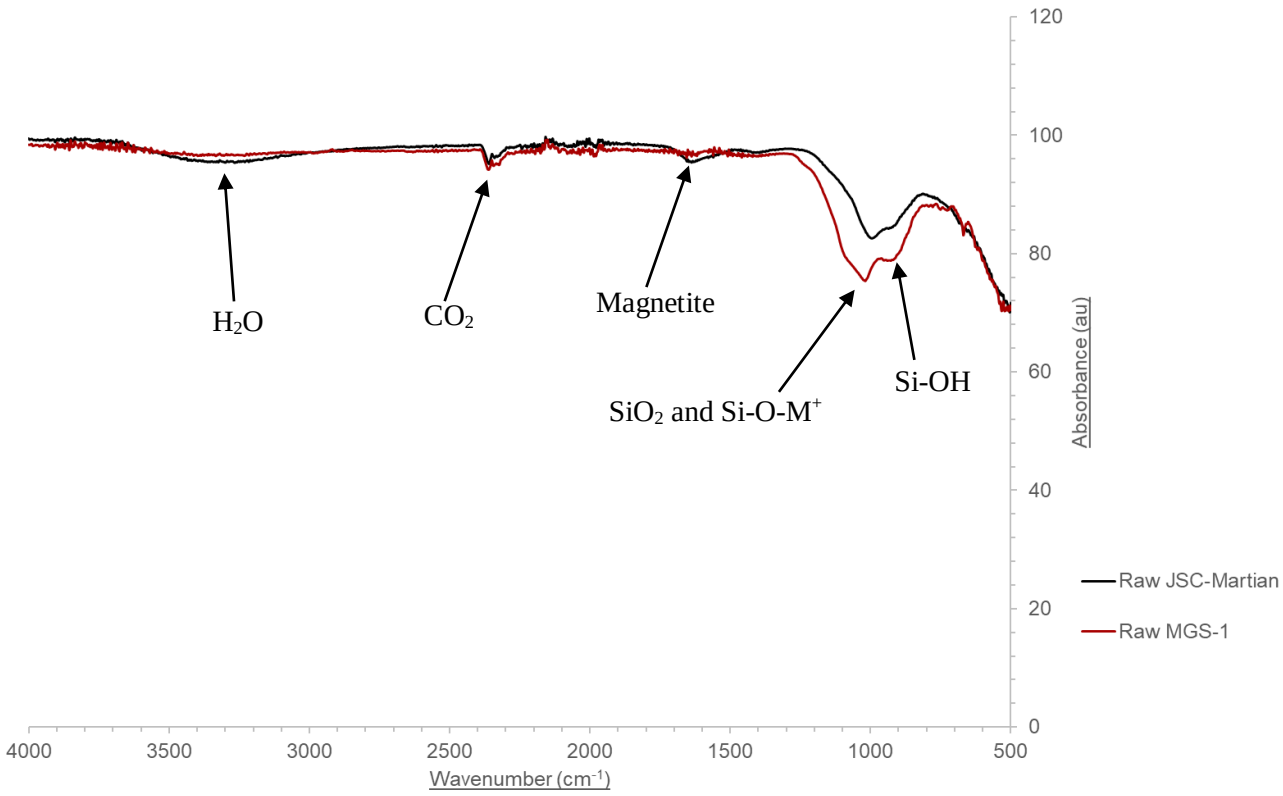

*Figure 38. Infrared spectra for the raw JSC-Martian and MGS-1 samples with a wavenumber range of 4000 cm^{-1} – 500 cm^{-1}. The slightly shouldered absorption band at ~ 1000 cm^{-1} – 900 cm^{-1} suggests the presence of SiO_2/Si-O-M^+ and Si-OH [45].

* It should be noted that results for the Martian simulants were collated for concise presentation and similarity in absorbance bands regarding IR analysis.

The infrared spectra of the raw JSC-Martian and MGS-1 simulants as shown in Figure 38 demonstrated the presence of CO_2 at ~ 2400 cm^{-1} (potentially trapped within certain minerals as discussed previously based on literature). The broad, relatively weak band at ~ 1000 cm^{-1} indicated the SiO_2/Si-O-M^+ characteristic peak as hypothesised. An almost negligible broad peak at ~ 1500 cm^{-1} indicated the possible presence of magnetite, which is known to exist in trace amounts within the JSC-Martian simulant as recorded in Table 4 [2], and therefore a low absorbance was to be expected. The slight broad band at ~ 3300 cm^{-1} emphasises the hygroscopic nature of the JSC-Martian simulant, as reported by Cannon et al [2]. The infrared spectrum of the MGS-1 simulant shown above in Figure 38 demonstrated a shouldered peak at ~ 1000 cm^{-1} – 900 cm^{-1} indicating the presence of SiO_2/Si-O-M^+ and Si-OH bands. These bands were expected due to the abundance of hydrated silica, although the individual compounds were not specifically identified within the chemical composition provided by Exolith [4], perhaps due to their combined low abundance of 3.0 wt. %.

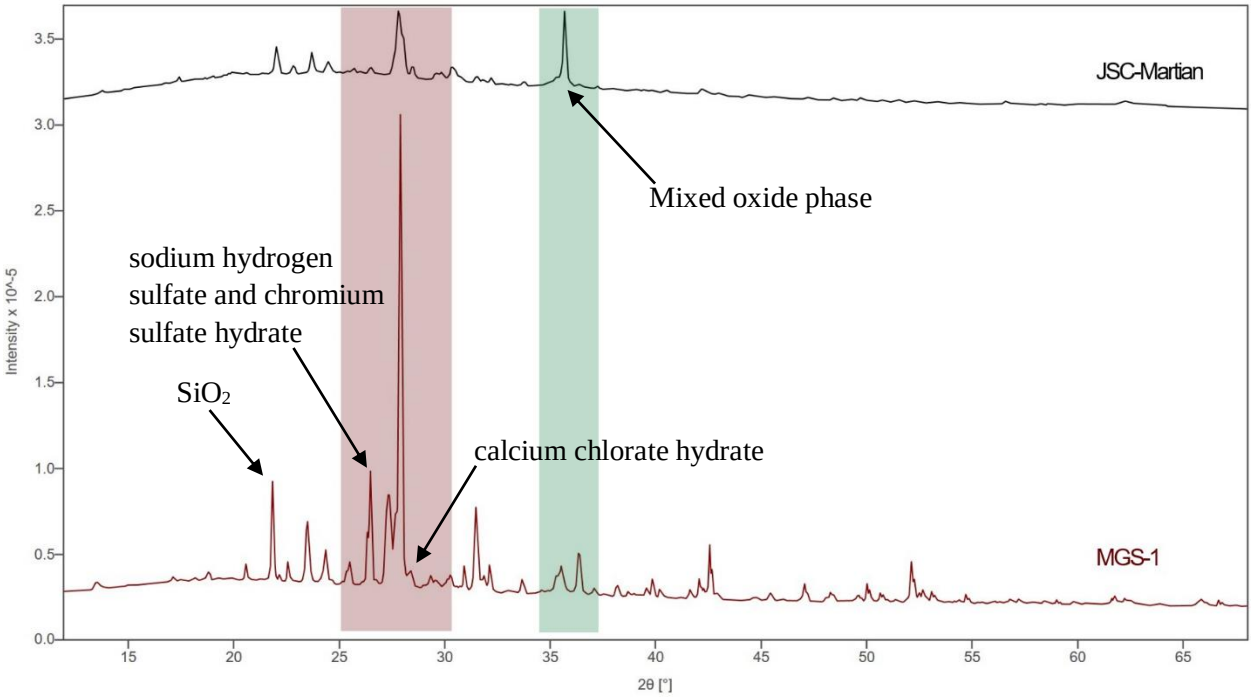

Figure 39. XRD diffractogram comparing the raw JSC-Martian and MGS-1 analogues between 15°-65° and a scan time of 3 hours. The highlighted regions emphasise the noticeable alterations in relative peak intensity between the two simulants.

XRD analysis of the JSC-Martian and MGS-1 simulants as shown above in Figure 39 indicated the presence of silicon oxide by the sharp, intense peak at ~ 22.0°. Feldspar mineral contributions were made apparent by the characteristic peaks between ~ 22.0° - 25°, and band values at ~ 22.0° and 27.8°, indicating the presence of sodium potassium aluminium silicate. The intense, shouldered peak at ~ 27.8° was found to be due to a mixed phase of feldspar contributions as previously discussed, alongside aluminium phosphate and oxocarbon compounds. Unexpectedly, chlorate mineral contributions were observed, which is of great relevance to the Martian surface due to the current and ongoing investigations of the presence of perchlorates [61]. The shouldered peak present at ~ 28.5° was suspected to be due to calcium chlorate hydrate, also characterised by the relatively sharp peak at ~ 23.7°. The less intense peak at ~ 30.3° suggested the presence of sodium chlorate. Sulfate minerals were characterised by diffraction angle values of ~ 26.5°, 30.3° and 35.7° (sodium hydrogen sulfate and chromium sulfate hydrate illustrated by the significantly more intense peak). The intense, sharp peak at ~ 35.7° regarding the JSC-Martian simulant was found to be due to a vast mix of different oxide phases, those being iron titanium oxide, manganese titanium oxide, chromium manganese oxide, calcium iron oxide, lithium iron oxide and as expected, oxocarbon compounds. Potassium oxide contributions were additionally observed at ~ 31.5°, demonstrating the contribution of compounds of relatively low abundance in comparison to more prominent oxides. Other phases present were identified as iron hydroxide sulfate, elemental chlorine, titanium oxide, silicon phosphate and hydrogen carbon sulfide. Expected SiO_2 contributions were observed by peak values of ~ 21.9° and 26.5°. A mixed phase was

also indicated by the peak at ~ 26.5° with contributions of sodium chlorate and sodium iron phosphate hydroxide hydrate. Speculated findings such as hydrated minerals is of great importance when analysing areas such as Gale Crater [24]. As expected, additional organic compounds were characterised by the fairly intense peak at ~ 31.5°, due to hydrogen carbon sulfide contributions. Aluminium-based mineral contributions were observed at angle values of ~ 23.5°, 24.4° and 36.4°, with identified compounds being aluminium hydrogen sulfate, sodium aluminium silicate (feldspar contribution) and aluminium oxide respectively. The presence of chlorate was additionally observed at ~ 36.4° (potassium magnesium chloride).

Preliminary characterisation of the Earth-based and synthesised Martian simulants indicated considerable differences in their mineralogy and mineralogical structures, as illustrated by Figure 39. The XRD diffractograms of the JSC-Martian simulant displayed its relatively uniform grain size distribution and sample homogeneity, consisting of finer grains (illustrated by the broader bandwidths compared to those for the MGS-1 simulant) in comparison to the MGS-1 simulant's initial wider grain size distribution illustrated by the variation in band widths. The most significant variation in mineralogical structure was indicated by the greater intensity of the silica/silicate peak for the MGS-1 simulant at ~ 25° - 30°. The MGS-1 simulant displayed a higher degree of crystallinity and range of oxide phases in comparison to the JSC-Martian simulant, demonstrating similar trends to the Lunar simulants JSC-Lunar and LHS-1.

3.2 Grain Size Distributions and Morphologies

Prior to analysing the mineralogical and chemical properties of the specified minerals, physical properties, namely surface textures and appearances, grain size distributions and morphologies were analysed by means of microscopy (optical and SEM). Considering that whether Earth-based or synthesised, simulants will be composed of various minerals blended together, either through years of natural weathering or ball milling in the laboratory, the most vital experimental variable was initial grain size distribution. Initial grain diameters will affect sample homogeneity and the interactions between grains during collisional impacts, for instance electrostatic forces of attraction between the grains, whether that be between grains within the same mineral, or different mineral reactants.

3.2.2 Constituent Raw Earth Materials

As shown in Figure 40, optical microscopy was utilised within the laboratory to analyse and observe surface texture and general appearance, including colour, an approximate idea of grain sizes where obvious and grain morphology. SEM was employed to analyse grain morphologies for all the pure, raw minerals being utilised to complement research, as illustrated in Figure 41. The same experimental

procedures were executed for the planetary analogues to draw comparisons between the Earth-based and synthetic simulants to assess how their source of origin affects their initial physical properties.

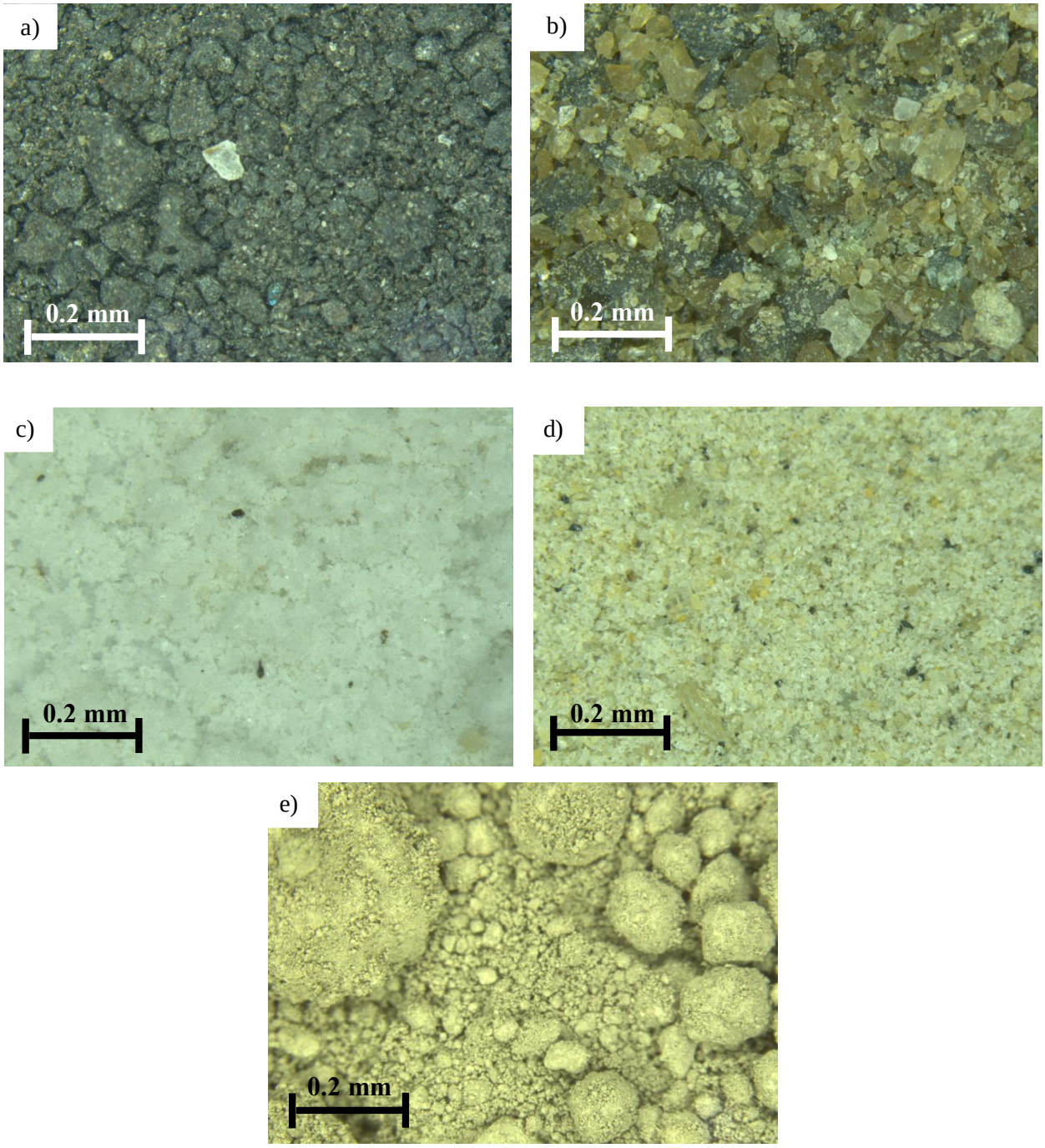

Figure 40. Optical images taken with a focal length of 0.2 mm of the pure, raw Earth minerals a) lava rock (basalt); b) pyroxene (bronzite); c) anorthosite; d) olivine; e) ilmenite.

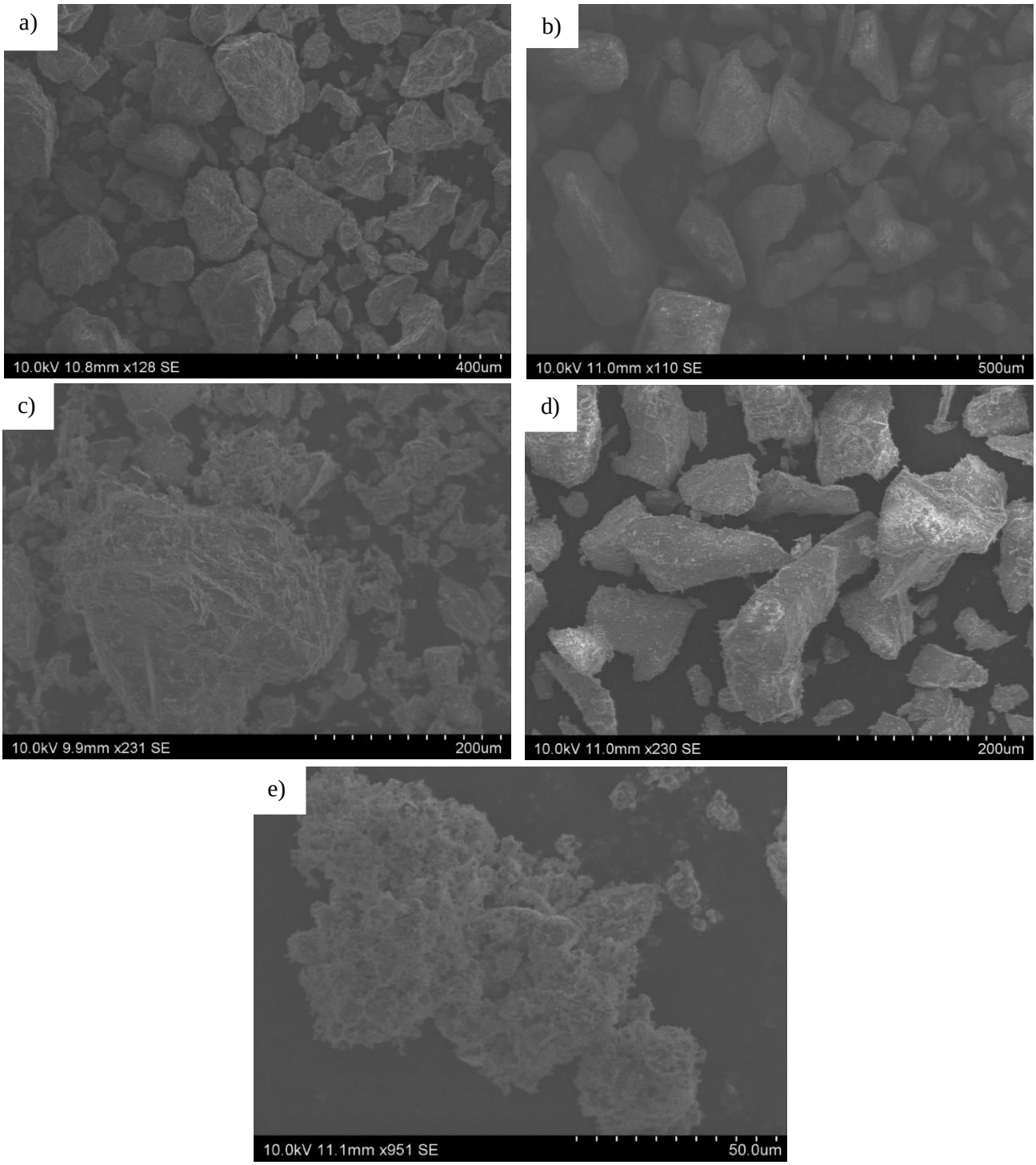

Figure 41. Secondary Electron Images (SEI) taken of the pure, raw Earth minerals a) lava rock (basalt); b) pyroxene (bronzite); c) anorthosite rock; d) olivine; e) ilmenite.

In order to plot grain size distributions for the raw Earth materials, calculating particle number values from the mass collected within each sieve tray was required. This was conducted by calculating grain volume (cm^3) from the mesh pore diameters (average) by assuming a sphere geometry. Individual grain mass was calculated through using literature density values (g/cm^3) and making the assumption density for each sample was uniform. Particle number was thus derived through dividing individual mass by the total mass collected in regards to the corresponding grain size diameter. It is important to note that for the scope of this thesis, assumptions were made in order to plot the grain size distributions. Particle size ranges for all materials were taken from Exolith to ensure the majority of grain diameters were taken into consideration during calculations [4]. An example of one calculation is shown below in concerning the grain size distribution of olivine:

Table 6a. Table showing calculations for grain volume (cm^3) and individual grain mass (g).

Average Grain Diameter (µm)	**Grain Volume (cm^3)**	**Individual Grain Mass (g)**
710.0 (using maximum of 1000 µm [4], midpoint between 1000 µm and 420 µm)	1.87 E-4	6.22 E-4
480.0	5.79 E-5	1.92 E-4
213.5	5.10 E-6	1.69 E-5
163.0	2.27 E-6	7.53 E-6
137.0	1.35 E-6	4.47 E-6
91.50	4.01 E-7	1.33 E-6
55.50	8.95 E-8	2.97 E-7
26.55	9.80 E-9	3.25 E-8

Table 6b. Table showing calculations for particle number values based on mass collected (g).

Average Grain Diameter (µm)	**Mass Collected (g)**	**Particle Number**
710.0 (using maximum of 1000 µm [4], midpoint between 1000 µm and 420 µm)	0.110	177
480.0	0.100	521
213.5	0.115	6800
163.0	0.120	15900
137.0	0.140	31300
91.50	0.675	507000
55.50	0.965	3250000
26.55	0.76	23400000

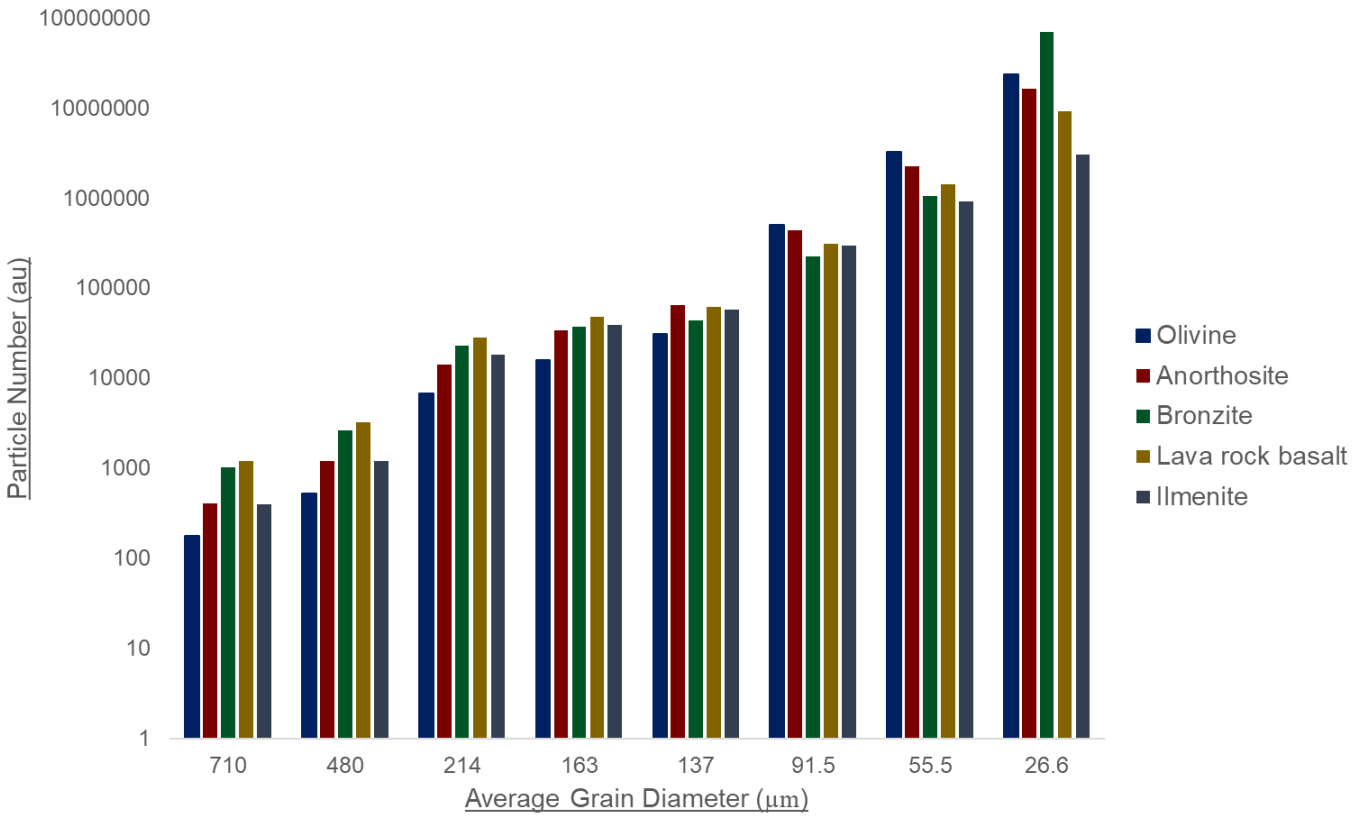

Figure 42. Grain size distribution for the pure, raw Earth materials.

Pure raw olivine was observed to consist of sharp, angular individual grains (quasi-spherical geometry), with noticeable smaller granules adhering to larger components. In addition to grain morphology, SEM analysis was able to demonstrate a general consensus of grain size distribution, which was detected to be fairly narrow and uniform (as demonstrated in Figure 41 d) shown above), complementing optical microscopy analysis and visual observations by eye. Milling studies reported by Kleiv *et al.* show the eventual agglomeration due to milling of olivine grains through sieving analysis, and secondary milling processes such as aggregation subsequently have an effect on grain size distribution and thus specific surface area [43]. The pure, raw olivine was observed to have a high proportion of finer, smaller more powdery grains. The olivine sample was found to contain impurities judging by the noticeable small, black and dark yellow/orange grains observed solely through microscopy as demonstrated in Figure 40 d) above. As shown in Figure 42 above, olivine's grain size distribution is narrow and uniform, with the majority of grains being of size ~ 26.6 µm.

Bronzites grain size distribution was observed to be wider and significantly more varied than individual olivine crystals. Pure, raw bronzite was found to consist of sharp, angular grains, similar to olivine, however coarser and noticeably less rounded grains, as seen in Figure 41 b) above. The generic surface texture of grains was noted to be fairly rough and not as powdery in comparison. Some grains observed had a slate-like surface appearance, as seen in Figure 43 below. The grain size distribution of the raw

bronzite as shown below in Figure 42 was wider than that of olivine, which was somewhat expected due to visibly larger, coarser grains coexisting alongside finer grains within the sample. Optical microscopy analysis of bronzite (pyroxene) as shown in Figure 40 b) above demonstrated grain colours (black, beige, yellow and white) suggesting impurities or variation in composition.

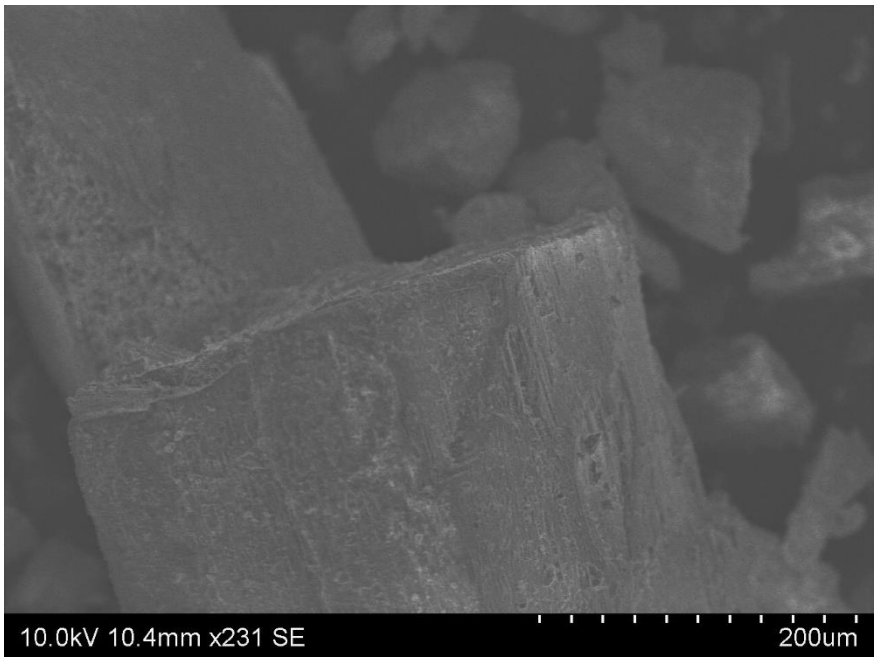

Figure 43. Secondary Electron Image (SEI) taken of an individual grain of the pure, raw bronzite sample to illustrate its slate-like surface texture.

The pure, raw anorthosite's initial grain size distribution was found to be similar to that of olivine, with SEM analysis also highlighting individual larger grains present (see Figure 41 c). The average granular texture was observed to be fine and powdery. Individual grain morphologies proved to be of various geometries, with some being round-edged, whilst others having sharper, more angled appearances. The grain size distribution shown in Figure 42 demonstrates this homogeneity, with a similar distribution to that of olivine. As seen in Figure 40 c) above, the mineral's general surface appearance is of a white powder, however only under an optical microscope were mafic minerals (Mg and Fe- rich silicate minerals with a dark appearance) present in anorthosite observed (small, black grains).

Ilmenite in its pure, raw form is the most distinct of the minerals analysed. Its prominent clumpy, clay/mud-like texture and appearance was observed by means of SEM, with Figure 41 e) showing several ilmenite grains clumped together. The sample's appearance and texture was observed to be paste-like, therefore this was expected. Including larger grains due to aforementioned clumping, ilmenite's grain size distribution was found to be wide and was of heterogeneous nature. Grain morphology, on average, was recorded to be irregularly spherical with soft, rounded edges, as seen in Figure 41 e) above. The plot shown in Figure 42 illustrates ilmenite's wider grain size distribution. Figure 40 e) above showing pure, raw ilmenite demonstrated its clumpy, mud/clay-like appearance and

surface texture. Microscopic data showed its fairly homogeneous nature, excluding clumped grains adhering to one another, presumably due to trapped moisture within the sample.

The lava rock basalt provided was fairly homogeneous, with SEM analysis demonstrating large grains, all with sharp angular edges, and of block-like geometries (illustrated in Figure 41 b). An example of an individual grain is shown more clearly in Figure 44 below. The grain size distribution shown in Figure 42 indicated a more relatively uniform distribution. Lava rock basalt as seen in Figure 40 a) above is of a black, coarse appearance, with minor white and blue-hued grains.

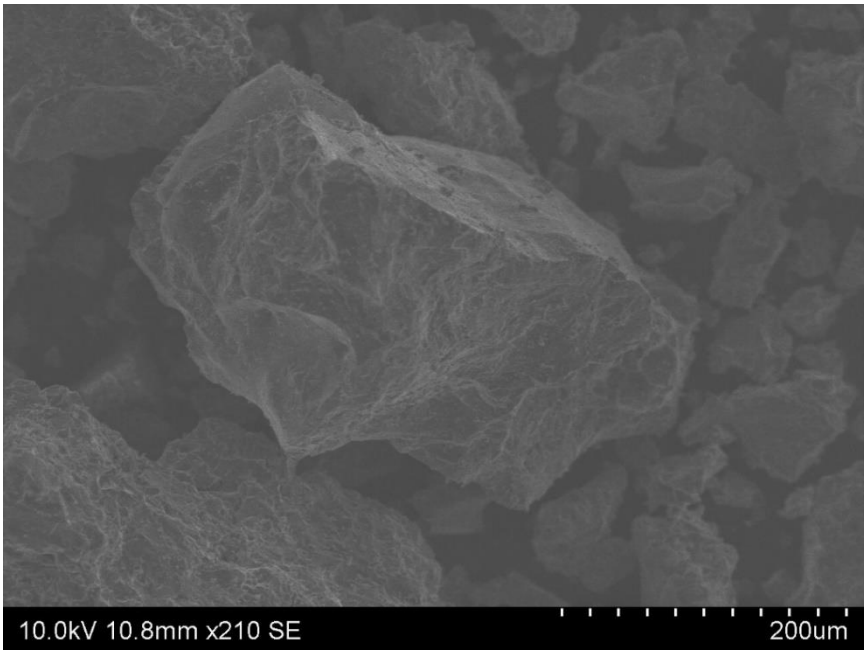

Figure 44. Secondary Electron Image (SEI) taken of an individual grain of the pure, raw lava rock (basalt) sample to emphasise its block-like morphology.

3.2.3 Regolith Analogues

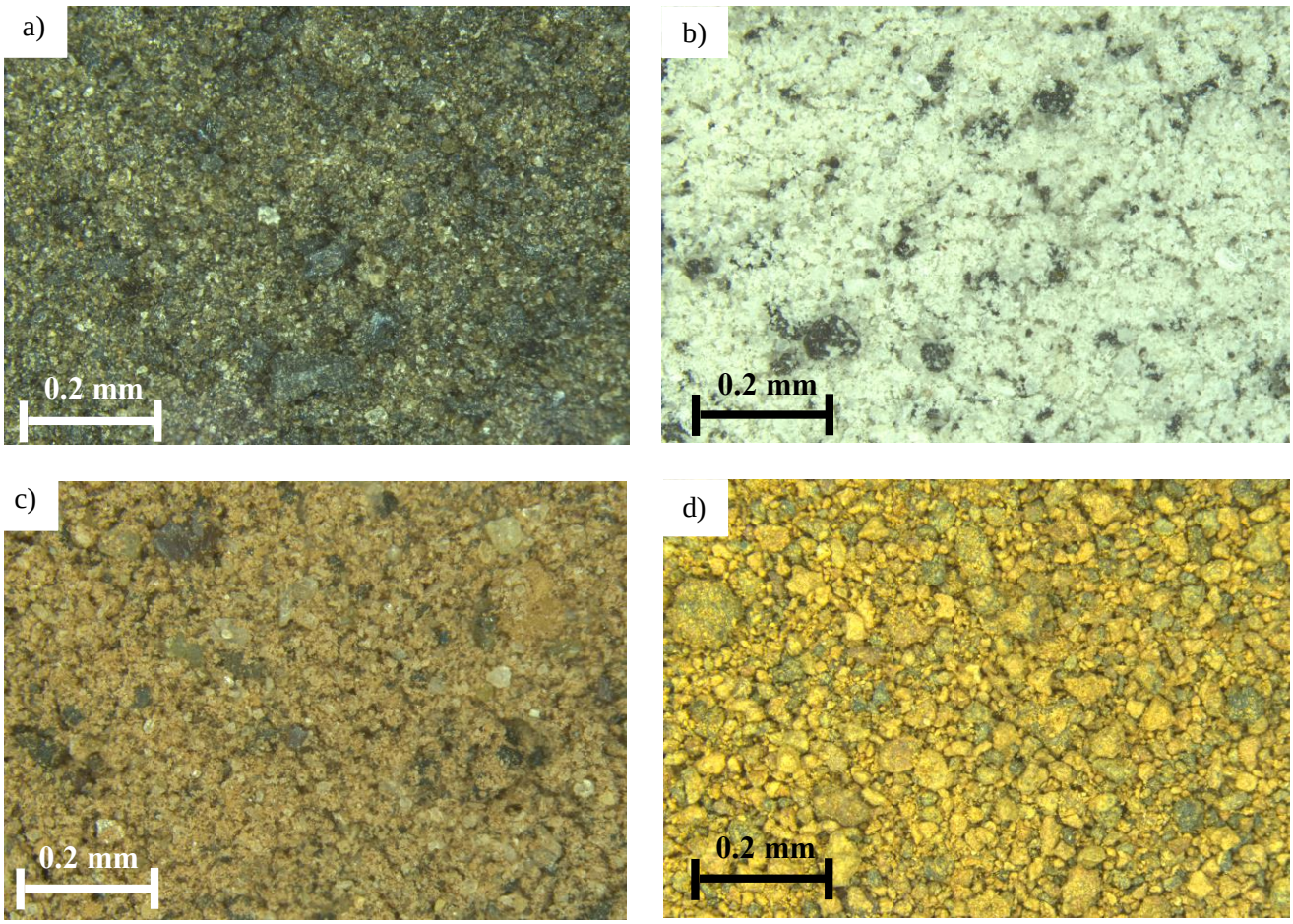

Figure 45. Optical images taken with a focal length of 0.2 mm of the raw planetary analogues a) JSC-Lunar; b) LHS-1; c) JSC-Martian; d) MGS-1.

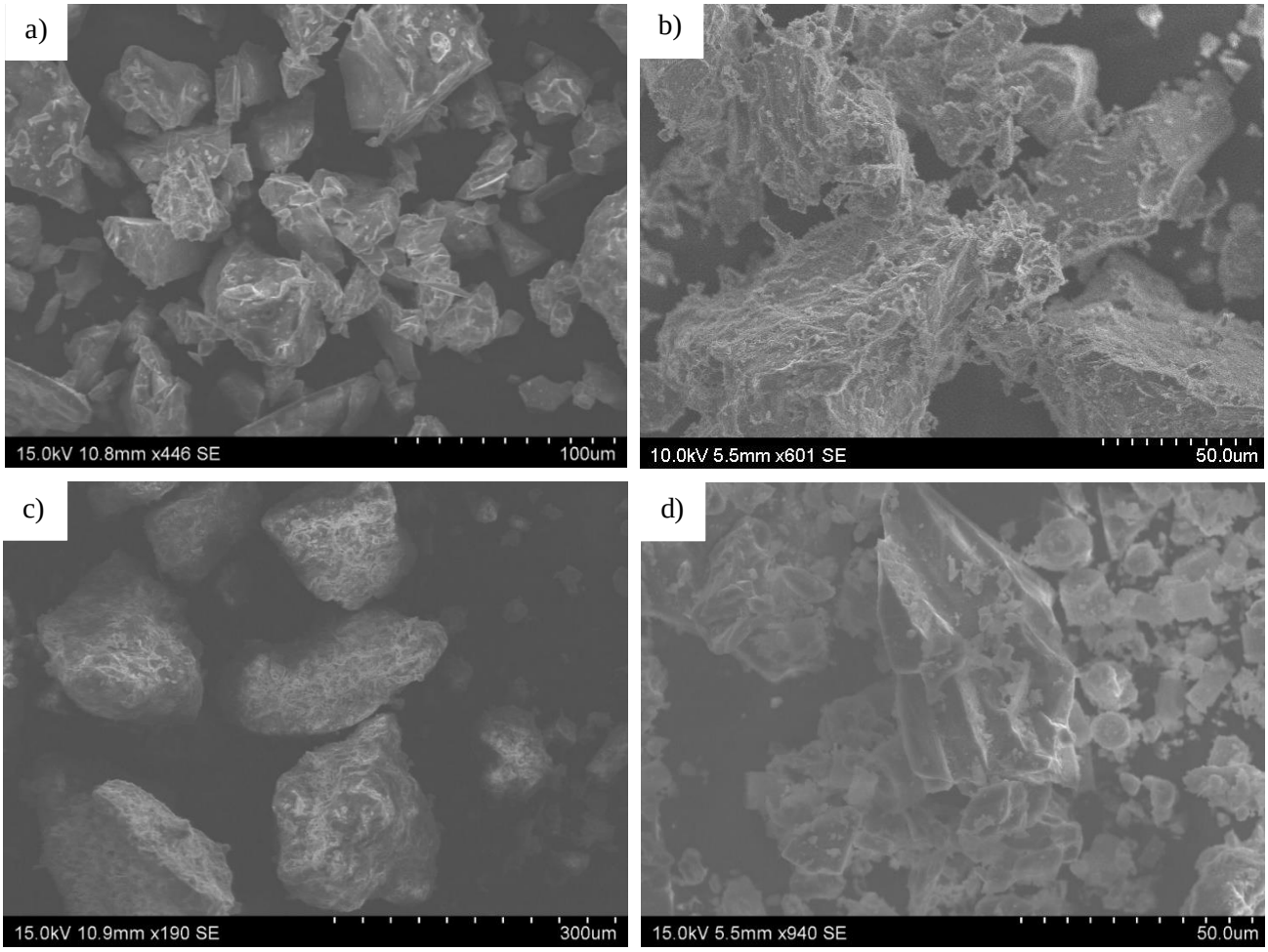

Figure 46. Secondary Electron Image (SEI) taken of the raw planetary analogues a) JSC-Lunar; b) LHS-1; c) JSC-Martian; d) MGS-1.

As demonstrated in Figures 45 a) and b), the general surface texture and appearance of the Earth-based JSC-Lunar simulant and synthesised LHS-1 are strikingly different, with the JSC-Lunar simulant being significantly darker (of a dark brown colour with individual, larger black grains) compared to the LHS-1 simulant which was observed to be of a much lighter, greyish white appearance, with noticeable larger black grains. As illustrated in Figures 46 a) and b), SEM analysis displayed the prominent variations in the Lunar simulants' granular surface textures and morphologies, with the Earth-based JSC-Lunar simulant consisting of a finer, smoother granular surface texture compared to LHS-1's noticeable adhering of smaller grains to larger ones and general rougher surface. The JSC-Lunar simulant's individual grains have sharp and angular edges, and the generic morphology was observed to be of a range of geometries, and not as rounded as predicted. Whereas in comparison, the LHS-1 simulant's grain morphology was noticeably block and angular shaped, and its surface texture slate-like. This morphology was intended by Exolith, as reported by Isachenkov et al [4, 12].

As illustrated by Figures 45 c) and d), there is a slight variation in surface texture and general appearance observed, with the Earth-based simulant JSC-Martian being slightly browner in colour, with individual black, green and white crystals present. The synthesised Martian simulant MGS-1 is noticeably more

orange hued, and even solely by optical microscopy its initial wider grain size distribution can be detected. SEM analysis as seen in Figures 46 c) and d) emphasized the contrast in granular surface texture and morphology, with the JSC-Martian simulant consisting of more rounded, finer grains compared to the MGS-1 simulant's sharper, angular grains with clear adherence of smaller grains to larger ones. Whilst SEM analysis of the Lunar and Martian analogues in their raw form has been previously reported by Exolith [4] and McKay D.S. *et al.* [11], a direct comparison between the Earth-based and synthetic simulants prior to modification had not been explored before.

3.3 Thermal Activation of the Raw, Pure Earth Materials

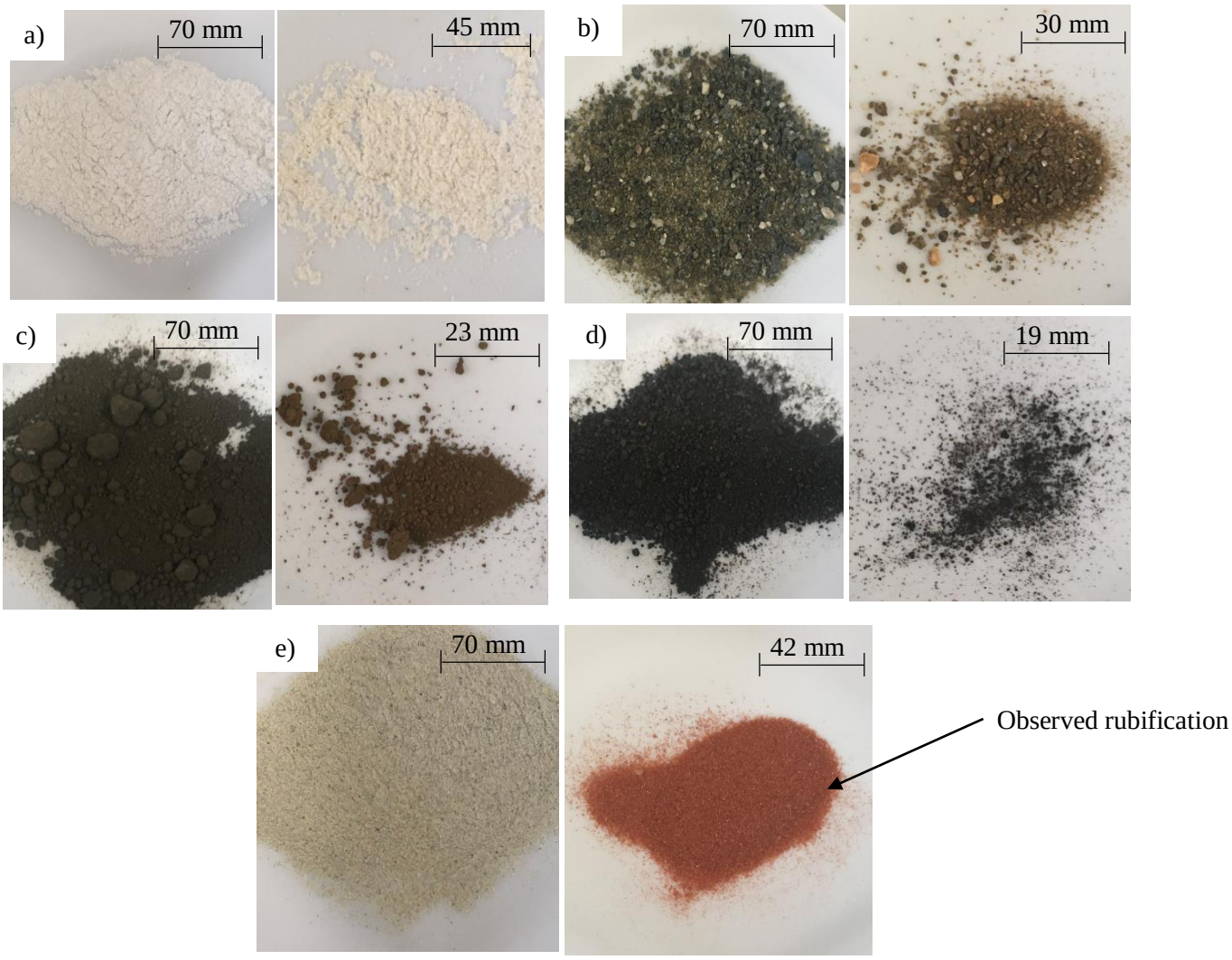

Figure 47. Photographs taken to compare the pure, raw Earth minerals and rock constituent samples at room temperature to those heated to 1000 °C a) anorthosite rock; b) pyroxene (bronzite); c) ilmenite; d) lava rock (basalt); e) olivine (labelled to illustrate rubification process as discussed in chapter 1).

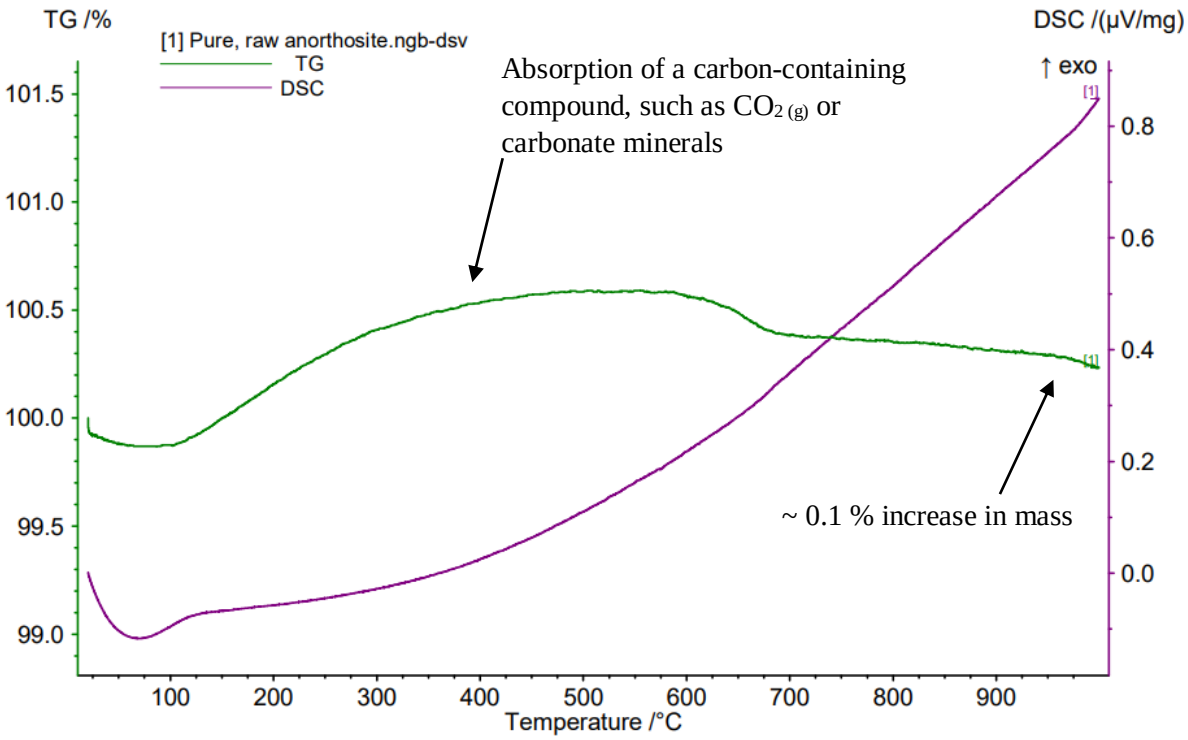

Figure 48. TGA-DSC curve for the raw anorthosite sample upon heating to 1000 °C under a constant flow of $N_{2\,(g)}$.

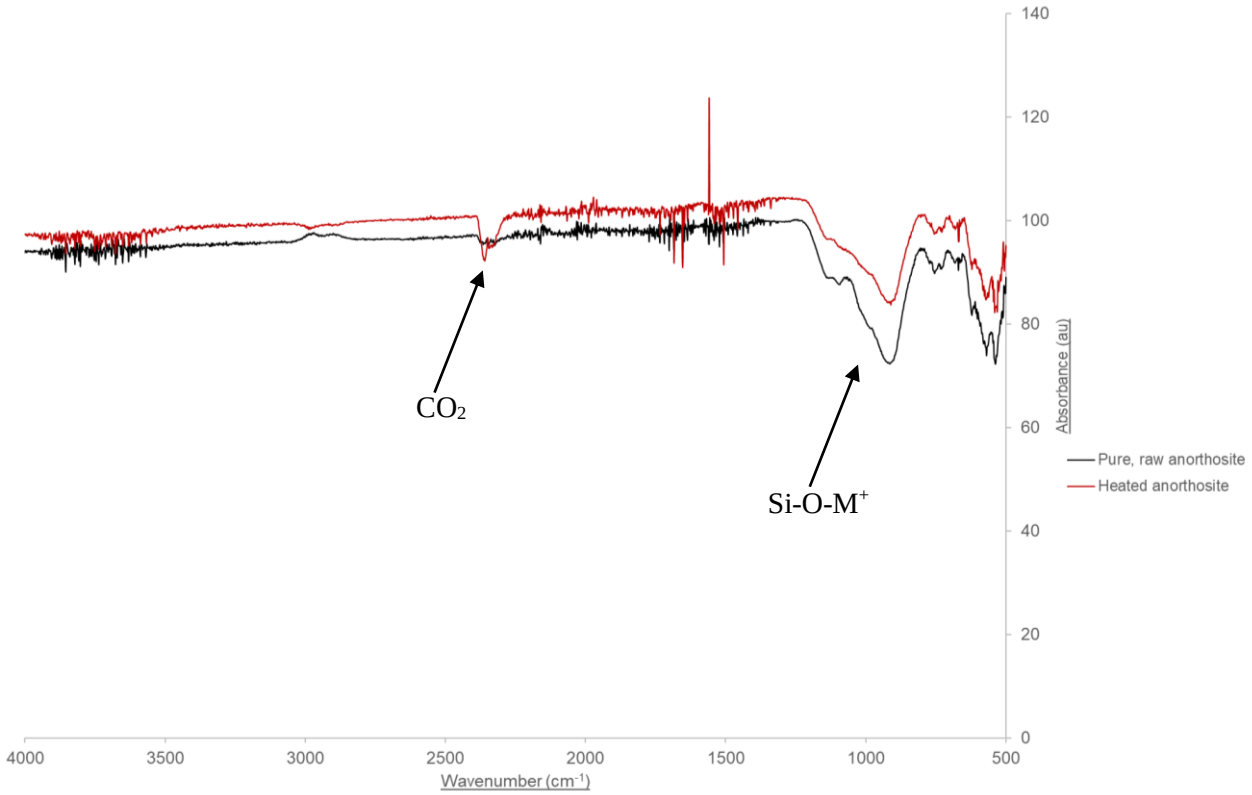

Figure 49. Infrared spectrum for the raw anorthosite sample heated to 1000 ℃ with a wavenumber range of 4000 cm^{-1} -500 cm^{-1}. Adsorption of CO_2 due to thermal activation is made apparent by the characteristic doublet peak at ~ 2400 cm^{-1}.

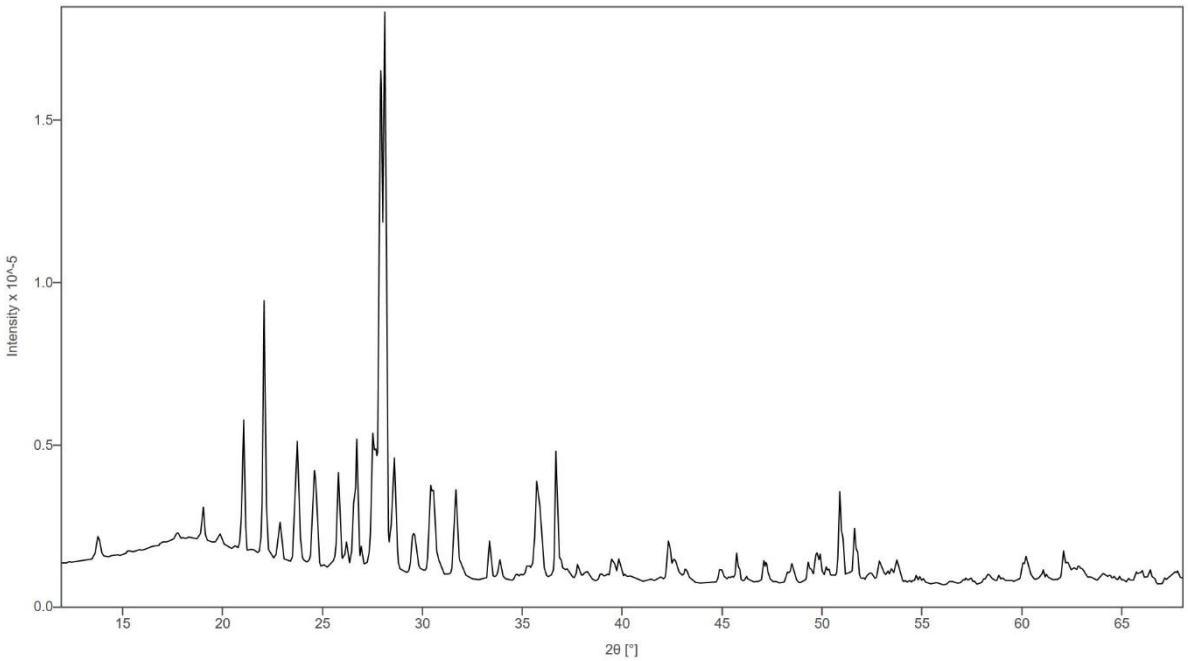

Figure 50. XRD diffractogram of the raw anorthosite sample heated to 1000 °C between 15°-65° and a scan time of 3 hours.

As shown in the TGA data above in Figure 48, heating the raw anorthosite to 1000 °C did not appear to cause a dramatic change in mass of the sample nor in its physical appearance as shown in Figure 47 a) with a slight increase towards the end of the experiment of ~ 0.1 %. The broad hump observed between temperatures 110 °C – 700 °C potentially suggests the absorption of a carbon-containing compound, such as $CO_{2\,(g)}$ or carbonate minerals due to thermal expansion of the mineral surface's cavities or pores. This adsorption of $CO_{2\,(g)}$ was further emphasised by IR spectroscopy, as illustrated in Figure 49 by the characteristic doublet peak at ~ 2400 cm^{-1} due to heating the raw anorthosite sample. However, the negative peak regarding the raw sample suggests the thermal expansion of mineral grains due to excitation of the asymmetric stretching vibrational mode of the CO_2 present within the grains is increasing the volume of space in the crystalline structure, thus enabling a greater proportion of IR light to pass through due to less interference. A decrease in Si-O-M^+ peak absorbance was observed at ~ 900 cm^{-1}. However, XRD analysis as demonstrated in Figure 50 did not suggest the contribution of any oxocarbon compounds or carbonate minerals. Despite a clear alteration in mineralogical structure as suggested by XRD analysis, mineralogy of the anorthosite sample remained fairly similar to prior to heating to 1000 °C, with the material still rich in sodium calcium aluminate silicates.

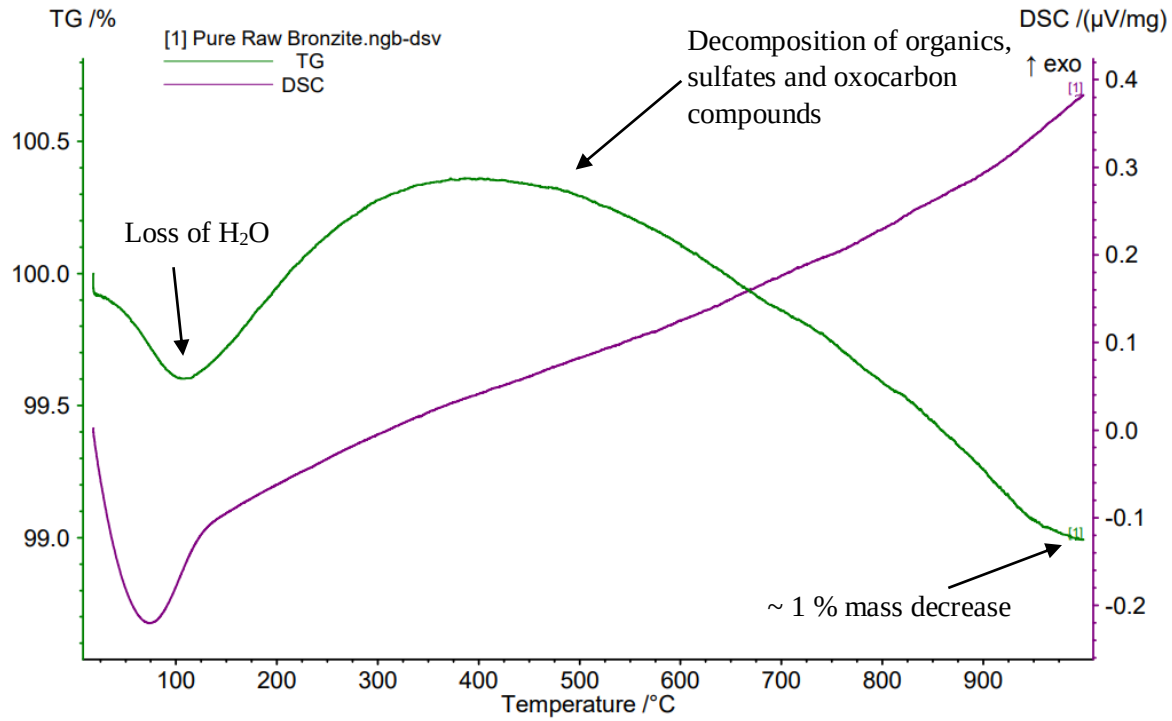

Figure 51. TGA-DSC curve for the raw bronzite sample upon heating to 1000 °C under a constant flow of $N_{2\,(g)}$.

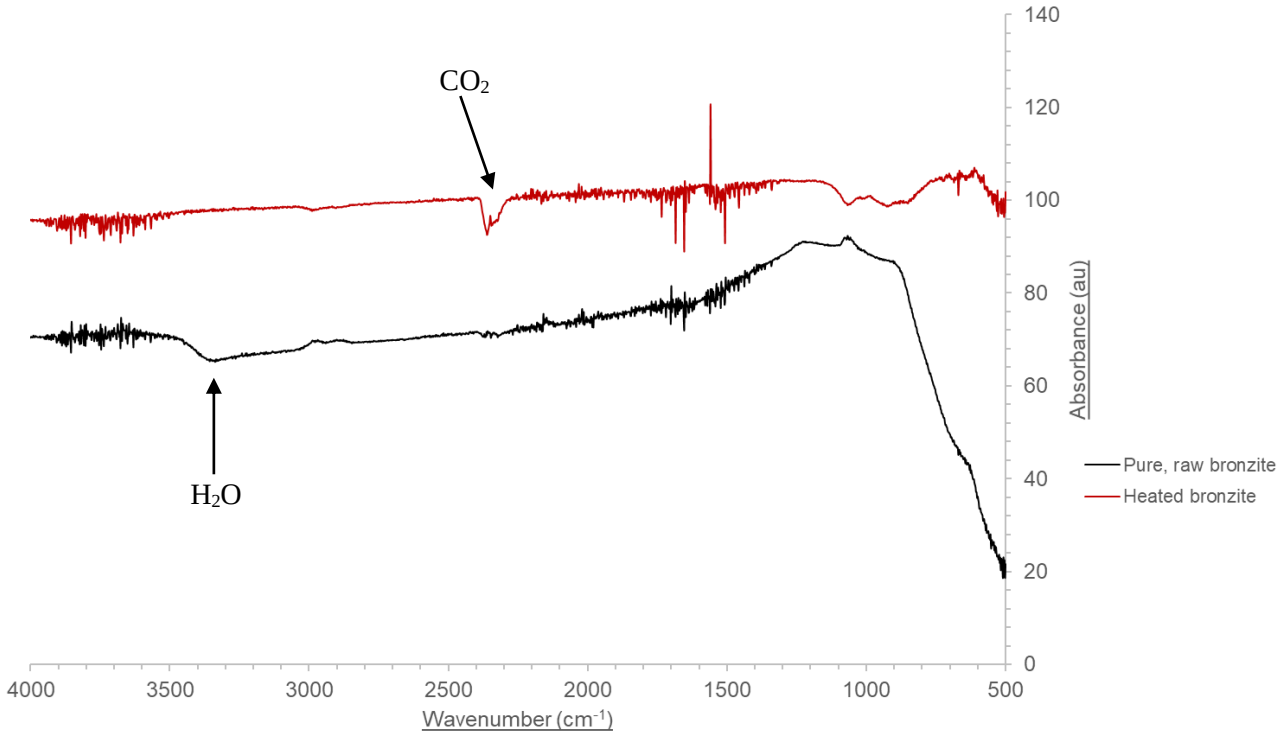

Figure 52. Infrared spectra for the raw bronzite sample heated to 1000 ℃ with a wavenumber range of 4000 cm^{-1} -500 cm^{-1}. Dehydration can be seen due to thermal processes from the reduction in the absorbance band at ~ 3400 cm^{-1}.

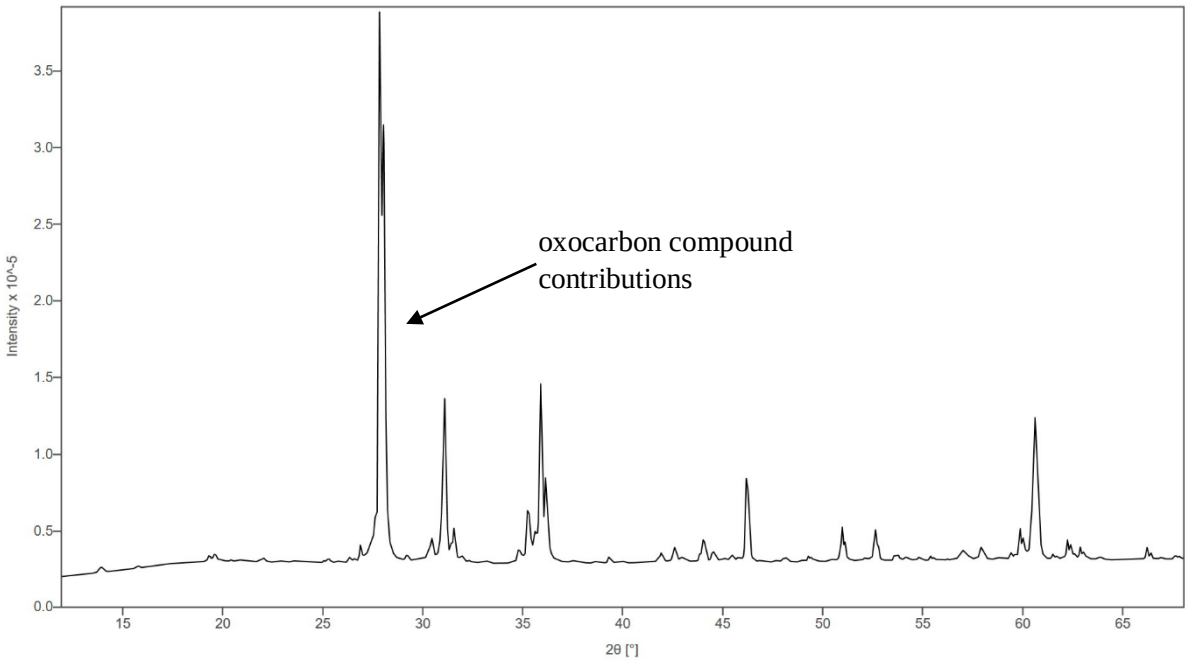

Figure 53. XRD diffractogram of the raw bronzite sample heated to 1000 °C between 15°-65° and a scan time of 3 hours.

Collected TGA data increased confidence in the large abundance of water and hydrated minerals present in the bronzite sample due to the sharp decline in % mass at ~ 100 °C indicating the loss of water as seen in Figure 51 above. IR results as illustrated in Figure 52 also indicate this loss of water due to a decrease in absorbance of bands at ~ 3400 cm^{-1} and < 800 cm^{-1}. The characteristic doublet peak at ~ 2400 cm^{-1} indicated the increase in $CO_{2\,(g)}$ uptake upon heating due to mineral surface activation and thus CO_2 being adsorbed onto grain surfaces. The DSC curve illustrated in Figure 51 demonstrates endothermic release of water from potential physical adsorption [38]. TGA analysis suggested the release of numerous potential organics and volatiles. At temperatures < 500 °C, the loss and decomposition of organics including carbonate minerals, sulfates and oxocarbon compounds (more prominently in this case gaseous CO_2) is suggested as seen in Figure 51 [38]. The broad TGA curve showed a greater loss in % mass in comparison to the anorthosite sample, of ~ 1 % and the disappearance of peaks characterised by hydrated minerals shown by XRD analysis would further emphasise this loss of these compounds. As illustrated in figure 53, the abundance of feldspar-rich minerals including magnesium iron silicates dramatically decreased, and as indicated by the peak at ~ 28.2°, oxocarbon compound contributions increased due to heating and thus increase in adsorption, possibly due to thermal activation of certain oxides found within the bronzite sample [47]. Physical observations upon heating included the general lighter, more orange-hued appearance of the bronzite sample, as illustrated in figure 47 b) above.

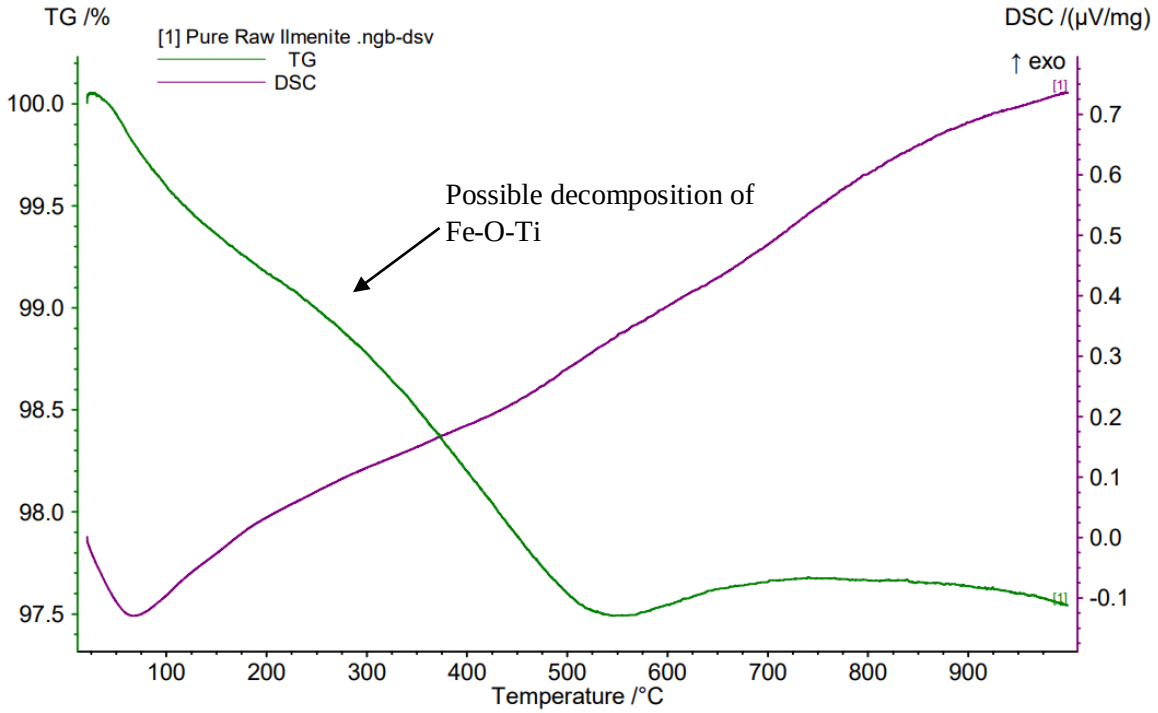

Figure 54. TGA-DSC curve for the raw ilmenite sample upon heating to 1000 °C under a constant flow of $N_{2\,(g)}$.

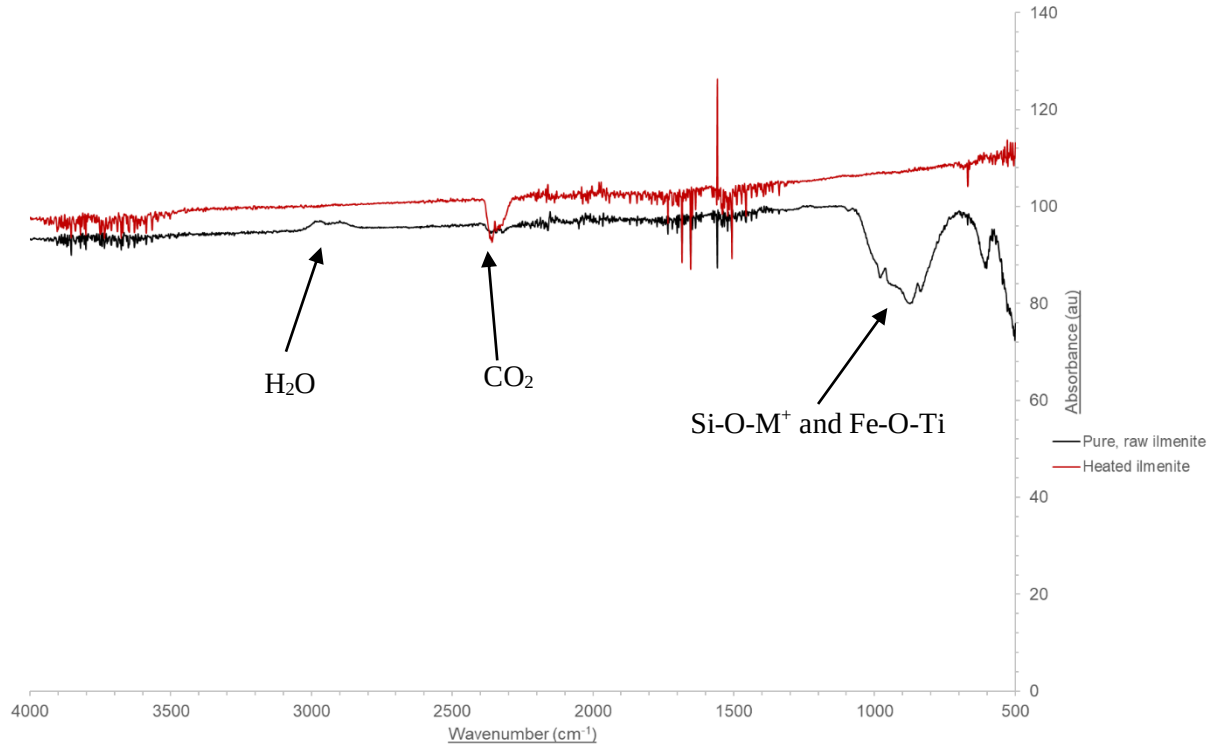

Figure 55. Infrared spectrum for the raw ilmenite sample heated to 1000 °C with a wavenumber range of 4000 cm^{-1} -500 cm^{-1}. Complete elimination of the Fe-O-Ti absorbance band at ~ 900 cm^{-1} is observed due to thermal activation.

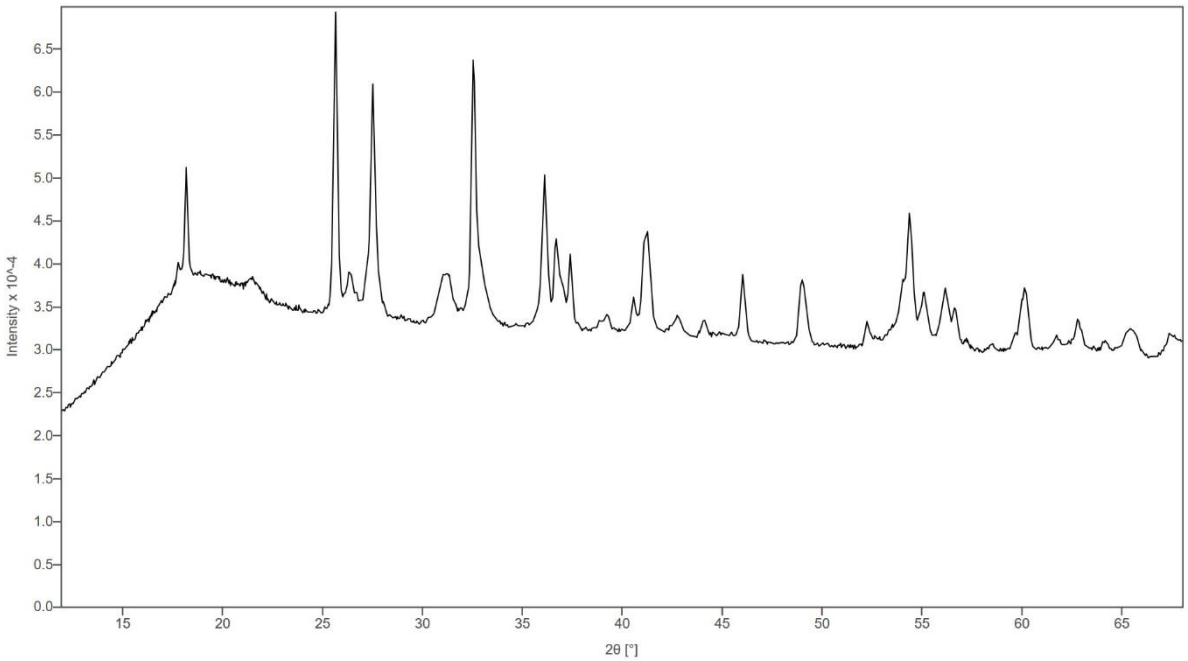

Figure 56. XRD diffractogram of the raw ilmenite sample heated to 1000 °C between 15°-65° and a scan time of 3 hours.

TGA analysis demonstrated a significant loss in % mass (~ 2.5 %) up to a temperature of ~ 500 °C (refer to Figure 54), which is characteristic for the loss of organic groups and volatiles such as carbonate minerals, oxocarbon compounds and sulfates. This particular observation is also evident for the adsorption of $CO_{2\,(g)}$ to mineral grain surfaces made evident by IR data as shown in Figure 56 by the characteristic $CO_{2\,(g)}$ doublet peak at ~ 2400 cm^{-1}. This sharp decline in % mass additionally suggests the potential for water which is physically adsorbed to organic surfaces, such as carbonates to be lost due to thermal activation. This minor loss of water was confirmed by IR analysis, with Figure 55 showing the disappearance of the slight broad peak at ~ 3400 cm^{-1} due to thermal conditions. A sudden drop in % mass as shown between ~ 100 °C – 500 °C usually indicates the loss of a specific functional group, which may possibly be indicated by the IR results in Figure 56 which illustrates the elimination of the Fe-O-Ti band observed at ~ 900 cm^{-1}, suggesting the thermal activation of a particular reaction pathway, thus the production of secondary minerals and compounds such as FeO and TiO_2. XRD analysis showed the effect of heating the ilmenite sample on iron abundance (as demonstrated in Figure 56), due to the significant decrease in background noise and thus fluorescence, but more prominently fewer iron phase-contributing peaks. At temperatures higher than 500 °C, a small exothermic broad peak is demonstrated, suggesting a potential stable phase transition [38]. The effect of heating the ilmenite sample was demonstrated by its lighter, browner appearance as illustrated in Figure 47 c) above.

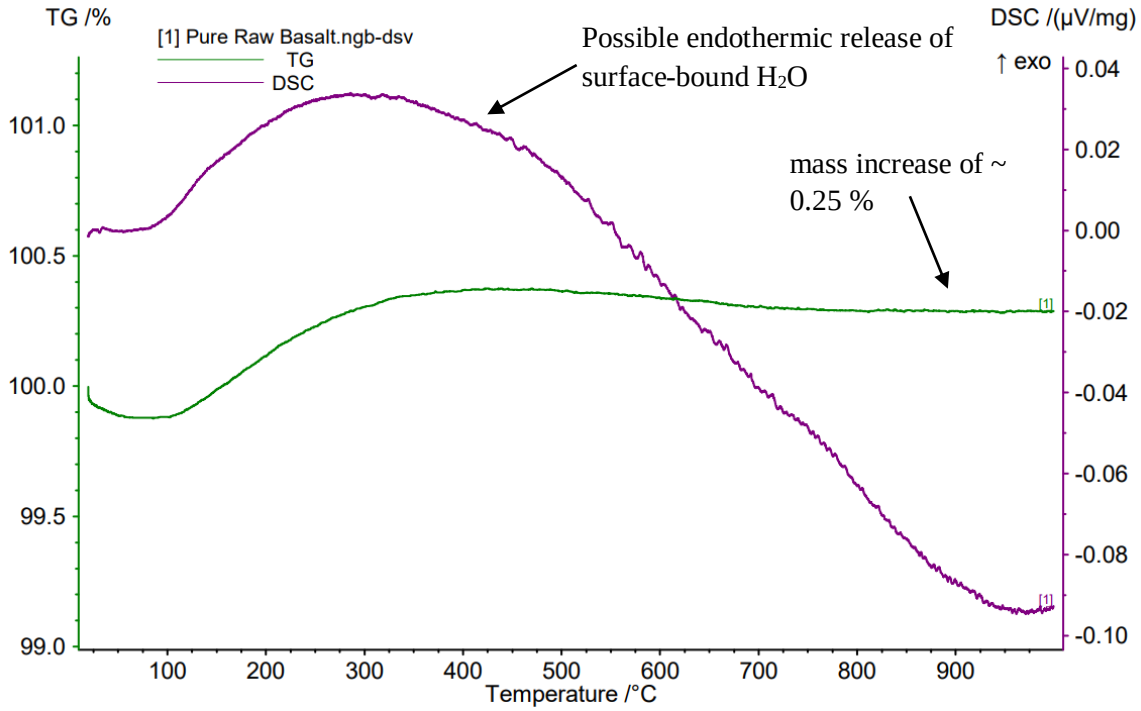

Figure 57. TGA-DSC curve for the raw basalt sample upon heating to 1000 °C under a constant flow of $N_{2\,(g)}$.

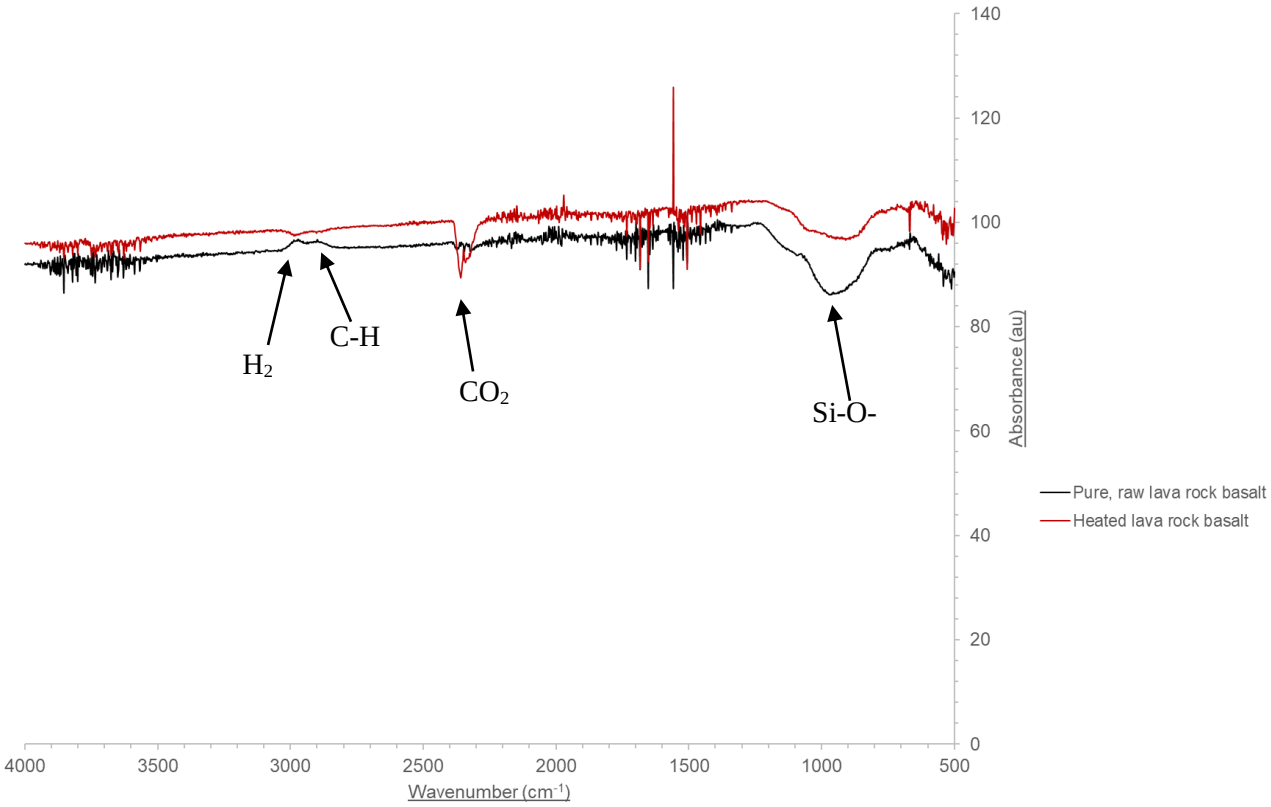

Figure 58. Infrared spectrum for the raw lava rock (basalt) sample heated to 1000 ℃ with a wavenumber range of 4000 cm^{-1} -500 cm^{-1}. Adsorption of CO_2 due to thermal activation is observed by the characteristic doublet peak at ~ 2400 cm^{-1}.

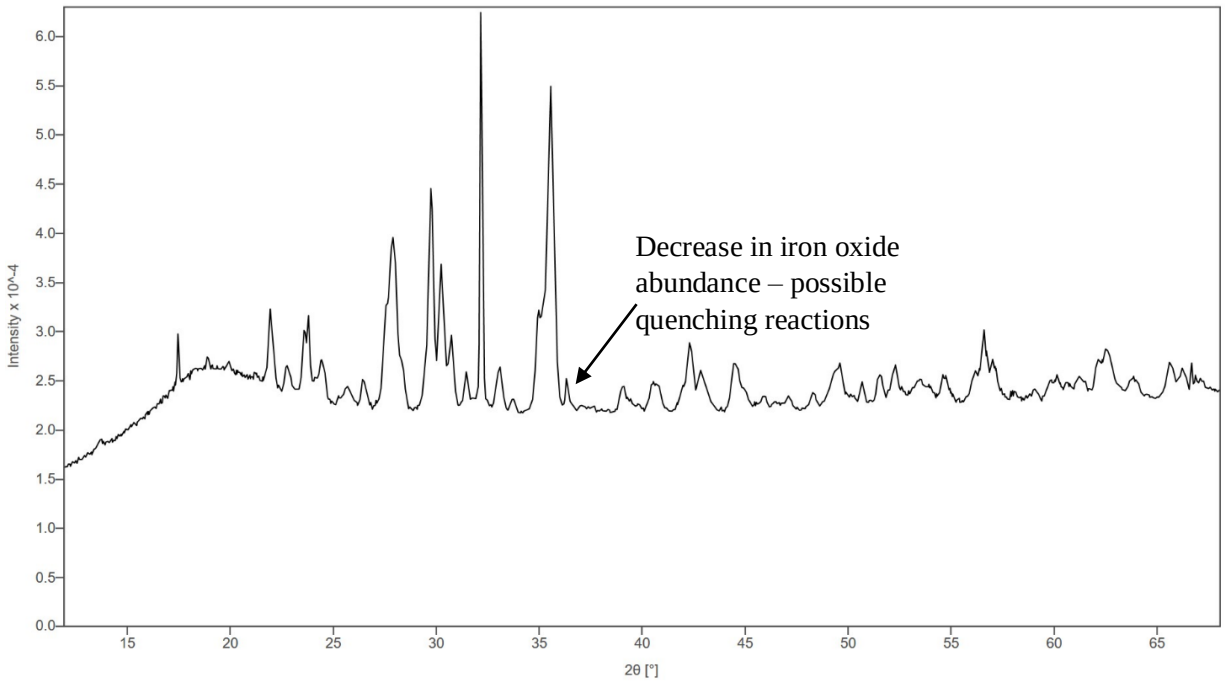

Figure 59. XRD diffractogram of the raw basalt sample heated to 1000 °C between 15°-65° and a scan time of 3 hours.

Figure 47 d) showed the little alteration in the lava rock basalt's appearance due to heating. As illustrated by the TGA-DSC curve in Figure 57, a slight % mass increase of ~ 0.25 % occurred due to heating, likely due to chemical changes which are indicated by the DSC curve which suggests the contribution of organics or alterations in hydrated minerals [38]. This is emphasised by the C-H stretching vibrational bands at ~ 3000 cm^{-1} seen in Figure 58. The slight broad peak at ~ 3000 cm^{-1} remained despite heating the sample to 1000 °C, suggesting reabsorption of atmospheric water once the sample's temperature had decreased. The significantly more prominent DSC curve also suggests a large endothermic release of a specific material which is physically bound to a mineral surface, possibly H_2O [38]. IR analysis indicates the absorption of CO_2, characterised by the peak at ~ 2400 cm^{-1} seen in Figure 58 (as mentioned for the minerals prior to this discussion). A decrease in Si-O-M^+ peak absorbance observed at ~ 900 cm^{-1} was illustrated yet again due to speculated chemical alterations, however unlike ilmenite, Si-O-M^+ bonds were still strong enough to display contributions to the chemical modification due to thermal activation, possibly due to basalt's higher silicate abundance. XRD analysis as shown in Figure 59 suggested the contribution of oxocarbon compounds due to a decrease in characterised diffraction angle values upon heating the basalt sample. A potential decrease in iron oxide abundance was also indicated by the improved signal to noise ratio of the peak angle value of ~35.5°, suggesting potential quenching reactions.

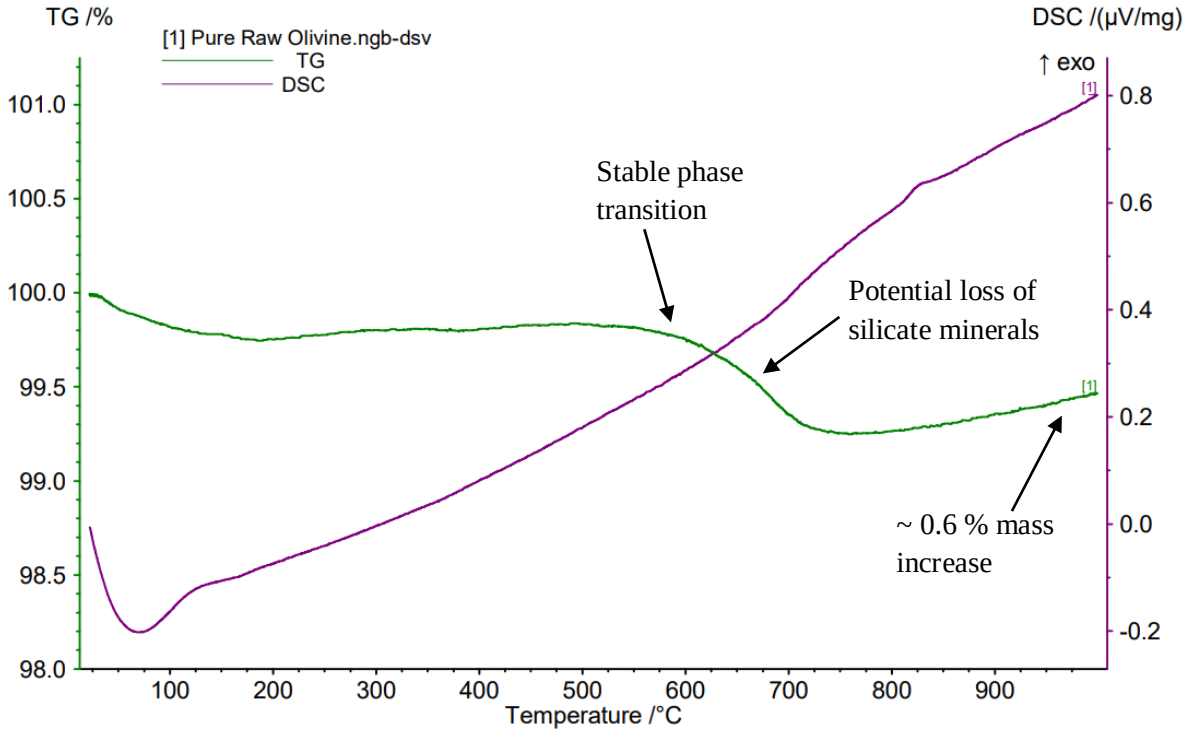

Figure 60. TGA-DSC curve for the raw olivine sample upon heating to 1000 °C under a constant flow of $N_{2\,(g)}$.

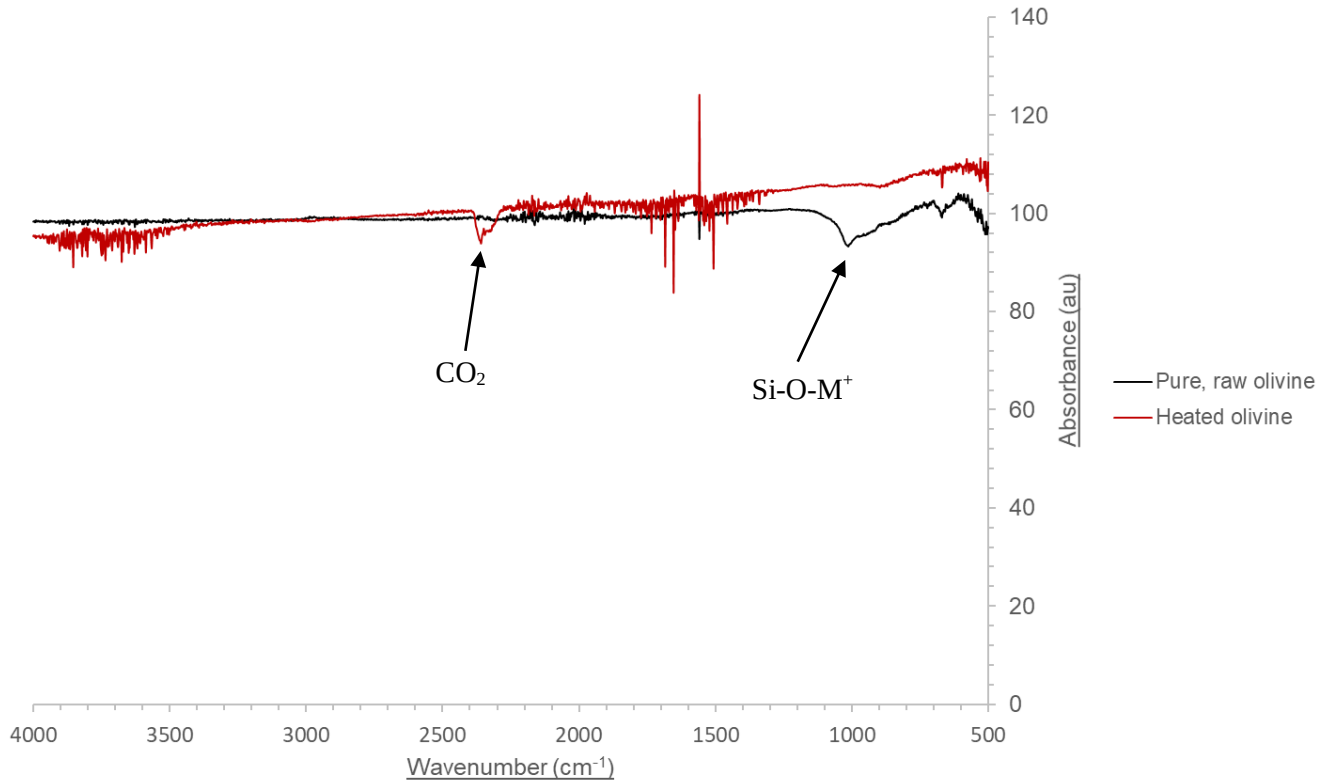

Figure 61. Infrared spectrum for the raw olivine sample heated to 1000 ℃ with a wavenumber range of 4000 cm^{-1} -500 cm^{-1}. Potential quenching of the Si-O-M^+ absorption band at ~ 900 cm^{-1} due to rubification is observed [21].

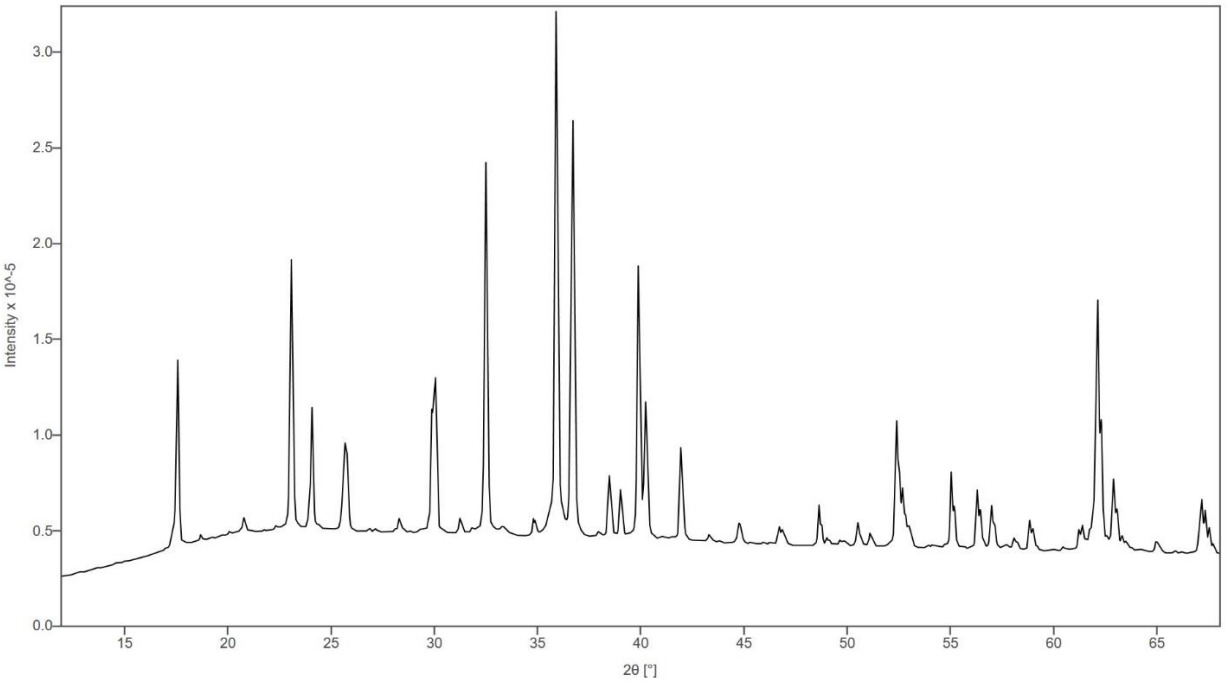

Figure 62. XRD diffractogram of the raw olivine sample heated to 1000 °C between 15°-65° and a scan time of 3 hours.

Figure 47 e) illustrates the significant alteration in the olivine sample's physical appearance due to heating to 1000 °C, with a colour change from a creamy white-green appearance to striking red. This process is known as rubification, whereby oxidation at higher temperature causes the release of iron from primary mineral materials and subsequently produces unbound iron oxide compounds which form red film coatings [21]. The TGA-DSC curve shown in Figure 60 indicates the slight decrease in % mass of ~ 0.6 %, which may potentially be due to a stable phase transition at ~ 600 °C, such as a more stable form of silica from a tetrahedral geometry to octahedral [63]. IR analysis shown in Figure 61 demonstrated the adsorption of $CO_{2\,(g)}$ as seen previously due to the absorbance band at ~ 2400 cm^{-1}. The effect of rubification may potentially be illustrated in Figure 61 due to the quenching of the Si-O-M^+ IR absorption band at ~ 900 cm^{-1} due to iron oxide abundance now being dominant [62]. This may be of particular relevance to the Martian surface (which is abundant in iron oxide) and atmosphere due to its highly oxidising nature and temperature [6,9]. The elimination of the diagnostic Si-O-M^+ peak at ~ 900 cm^{-1} was observed, and this potential decrease in silicate-based mineral abundances was further emphasised by XRD analysis as shown in Figure 62, displaying a decrease in peak intensities, mainly accounted for magnesium silicate minerals. The drop in % mass shown by TGA data at ~ 700 °C suggests the loss of a specific functional group (or quenching of), and so there is an increase in confidence with this prediction of the loss of the majority of silicate mineral contributions due to dominating iron oxide phases. To increase confidence in findings, analytical techniques such as VIS-NIR (Visible Near Infrared spectroscopy) should be employed to observe electronic transitions causing the rubification process. On the Martian surface, interactions between the free iron oxides and

electromagnetic radiation will cause such reddening of the surface sand [21]. Materials which change colour due to heating are thermochromic, and such colour changes are reversible upon cooling and thus analysis was conducted immediately and without cooling [63].

3.4 Summary and Conclusions

The work presented in this chapter illustrates the significance of preliminary characterisation of not only the planetary analogues in their raw form, but their constituent Earth minerals. Experimenting with the raw, pure individual minerals subsequently enabled their physical properties to be observed, and their potential chemical and mineralogical behaviour to be speculated. Due to the complex nature of internal self-sustaining reactions occurring within the milling reaction system, and the geochemically complicated chemistry of mineral surface interactions, understanding individual mechanochemical-induced affects such as the increased absorption of CO_2 due to increased specific surface area and thermal expansion of surface pores is essential in subsequently analysing the mechanochemical alterations of the analogue materials themselves.

Chapter 4: Mechanochemical Activation of Planetary Analogues

Following the preliminary characterisation discussed within chapter 3, the effect of ball milling (and differing modes of ball milling) on the simulants' mineralogy, mineralogical structure and chemical composition was assessed. Mechanochemical activation induced by means of ball milling was predicted to cause noticeable alterations to the Lunar and Martian simulants' mineralogical structures and chemical composition and mode of chemical bonding. This was due to the purposeful, controlled shearing of the crystalline layers within the materials' structural networks through abrasion, thus causing the activation of reaction pathways and the increase in reactivity of mineral surfaces through an increase in chemically active sites due to larger specific surface areas [28,29], as discussed in chapter 1.

Additionally, the type of mechanochemical energy and duration of milling that the regolith simulants were subjected to was varied to analyse the effect of differing mechanochemical modes on the mineralogical structure and chemical properties. Depending on the type of ball mill apparatus utilised, specific abrasion mechanisms occurring on the Lunar and Martian surface were simulated within the laboratory. The Retsch MM301 mixer mill and Fritsch P23 mini mixer mill were employed to replicate regolith transport over longer distances (as discussed in chapter 2). Repeated abrasion processes through collisional impacts were therefore simulated by utilising the Retsch MM301 and Fritsch P23. Notably, secondary collisional impacts, for instance due to meteoroidal impact ejecta striking the Lunar and Martian surface are also simulated by these types of milling. In order to simulate more localised abrasion (within confined areas like small craters) the University of Kent's P7 planetary micromill was employed (as discussed in chapter 2).

As discussed within this chapter, comparisons between the Earth-based and synthesised simulants were formulated using an array of analytical techniques to assess their differences in behaviour when subjected to identical milling conditions. Considering that all of the simulants have a high proportion of inorganic compounds, Raman spectroscopy was employed in addition to ATR-FTIR, however a great amount of fluorescence obscured the data, and so was omitted and ATR-FTIR employed as the sole and main spectroscopy analytical technique (refer to chapter 1).

4.1 Mechanochemical Induced Modifications in Mineralogy and Chemistry

As discussed in more detail in chapter two, the University of Kent's Rigaku MiniFlex 600 XRD was employed to analyse the effect of ball milling on the physical and chemical properties of the regolith analogues being utilised within research. Abrasive techniques such as milling and thus the shearing of

crystalline layers (increasing the percentage of amorphous content within a given material) was anticipated to generate mechanochemical-driven reactions, and mechanochemical activation of reaction pathways, potentially increasing the reactivity of mineral surfaces and the generation of oxidising species. It was anticipated that the blending of such materials would yield in the production of secondary minerals, and an enhancement in the contribution of certain minerals due to an increase in their specific surface area and thus reactivity. Mechanochemical activation can be perceived differently at the macro and microscale for a crystalline lattice structure. At the macroscale, deformation within a lattice due to abrasion is situated in interfaces between minerals with varying properties. Whereas at the microscale, minerals' grain boundaries have varying mechanochemical properties. When deformations are formed at mineral grain boundaries, dislocations within the lattice structure go towards the surface and thus produce charged species such as surface radicals. Through fracturing of the material and therefore silica bonds, due to bond breakage, the surface radicals formed thus mean charged silica and oxygen ionic sites are vacant. Stillings e*t al*. suggests that the formation of such reactive species may allow CO_2 to diffuse to lattice interstitials more efficiently and with greater ease, perhaps due to the lowering of activation energy (E_a) needed for chemical adsorption. The adsorbed CO_2 is proposed to be insoluble, and made apparent by leaching experiments due to the stable bonds between the CO_2 and charged surface. Chemical adsorption of CO_2 has been shown to weaken ionic bonding within the crystalline lattice, therefore allowing cations such as Ca^{2+} and Mg^{2+} to leach into the solution which can further react with CO_2 to precipitate CO_3^{2-} and thus carbonate minerals such as $CaCO_3$ [29].

The intensity of peaks within XRD measurements is dependent on the relative abundance of molecules/crystals within a particular fixed given volume/spacing. Therefore, it can be assumed that as the abundance increases, and thus the more densely packed the space is, the more intense the peak measurement will be [64]. Ball milling causes the shearing of crystalline layers within a material, and in general, the breakdown of larger molecular structures into smaller segments. Mechanochemical deconstruction of a material by means of ball milling thus means an increase in surface area. This increase will inevitably decrease the abundance of molecules within a fixed volume of space, reducing the density (when considering individual grains). Nonetheless, for a given sample volume, a decrease in grain size leads to closer packing, reducing voids present within the structural network and thus increasing density. However, XRD techniques measure over numerous grains, therefore exact intensities can only be speculated, whereas relative peak intensities when comparing diffractograms can be discussed with greater confidence due to preliminary characterisation results as discussed in the previous chapter.

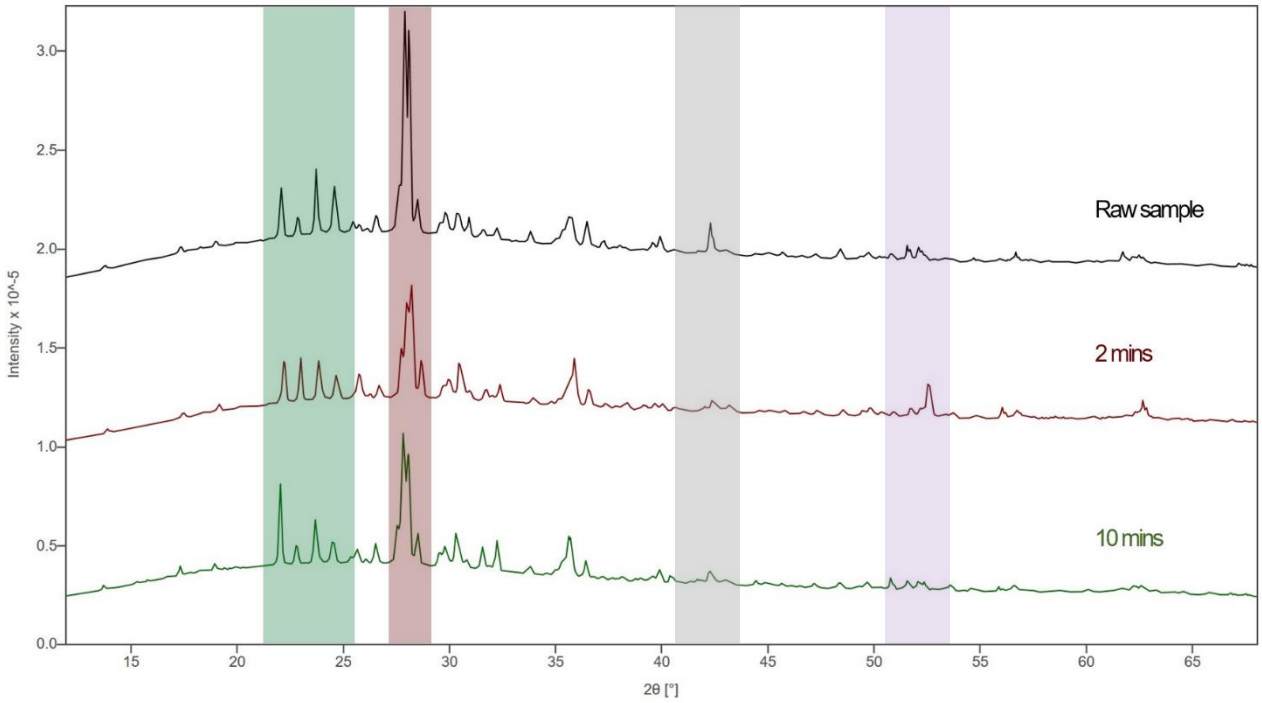

Figure 63. XRD diffractograms demonstrating the effect of milling (Retsch MM301 mixer mill) JSC-Lunar simulant for 2 and 10 minutes between 15°-65° and a scan time of 3 hours. Highlighted peaks illustrate examples of noticeable changes in relative peak intensity between samples, in particular the speculated feldspar silicate mineral contribution at ~ 27.9°.

As illustrated in Figure 63, XRD analysis shows the effect of milling using the Retsch MM301 mixer mill on the mineralogy and mineralogical structure for the Earth-based JSC-Lunar simulant. As anticipated, an increase in extent of abrasion (milling time) caused alterations in the relative peak intensities. The most significant variation in mineralogical structure was indicated by a decrease in peak intensity at ~ 27.9° and an increase in peak intensity at ~ 22.1° after 10 minutes milling. Ball milling of the JSC-Lunar simulant for 10 minutes showed less of an effect on peak intensity in comparison to the initial 2 minutes, however, there was a general relative decrease between 15°-65°, indicating that crystallinity is affected by the inflicted abrasion. An increase in intensity was noted at ~ 53.9 upon milling for 2 minutes, perhaps due to closer packing of grains. Perhaps due to the quenching of feldspar contributions and the increase in titanium oxide contributions, suggested by the Highscore software utilised [41]. It is important to note that the cause (s) of modifications in peak intensity cannot be identified with great confidence, as this will vary due to sample loading and instrumental setting variations. However, throughout this thesis, relative peak intensities between samples have been described.

The JSC-Lunar simulant subjected to 2 minutes of milling at a frequency of 10 Hz caused a slight reduction in grain size as discussed within this chapter. As previously discussed, the variation in relative

peak intensity upon milling indicates differing mechanochemical effects on certain mineral constituents within the JSC-Lunar simulant due to varying surface areas, and therefore potentially, reactivity rates. Within the reaction vessel, some areas of the material will be impacted by ball bearings and the material itself more frequently than others due to randomised contact, therefore increasing the likelihood of lattice deformations within a given area of the crystalline network. The XRD diffractograms suggest changes in contributions from specific mineral components, and in particular feldspar minerals, for instance sodium calcium aluminium silicate, indicated by the diagnostic main feldspar peak at ~27.9° (which applies to all of the silica-based analogues utilised within this research). The aforementioned increase in relative peak intensity observed at ~ 22.1° for the JSC-Lunar simulant when subjected to 10 minutes of milling (as illustrated by Figure 63) could possibly be due to an increase in average density due to void reduction and thus more closely packed grains within a given unit volume due to individual grain sizes decreasing in diameter.

In general, ball milling of the Earth-based JSC-Lunar simulant had an insignificant effect on the mineralogical composition, with an assumed minor production of secondary minerals through mechanochemical activation. Even prior to milling, the presence of carbonated minerals was potentially observed due to the peak angle value of ~ 27.9°, suggesting trapped carbon within the feldspar mineral content. This was speculated to be due to carbonates and not an oxocarbon compound such as CO_2 due to no infrared spectroscopic evidence of CO_2 apart from after milling for 10 minutes, as seen below in Figure 64.

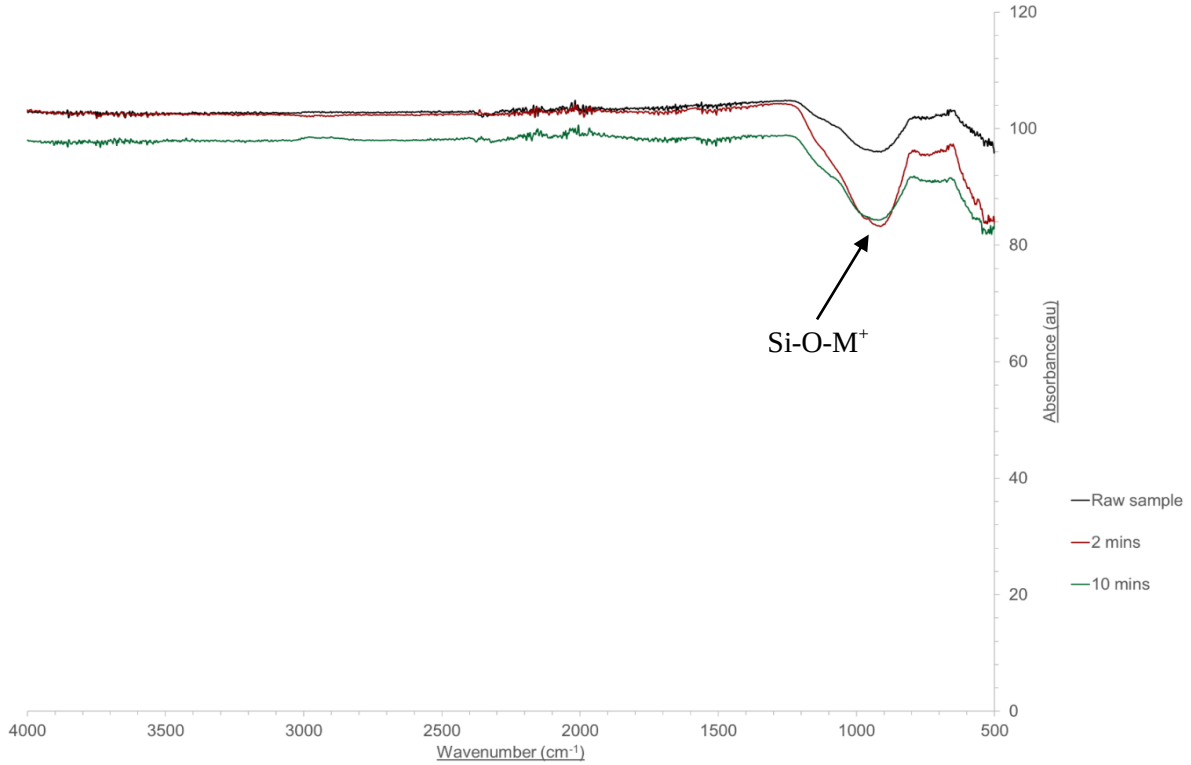

Figure 64. Infrared spectra with a wavenumber range of 4000 cm^{-1} -500 cm^{-1} demonstrating the effect of milling (Retsch MM301 mixer mill) for 2 and 10 minutes on the JSC-Lunar simulant's chemical composition. An increase in band absorbance can be seen at ~ 900 cm^{-1} upon milling for 2 minutes.

The infrared spectra of the JSC-Lunar simulant shown in Figure 64 illustrates the effect of milling on the Si-O-M^+ (M^+ = metal cation) bond as characterised by the change in absorbance for the band at ~ 900 cm^{-1} [46]. The slight shoulder observed most distinctly for 2 minutes of milling at ~ 1090 cm^{-1} indicates the antisymmetric SiO_4 stretching vibrational modes, a feature commonly observed in quartz samples [46]. After 2 minutes of milling, the relative absorbance of these bands increase as expected due to the decrease in grain size, thus subsequently causing an increase in specific surface area and more closely packed grains and therefore an increase in overall density, allowing more contact between the infrared radiation beam and sample's surface. The large decrease in absorbance observed for the JSC-Lunar simulant when subjected to 10 minutes of milling in comparison to 2 minutes could potentially be due to grain size being too miniscule and thus IR penetration depth and thus wavelength not having a long enough path length, however good coverage of the ATR crystal was ensured. Another potential explanation for such a decrease could be the fine grains comprising the JSC-Lunar sample after 10 minutes of milling, therefore decreasing contact between radiation and the sample.

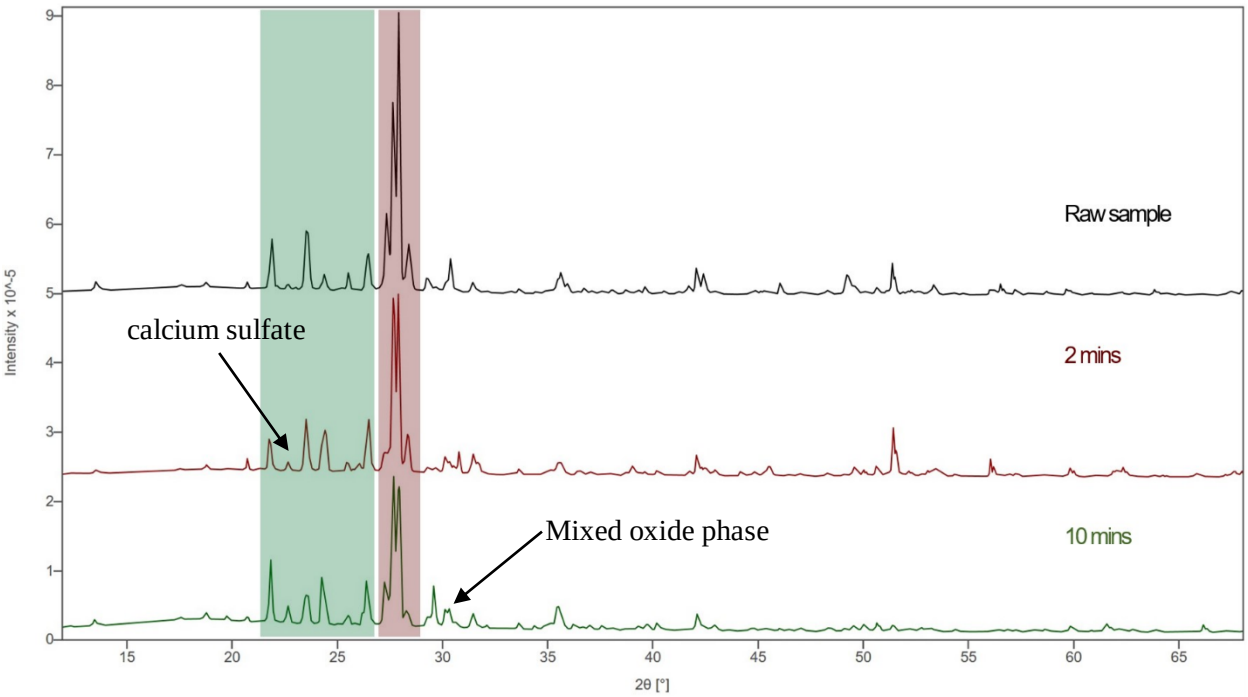

Figure 65. XRD diffractograms demonstrating the effect of milling (Retsch MM301 mixer mill) for 2 and 10 minutes on the LHS-1 simulant between 15°-65° and a scan time of 3 hours. Highlighted peaks illustrate noticeable changes in relative peak intensity between samples, in particular the speculated feldspar silicate mineral contribution at ~ 27.9°.

Figure 65 illustrates the decrease in relative peak intensity regarding feldspar peak contributions at ~ 27.9°. Nonetheless, an increase in intensity was simultaneously identified at ~ 21.7° between 0 and 10 minutes of milling, as observed with the JSC-Lunar simulant, thus indicating a greater SiO_2 contribution. This variation in surface area of the feldspar minerals indicates the possibility of simultaneous surface and localised reactions occurring within the milling reaction system as a whole,

with varying extents of abrasion. XRD analysis of the synthesised LHS-1 simulant emphasises its high degree of crystallinity due to sharp, intense peaks, and considering the fact that this Lunar simulant is analogous to the Lunar highlands which are of higher crystallinity in comparison to the average surface/subsurface bedrock on the Moon, it can be assumed that its mineralogy and mineralogical structure including crystalline phases and its alteration due to experimental weathering is potentially well-matched when interpreting the highland regions, however the JSC-Lunar simulant allows interpretation of the average Lunar surface including more amorphous components (as shown in figure 63 by the raised hump observed before ~ 20°), perhaps making it more suitable for laboratory experiments.

Regarding mineralogical composition, subjecting the LHS-1 simulant to 2 minutes of milling seemingly yielded in the production of calcium sulfate, indicated by the peak present at ~ 23.6°. Several different oxide phases were potentially produced by means of milling, for instance phosphate oxide, calcium titanium oxide, potassium oxide, iron titanium oxide and calcium iron oxide, all suggested by the peak angle value of ~ 30.0°. In contrast to the Earth-based JSC-Lunar simulant, abrasion appeared to have more of an effect on the LHS-1 simulant, given the more significant generation of oxide compounds. As the Lunar highlands are more exposed to meteoritic impacts and thus the surface more frequently 'gardened', regolith recovered here is expected to be more chemically diverse.

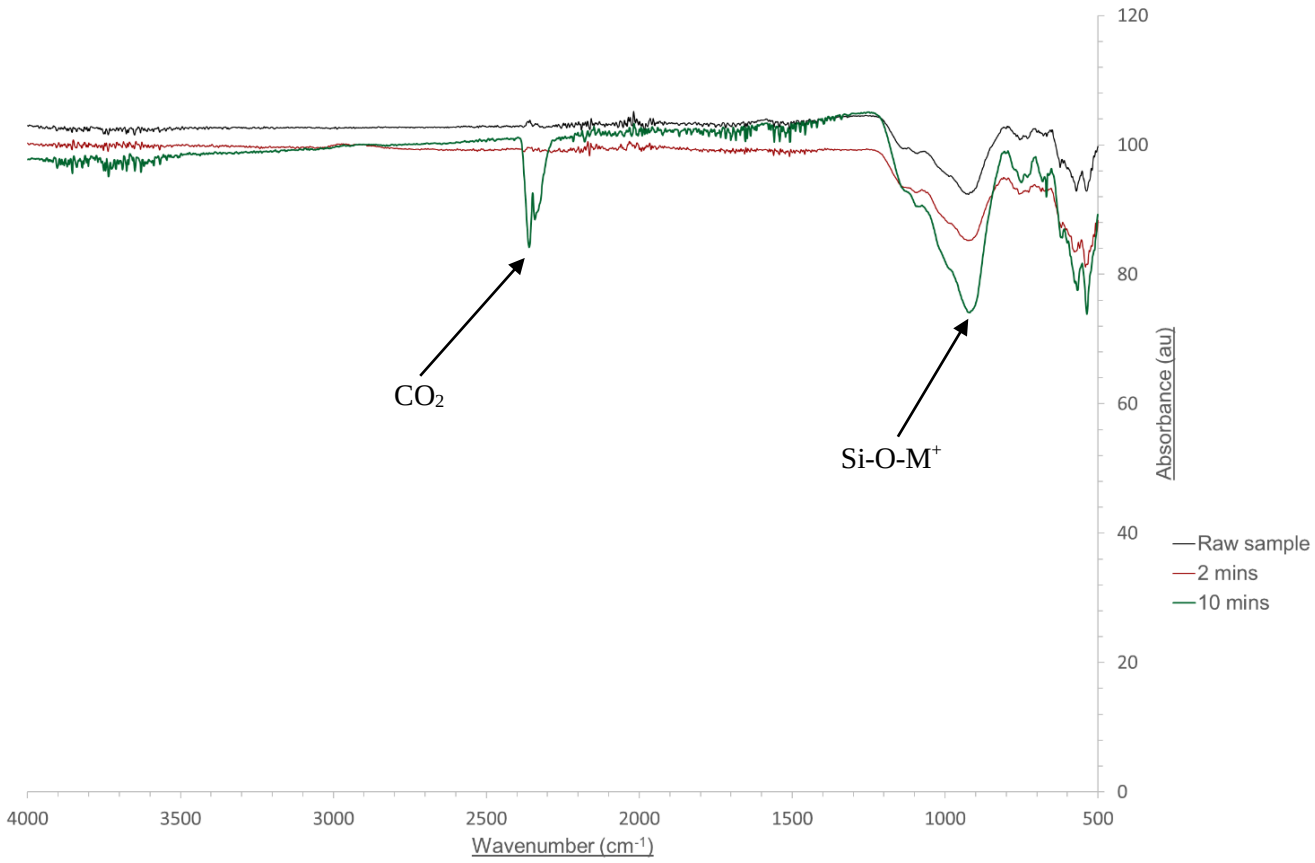

Figure 66. Infrared spectra with a wavenumber range of 4000 cm^{-1} -500 cm^{-1} demonstrating the effect of milling (Retsch MM301 mixer mill) for 2 and 10 minutes on the LHS-1 simulant's chemical composition. Milling for 10 minutes can be seen to cause the increased uptake of CO_2 due to the characteristic doublet peak at ~ 2400 cm^{-1}.

Considering the synthetic LHS-1 simulant, an increase in absorbance of the Si-O-M^+ (M^+ = metal cation) band (~ 900 cm^{-1}) was observed in Figure 66 shown above as milling time increased from 0 to 10 minutes. The characteristic doublet peak at 2400 cm^{-1} for CO_2 was identified regarding the LHS-1 sample milled for 10 minutes. A slight absorbance band at ~ 1500 cm^{-1} can be observed, suggesting carbonate mineral contributions. Similarly, to the Earth-based JSC-Lunar simulant, the increase in band absorbance for silicate-based minerals was due to a decrease in average grain size and increase in surface area and thus a more densely packed sample, allowing more contact between the material's surface and the infrared radiation. However, in contrast to the JSC-Lunar simulant, a continuous increase in band absorbance was displayed during milling to 10 minutes. As the grain size distribution and average granular diameter of LHS-1 was initially wider and larger due to minimal milling for the purpose of achieving a specific grain size distribution, this could potentially mean that 2 minutes of milling did not decrease the average grain size down to a scale small enough to show the maximum Si-O-M^+ absorbance band and thus the number of active surface M^+ present. Considering the pre-weathered and abraded state of the JSC-Lunar sample due to natural environmental processes, the maximum number of surface M^+ cations had already been achieved through milling, followed by further

abrasion which perhaps quenched the surface M^+ cations through induced chemical reactions and the formation of new bonds. A noticeable difference in results between the Earth-based and synthetic Lunar analogues was the absorption of gaseous CO_2 upon milling the LHS-1 simulant for 10 minutes at a frequency of 10 Hz. Numerous plausible reaction mechanisms for the absorption of $CO_{2\,(g)}$ have been speculated, including the presence of carbonate minerals and atmospheric uptake. Due to fluid inclusions in minerals (cavities that contain trapped gas during the mineral growth process), silicate minerals found on Earth are often abundant in $CO_{2\,(g)}$ [58]. Due to milling increasing the number of chemically active sites on the mineral surface [28, 29], this can potentially cause a greater adsorption/uptake of $CO_{2\,(g)}$. Mechanochemical activation subsequently reduces grain size and increases the specific surface area [28], therefore allowing greater CO_2 sequestration due to increased diffusion.

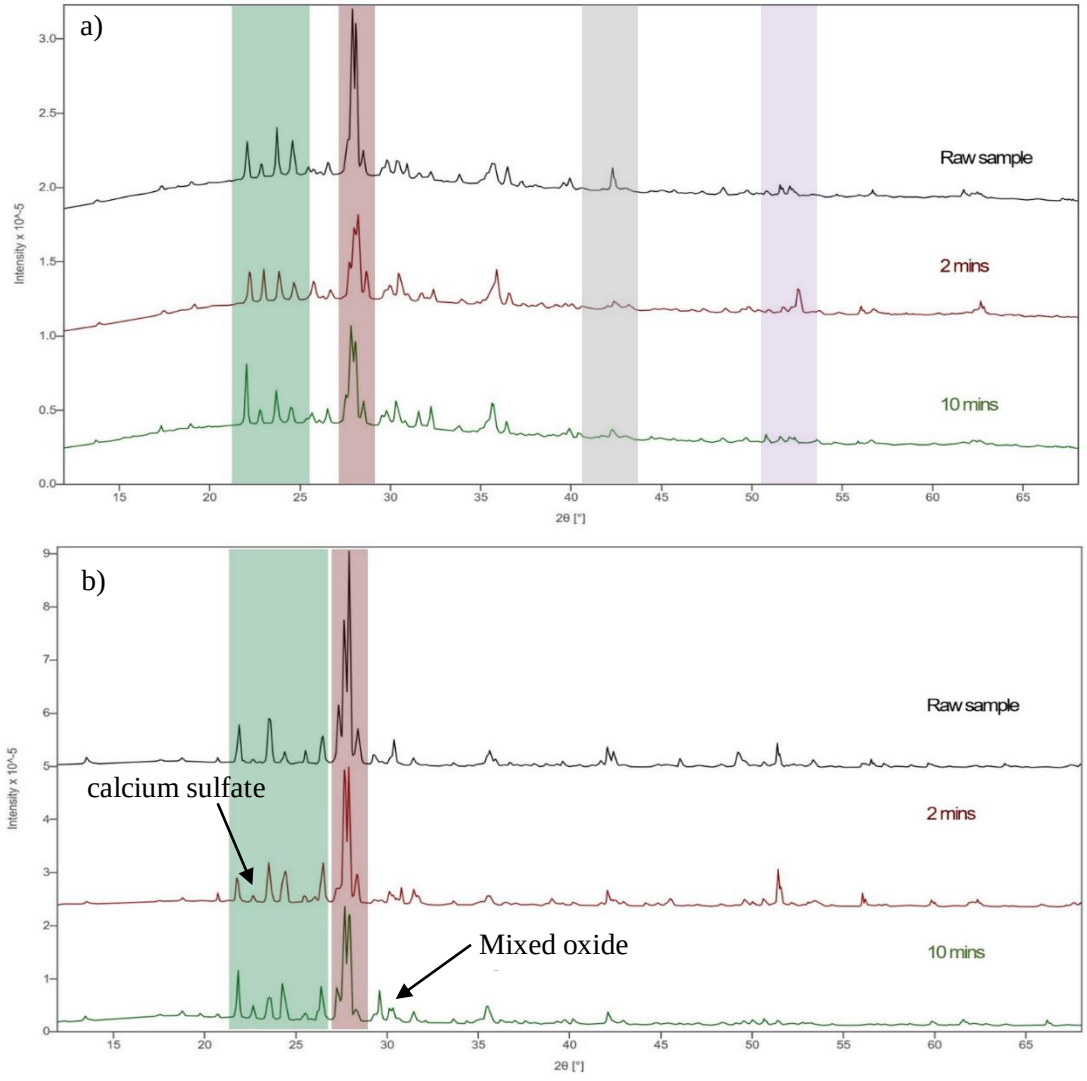

Figure 67. XRD diffractograms comparing the effect of milling (Retsch MM301 mixer mill) for 2 and 10 minutes on the a) Earth-based JSC-Lunar simulant and b) synthesised LHS-1 simulant between 15°-65° and a scan time of 3 hours. Highlighted peaks illustrate noticeable changes in relative peak intensity between samples, in particular the speculated feldspar silicate mineral contribution at ~ 27.9°.

Based on XRD results, milling utilising the Retsch MM301 set under identical experimental conditions had varying effects on the mineralogical structure and mineralogy for the JSC-Lunar and LHS-1 simulants. On average a higher relative peak intensity was observed for the LHS-1 simulant compared to the JSC-Lunar simulant after 10 minutes of milling (considering peak height ratios), perhaps indicating more densely packed surface grains within the sample. As the LHS-1 simulant was synthesised in the laboratory through the blending of individual minerals (primarily anorthosite), the wider range of milling products and alterations in mineralogy was expected as seen in Figure 67 above. Whereas considering the natural origin of the Earth-based Lunar simulant which had already been weathered for a significant period of time, the less pronounced changes in mineralogy were anticipated due to a maximum number of active surface M^+ cations present prior to milling, as discussed previously.

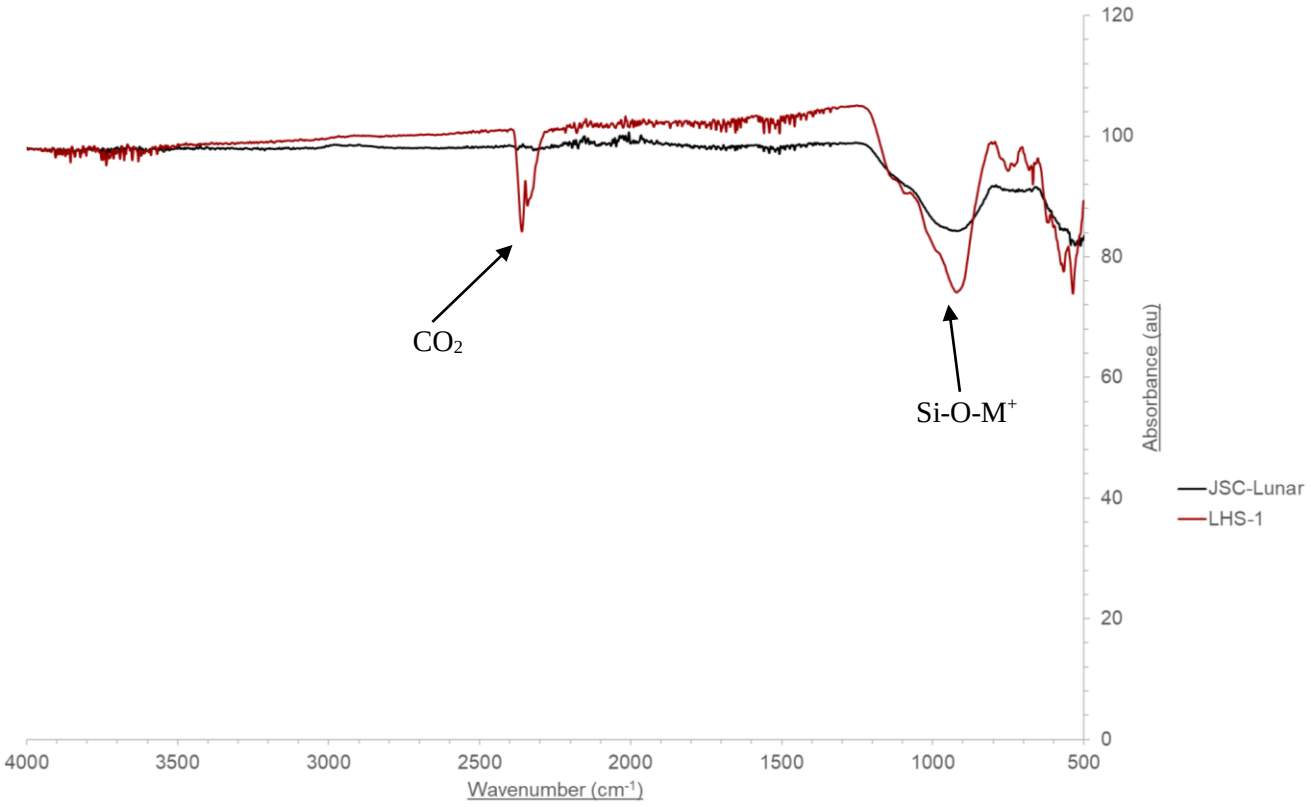

Figure 68. Infrared spectra with a wavenumber range of 4000 cm^{-1} -500 cm^{-1} comparing the effect of milling (Retsch MM301 mixer mill) for 10 minutes at a frequency of 10 Hz on the JSC-Lunar and LHS-1 simulants. Greater absorbance values can be seen for the synthesised LHS-1 simulant.

As shown in Figure 68, 10 minutes of milling the LHS-1 simulant potentially caused further uptake of atmospheric CO_2, as illustrated by the doublet peak at ~ 2400 cm^{-1} (characteristic for this molecule), but was not observed for the Earth-based JSC-Lunar simulant, possibly due to the LHS-1 simulant possessing a higher concentration of Ca^{2+} and Mg^{2+} cations. Whilst both Lunar simulants displayed the characteristic Si-O-M^+ (M^+ = metal cation) band at ~ 900 cm^{-1}, the relative absorbance was considerably greater for the LHS-1 simulant, suggesting a higher concentration of free M^+ cations as discussed

previously due to a lesser extent of milling in comparison to the pre-weathered JSC-Lunar simulant. XRD analysis indicated a larger average grain size regarding the LHS-1 simulant in comparison to the JSC-Lunar simulant, yet infrared spectroscopy results suggested a greater change in grain size due to a greater absorption band at ~ 900 cm^{-1}. The JSC-Lunar simulant displayed a broader peak at ~ 900 cm^{-1} in comparison to the LHS-1 simulant, thus indicating coarser, less fine granules.

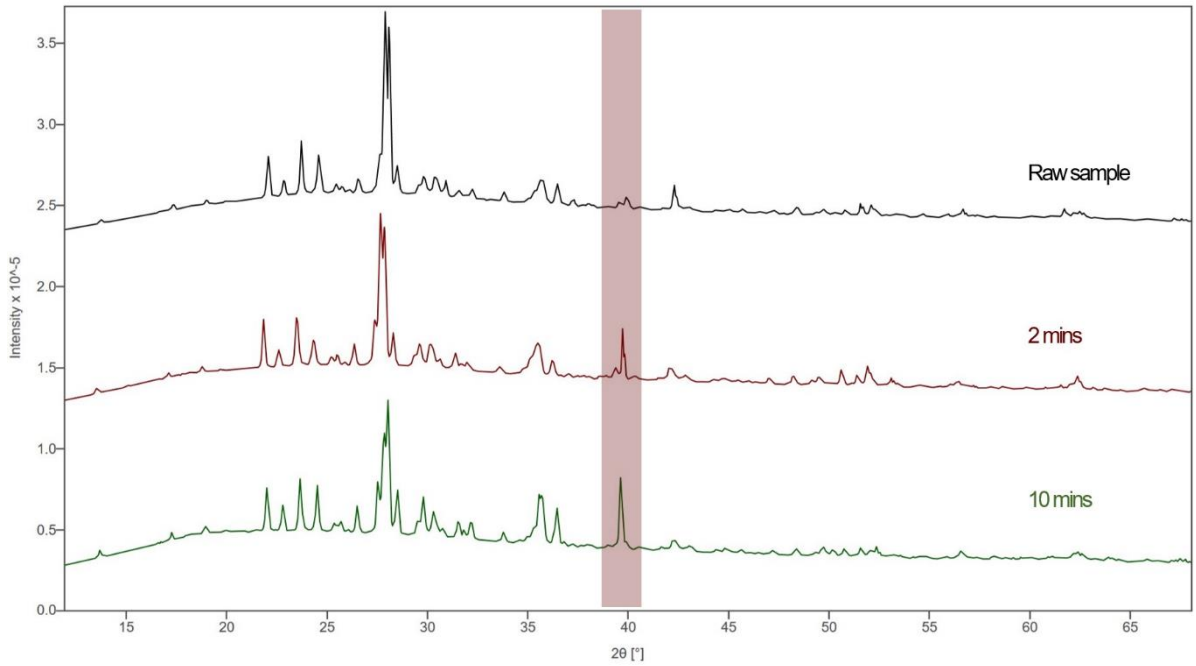

Figure 69. XRD diffractograms demonstrating the effect of milling (Fritsch P23 mini mixer mill) for 2 and 10 minutes on the JSC-Lunar simulant between 15°-65° and a scan time of 3 hours. Highlighted peaks illustrate the emergence of an unassigned peak at ~ 39.7° due to milling.

XRD analysis of the JSC-Lunar simulant milled by a Fritsch P23 mini mixer mill showed similar relative intensities for the majority of peaks for each milling time, indicating insignificant alterations in mineralogical structure. This suggests the vertical and circular mode of milling has less of an effect on grain size distribution and thus surface area in comparison to the Retsch MM301 mixer mill. Other than a potential increase in oxocarbon compound contributions as suggested by the peak angle values at ~ 28.0° and 31.4°, milling the JSC-Lunar simulant for 2 minutes (Fritsch P23 mini mixer mill) appeared to have little difference in the effect on mineralogy in comparison to the Retsch MM301 mixer mill. However, it is important to note that a different frequency of 30 Hz was utilised, introducing another variable that could influence the abrasion processes occurring. The appearance of a relatively sharp peak at a diffraction angle value of ~ 39.7° as illustrated in Figure 69 could not be conclusively assigned, but was observed to increase in intensity with increased milling time. Upon milling for 10 minutes, XRD analysis suggested a possible increase in manganese phosphate contributions, characterised by the peak at ~ 22.0°, indicating longer milling times may activate a higher proportion of chemically diverse reactive sites [28, 29].

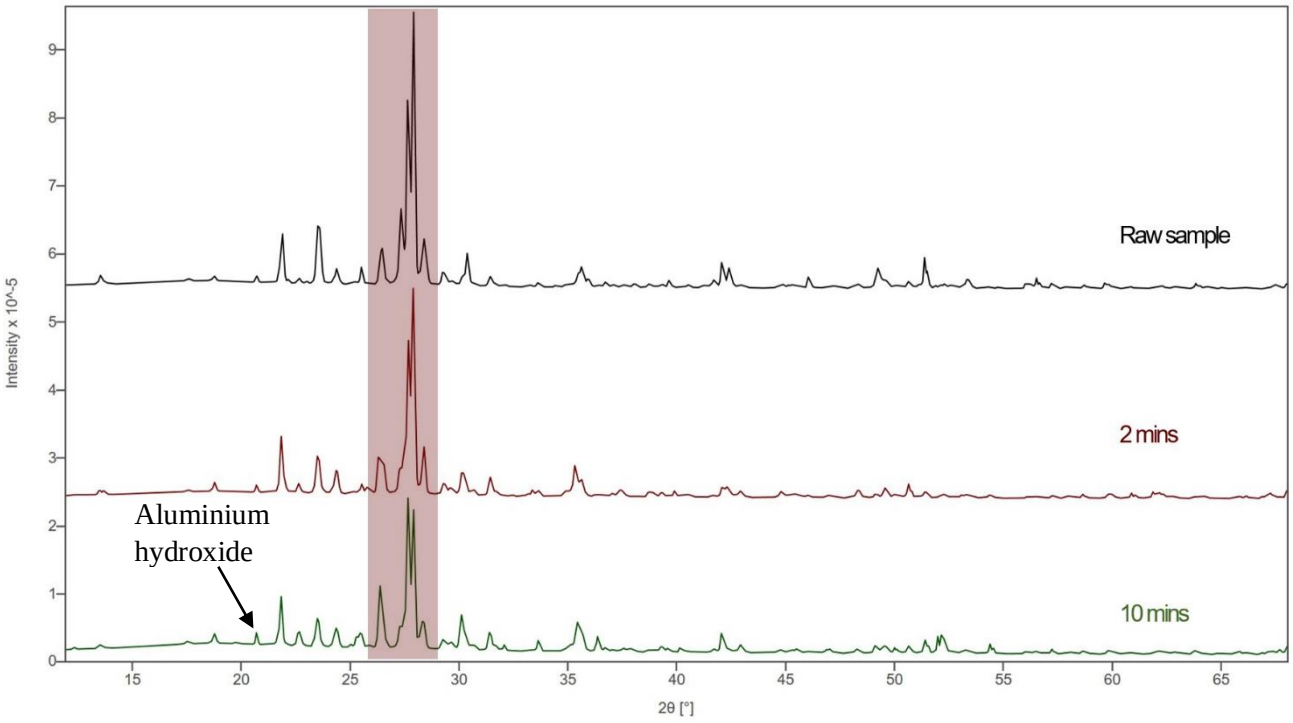

Figure 70. XRD diffractograms demonstrating the effect of milling (Fritsch P23 mini mixer mill) for 2 and 10 minutes on the LHS-1 simulant between 15°-65° and a scan time of 3 hours. Highlighted peaks illustrate noticeable changes in relative peak intensity between samples, in particular the speculated feldspar silicate mineral contribution at ~ 27.9°.

Similarly to data gathered from milling utilising the Retsch MM301, a general decrease in peak intensity over time was observed when using the P23 mill. However, in the same manner as the JSC-Lunar simulant, little variation in mineralogy was observed when utilising both the Retsch MM301 and Fritsch P23 millers, with similar peak values. However, unlike the JSC-Lunar simulant, as illustrated in Figure 69, 2 minutes of milling did not show clear evidence for oxocarbon compounds prior to longer milling times. Upon milling for 10 minutes, oxocarbon compound contributions were potentially increased, as suggested by the relatively intense peak at ~ 27.9°. The mixed contribution of carbon-containing and feldspar minerals demonstrated by all of the silica-based analogues suggests trapped carbon within these compounds which is discussed by Stillings *et al.*, suggesting atmospheric uptake of CO_2 [29].

A longer milling time of 10 minutes potentially increased the concentration of hydroxide minerals. For example, the peak at ~ 21.8° suggests the possible presence of aluminium hydroxide and the peak at ~ 27.7° potentially indicating iron sulfate hydroxide contributions existing as a mixed phase alongside magnesium sulfate, hydrogen carbon sulfide and feldspar minerals. As discussed earlier, within the ball mill reaction system, the manner in which mineral reactants interact will vary depending on the amount and type of collisional energy and impacts, but also the vessel geometry. The greater the number of

chemically active sites are activated, the more potential for reactive mineral surfaces, and the production of reactive oxygen species. When using the Fritsch P23 mini mixer mill, it was expected the material would be weathered to a greater extent due to the increased number of ball bearing-material interactions within a smaller spatial volume (due to the smaller hardened steel ball bearings as shown in chapter 2).

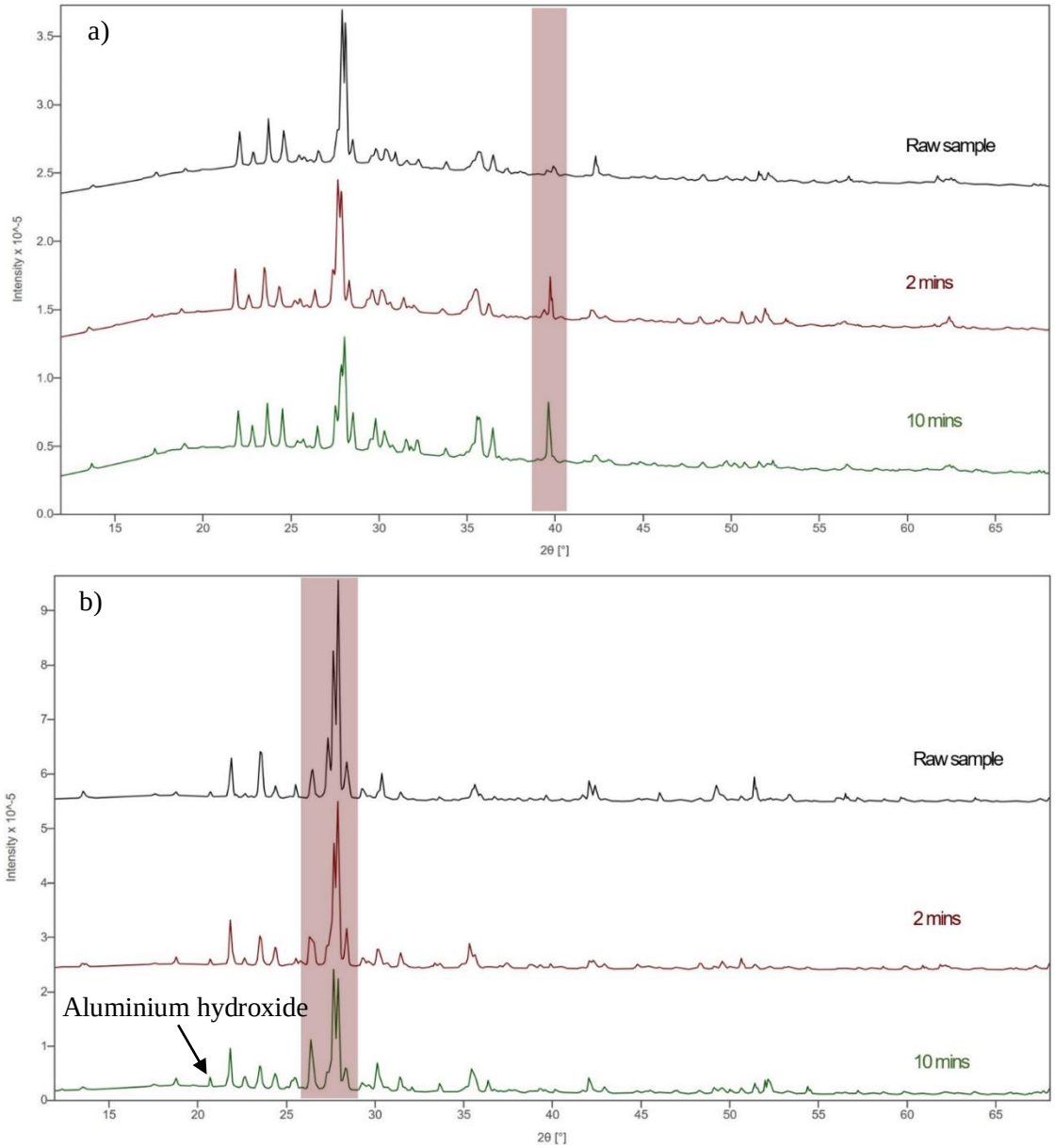

Figure 71. XRD diffractograms comparing the effect of milling (Fritsch P23 mini mixer mill) for 2 and 10 minutes on the a) Earth-based JSC-Lunar simulant and b) synthesised LHS-1 simulant between 15°-65° and a scan time of 3 hours. Highlighted peaks illustrate noticeable changes in relative peak intensity between samples, in particular the speculated feldspar silicate mineral contribution at ~ 27.9°.

As previously noted, the higher degree of crystallinity of the synthesised LHS-1 simulant is apparent in the XRD diffractograms, with the slightly more amorphous Earth-based JSC-Lunar simulant exhibiting an increased curvature in its baseline.

As discussed within chapter 2, iron and iron oxide contamination was more apparent when employing the Retsch MM301 mixer mill in comparison to the Fritsch P23 mini mixer mill. As anticipated, XRD analysis demonstrated little to no effect on the iron abundance within the simulants utilised, with similar results when using both ball mills, for instance as seen in Figures 63 and 69. Therefore, whilst rust contamination was inevitably and uncontrollably present, it appears to have had no bearing on the observed results when comparing the effects of the different ball mills.

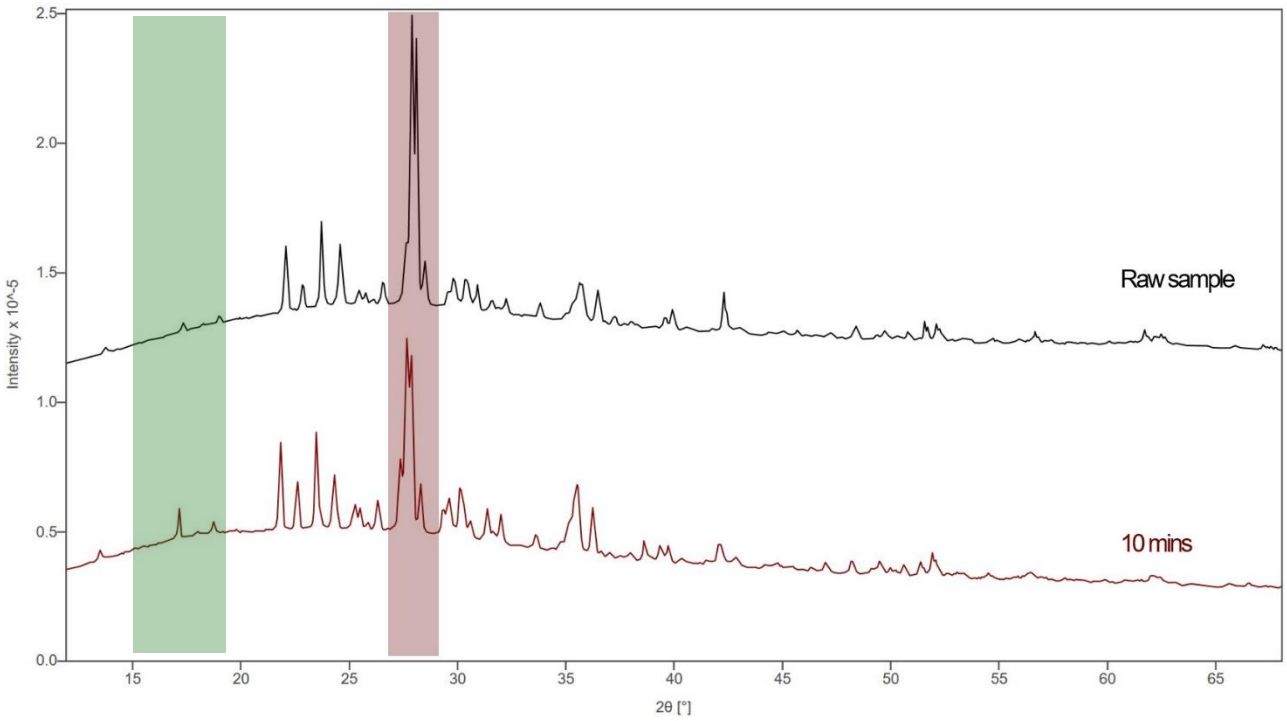

Figure 72. XRD diffractogram demonstrating the effect of milling (P7 planetary micromill) for 10 minutes on the JSC-Lunar simulant between 15°-65° and a scan time of 3 hours. Highlighted peaks illustrate noticeable changes in relative peak intensity between samples, in particular the speculated feldspar silicate mineral contribution at ~ 27.9°.

In comparison to the two previous milling types employed (Retsch MM301 and Fritsch P23), the P7 planetary micromill had almost neglible effects on the mineralogical structure of the JSC-Lunar simulant after 10 minutes of milling (using a frequency of 400 rpm), as illustrated in Figure 72. Other than a slight decrease in intensity for the characteristic feldspar peak at ~ 27.7° as anticipated, the only additional noticeable difference was the increase in peak intensity at ~ 17.9° after milling. This was somewhat unexpected, due to a combination of the planetary micromill's simultaneous elliptical and vertical mechanical motion and the small hardened steel ball bearings should have provided efficient grinding of the simulant grains.

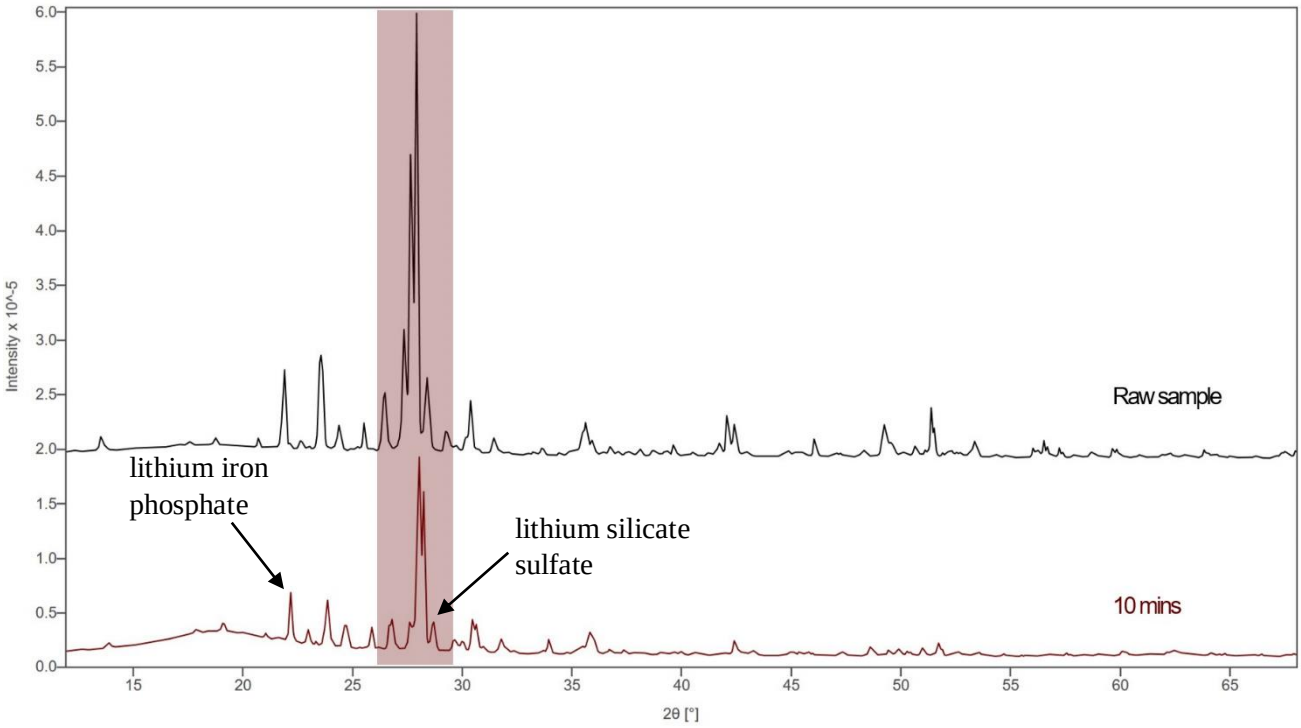

Figure 73. XRD diffractograms demonstrating the effect of milling for 10 minutes on the LHS-1 simulant using the P7 planetary micromill between 15°-65° and a scan time of 3 hours. Highlighted peaks illustrate noticeable changes in relative peak intensity between samples, in particular the speculated feldspar silicate mineral contribution at ~ 27.9°.

A notable decrease in peak intensity at a diffraction angle of ~ 28.0° was observed as displayed in Figure 73. A general decrease in relative peak intensity can be seen, compared to a variation in peak height ratios as seen based on XRD results for Retsch MM301 and Fritsch P23 ball millers, suggesting a more homogenised sample as a result of 10 minutes of milling. Lithium-based minerals such as lithium iron phosphate and lithium silicate sulfate were potentially indicated by peak angle values of ~ 28.0° and 23.9°, suggesting the activation of mineral surfaces already present in low abundances in the raw LHS-1 sample.

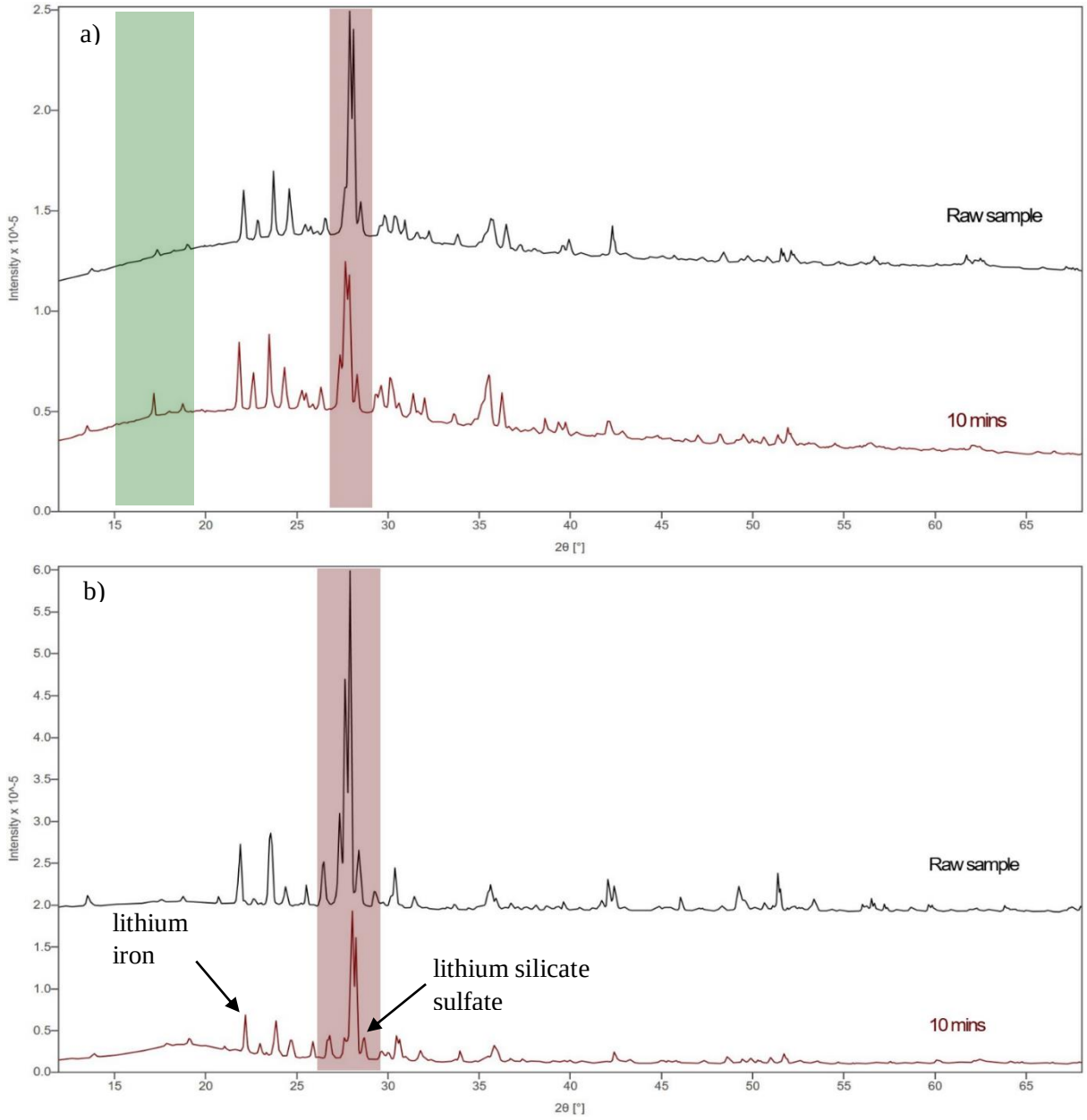

Figure 74. XRD diffractograms comparing the effect of milling (P7 planetary micromill) for 2 and 10 minutes on the a) Earth-based JSC-Lunar simulant and b) synthesised LHS-1 simulant between 15°-65° and a scan time of 3 hours. Highlighted peaks illustrate noticeable changes in relative peak intensity between samples, in particular the speculated feldspar silicate mineral contribution at ~ 27.9°.

A greater relative peak intensity at an angle diffraction value of ~ 28.0° can be seen for the synthesised LHS-1 simulant in comparison to the Earth-based JSC-Lunar simulant, as illustrated in Figure 74 above, again indicating a more densely packed sample.

A comparison was made between the three different ball mills employed to assess the how their varying mechanical modes may have altered the mineralogy and mineralogical structures of the Earth based and synthetic simulants. as shown below in Figures 62 and 63.

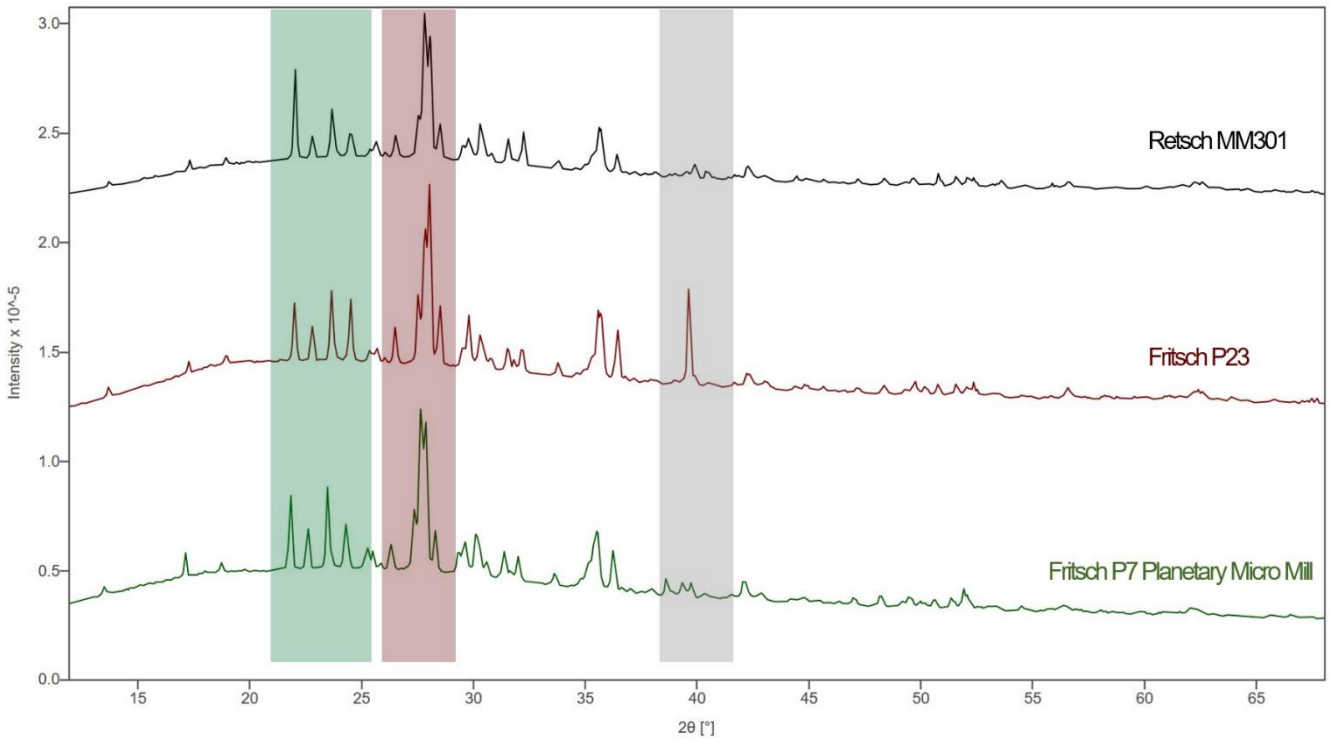

Figure 75. XRD diffractograms illustrating the effect of different mechanical modes of milling on the JSC-Lunar simulant's mineralogical structure between 15°-65° and a scan time of 3 hours. Highlighted peaks illustrate noticeable changes in relative peak intensity between samples. Insignificant variations can be seen.

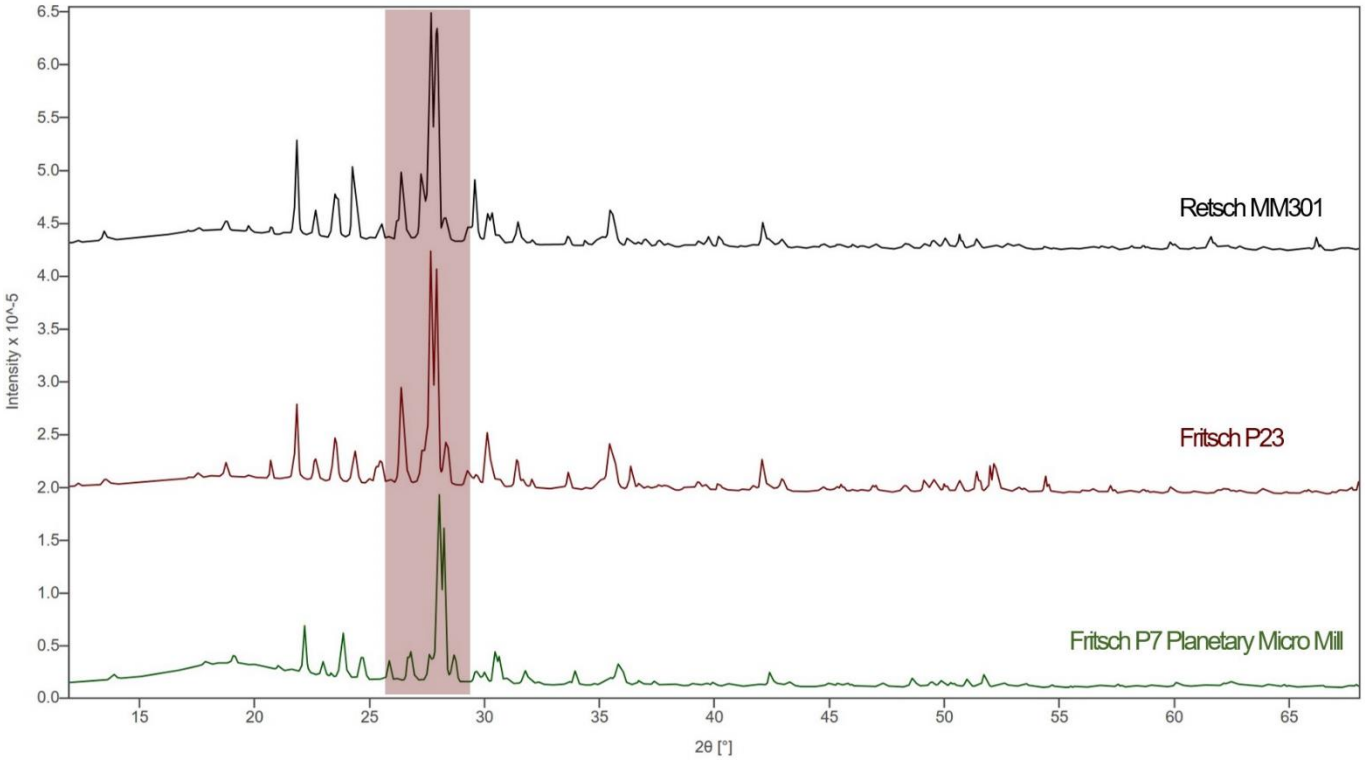

Figure 76. XRD diffractograms illustrating the effect of different mechanical modes of milling on the LHS-1 simulant's mineralogical structure between 15°-65° and a scan time of 3 hours. Insignificant variations can be seen.

As indicated by Figures 75 and 76, different milling techniques showed no significant variation on the mineralogical structure of both the Earth-based and synthesised Lunar simulants, other than the appearance of a peak at ~ 39.9° due to milling the JSC-Lunar simulant with the Fritsch P23 mill. However, longer milling times (for instance an hour) and varying frequencies could be set to analyse this experimental factor in greater depth. The JSC-Lunar simulant's mineralogy seemed to be more prone to alterations depending on the milling apparatus being utilised in comparison to the LHS-1. A plausible explanation for this could be that the Earth-based JSC-Lunar simulant's initial sample form was in a weathered state prior to milling as discussed earlier, potentially already increasing mineral surface reactivity, and lowering the activation energy required for the ignition of the self-sustaining reactions to proceed. This is suggested by work conducted by Stillings *et al*, which explains the lowered activation energy due to crystal lattice deformations driven by mechanochemical activation [29]. Despite this, utilisation of the LHS-1 simulant on Earth may be more beneficial due to its initial wider grain size distribution, however its analogous function is limited to the highland regions of the Moon, whereas the JSC-Lunar simulant simulates a more average composition of the Lunar surface.

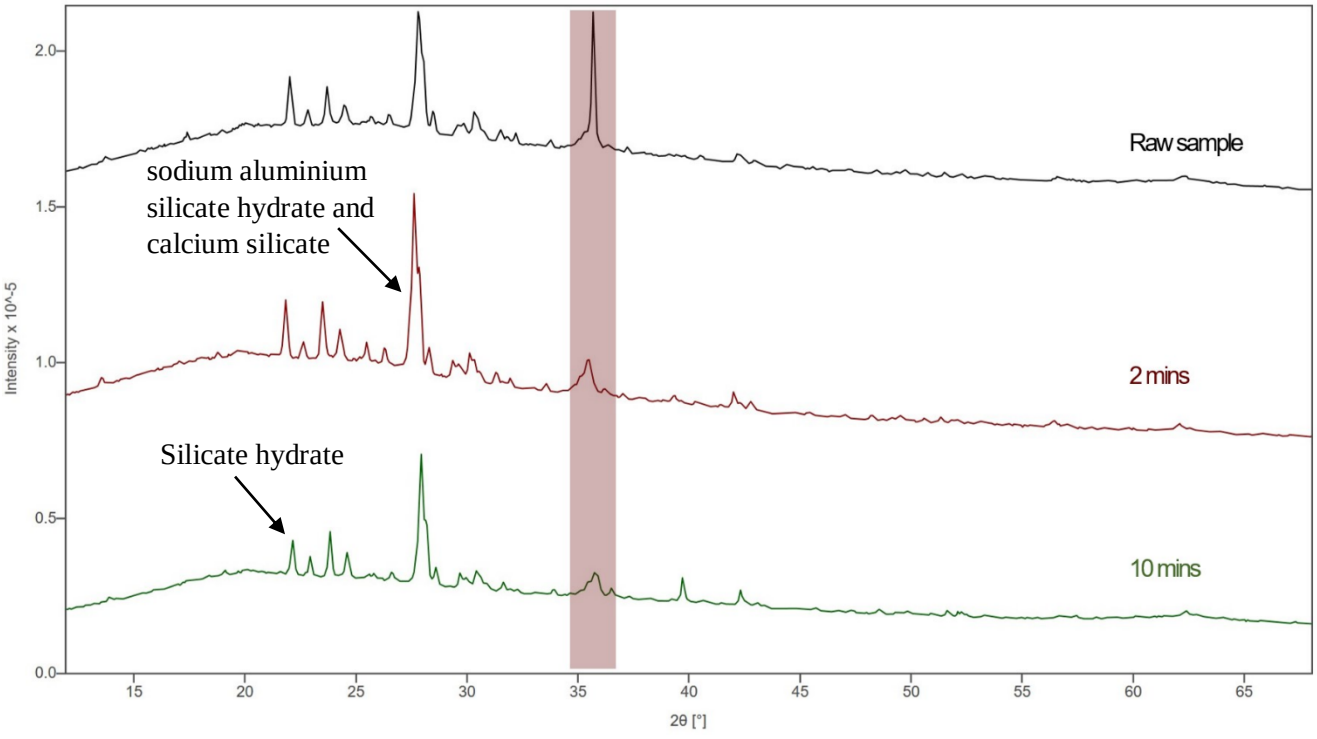

Figure 77. XRD diffractograms demonstrating the effect of milling (Retsch MM301 mixer mill) for 2 and 10 minutes on the JSC-Martian simulant between 15°-65° and a scan time of 3 hours. Highlighted peaks illustrate noticeable changes in relative peak intensity between samples, in particular the peak at ~ 37.7°.

As illustrated in Figure 77, there was a significant decrease in peak intensity at ~ 37.7°, indicating an increase in reactivity of a mixed phase of oxides, namely iron titanium oxide, chromium manganese oxide, calcium iron oxide, lithium iron oxide and oxocarbon compounds. This sharp decline in intensity was observed after 2 minutes of milling, therefore suggesting a potential rapid activation stage within the milling process. Milling for 2 and 10 minutes at a frequency of 10 Hz potentially caused the production of silicate hydrate, as suggested by the peak at ~ 21.8°. Other hydrated minerals were also identified, including sodium aluminium silicate hydrate and calcium silicate hydrate at a peak value of ~ 27.9°, potentially suggesting the presence of trapped moisture from the atmosphere before milling.

Other than this noticeable alteration in mineralogical abundance suggested by XRD analysis, the intensity of the main feldspar contributing peak at ~ 28.0° remained relatively similar, indicating that the physical and chemical processes occurring on the microscopic scale during milling were relatively insignificant, however, further analyses would need to be conducted to understand the true nature of what is occurring within the reaction system (refer to discussed future work in chapter 6).

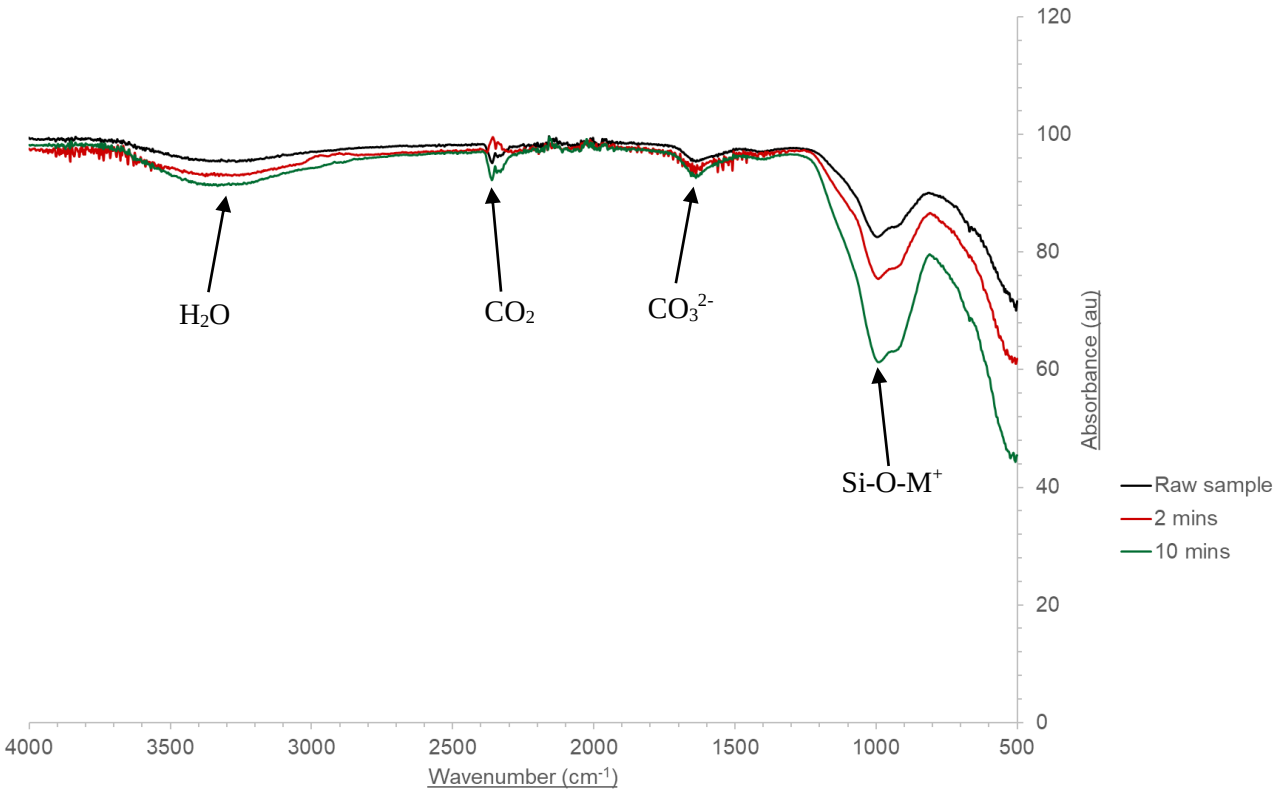

Figure 78. Infrared spectra with a wavenumber range of 4000 cm^{-1} -500 cm^{-1} demonstrating the effect of milling (Retsch MM301 mixer mill) for 2 and 10 minutes on the JSC-Martian simulant's chemical composition. Milling for 10 minutes can be seen to cause the increased uptake of CO_2 due to the characteristic doublet peak at ~ 2400 cm^{-1}. The broad absorbance band at ~ 3400 cm^{-1} suggests water contributions perhaps from atmospheric uptake.

The infrared spectrum shown in Figure 78 above for the Earth-based JSC-Martian simulant further emphasised the potential for moisture within the JSC-Martian simulant's sample as indicated by the broad band at ~ 3400 cm^{-1}, most likely from atmospheric contamination or as speculated from XRD results discussed earlier, hydrated minerals such as calcium silicate hydrate. As discussed in chapter 1, the JSC-Martian analogue has been previously reported to be hygroscopic [2]. This may suggest that the hydrated minerals are due to this environmental factor, and not the interaction between the minerals during dry-conditioned ball milling. The slightly less broad band at ~ 1700 cm^{-1} suggests the contribution of carbonate minerals. As anticipated from the XRD analysis due to the speculated introduction of oxocarbon compounds, the absorbance of CO_2 was also observed in the IR spectrum by the characteristic doublet peak at ~ 2400 cm^{-1} upon milling for both 2 and 10 minutes. Similarly, to Lunar simulants, an increase in milling time of JSC-Martian material caused an increase in the Si-O-M^+ (M^+ = metal cation) band at ~ 900 cm^{-1} due to a decrease in grain size, and therefore an increase in surface area. An increase in specific surface area increases the number of active surface M^+ cations available, thus there is greater absorption of infrared radiation.

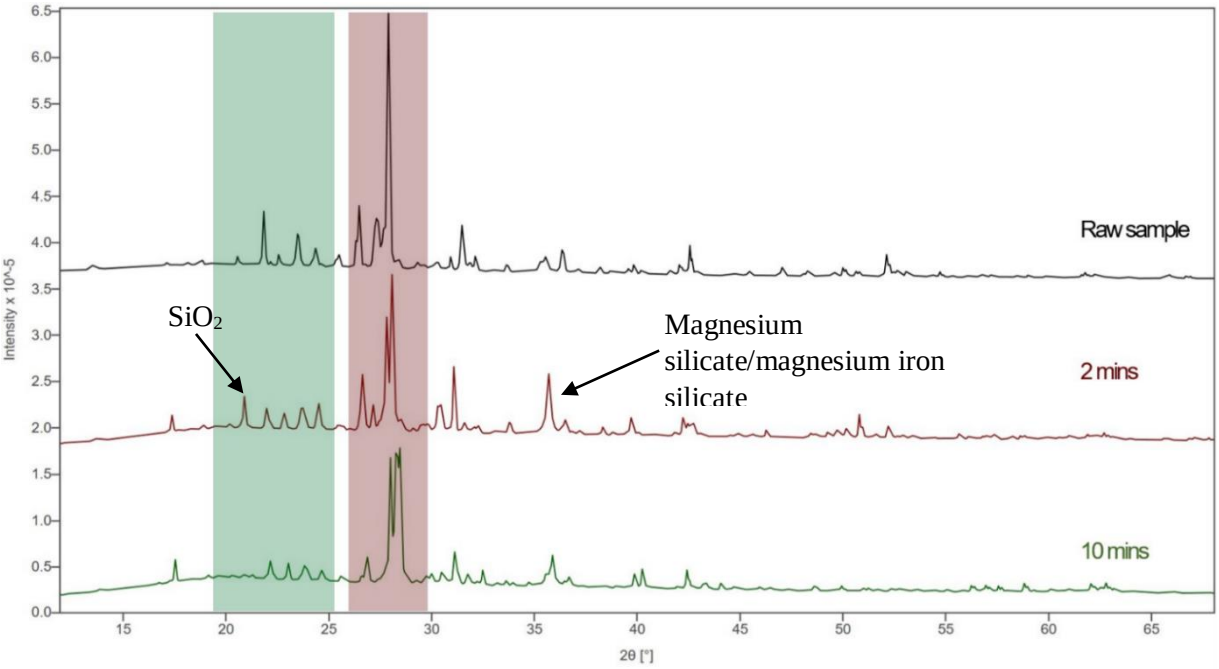

[2]Figure 79. XRD diffractograms demonstrating the effect of milling (Retsch MM301 mixer mill) for 2 and 10 minutes on the MGS-1 simulant between 15°-65° and a scan time of 3 hours. Highlighted peaks illustrate noticeable changes in relative peak intensity between samples, in particular the speculated feldspar silicate mineral contribution at ~ 27.9°.

[2] Due to the clumping and a paste-like texture of the MGS-1 simulant milled for 10 minutes, sample loading for XRD analysis became difficult in regards to sufficient coverage.

As illustrated by Figure 79, the most notable alteration upon milling for 2 and 10 minutes was observed at a peak angle value of ~ 28.1°, potentially characterised by feldspar minerals and oxocarbon compounds. With milling however, the generation of iron titanium oxide sulfite and titanium oxide sulfate was suggested. The peak at ~ 35.7° suggests the presence of magnesium silicate/magnesium iron silicate, which becomes more apparent upon a milling for 2 minutes, indicating this may be a by-product or intermediate, and not produced during self-sustaining reactions for longer periods of time. The characteristic SiO_2 peak at ~ 21.9° was observed as expected, however intensity decreased due to milling.

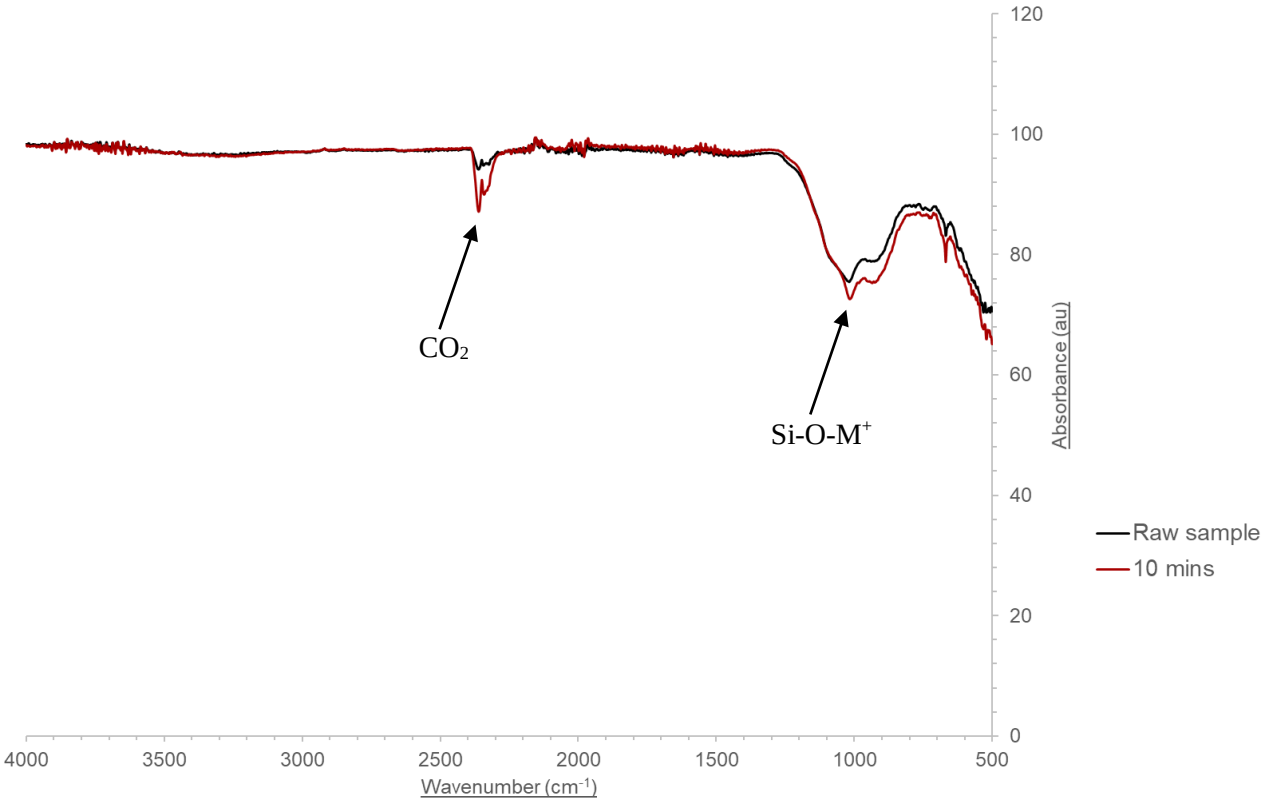

Figure 80. Infrared spectra with a wavenumber range of 4000 cm^{-1} -500 cm^{-1} demonstrating the effect of milling (Retsch MM301 mixer mill) for 10 minutes on the MGS-1 simulant's chemical composition. Milling for 10 minutes can be seen to cause the increased uptake of CO_2 due to the characteristic doublet peak at ~ 2400 cm^{-1}.

The increase in adsorption of $CO_{2\,(g)}$ was observed upon milling the MGS-1 simulant indicated by the characteristic doublet peak at ~ 2400 cm^{-1} in the IR spectrum. As seen in Figure 80, this band is enhanced by milling, suggesting the possible entrapment of carbon-containing compounds within one of the minerals/numerous minerals which comprise the MGS-1 simulant, or CO_2 capture from the atmosphere. The interaction of minerals during the self-sustaining reaction stage may cause mineral deformation and diffusion of CO_2 into the lattice interstitials due to a lowered activation energy [29]. The increase in absorbance due to milling as demonstrated by the characteristic Si-O-M^+ (M^+ = metal cation) bond

at ~ 900 cm^{-1} was due to a decrease in grain size, and therefore an increase in surface area and number of active surface M^+ cations, as discussed previously.

On the Martian surface, the presence of organics such as carbonates has been investigated, for instance Chevrier *et al.* has discussed the probable high concentration of carbonates in the primitive Martian environment and their importance in understanding the dynamics between the atmosphere and hydrosphere [20], and therefore the MGS-1 simulant was synthesised by incorporating specific organic constituents (as discussed in chapter 3). However, the possibility of observing trace organics through ATR-FTIR spectroscopic analyses is low due to minerals present dominating the yielded results.

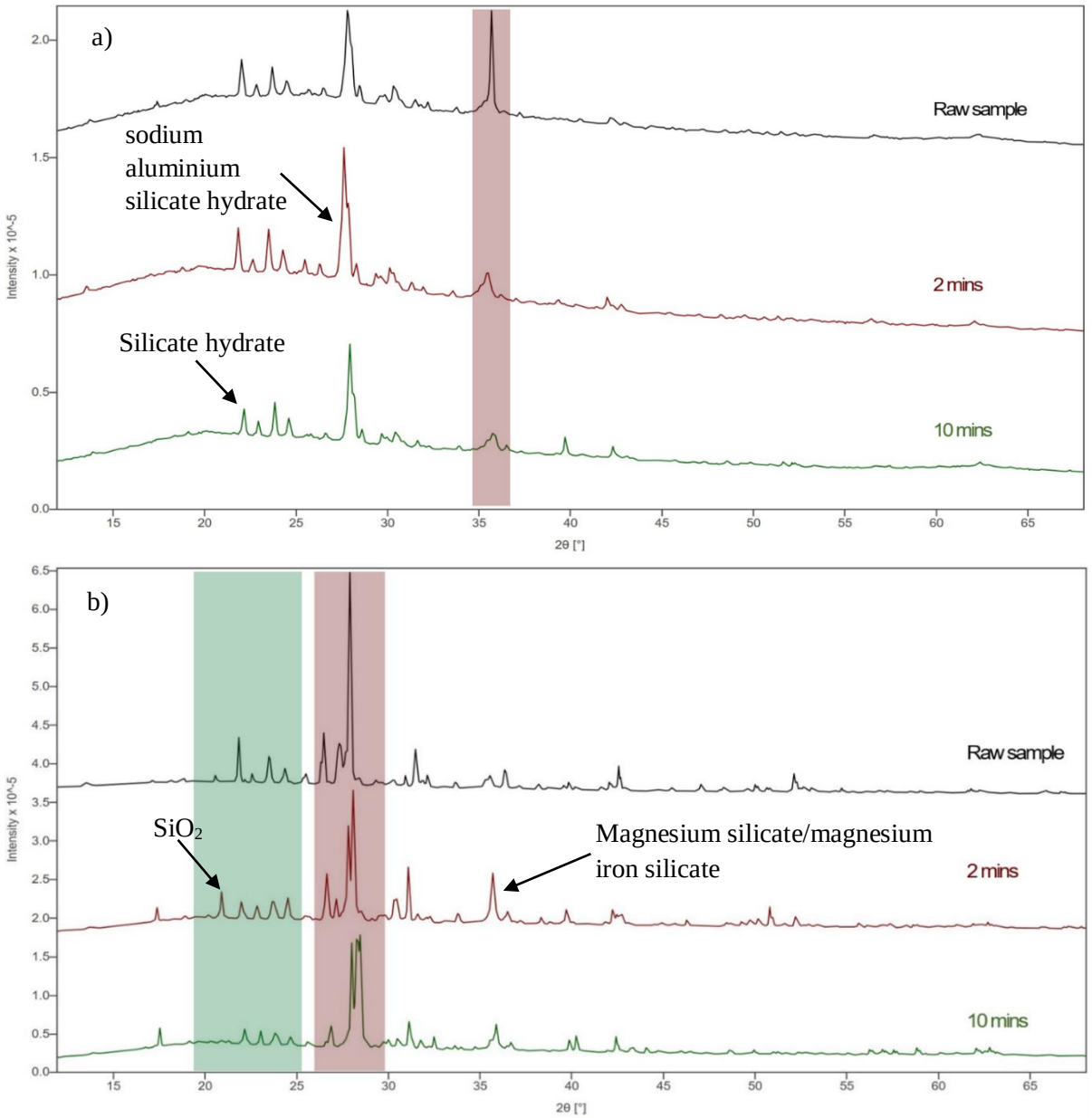

Figure 81. XRD diffractograms comparing the effect of milling (Retsch MM301 mixer mill) for 2 and 10 minutes on the a) Earth-based JSC-Martian simulant and b) synthesised MGS-1 simulant between 15°-65° and a scan time of 3 hours. Highlighted peaks illustrate noticeable changes in relative peak intensity between samples, in particular the speculated feldspar silicate mineral contribution at ~ 27.9°.

Despite subjecting both the Martian simulants to identical milling conditions, the materials behaved significantly differently, as shown in Figure 81. The synthesised MGS-1 simulant displayed a high peak average intensity, due to its initial wider grain size distribution and the clumping observed after 10 minutes of milling, decreasing the average surface area. The MGS-1 simulant also appeared to be composed of a greater variety of oxide phases, before and after milling, potentially due to the initial synthesis involving the blending of individual (but multiple) minerals. The MGS-1 simulant appeared to be more crystalline, due to its higher abundance of glass basalt in comparison to the JSC-Martian simulant in order to replicate the average composition of the Martian surface.

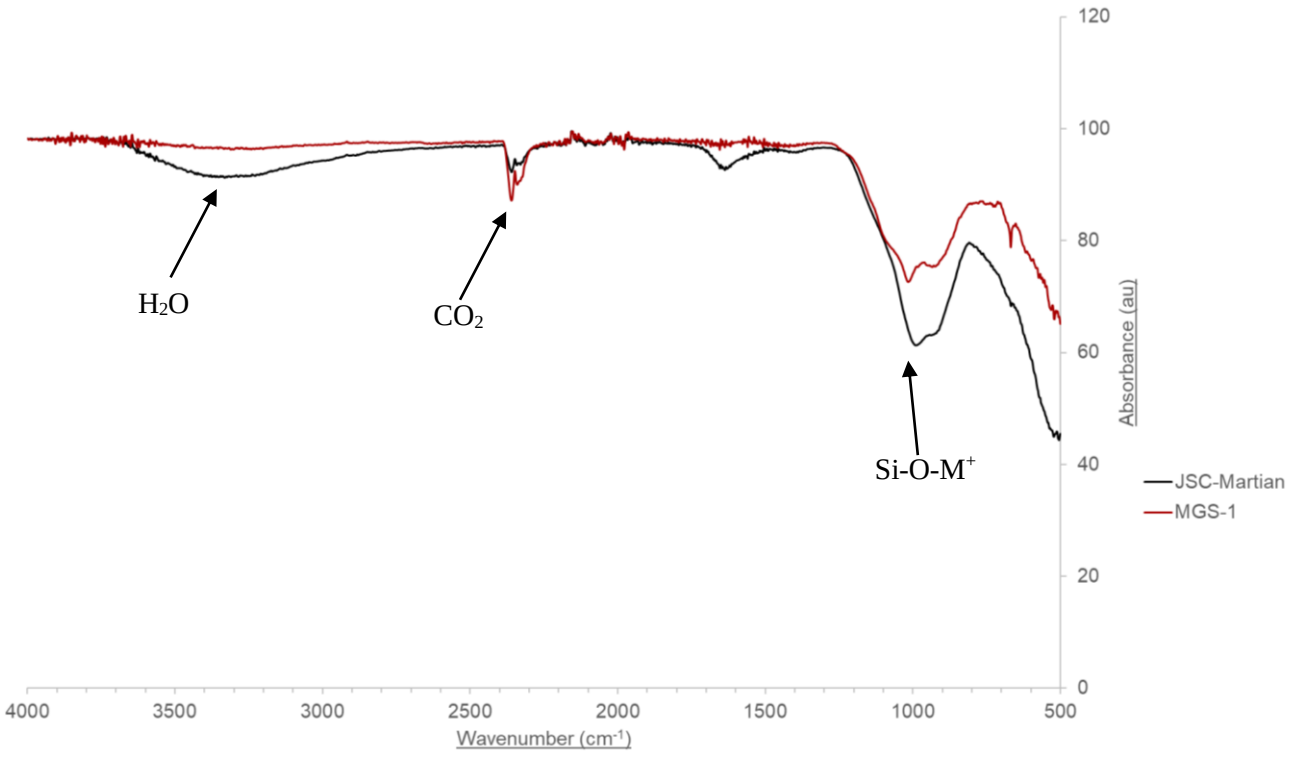

Figure 82. Infrared spectra with a wavenumber range of 4000 cm^{-1} -500 cm^{-1} comparing the effect of milling (Retsch MM301 mixer mill) for 10 minutes at a frequency of 10 Hz on the JSC-Martian and MGS-1 simulants. The hygroscopic nature of the JSC-Martian simulant is significantly evident by the broad absorbance band at ~ 3400 cm^{-1}.

As illustrated in the IR spectra above, the adsorption of CO_2 upon milling was more apparent for the synthesised MGS-1 simulant in comparison to the Earth-based JSC-Martian simulant, potentially due to the higher abundance of quartz, a silicate mineral which is more efficient regarding CO_2 sequestration compared to other minerals and thus has been used in previous research for ampoules [22, 29]. The MGS-1 simulant did not appear to possess the same spectral band at ~ 3400 cm^{-1} indicating trapped moisture, suggesting it may be less hygroscopic than the JSC-Martian simulant (refer to chapter 5 for more detail). In agreement with prior XRD analysis, the more intense Si-O-M^+ (M^+ = metal cation) band

absorbance at ~ 900 cm^{-1} for the JSC-Martian simulant was due to a greater increase in surface area and due to natural environmental weathering prior to being milled in the laboratory, perhaps a maximum number of active surface M^+ cations being generated.

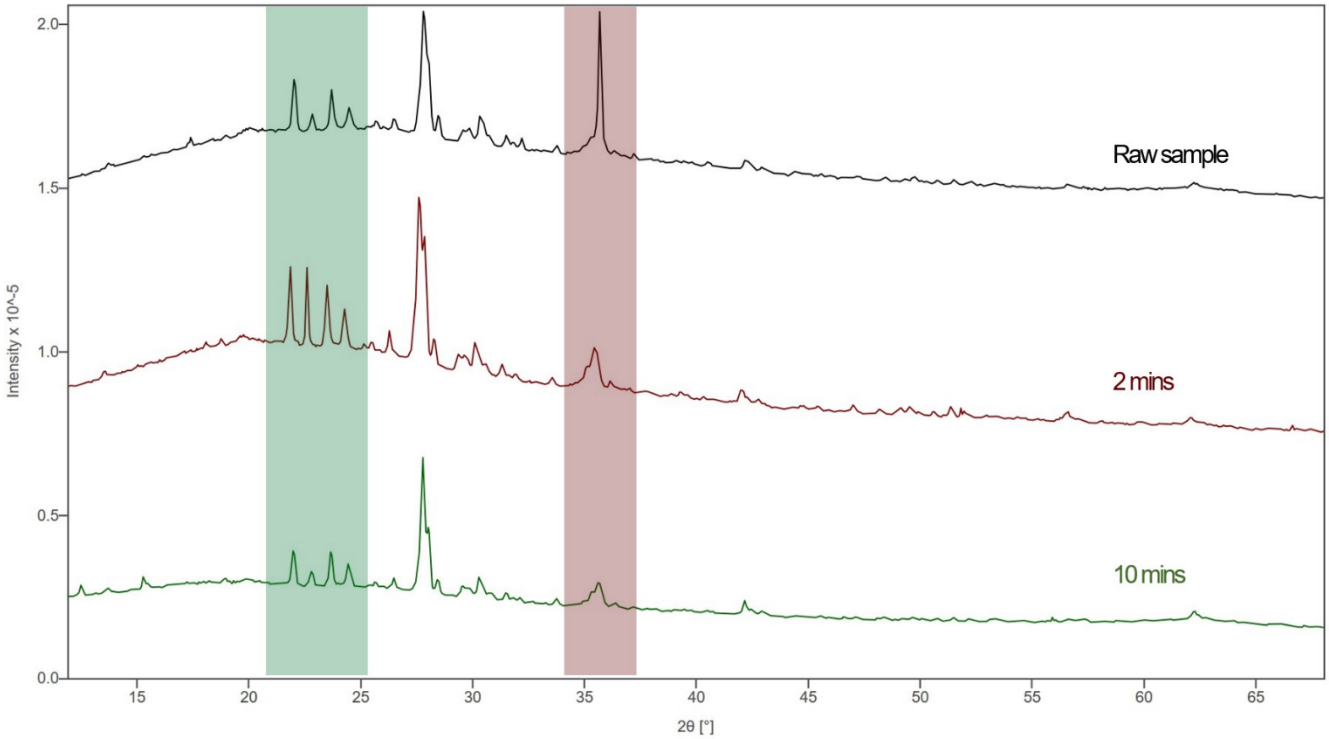

Figure 83. XRD diffractograms demonstrating the effect of milling (Fritsch P23 mini mixer mill) for 2 and 10 minutes on the JSC-Martian simulant between 15°-65° and a scan time of 3 hours. Highlighted peaks illustrate noticeable changes in relative peak intensity between samples, in particular the speculated feldspar silicate mineral contribution at ~ 27.9°.

As illustrated in Figure 83 above, XRD analysis showed the little effect milling for 2 and 10 minutes by means of utilising the Fritsch P23 mini mixer mill had on the crystalline structure of the Earth-based simulant JSC-Martian, again potentially due to its natural weathering prior to purposeful and controlled abrasion within the laboratory. The complete/almost disappearance of the iron manganese oxide peak at ~ 35.5° when comparing 0 minutes of milling (as highlighted in Figure 83 above) to 2 minutes suggests this oxide phase participating in mechanochemical-driven reactions during the milling process, thus being converted into other compounds, and as seen through analysis of the same diffraction angle value, potentially hydrated silicate minerals, for instance potassium hydrogen aluminium silicate, calcium manganese silicate and potassium aluminium silicate hydroxide.

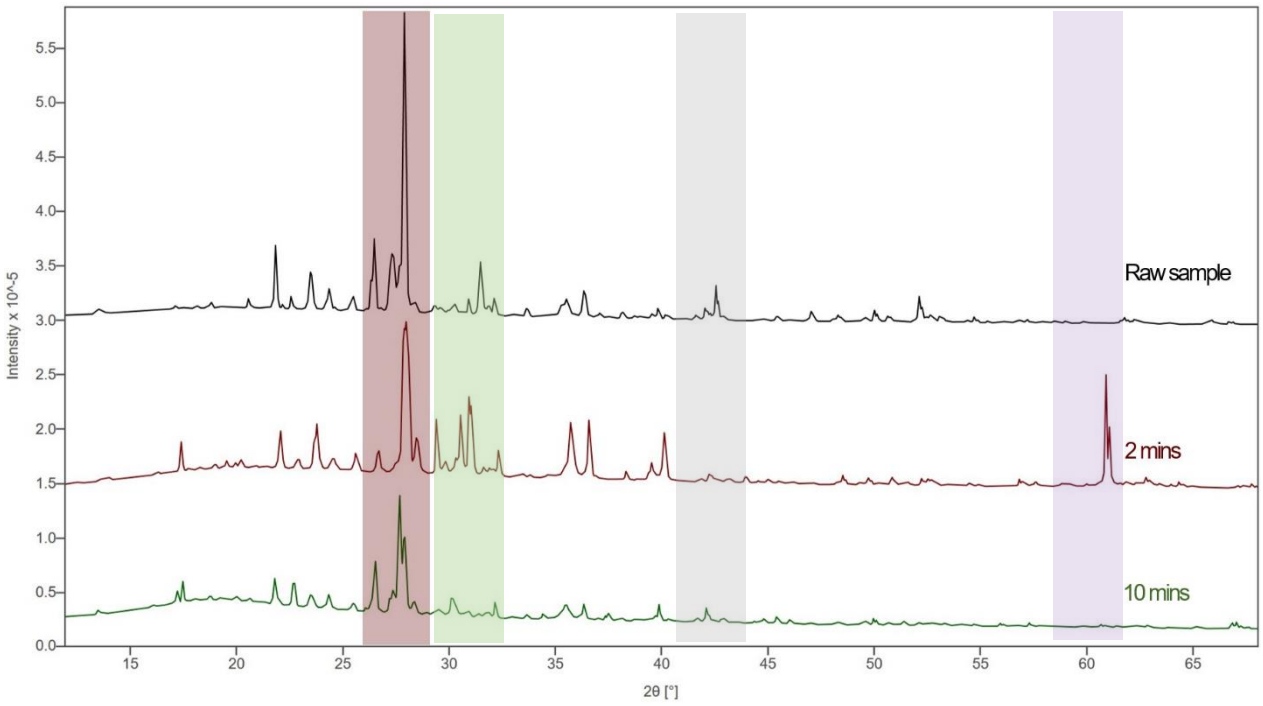

Figure 84. XRD diffractograms demonstrating the effect of milling (Fritsch P23 mini mixer mill) for 2 and 10 minutes on the MGS-1 simulant between 15°-65° and a scan time of 3 hours. Highlighted peaks illustrate noticeable changes in relative peak intensity between samples, in particular the speculated feldspar silicate mineral contribution at ~ 27.9°.

XRD analysis indicated that employing the Fritsch P23 mini mixer mill had a somewhat pronounced effect on the MGS-1 simulant's mineralogy and mineralogical structure, in particular the highlighted regions of Figure 84 as illustrated above. The sharp decrease in relative peak intensity at ~ 27.9°, the characteristic peak for feldspar minerals, suggested a potential quenching reaction, yielding in secondary minerals. A period of 10 minutes of milling demonstrated the production of magnesium iron silicate hydroxide, potassium chromium oxide and sodium magnesium sulfate hydrate at ~ 27.9°, hinting at the generation of additional oxide and hydrate minerals, and secondary minerals from primary. The appearance of a sharp peak at ~ 62.4° due to 2 minutes of milling was uncharacterised. Milling for 2 minutes seemed to cause an increase in intensity, whilst milling for a longer period of time caused a decrease. This is demonstrated most notably by the disappearance of the peak at ~ 62.4°.

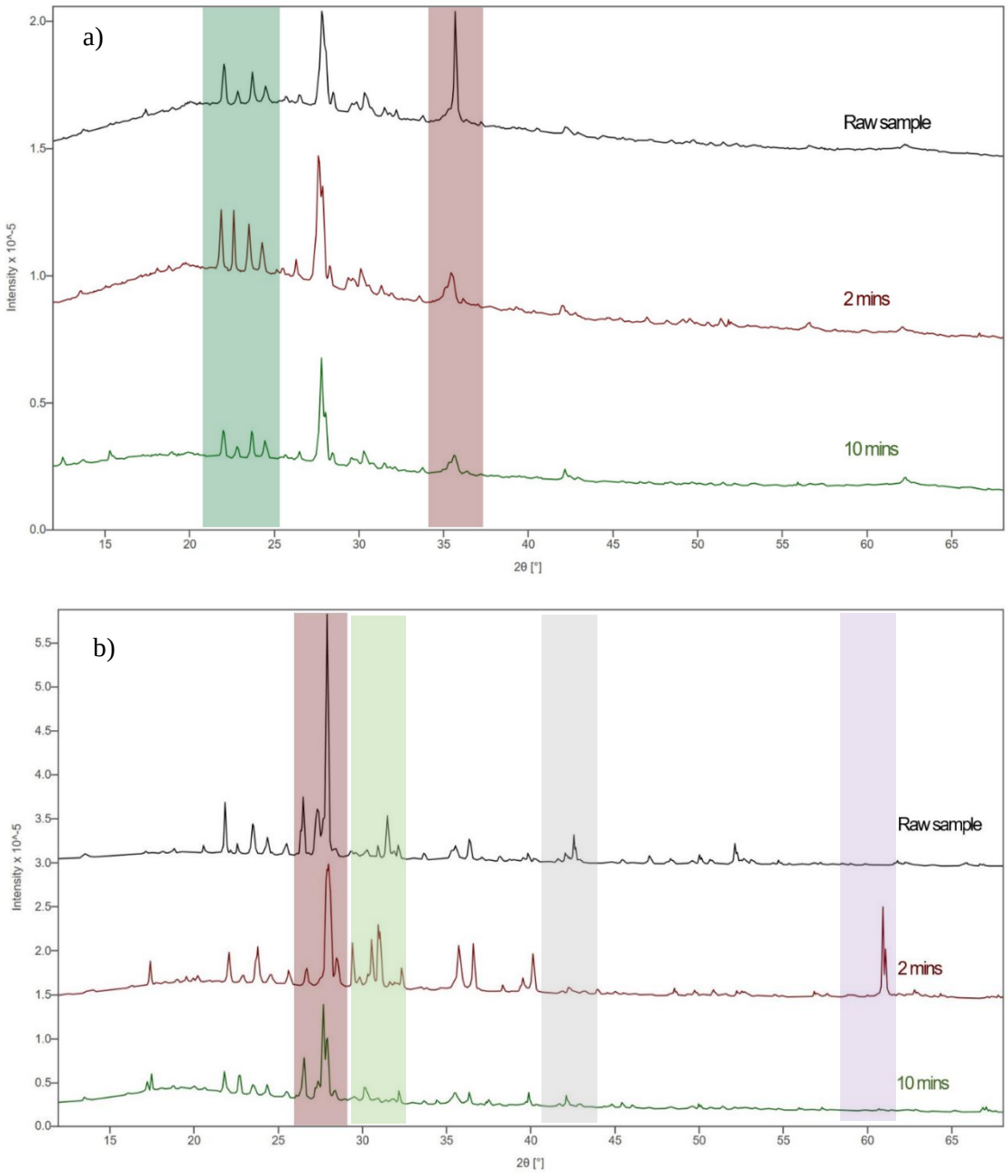

Figure 85. XRD diffractograms comparing the effect of milling (Fritsch P23 mini mixer mill) for 2 and 10 minutes on the a) Earth-based JSC-Martian and b) synthesised MGS-1 simulants between 15°-65° and a scan time of 3 hours. Highlighted peaks illustrate noticeable changes in relative peak intensity between samples, in particular the speculated feldspar silicate mineral contribution at ~ 27.9°.

Employing the Fritsch P23 in regards to the JSC-Martian simulant seemed to pose less of a change in mineralogical structure in comparison to the MGS-1 simulant as seen in Figure 85 above. This was perhaps due to the more varied and extensive initial composition of the MGS-1 simulant, and the pre-weathered nature of the JSC-Martian simulant and thus potential quenching of some of its surface M^+ cations due to further milling within the laboratory.

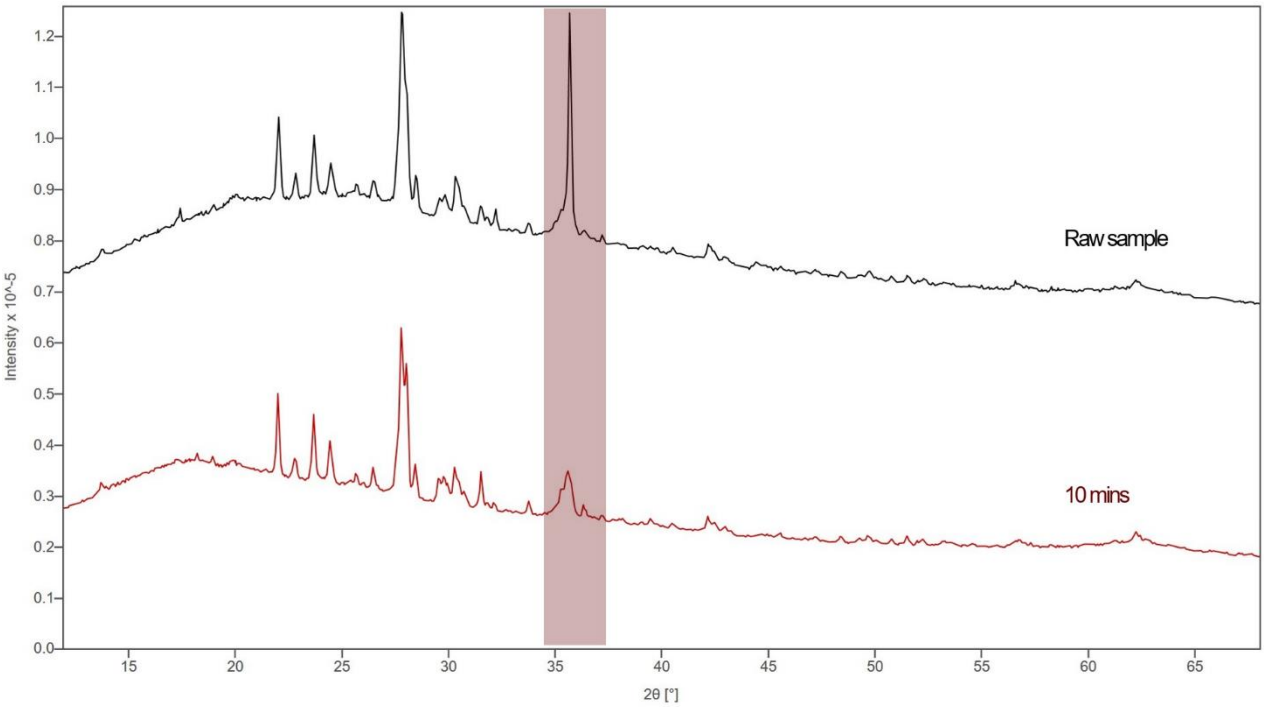

Figure 86. XRD diffractograms demonstrating the effect of milling (P7 planetary micromill) for 10 minutes on the JSC-Martian simulant between 15°-65° and a scan time of 3 hours. Highlighted peaks illustrate noticeable changes in relative peak intensity between samples, in particular the decrease observed at ~ 35.7°.

XRD analysis of the Earth-based JSC-Martian simulant milled for 10 minutes utilising the University of Kent's P7 planetary micromill showed the most drastic decrease in relative peak intensity at a diffraction angle value of ~ 35.7°, characterised by iron manganese oxide. Other than the evident potential increase in abundance of this oxide, other phases only slightly increased in abundance, most notably the characteristic feldspar and oxocarbon compound peak, at ~ 27.8°.

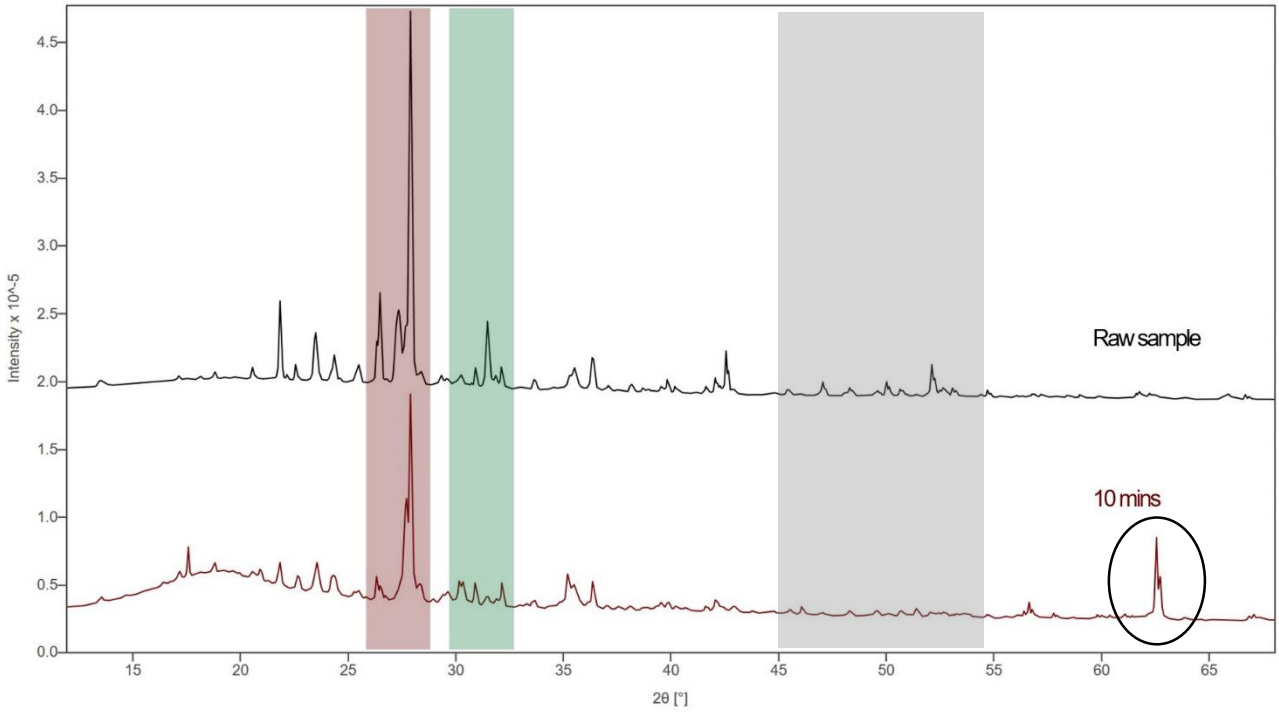

Figure 87. XRD diffractograms demonstrating the effect of milling (P7 planetary micromill) for 10 minutes on the MGS-1 simulant between 15°-65° and a scan time of 3 hours. Highlighted peaks illustrate noticeable changes in relative peak intensity between samples, in particular the speculated feldspar silicate mineral contribution at ~ 27.9°.

As illustrated in Figure 87 shown above, the synthesised MGS-1 simulant's mineralogy and mineralogical structure was altered fairly significantly, with a noticeable decrease in peak intensity, in particular concerning the peak at ~ 27.9°, characteristic for feldspar minerals. This peak in particular was due to a wide range of oxide phases, including potassium carbon hydrogen oxide, sodium titanium oxide phosphate and titanium oxide. The appearance of the peak at ~ 63.5° due to milling was unidentified. There was a general decrease in peak intensity between ~ 45.3° - 53.7°. In addition to oxides, sulfates for instance potassium sulfate, sodium sulfate hydrate and sodium sulfate were potentially present. In general, numerous peaks indicated the possibility of hydrated silica-based mineral contributions, which was anticipated due to the hydrated silica mineral component of the raw MGS-1 simulant.

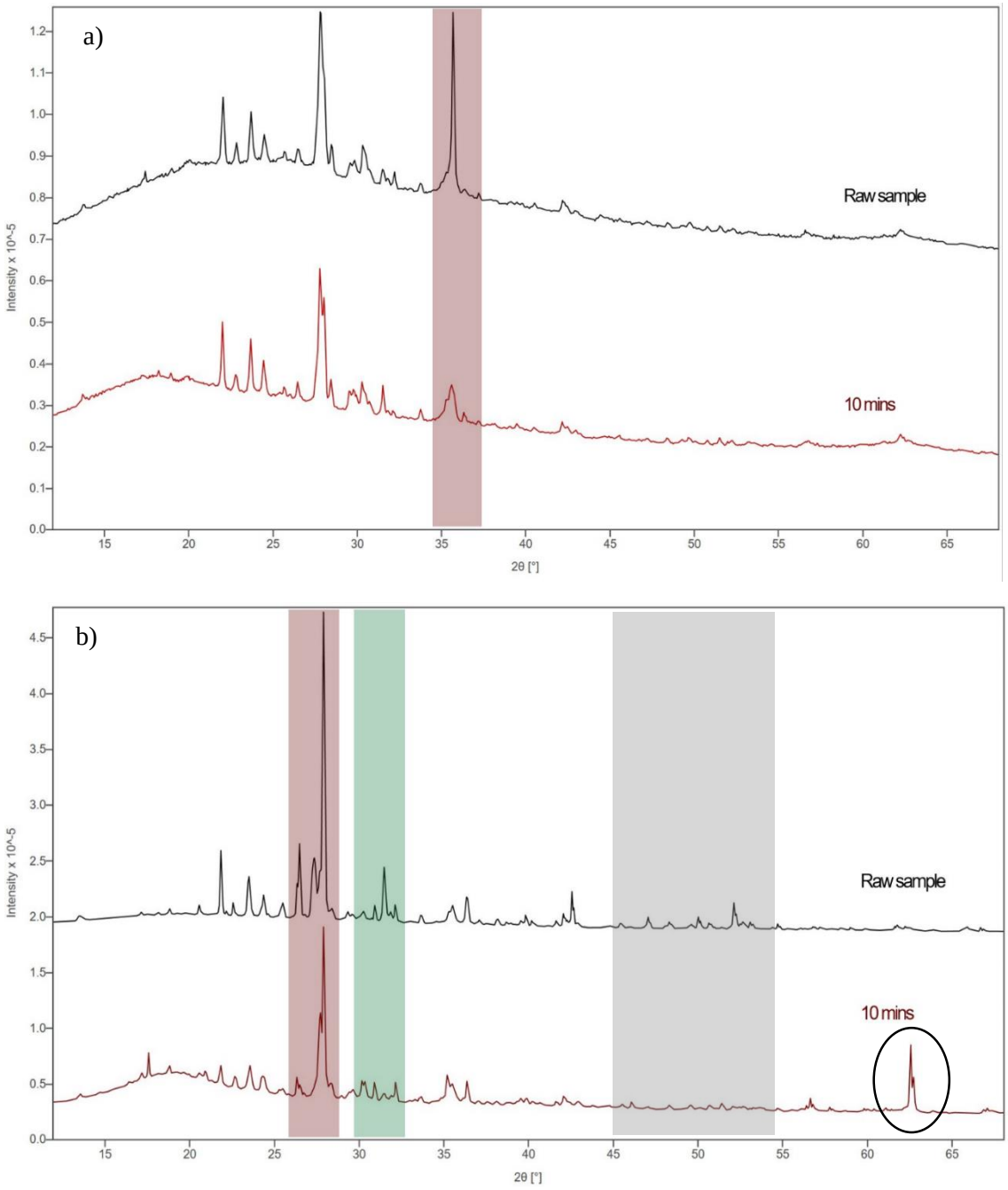

Figure 88. XRD diffractograms comparing the effect of milling (P7 planetary micromill) for 10 minutes on both the Earth-based JSC-Martian simulant and synthesised MGS-1 simulant between 15°-65° and a scan time of 3 hours. Highlighted peaks illustrate noticeable changes in relative peak intensity between samples, in particular the speculated feldspar silicate mineral contribution at ~ 27.9°.

As demonstrated by the comparative XRDs shown above in Figure 88, whilst MGS-1 had a general higher relative peak intensity, suggesting more densely packed grains due to milling within the loaded sample. The higher number of peaks also perhaps indicated the more diverse chemistry of the MGS-1 compared to the JSC-Martian simulant. This is of great relevance to the Martian surface, as the synthesised MGS-1 is representative of the standardised regolith composition of Mars. Figure 89. XRD

diffractograms illustrating the effect of different mechanical modes of milling on the JSC-Martian simulant's mineralogical structure between 15°-65° and a scan time of 3 hours. Insignificant variations can be seen.

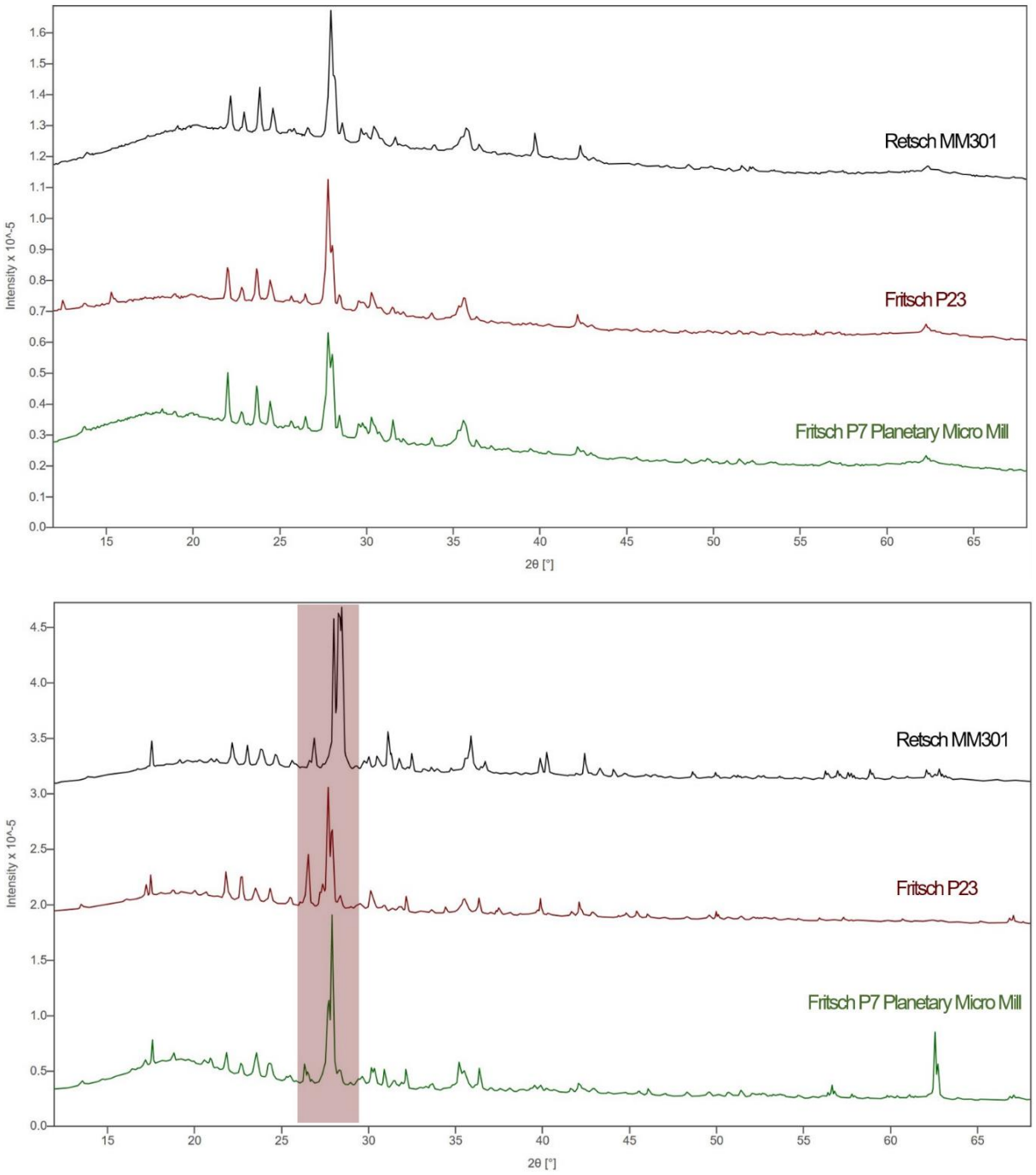

Figure 90. XRD diffractograms illustrating the effect of different mechanical modes of milling on the MGS-1 simulant's mineralogical structure between 15°-65° and a scan time of 3 hours. Whilst little variation in relative peak intensity between samples can be seen, there is a more noticeable difference in comparison to the JSC-Martian simulant as seen in Figure 89.

Following a similar trend concerning the Earth-based and synthetic simulants being studied, the difference in the type of ball miller apparatus employed to assess any potential alterations of the mineralogical structure and composition seemed to have more of an apparent effect on the synthesised MGS-1 simulant in comparison to the Earth-based JSC-Martian simulant, as illustrated in Figures 88 and 89 shown above. The wider initial grain size distribution and blending of minerals during synthesis for the MGS-1 simulant compared to the JSC-Martian simulant which had already been naturally weathered prior to milling within the laboratory may be a plausible explanation for this evident difference in behaviour when subjected to identical milling conditions. In addition to this, the synthesised MGS-1 simulant has a more extensive composition and wider range of oxide phases present, potentially leading to a greater number of different mechanochemically-induced reaction pathways during the milling process and thus induced chemistry.

4.2 Effect of Ball Milling on Grain Size Distributions

As discussed in detail in chapter 2, the grain size distributions regarding the simulants milled for 2, 4, 6, 8 and 10 minutes employing the Retsch MM301 mixer mill were measured by means of utilising a set of tray sieves of mesh pore sizes 420 µm - < 53 µm and recording the mass retained.

The effect of ball milling on grain size distribution, grain morphologies and surface textures of the regolith analogues was observed by means of SEM, comparing appearances of simulants milled for 2 minutes (minimum milling time within research) to those milled for 10 minutes (maximum milling time within research)

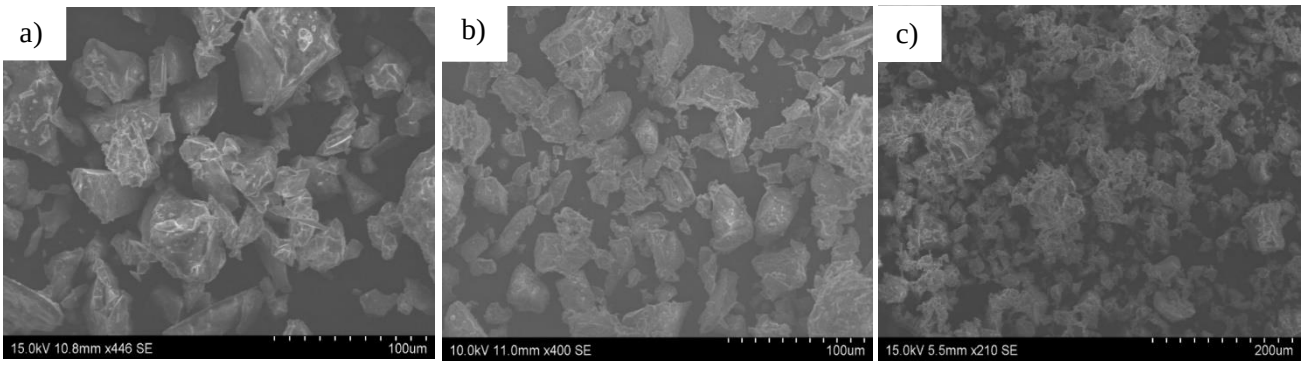

Figure 91. Secondary Electron Images (SEI) taken of a) the raw JSC-Lunar simulant b) the JSC-Lunar simulant milled for 2 minutes (Retsch MM301) at a magnification of x400; c) the JSC-Lunar simulant milled for 10 minutes (Retsch MM301) at a magnification of x210.

In order to plot grain size distributions for the raw Earth materials, calculating particle number values from the mass collected within each sieve tray was required. This was conducted by calculating grain volume (cm^3) from the mesh pore diameters (average) by assuming a sphere geometry. Individual grain mass was calculated through using literature density values (g/cm^3) and making the assumption density for each sample was uniform. Particle number was thus derived through dividing individual mass by the total mass collected in regards to the corresponding grain size diameter. It is important to note that for the scope of this thesis, assumptions were made in order to plot the grain size distributions. Particle size ranges for all materials were taken from Exolith to ensure the majority of grain diameters were taken into consideration during calculations [4]. An example of one calculation is shown below concerning the grain size distribution of the JSC-Lunar simulant:

Table 7a. Table showing calculations for grain volume (cm^3) and individual grain mass (g).

Pore Diameter (µm)	**Grain Volume (cm^3)**	**Individual Grain Mass (g)**
710.0	1.87 E-4	5.42 E-4
480.0	5.79 E-5	1.68 E-4
213.5	5.10 E-6	1.48 E-5
163.0	2.27 E-6	6.58 E-6
137.0	1.35 E-6	3.92 E-6
91.50	4.01 E-7	1.16 E-6
55.50	8.95 E-8	2.60 E-7
31.50	1.64 E-8	4.75 E-8

Table 7b. Table showing calculations for particle number values based on mass collected (g).

Pore Diameter (µm)	**Mass Collected (g)**		**Particle Number**	
	2 mins	**10 mins**	**2 mins**	**10 mins**
710	0.05	0.02	92	37
480.0	0.05	0.01	300	60
213.5	0.135	0.01	9100	680
163.0	0.165	0	25000	0
137.0	0.135	0.04	34000	10000
91.50	0.35	0.365	300000	310000
55.50	0.61	0.935	2300000	3600000
31.50	0.74	1.24	16000000	26000000

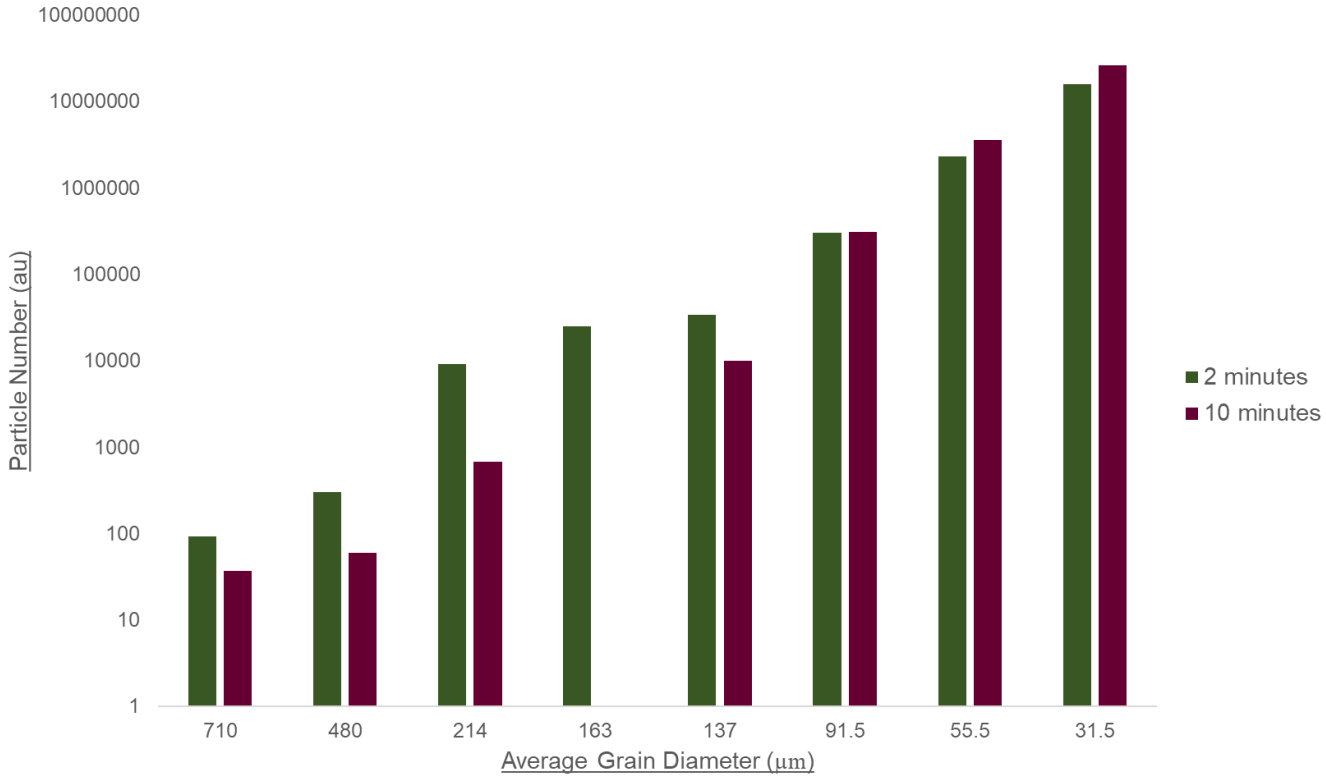

Figure 92. Grain size distribution curve for the JSC-Lunar simulant demonstrating the effect of milling on sample homogeneity.

As illustrated in Figure 91, a significant contrast in grain morphology and general size distribution can be observed between milling for 2 and 10 minutes as expected. Figure 91 demonstrates negligible difference between the raw JSC-Lunar simulant and the simulant milled for 2 minutes, with general grain morphology still possessing fairly sharp and angular edges. Whereas the JSC-Lunar simulant

milled for 10 minutes (at a same frequency of 10 Hz) was observed to consist of much finer, smaller grains, including a wider variety of grain morphologies, but lacking any sharper appearances.

Measuring the grain size distribution by means of sifting demonstrated the predicted directly proportional correlation between milling time (minutes) and sample homogeneity as illustrated in Figure 92 above. As the milling time increases, the average grain diameter decreases and thus the abundance of finer grains increases. Therefore, an increase in sample homogeneity should be observed. The grain size distribution plot as seen in Figure 92 above demonstrated this, with the number of finer particles (average grain diameters of 55.5 µm and 31.5 µm) increasing after 10 minutes of milling. Figure 92 additionally shows the relatively narrow grain size distribution of the JSC-Lunar simulant after milling for only 2 minutes. Due to a potential experimental and handling factors and errors, a few exceptions were identified through analysis of sifting data, as seen by negative data values.

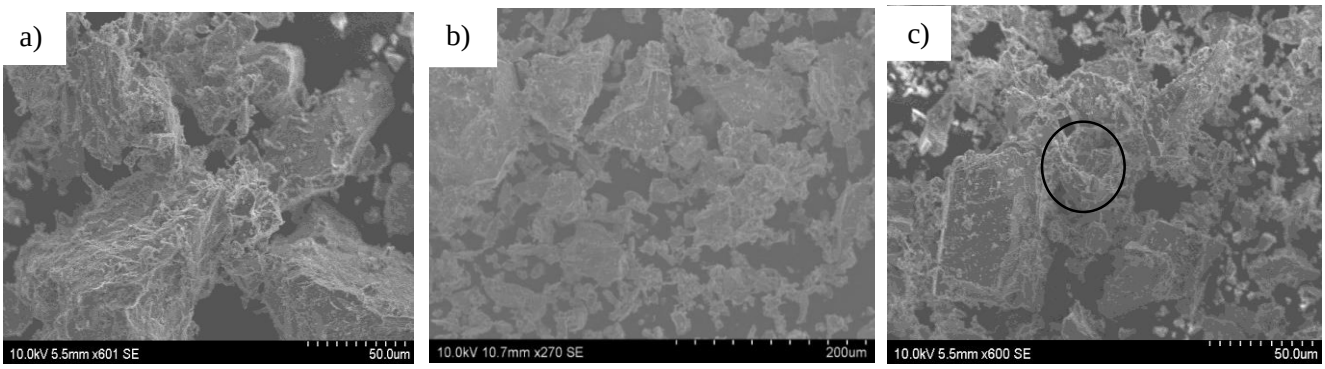

Figure 93. Secondary Electron Images (SEI) taken of a) the raw LHS-1 simulant b) the LHS-1 simulant milled for 2 minutes (Retsch MM301 mixer mill) at a magnification of x270; c) the LHS-1 simulant milled for 10 minutes (Retsch MM301 mixer mill) at a magnification of x600.

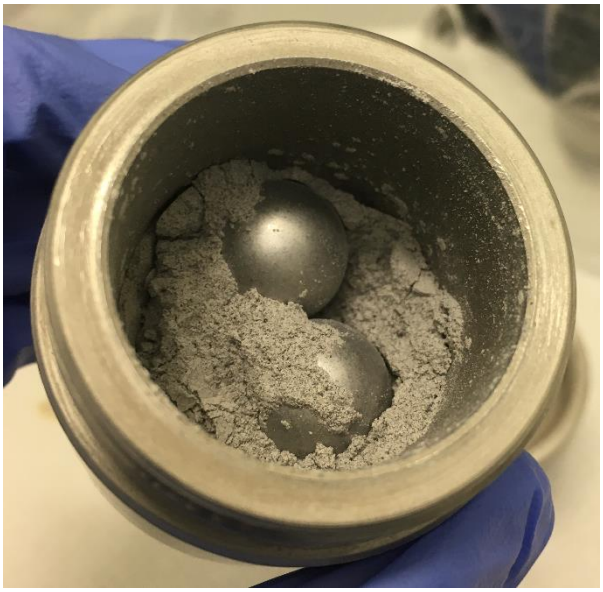

Figure 94. Photograph taken of the LHS-1 simulant milled (Retsch MM301 mixer mill) for 10 minutes at a frequency of 10 Hz.

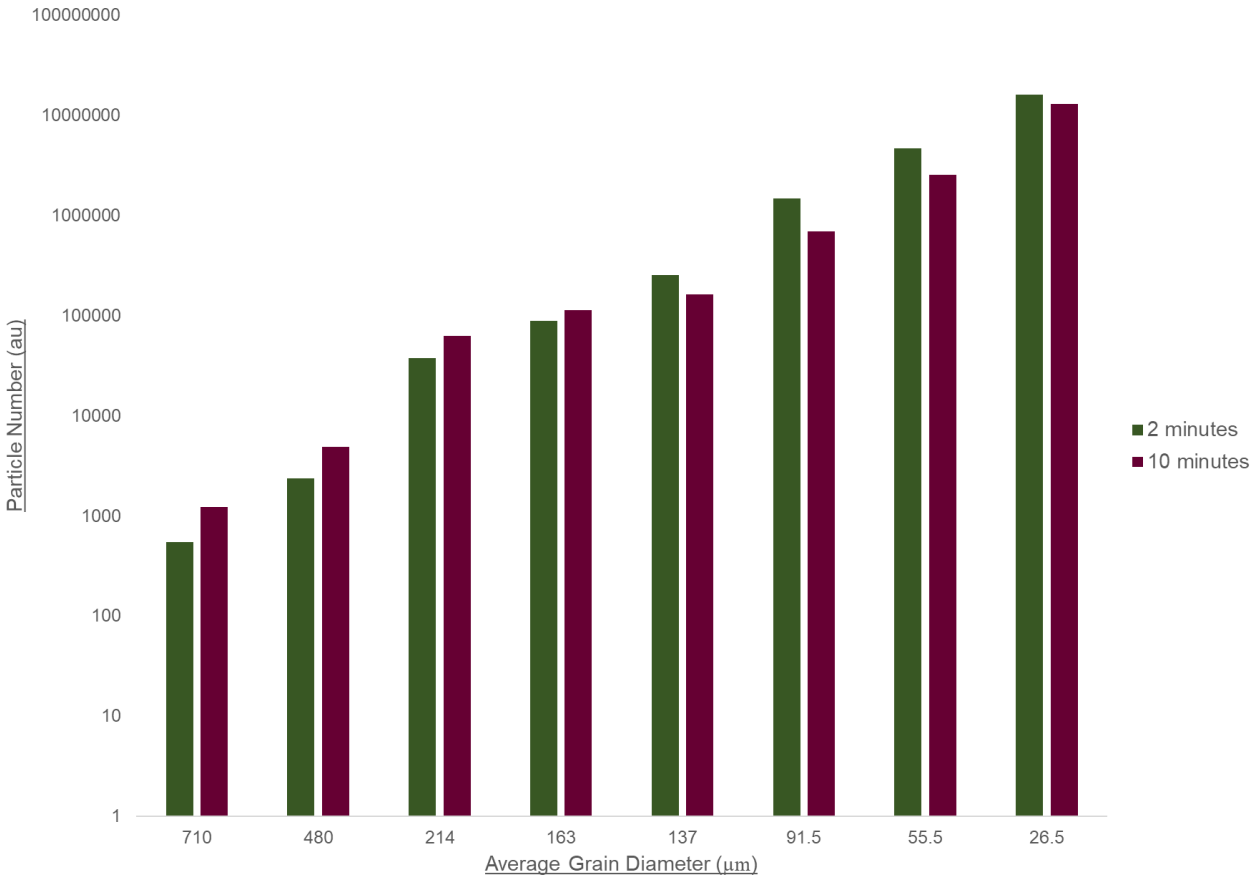

Figure 95. Grain size distribution curve for the LHS-1 simulant demonstrating the effect of milling on sample homogeneity.

SEM analysis as shown in Figure 93 illustrated the more noticeable alteration to surface texture and grain morphology, with 2 minutes of milling causing the expected and standard breakdown of larger grains into smaller segments, whereas 10 minutes at the same frequency (10 Hz) caused the effect of small grains adhering to larger ones, as clearly demonstrated through observation of the surface texture. In addition, SEM microphotography illustrated the wide grain size distribution, and the LHS-1 simulant's heterogeneous nature. Such adhering of grains was observed immediately after milling for 10 minutes, as shown in Figure 94 above which illustrates the clumpy, paste-like texture obtained. As discussed in chapter one, one potential cause of such adhering is granular electrification and tribo-electrification, suggesting the charging of grains upon milling the synthesised LHS-1 simulant [13].

The wide grain size distribution of the LHS-1 simulant and its grains' adhering properties was indicated by the grain size distribution curve as shown in Figure 95. This emphasises the immensely wide grain size distribution, in particular in comparison to the Earth-based JSC-Lunar simulant where grains were proved to be more uniform. The aforementioned clumping and adhering of grains was indicated by the decrease in abundance of finer particles (< 137 µm) after 10 minutes of milling, therefore increasing their average diameter due to agglomeration of granular particulates.

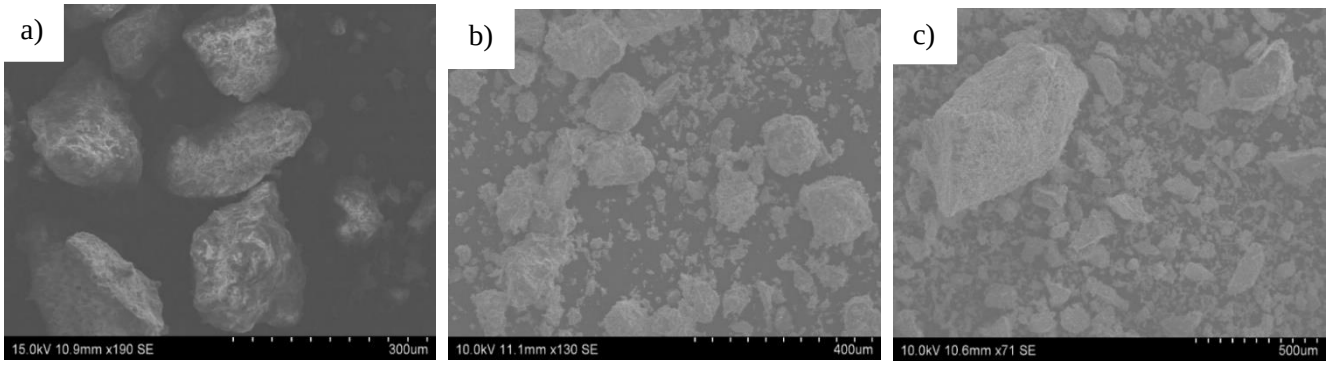

Figure 96. Secondary Electron Images (SEI) taken of a) the raw JSC-Martian simulant b) the JSC-Martian simulant milled for 2 minutes (Retsch MM301 mixer mill) at a magnification of x130; c) the JSC-Martian simulant milled for 10 minutes (Retsch MM301 mixer mill) at a magnification of x71.

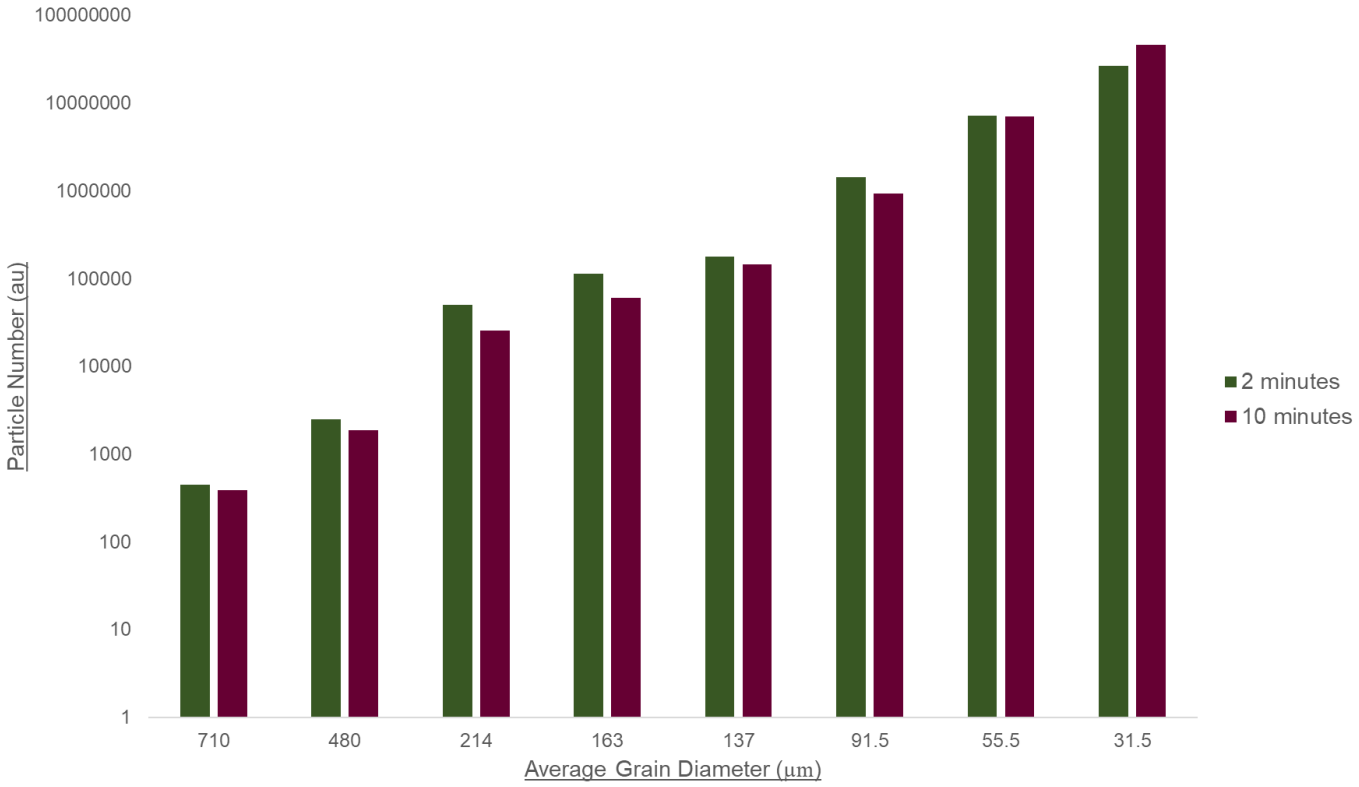

Figure 97. Grain size distribution curve for the JSC-Martian simulant demonstrating the effect of milling on sample homogeneity

Subjecting the Earth-based JSC-Martian simulant to identical ball milling conditions yielded similar results to that of the Earth-based JSC-Lunar simulant. As observed in Figure 96, 2 minutes of milling had only slight effects on the reduction in grain size and increase in fine granular textures. No significant variation in grain texture nor size could be seen after 10 minutes of milling. A fairly uniform distribution of grain sizes was observed, with only a minor proportion of larger grains despite milling for a period of 10 minutes.

The fairly heterogeneous nature of the Earth-based JSC-Martian simulant is illustrated by the narrow grain size distribution plot seen in Figure 96. The hypothesised effect of milling was observed for the average grain size of 55.5 µm however, was not consistent within the data as seen above. This could perhaps be due to the hygroscopic nature of the JSC-Martian simulant, and thus agglomeration of granular particulates.

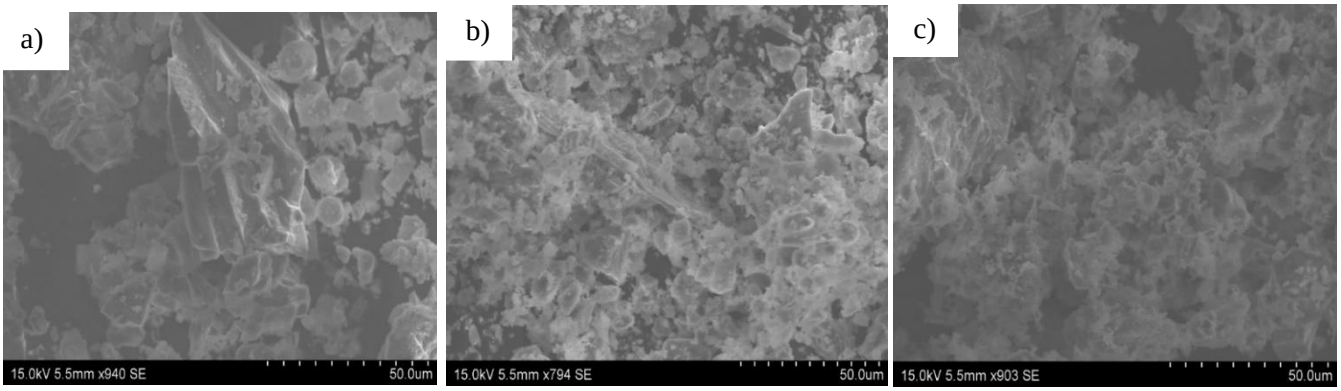

Figure 98. Secondary Electron Images (SEI) taken of a) the raw MGS-1 simulant b) the MGS-1 simulant milled for 2 minutes (Retsch MM301 mixer mill) at a magnification of x794; c) the MGS-1 simulant milled for 10 minutes (Retsch MM301 mixer mill) at a magnification of x903.

Figure 99. Photograph taken of the MGS-1 simulant milled (Retsch MM301 mixer mill) for 10 minutes at a frequency of 10 Hz.

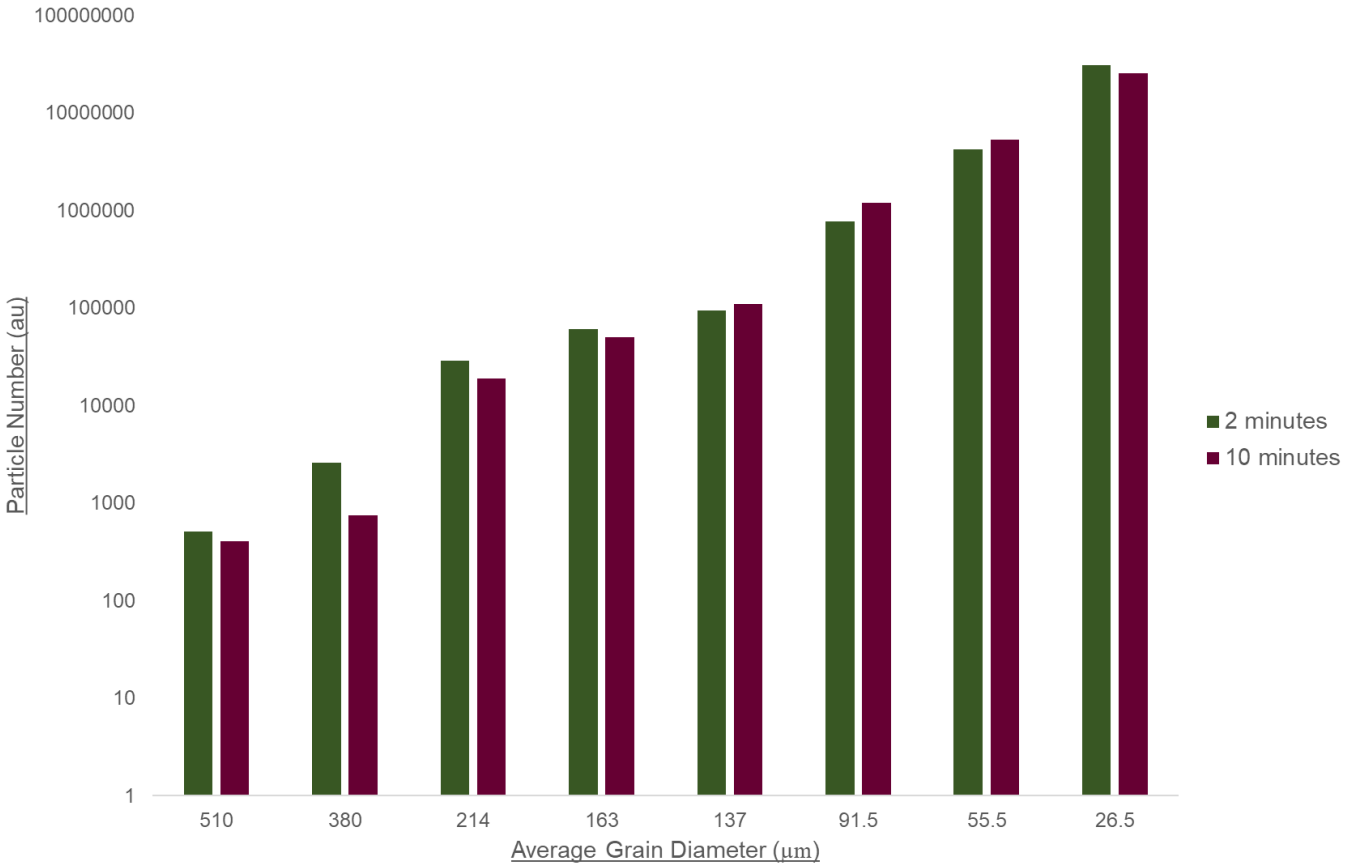

Figure 100. Grain size distribution curve for the MGS-1 simulant demonstrating the effect of milling on sample homogeneity.

Similarly, to the synthesised Lunar simulant LHS-1 the MGS-1 simulant displayed noticeable clumping and had a cement, paste-like textural appearance after being subjected to 10 minutes of milling, as illustrated by Figure 99 shown above. In contrast to the Earth-based JSC-Martian simulant, despite not yet demonstrating a degree of cementation, milling had an immediate effect of 2 minutes on the surface texture and general blending of the material. Such adhering of grains was possibly due to tribo-electric effects, which is of great relevance to the Martian surface when interpreting properties of sand recovered from plains which have been exposed to events such as dust devils [14]. The initial grain size distribution of the MGS-1 simulant was previously known to be wider than that of the Earth-based JSC-Martian simulant, which was demonstrated by SEM analysis as seen in Figure 98 above. The grain size distribution seen in Figure 100 for that of the synthesised MGS-1 simulant emphasised its heterogeneous nature. As expected due to evident adhering of grains, a general decrease in particle number was shown in Figure 100 after milling for 10 minutes, further illustrating the importance of the effect of clumping and agglomeration of grains on surface area and how this affects rates of reactivity. Whilst milling at room temperature does not have a significant effect on the surface area of a material, especially considering abrasion is temperature dependent, the surface area does increase slightly [42] (refer to chapter one).

4.3 Thermal and mechanochemical activation

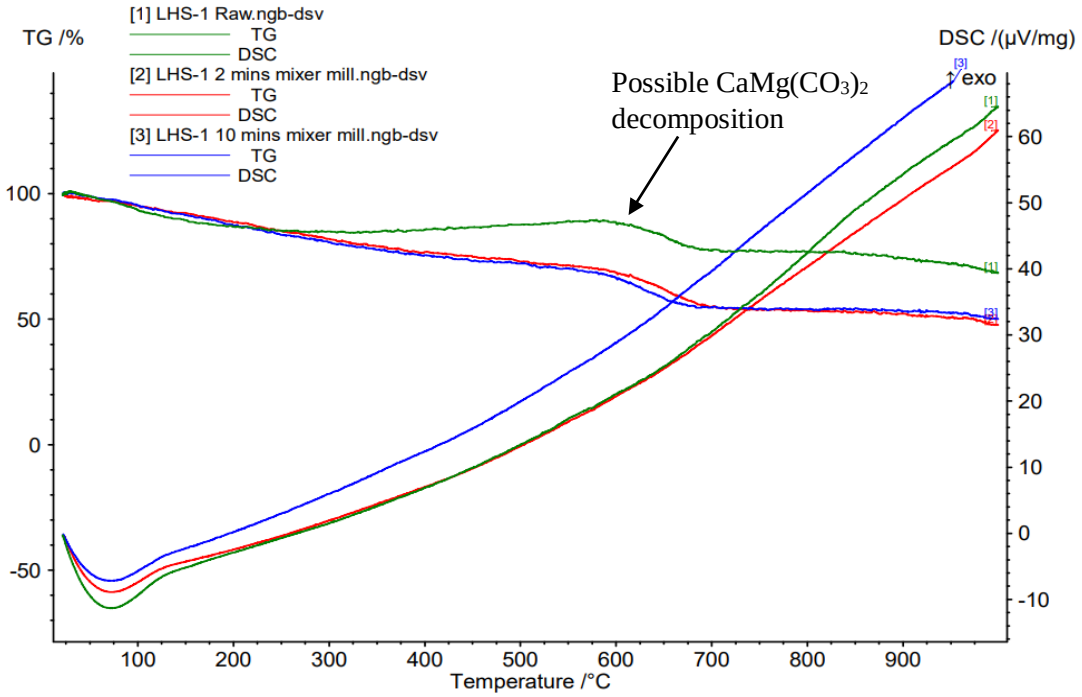

Figure 101. TGA-DSC curve for the LHS-1 sample milled for 0, 2 and 10 minutes upon heating to 1000 °C under a constant flow of $N_{2\,(g)}$. An increase in % mass loss can be seen with increasing milling time

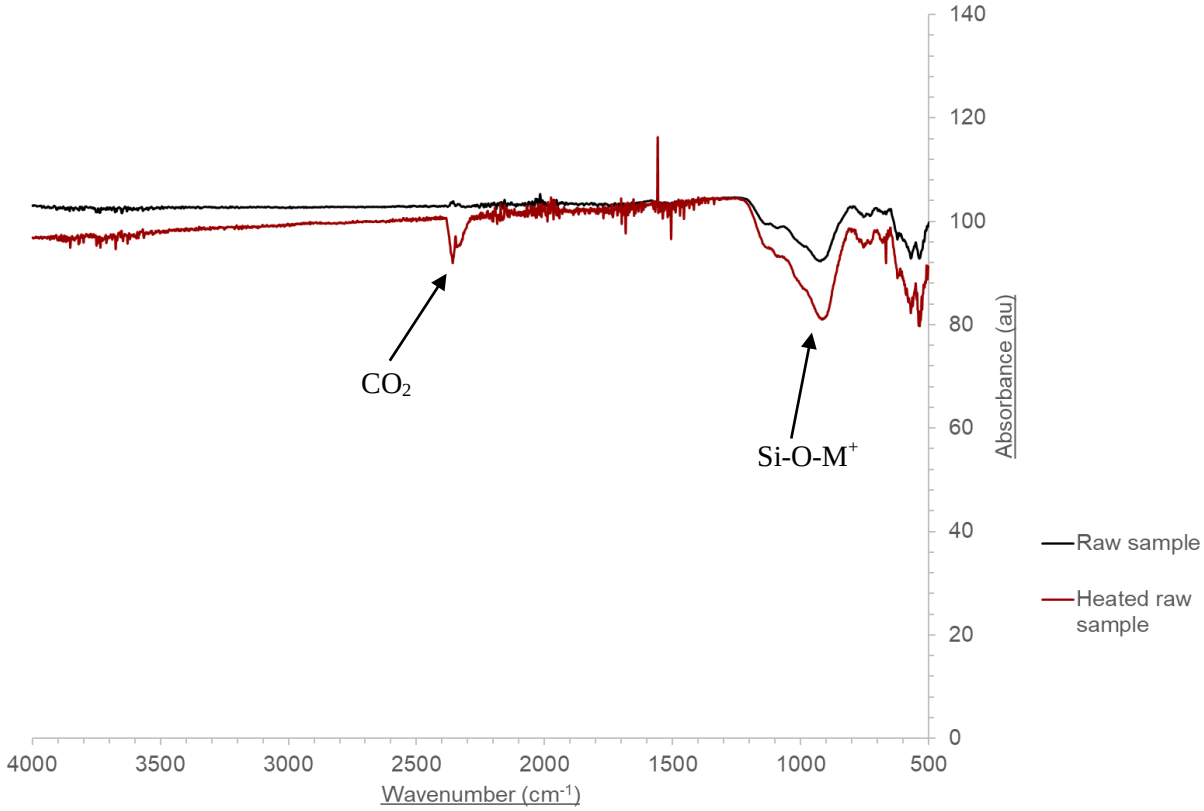

Figure 102. Infrared spectra for the raw LHS-1 sample heated to 1000 ℃ with a wavenumber range of 4000 cm^{-1} -500 cm^{-1}. An increase in $CO_{2\,(g)}$ adsorption due to thermal activation of mineral cavities can be seen from the characteristic doublet peak at ~ 2400 cm^{-1}.

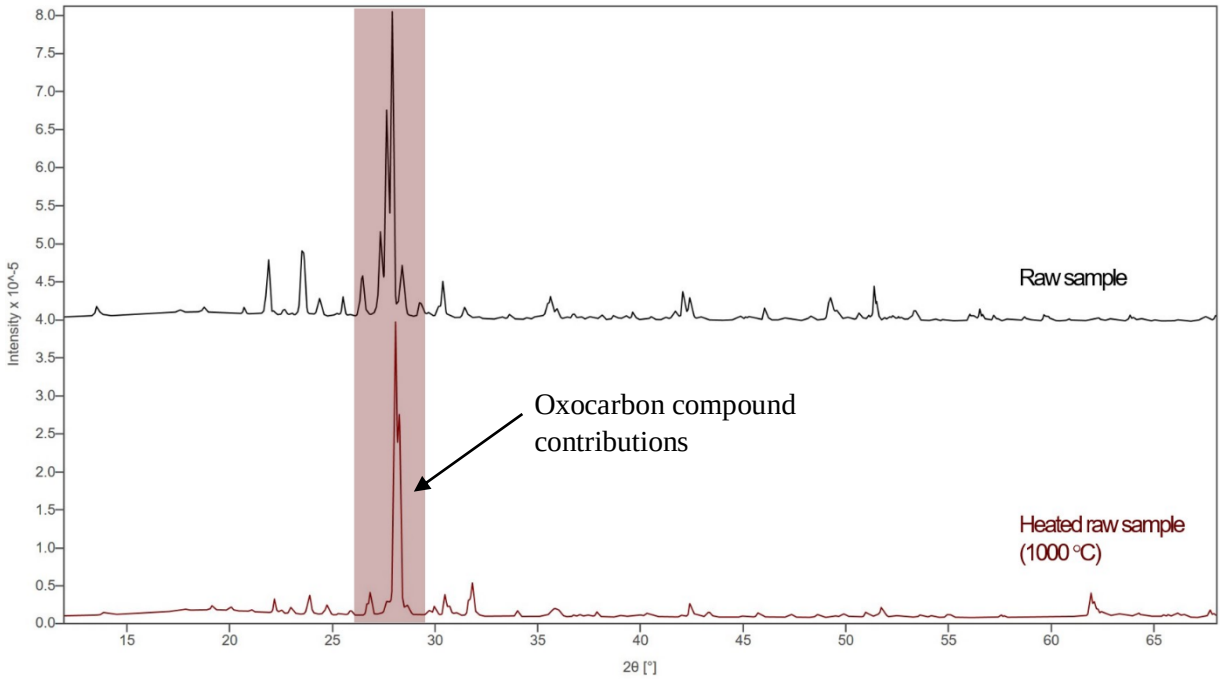

Figure 103. XRD diffractogram of the raw LHS-1 sample heated to 1000 °C between 15°-65° and a scan time of 3 hours. Highlighted peaks illustrate the noticeable changes in relative peak intensity upon heating at ~ 27.9°.

As illustrated in Figure 101, TGA data demonstrated a greater decrease in % mass upon milling. As the LHS-1 simulant was milled for longer milling times, the grain size inevitably decreased, and thus surface area increased, allowing thermal expansion of a greater number of mineral pores/cavities. This is illustrated by the TGA-DSC profile (with the DSC curve displaying transformations such as melting and crystallisation [38]) in Figure 101, whereby the potential endothermic evaporation of water which is physically adsorbed to mineral surfaces is increased with increasing milling time, typically at 100 °C [38,39]. However, the small % mass loss on average suggests that the LHS-1 simulant is not hygroscopic and has a low abundance of water, which is matched with DTA-TG analysis of sampled Apollo samples [12]. The adsorption of CO_2 was indicated by IR analysed as demonstrated in Figure 102 by the characteristic peak at ~ 2400 cm^{-1}. As the synthesised LHS-1 simulant is primarily composed of anorthosite and glass-rich basalt (74.4 wt. % and 24.7 wt. % respectively), as shown in chapter 3, both appeared to adsorb CO_2 and produce carbonate minerals, these observations are fitting with previously discussed data regarding the simulant's constituent minerals. Heating the raw LHS-1 sample appeared to increase the corresponding Si-O-M^+ band absorbance at ~ 900 cm^{-1} perhaps due to thermal expansion of mineral surface pores and thus greater absorption of infrared radiation. Silica bonds are extremely stable and require high activation energies to be altered. At high temperatures of ~1000 °C, silica based materials such as the LHS-1 simulant may be modified in terms of geometry due to breaking and reforming of bonds. This modification could potentially increase the reactivity of the usually stable Si-O-M^+ bond, and increase its absorption of infrared radiation. XRD analysis of the heated raw LHS-1 simulant illustrated a loss in the number of peaks as demonstrated in Figure 103, and an emergence

of oxocarbon compounds contributions, at a peak angle value of ~ 28.0°, agreeing with IR data as previously discussed. Heating of the raw LHS-1 simulant appeared to activate certain reaction pathways causing the production of secondary minerals such as feldspars, as suggested by the relatively intense peak at ~ 28.0°, possibly due to thermal attacks of the pre-existing primary minerals [65]. The hump conformation seen at ~ 540°C may be due to carbonate mineral decomposition, as Stillings *et al.* reports $CaMg(CO_3)_2$ has a decomposition temperature of 538 °C, thus suggesting release of CO_2 [29].

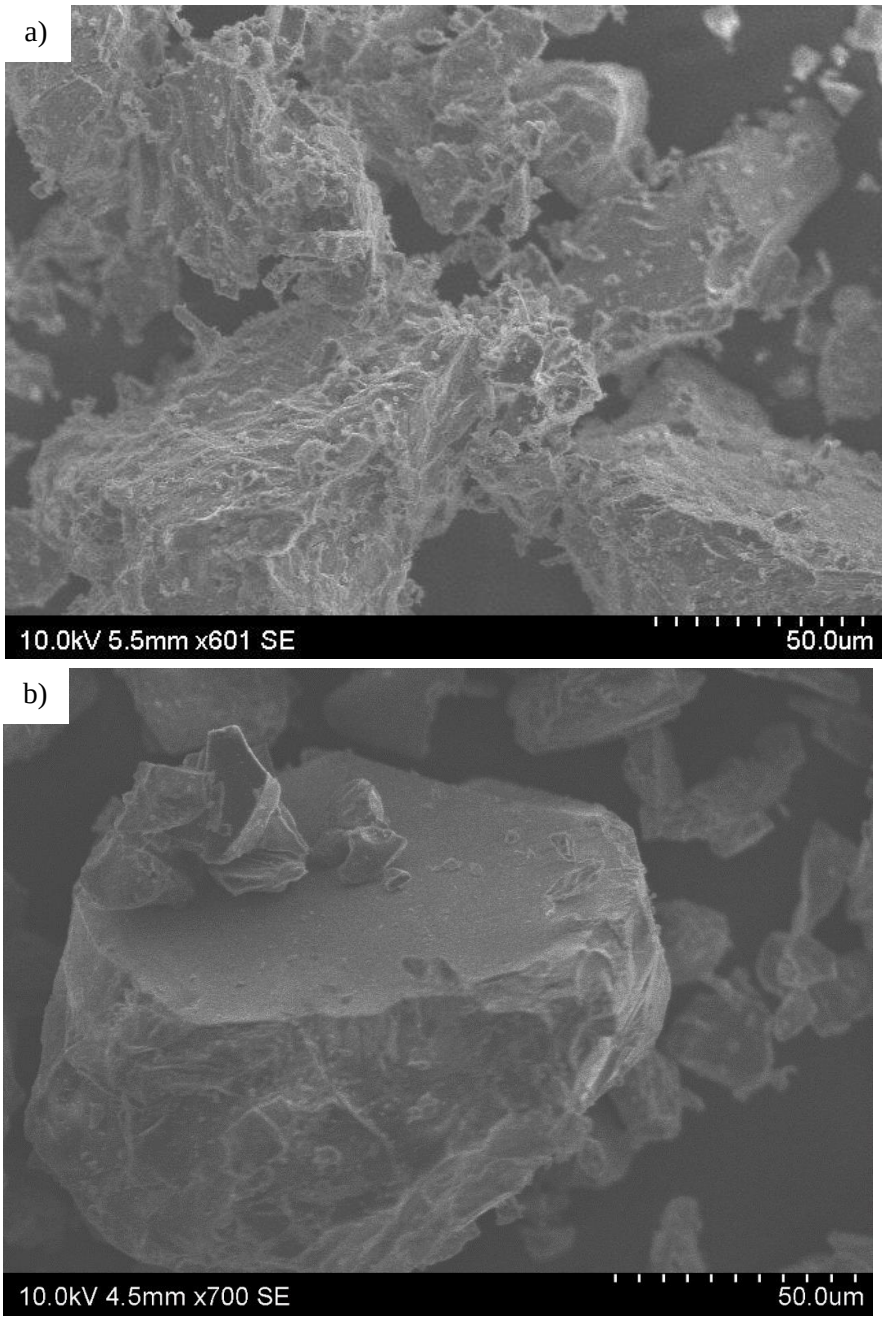

Figure 104. SEM image taken of the raw LHS-1 simulant at a magnification of x601 at a) 25 °C; b) heated to 1000 °C at a magnification of x700.

SEM analysis of the heated raw LHS-1 simulant heated to 1000 °C is displayed in Figure 104 as an example to illustrate the little effect heating the simulants had on their physical morphologies.

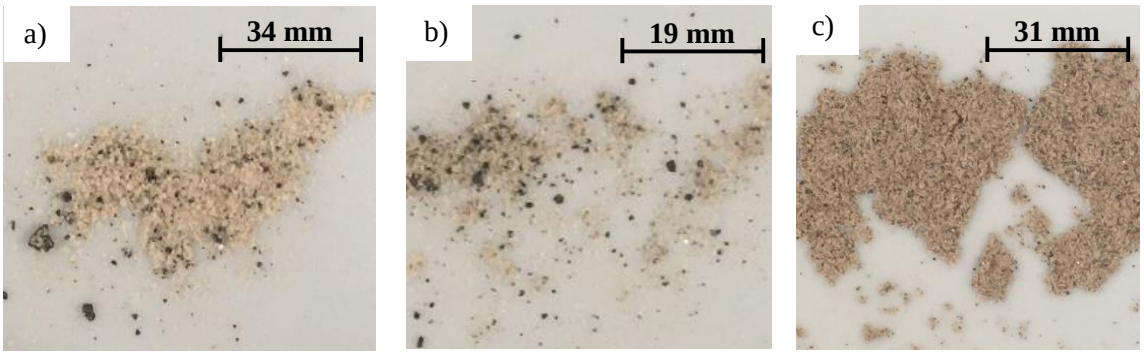

Figure 105. Photographs taken of the heated LHS-1 sample milled for a) 0 minutes; b) 2 minutes; c) 10 minutes. Figure 105 c) demonstrates the darkening in colour for the LHS-1 sample milled for 10 minutes upon heating compared with similarly heated samples milled for 0 and 10 minutes, indicating enhanced thermally induced chemistry.

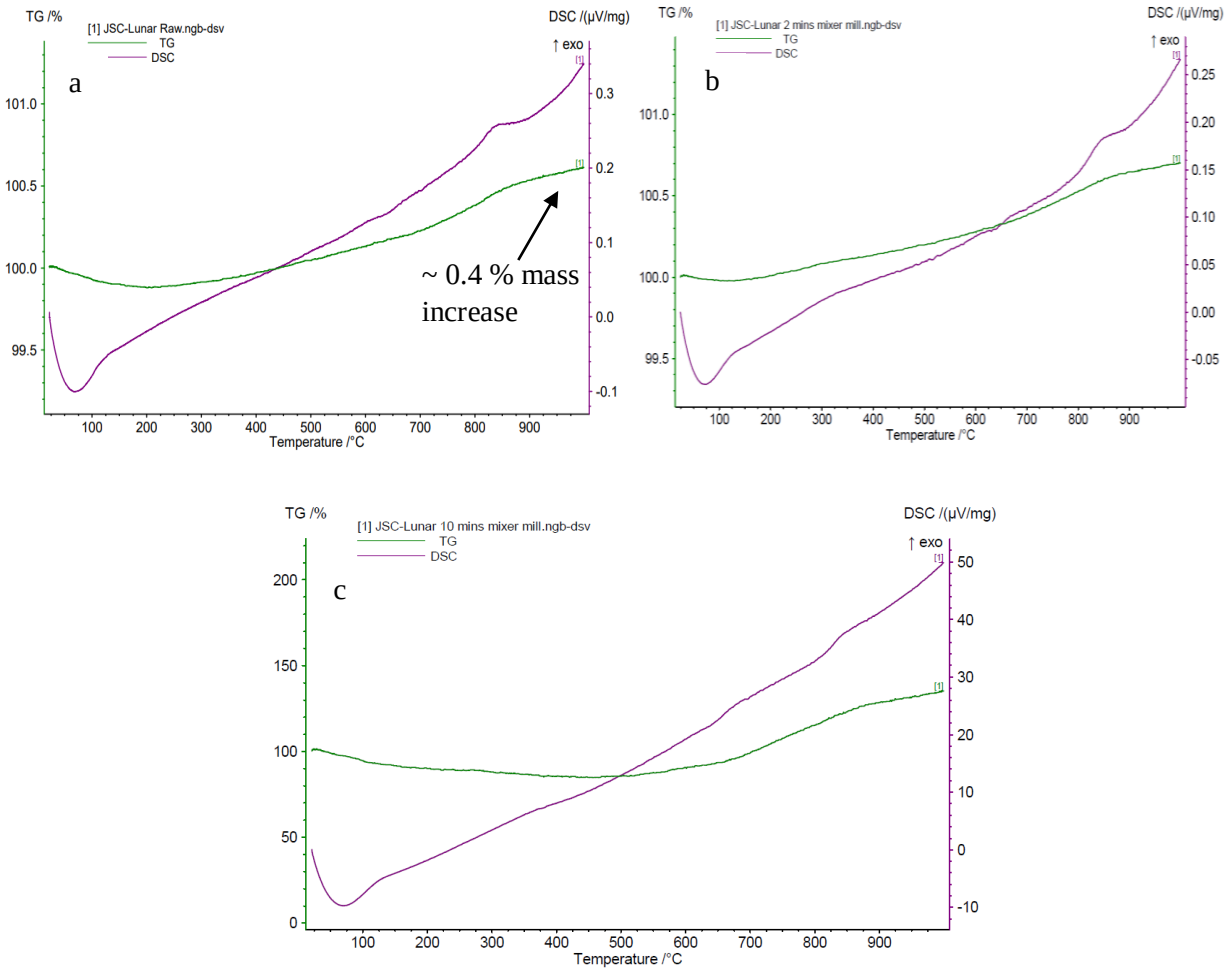

Figure 106. TGA-DSC curve for the JSC-Lunar sample upon heating to 1000 °C under a constant flow of $N_{2\,(g)}$ for the a) raw sample; b) milled for 2 minutes; c) milled for 10 minutes. Little difference was seen in TGA-DSC results when comparing the raw sample to milled for 2 and 10 minutes.

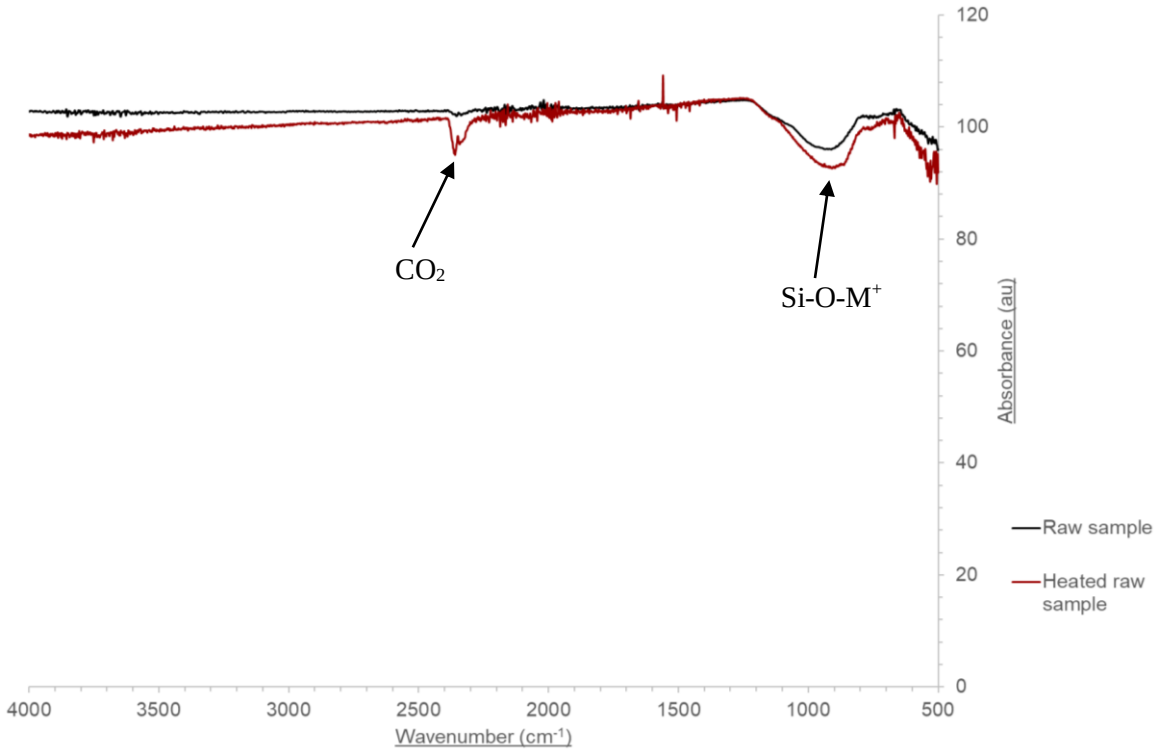

Figure 107. Infrared spectra for the raw JSC-Lunar sample heated to 1000 ℃ with a wavenumber range of 4000 cm^{-1} -500 cm^{-1}. An increase in $CO_{2\,(g)}$ adsorption due to thermal activation of mineral cavities can be seen from the characteristic doublet peak at ~ 2400 cm^{-1}.

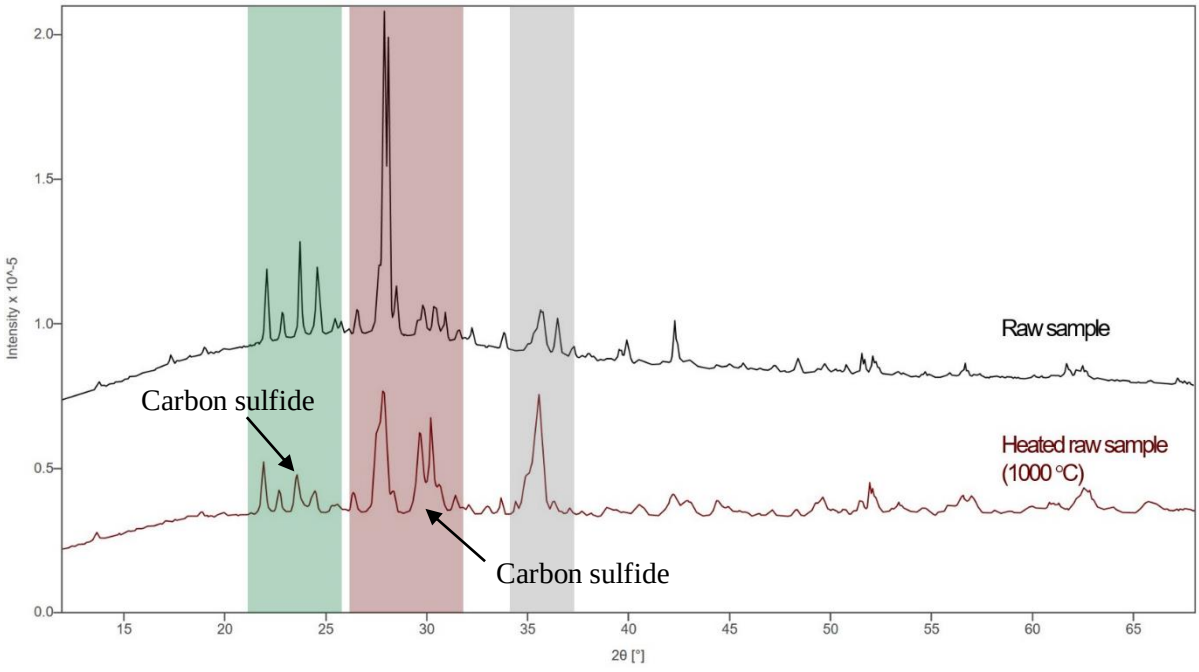

Figure 108. XRD diffractogram of the raw JSC-Lunar sample heated to 1000 °C between 15°-65° and a scan time of 3 hours. Highlighted peaks illustrate the noticeable changes in relative peak intensity upon heating, in particular the speculated feldspar silicate mineral contribution at ~ 27.9°.In contrast to

the synthesised LHS-1 simulant, heating the JSC-Lunar simulant to 1000 °C appeared to cause little effect on its chemical and mineralogical properties upon milling. TGA data for the raw JSC-Lunar simulant is shown in Figure 106 a) indicated a slight and steady increase in % mass of ~ 0.4 %, suggesting uptake of moisture. IR data indicated the adsorption of $CO_{2\,(g)}$ due to the characteristic doublet peak at ~ 2400 cm^{-1} shown in Figure 107. As discussed previously, the increase in band absorbance at ~ 900 cm^{-1} was expected, as both Lunar simulants are silica-based, and thus stable O-Si-O bonds are weakened due to thermal activity and thus lowering of activation energy [29]. The Earth-based JSC-Lunar simulant is mainly composed of glass basalt, which demonstrated a slight increase in % mass. The lack of any drastic peak changes indicates the JSC-Lunar simulant does not consist of any volatile components [12]. As shown in Figure 108, heating of the raw JSC-Lunar analogue perhaps increased feldspar reactivity, with a suggested increase in feldspar contributions through peak characterisation showing the majority of the XRD pattern to be due to sodium aluminium silicates [41]. Carbon-containing minerals such as carbon sulfide were potentially indicated by diffraction angle values of ~ 24.5° and 29.9°, possibly formed due to increased CO_2 adsorption and thus interaction with surface minerals ions.

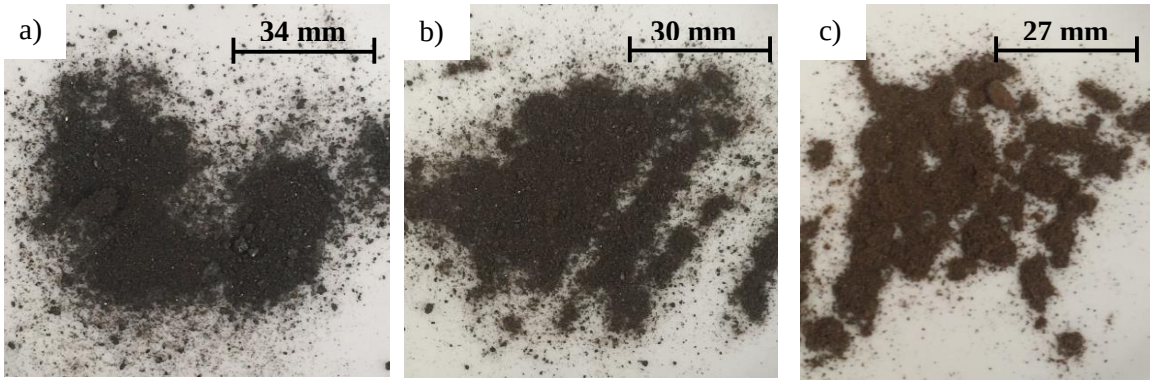

Figure 109. Photographs taken of the heated JSC-Lunar sample milled for a) 0 minutes; b) 2 minutes; c) 10 minutes.

As shown in Figure 109 above, the more abraded JSC-Lunar samples appear lighter in colour due to heating, suggesting due to a greater number of active surface M^+ ions, thermal activation and thus expansion of cavities is increased due to greater availability and specific surface area.

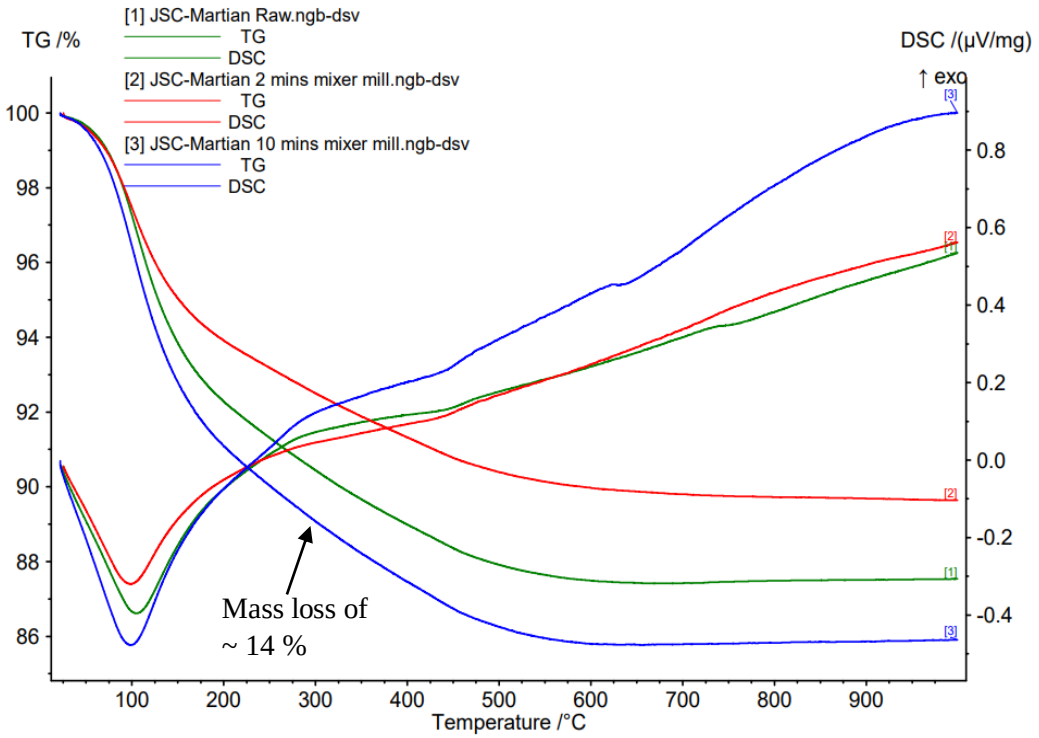

Figure 110. TGA-DSC curve for the JSC-Martian sample milled for 0, 2 and 10 minutes upon heating to 1000 °C under a constant flow of $N_{2\,(g)}$. Despite a steady % mass loss, a decrease can be seen for 2 minutes, perhaps due to greater atmospheric water retention considering the material's hygroscopic properties.

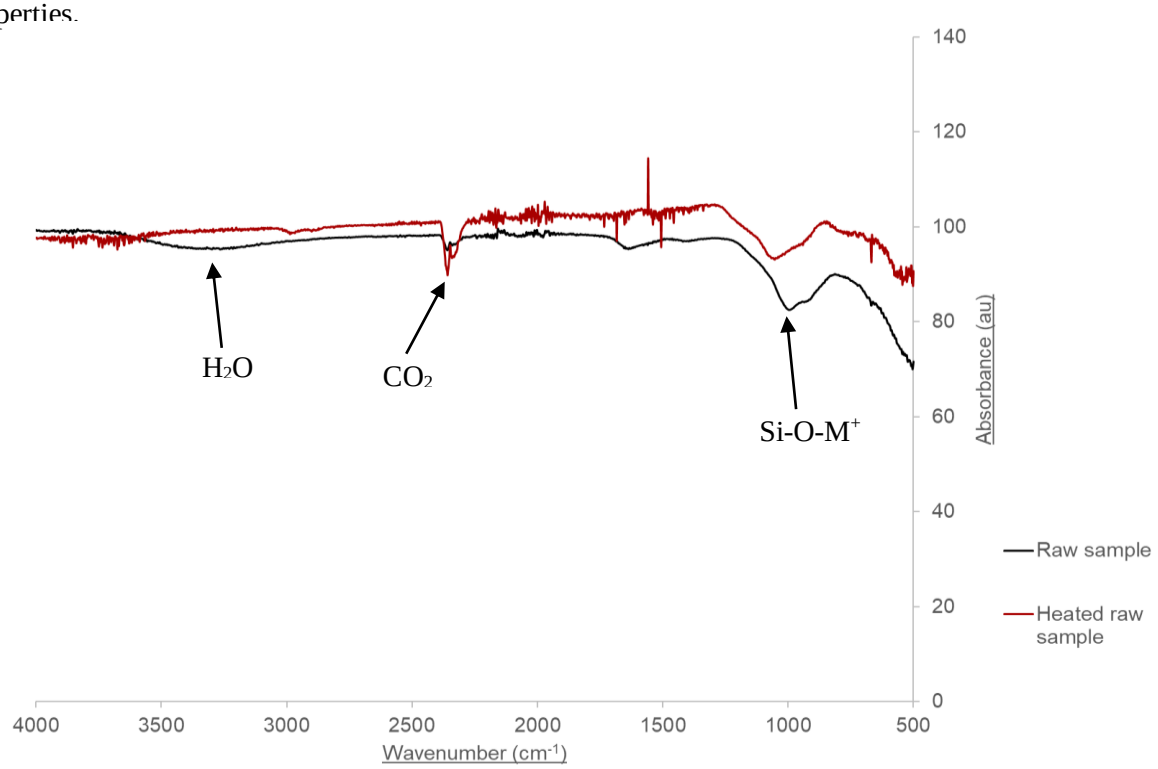

Figure 111. Infrared spectra for the raw JSC-Martian sample heated to 1000 ℃ with a wavenumber range of 4000 cm^{-1} -500 cm^{-1}. Elimination of the broad absorbance band at ~ 3400 cm^{-1} upon heating indicates the loss of water.

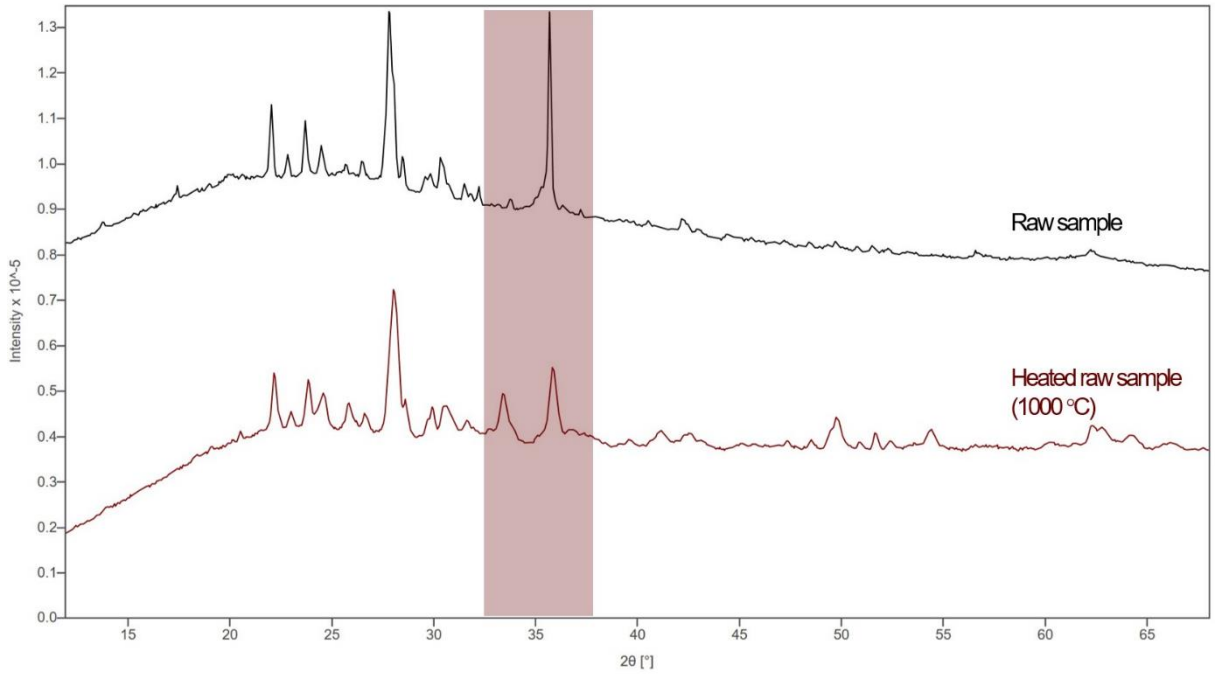

Figure 112. XRD diffractogram of the raw JSC-Martian sample heated to 1000 °C between 15°-65° and a scan time of 3 hours. Highlighted peaks illustrate the noticeable changes in relative peak intensity upon heating, in particular the observed decrease at ~ 36°.

As illustrated in Figure 110, TGA analysis of the Earth-based JSC-Martian simulant displayed a steady % mass loss upon heating, with the JSC-Martian sample milled for 10 minutes showing the greatest change in mass of ~ 14 % as expected due to smaller grain sizes and thus greater absorption of thermal energy. Nonetheless, 2 minutes of milling appeared to have less of a reduction in % mass compared to the raw JSC-Martian simulant. Few volatile components were released as indicated by the steady, constant % mass decrease. The rather constant % mass at > 600 °C suggests no matter the extent of milling, little to no effect is seen past this point of heating. IR analysis shown in Figure 111 above suggests a release of surface bound water, with the disappearance of the broad peak at ~ 3400 cm^{-1}. IR analysis additionally demonstrated the adsorbance of $CO_{2\,(g)}$, as anticipated. As illustrated in Figure 112, XRD analysis of the heated raw JSC-Martian sample demonstrated the potential decrease in certain oxide phase contributions such as iron titanium oxide, manganese chromium oxide and the increase in feldspar contributions.

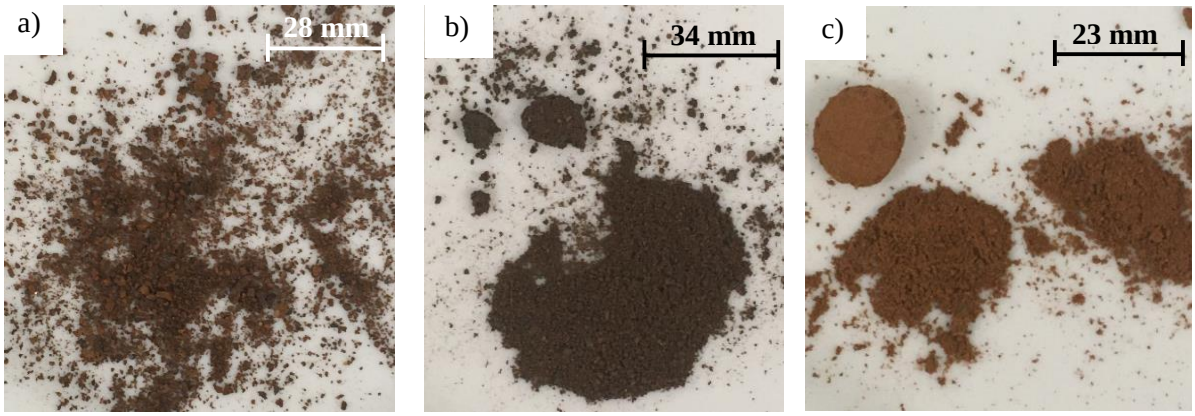

Figure 113. Photographs taken of the heated JSC-Martian sample milled for a) 0 minutes; b) 2 minutes; c) 10 minutes.

Figure 113 c) shown above demonstrates pellet formation upon heating, perhaps due to closely packed grains.

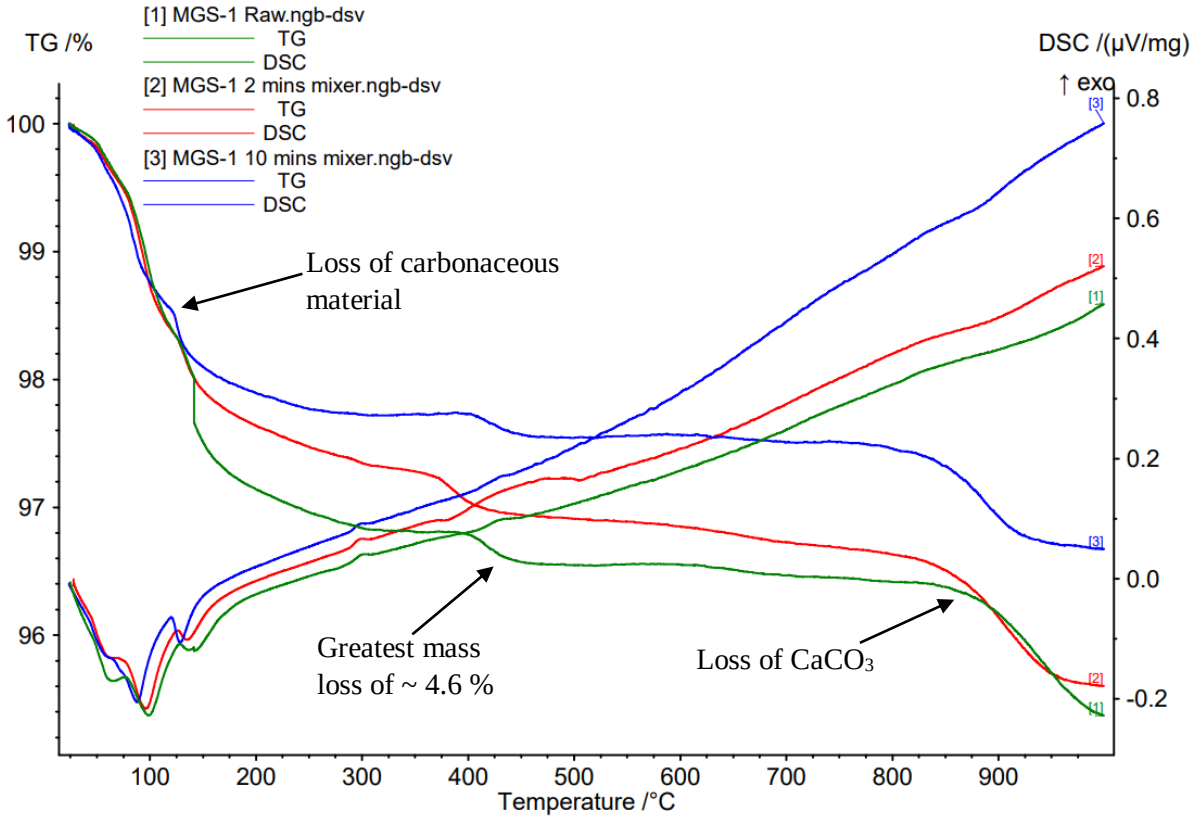

Figure 114. TGA-DSC curve for the MGS-1 sample milled for 0, 2 and 10 minutes upon heating to 1000 °C under a constant flow of $N_{2\,(g)}$. A decrease in % mass loss can be seen due to 10 minutes of milling, perhaps due to uptake of $CO_{2\,(g)}$.

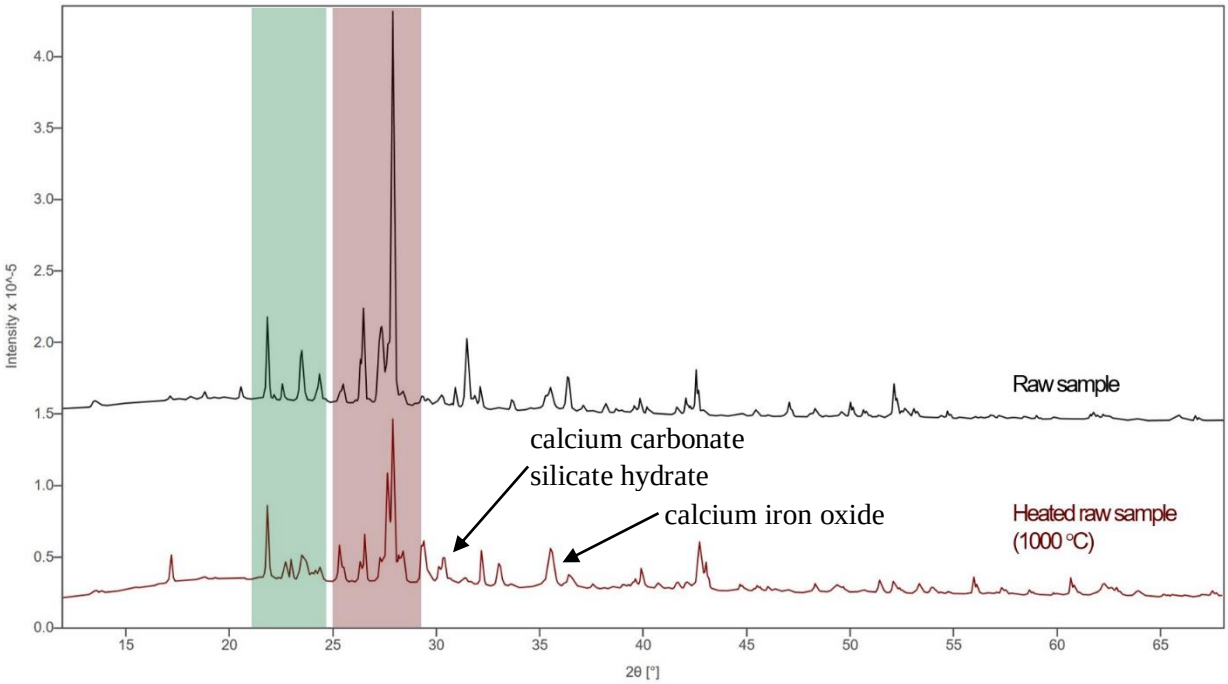

Figure 115. XRD diffractogram of the raw MGS-1 sample heated to 1000 °C between 15°-65° and a scan time of 3 hours. Highlighted peaks illustrate the noticeable changes in relative peak intensity upon heating, in particular the speculated feldspar silicate mineral contribution at ~ 27.9°. It should be noted that ATR-FTIR data for the heated MGS-1 samples could not be acquired due to time restraints, however similar results to the other heated simulants were anticipated.

Unlike the three previously mentioned simulants, heating of the raw and milled MGS-1 samples displayed the most contrasting TGA results. The raw MGS-1 sample appeared to have the greatest reduction in % mass of ~ 4.6 %, whereas 10 minutes of milling had the smallest decrease of ~ 3.2 %. The variations in the DSC profile may perhaps be due to homogenisation. Due to observed clumping after 10 minutes of milling, incorporated moisture was anticipated, which would increase the overall % mass. The small hump observed at ~ 150 °C regarding the sample milled for 10 minutes indicates something other than water is bound to the sample, which is lost at this temperature, possibly a carbonaceous material for instance carbonate minerals. The small exothermic peaks observed at ~ 400 °C suggest a stable phase transition upon heating. The sudden decline in % mass at ~ 860 °C suggests the loss of $CaCO_3$ [29] and > 800 °C stable, volatile compounds present with the MGS-1 samples, for instance perhaps volatile short chain hydrocarbons. Concerning temperatures < 500 °C, the loss of carbonaceous groups such as carbonate minerals, and the release of $CO_{2\,(g)}$ was suggested. XRD results shown in Figure 115 suggested the introduction of calcium-rich minerals such as calcium carbonate silicate hydrate and calcium iron oxide at peak angles of ~ 30.4° and 35.6° due to heating, agreeing with TGA results.

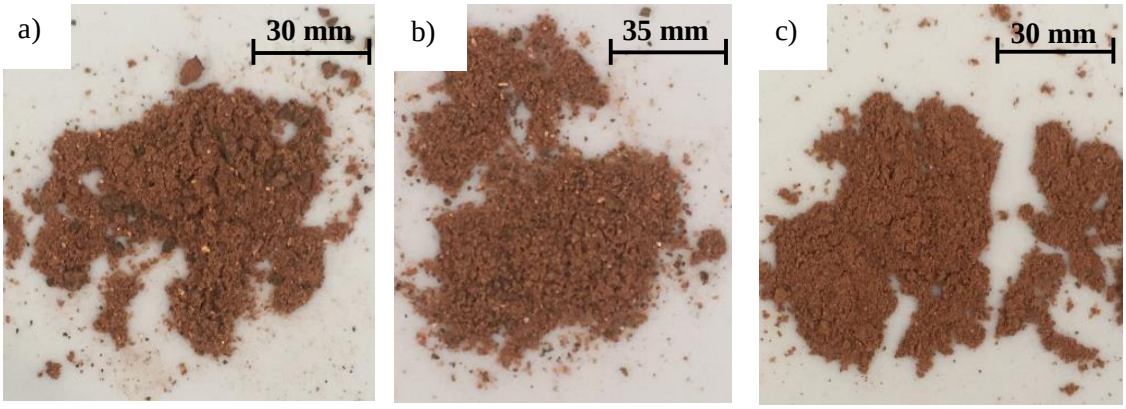

Figure 116. Photographs taken of the heated MGS-1 sample milled for a) 0 minutes; b) 2 minutes; c) 10 minutes.

As illustrated in Figure 116 above, little variation in physical appearance can be seen upon heating the MGS-1 sample.

4.4 Summary and Conclusions

The results presented in this chapter illustrate the significant observed effects of mechanochemical and thermal activation of the minerals within the planetary analogue materials. Preliminary characterisation has shown that whilst there are noticeable alterations in mineralogy upon milling, in particular the production of secondary minerals due to mechanochemical activation, little difference has been observed when comparing varying milling types. This is an invaluable finding within this stage of research, as it implies that on the Lunar and Martian surface, whilst mineralogy and the production of ROS due to regolith transport is apparent, the manner in which the surface is abraded may yield similar effects. The effect of milling on the number of chemically available and thus active M^+ surface ions has been made evident by ATR-FTIR spectroscopic analysis through an increase in IR absorbance due to longer milling times and thus greater abrasion. This may also increase confidence in CO_2 sequestration results due to mechanochemical-induced expansion of mineral cavities, which is discussed by Stillings *et al.* whereby proposed mechanisms have suggested increased CO_2 diffusion through migration to lattice interstitials. This increase in active M^+ surface ions on minerals is relevant to the generation of ROS on the Lunar and Martian surface, and correlates to research conducted by Edgar *et al.* and experiments with abraded silicates and aqueous alterations. The uptake of CO_2 is highly relevant to the Martian surface, and the potential environmental processes occurring between the atmosphere and regolith, but also the formation of carbonates. However, understanding additional environmental processes such as mixing of ices within the surface/subsurface soil and the transport of regolith-ice mixtures and deposits, for instance within the Lunar cold traps, is essential when comparing regolith and the potential geochemically-induced changes in its physical and chemical properties recovered from different plains on a planetary surface.

Results Chapter 5: Incorporation of Water Ice and Simulating Icy Environmental Conditions

As explored within chapter 1, water ice is known to exist both on the Lunar and Martian surface, surviving under different environmental conditions [18, 20]. The mixing of water ice with regolith as surface dust is transported from one geographical area to another will inevitably cause alterations in mineralogy and chemical composition due to aqueous alteration and other geochemical-driven mineral-water reaction processes occurring. The combination of surface and/or subsurface regolith and water ice and subsequent mixing through weathering means the presence of certain minerals, such as hydrated silica-based compounds, are likely to be identified on the planetary surfaces themselves.

The effect of such icy environmental conditions on the mineralogical and chemical properties of Lunar and Martian regolith was simulated in the laboratory by means of ball milling (employing the University of Kent's Retsch MM301 mixer mill). Both the Earth-based and synthetic analogues were combined with three different forms of ice; deionised, distilled and tap water ice (see chapter 2). Variations in mineralogical and elemental composition of the different regolith analogues were anticipated when using the three forms of water ice (as discussed within subsection 6.1). A constant percentage ratio of 75:25 regolith to water ice was used for all milling experiments in the stainless steel reaction vessel to ensure a consistent volume of water being incorporated into the reaction. However, as noted in chapter 2, milling reactions were water-driven rather than ice due to melting (caused by the combination of an intended crushing of ice using a pestle and mortar and internal reaction temperature increase due to friction during milling).

6.1 The Effect of Water Ice Treatment

As shown in Table 7, due to the lack of minerals present in deionised and distilled water, these two ice treatments were predicted to have less of an effect on the mineralogical composition of the regolith analogues in comparison to tap water. Considering the milling process and its increase in the number of chemically active sites on the surface of grains and specific surface area, the integration of water into the crystalline structure was predicted, therefore increasing the abundance of hydrated minerals. The presence of water may increase the rate of diffusion as it can be considered a lubricant when comparing to dry milling, therefore less sufficient grain reduction can be speculated. It was hoped that conducting milling experiments with differently treated water ice could account for a more diverse set of possible minerals and salts found within water ice on the Lunar and Martian surfaces. For example, could these experiments provide an initial prediction for whether water ice found at the Martian poles in low abundance contain different minerals to ice located within a different geographical area.

Table 8. Relative elemental compositions of deionised, distilled and tap water [67].

Water Treatment	**Elements Present**
Deionised water	Almost no minerals present, only trace amounts
Distilled water	No fluorides and minerals
Tap water	Ca^{2+}, Mg^{2+}, Na^{+}, K^{+}, Fe^{2+}, Mn^{2+}, Cu^{2+}, Zn^{2+}, P^{3-}, Cl^{-}, S^{2-} and F^{-}

6.2 Potential Alterations in Mineralogy and Chemical Composition

As discussed within chapter 2, all 25 % water ice 75 % regolith mixtures were milled utilising the Retsch MM301 at milling times of 2 and 10 minutes and a frequency of 10 Hz and subsequently dried in a Na_2CO_3 desiccator for > 24 hours before XRD analysis. XRD was employed to try and assess how the incorporation of water ice potentially affected the mineralogy of the simulants, for example, the introduction of hydrated minerals. It is important to note that all data shown below is specifically regarding bottom layer extractions of the samples, unless stated otherwise. Pre-dried samples were run on the ATR-FTIR spectrophotometer, and dried sample on the XRD apparatus. It was assumed that more than solely just a layer of water would be highlighted by subsequent analyses, such as the introduction of hydrated minerals due to regolith-water ice integration.

Despite running samples with 25 % distilled, deionised and tap water ice, the XRD data collected showed negligible differences, with the clearest peaks observed in the deionised water ice diffractogram, as illustrated in Figure 97 below (additional example data for other water treatments shown in appendix 4). Consequently, the majority of acquired results presented in this chapter are for the deionised water ice milling experiments to illustrate its influence on the mineralogical and chemical properties of the Lunar and Martian simulants. Similarly, FTIR spectroscopic data is principally shown for the deionised water experiments, as little variation in the spectral band positions or strengths were shown when using the other water ices.

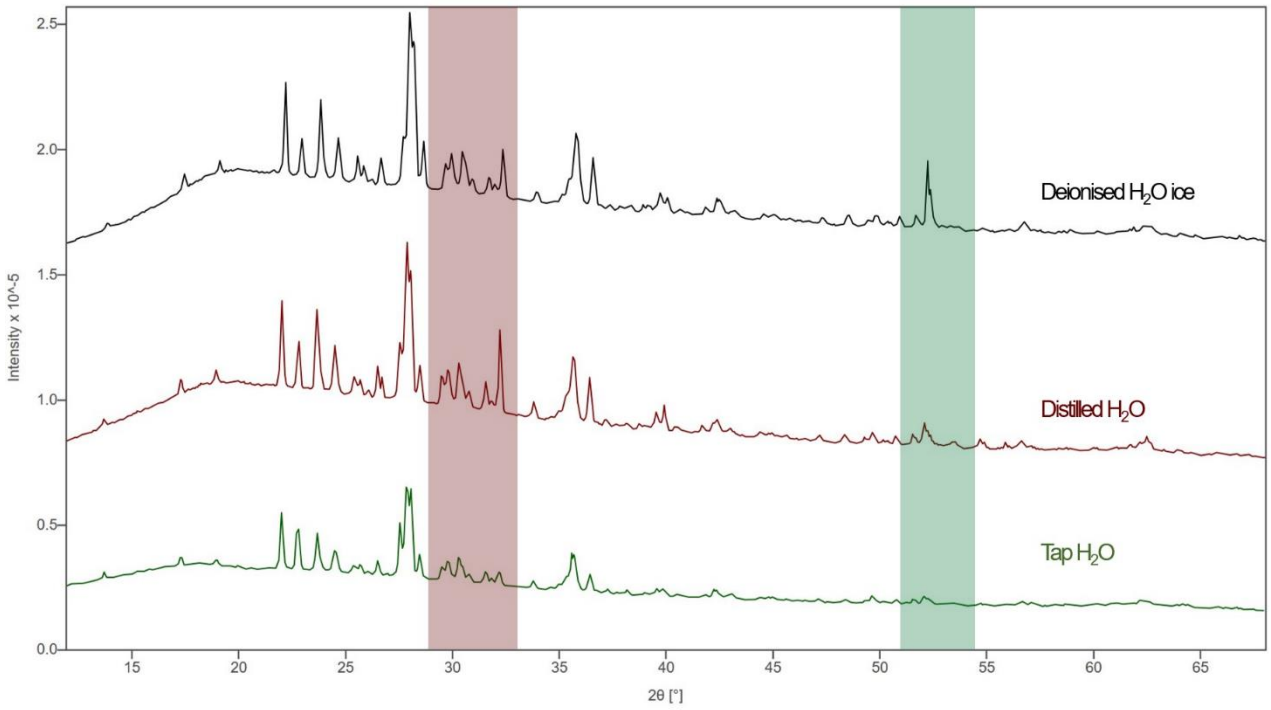

Figure 117. XRD diffractogram demonstrating the effect different water ice treatments on the mineralogy of the JSC-Lunar simulant upon milling for 10 minutes at a frequency of 10 Hz. Scan taken between to 1000 °C between 15°-65° and a run time of 3 hours. Highlighted regions illustrate noticeable variations in relative peak intensities between samples.

As illustrated in Figure 117, there was little difference observed in mineralogical structure of the JSC-Lunar simulant when comparing the effects of milling with deionised, distilled and tap water ice. Nonetheless, the incorporation of tap water ice seemed to cause a noticeable decrease in the relative peak intensities despite the same milling time, potentially suggesting the incorporation of other minerals through potential leaching of minerals into solution. Stillings *et al.* discusses the combined effect of milling and incorporation of water. It is suggested that adsorbed CO_2 within polymineralic materials such as planetary analogues is insoluble, thus minerals such as Ca^{2+} can be leached into solution, forming hydrated minerals. Stillings *et al.* also comments on the possibility that adsorbed CO_2 may weaken ionic bonds within the lattice structure, thus allowing a higher concentration of ions to be leached into solution [29].

As previously discussed in chapter 2, upon contact with the regolith material and stainless steel ball bearings, rapid melting of the water ice was observed and thus should be taken into consideration when studying collected observations and results

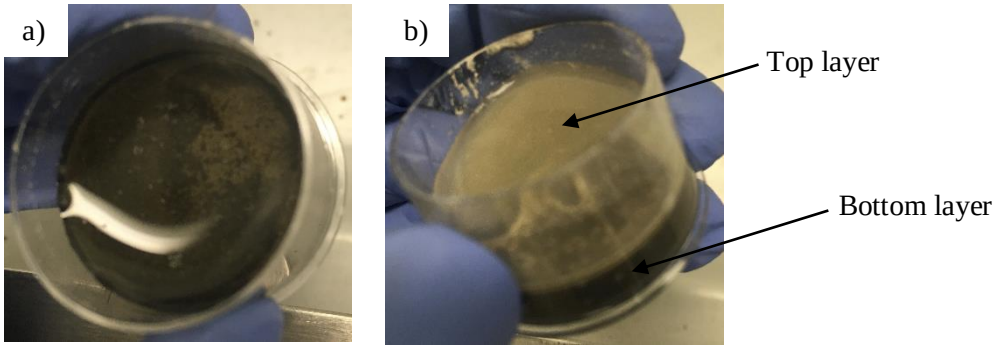

Figure 118. Photographs taken of the Earth-based JSC-Lunar simulant milled at a frequency of 10 Hz with 25 % deionised water ice for a) 2 minutes; b) 10 minutes.

As seen in Figure 118, the physical appearance of the 25 % deionised water ice 75 % JSC-Lunar regolith simulant mixture milled for a) 2 and b) 10 minutes was significantly different. 2 minutes of milling yielding a much darker, black mixture with a thin, transparent top layer which appeared to be almost entirely water situated above a layer of wet simulant, whereas 10 minutes of milling caused a greater separation of layers with the top layer observed to be more viscous and consisting of dispersed grains. A general even distribution of regolith was observed regarding both samples. On the Lunar surface, the ability for regolith to retain water may considerably affect the mineralogy of a given area found within cold traps, with varying extents of hydrated minerals present and different induced chemistry driven by hydrological reactions such as aqueous alteration.

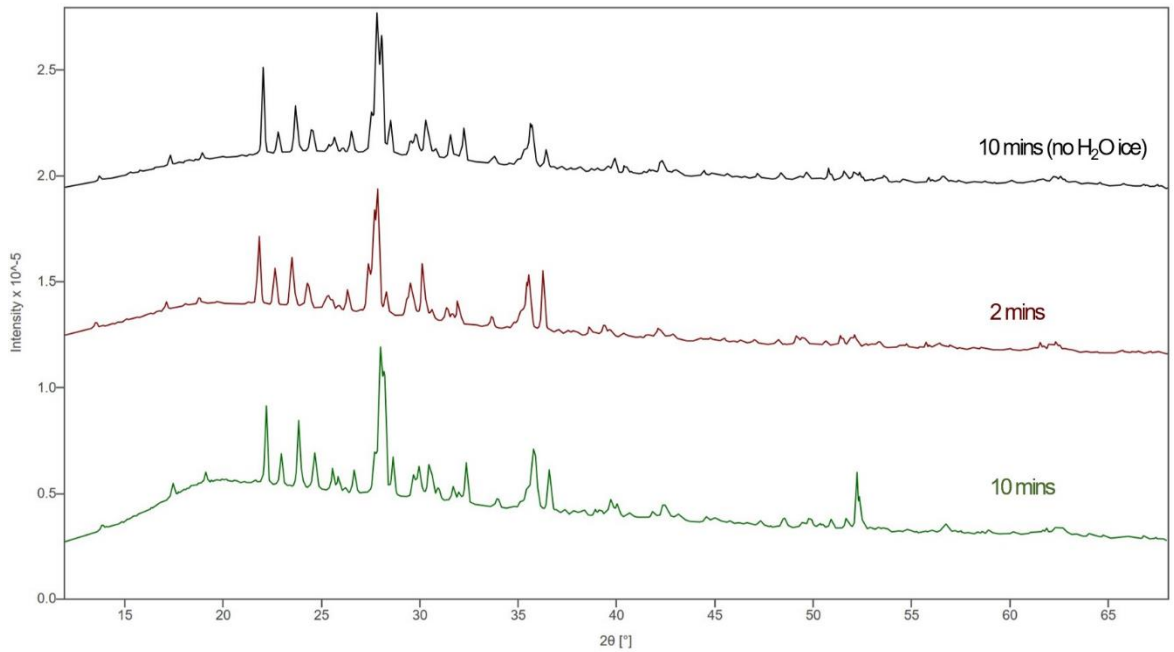

Figure 119. XRD diffractogram demonstrating the effect of milling the JSC-Lunar simulant with 25 % deionised H_2O ice on mineralogy. Scan taken between 15°-65° and a run time of 3 hours.

As observed in Figure 119, the incorporation of deionised water ice seemed to have neglible effects on the mineralogy and mineralogical structure of the Earth-based JSC-Lunar simulant. A lack of hydrated

minerals was identified by XRD analysis, where peaks characterised by hydrated minerals would possibly be indicated by a decrease in relative intensity of particular contributions, for instance calcium-silicates due to leaching and thus dissolution [29]. Longer milling times at lower temperatures may potentially be required to assess the true possible effect of water ice on the crystalline structural network. This is perhaps more likely to lead to hydrated minerals due to further integration of the regolith ice mixtures, and thus a more complete reaction between water and minerals, increasing concentration of dissolved ions such as [Ca^{2+}] and [Mg^{2+}] due to leaching [29].

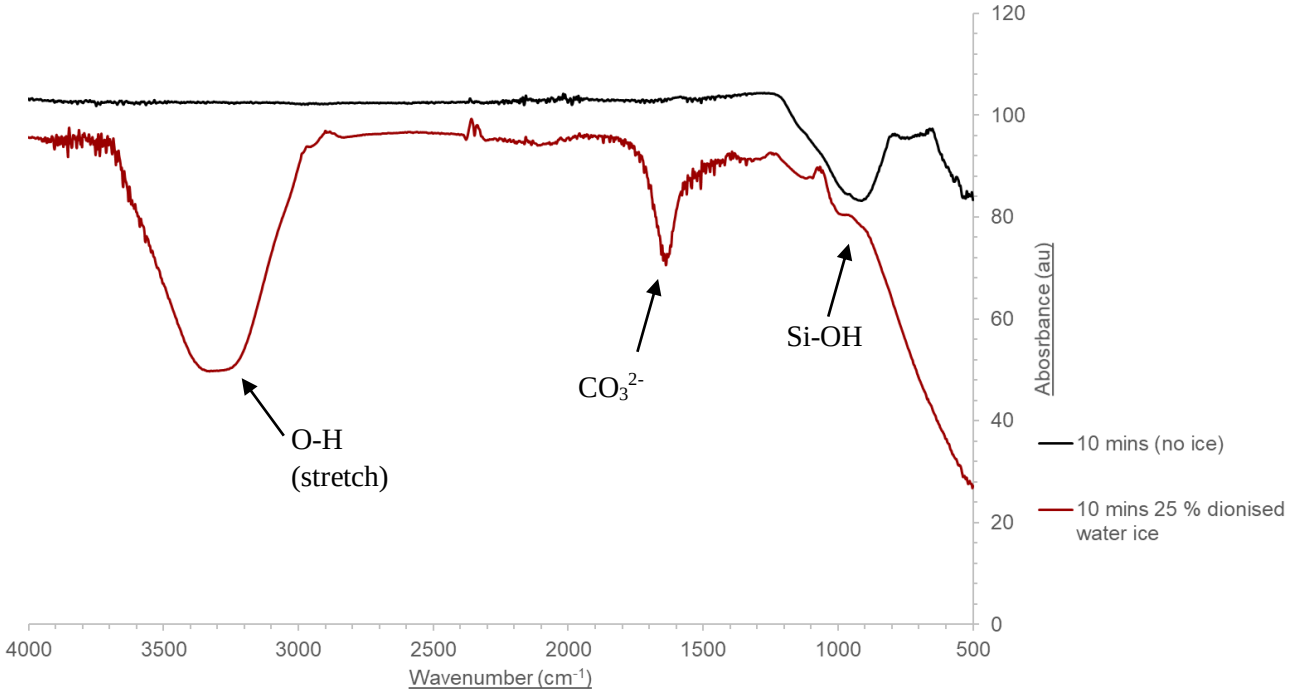

Figure 120. Infrared spectra (wavenumber range of 4000 cm^{-1}-500 cm^{-1}) assessing the effect of milling JSC-Lunar simulant with 25 % deionised water ice for 10 minutes. The incorporation of water is illustrated by the Si-OH absorbance band at ~ 950 cm^{-1}.

Infrared spectroscopy illustrated the effect of the incorporation of deionised water ice, as shown in Figure 120 by the characteristic O-H stretching band at ~ 3250 cm^{-1}. The effect of deionised water ice had on the silicate minerals found within the JSC-Lunar simulant is demonstrated by the broad band observed between 950 and 810 cm^{-1} indicating the presence of Si-OH bonds, as anticipated. The sharper, higher absorbance peak displayed at ~ 1600 cm^{-1} suggests the contribution of carbonate minerals. Numerous plausible reactions within the milling process may occur to yield such results. As reported by Stillings e*t al.*, the increased adsorption observed in infrared analysis due to milling with water ice for 10 minutes could perhaps be due to a) mechanical activation-induced lattice deformations located at mineral boundaries, causing dislocations which cause charged species and surface radicals thus lowering the activation energy needed for CO_2 adsorption, allowing cationic leaching and b) in return, cationic leaching may cause cations to react with CO_2, yielding in the precipitation of carbonates. Reaction mechanisms between O-Si-O bonds and H_2O has been reported by Zhou *et al.* suggesting the

production of H_2SiO_3 [68]. Whilst chemical reactions between inorganic cations and water has been studied, silicon dioxide chemistry has less reported literature. A general reaction scheme between Alkaline Earth Metals such as calcium and water and the production of hydrogen gas is shown below [69]:

$$M_{(s)} + 2H_2O_{(l)} \rightarrow M(OH)_{2\,(aq)} + H_{(2)\,(g)}$$

Stillings *et al.* proposes a mechanism for the production of carbonates, reported from leaching experiments conducted with granite and basalt. Work conducted suggests that when polymineralic rocks such as basalt are reacted with water, weakened bonds (and the subsequent release of ions such as Ca^{2+} and Mg^{2+} from leaching) due to CO_2 adsorption within the lattice (refer to chapter 4) are broken with more ease, thus producing aqueous carbonates [29]. As discussed previously, the lubricant behaviour of water during milling may accelerate diffusion of CO_2 to the crystal lattice interstitial areas, perhaps increasing the rate of reaction yielding in carbonates.

As an analytical technique, ATR-FTIR spectroscopy appeared to indicate more prominent effects of the incorporation of water ice and the hydroxylation of O-Si-O bonds.

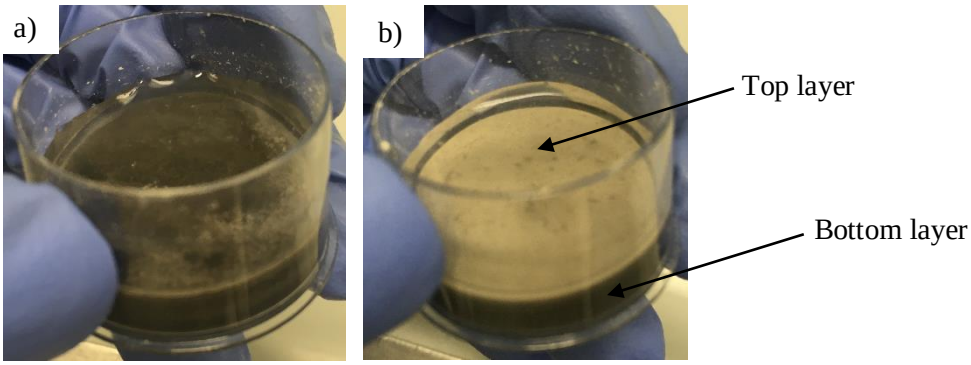

Figure 121. Photographs taken of the Earth-based JSC-Lunar simulant milled (Retsch MM301 at a frequency of 10 Hz) with 25 % tap H_2O ice for a) 2 minutes; b) 10 minutes.

As seen in Figures 121 a) and b), the physical appearance of the 25 % tap water ice 75 % JSC-Lunar regolith simulant mixture between a) 2 and b) 10 minutes was significantly different, with 2 minutes of milling yielding a much darker, black mixture with a thicker top layer in comparison to the incorporation of deionised water ice. 10 minutes of milling caused greater separation of layers, and a lighter colour at the surface. However, in comparison to the deionised water sample, milling for 10 minutes with water ice seemingly caused lighter coloured grains to settle at the top of the sample, suggesting the formation of another layer.

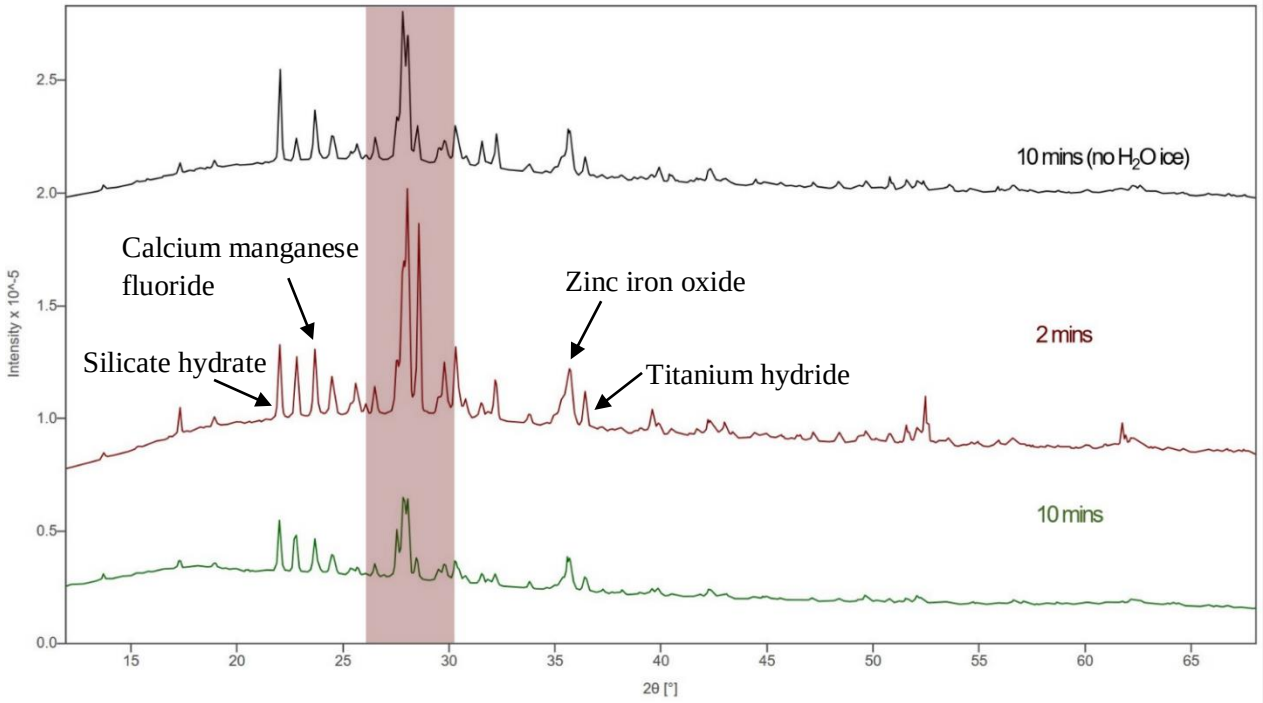

Figure 122. XRD diffractogram demonstrating the effect of milling the JSC-Lunar simulant with 25 % tap water ice. Scan taken between 15°-65° and a run time of 3 hours. Highlighted regions illustrate noticeable variations in relative peak intensities between samples.

XRD analysis shown above in Figure 122 illustrated the effect of the potential incorporation anions such as fluorides, chlorides and phosphates originating from the tap water ice within the mineralogical composition of the JSC-Lunar simulant. The addition of mineral phases such as iron fluoride hydrate and manganese fluoride phosphate (~ 28.0°) were suggested, in combination with the common feldspar mineral contributions such as sodium aluminium silicates. Calcium manganese fluoride was also potentially observed at a peak angle ~ 23.7°. Furthermore, the peak at ~ 35.6° suggested the presence of zinc iron oxide, which was considered reasonable given the tap water contained small quantities of zinc. Hydrated minerals, for instance silicate hydrate and titanium hydride were also speculated by peaks at diffraction angles of ~ 22.0° and 36.4° respectively.

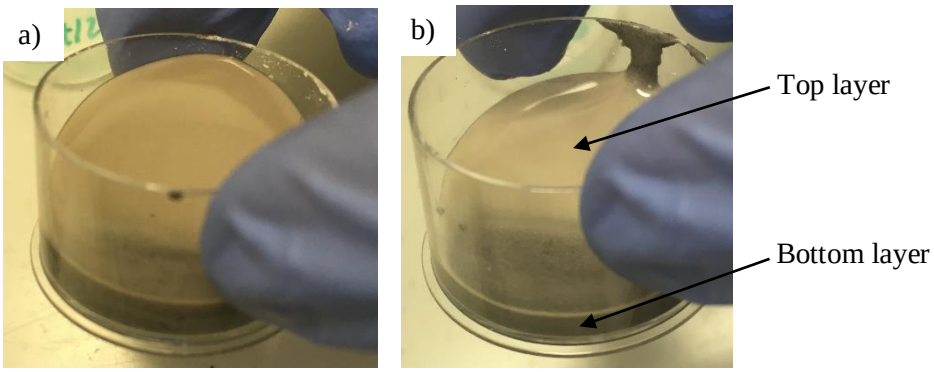

Figure 123. Images taken of the synthesised LHS-1 simulant milled (Retsch MM301 at a frequency of 10 Hz) with 25 % deionised H_2O ice for a) 2 minutes; b) 10 minutes.

As seen in Figure 123, the physical appearance of the 25 % deionised water ice 75 % LHS-1 regolith simulant mixture between a) 2 and b) 10 minutes was similar, with both milled samples possessing a noticeable top surface layer consisting of integrated regolith material, as observed by its cloudy colour.

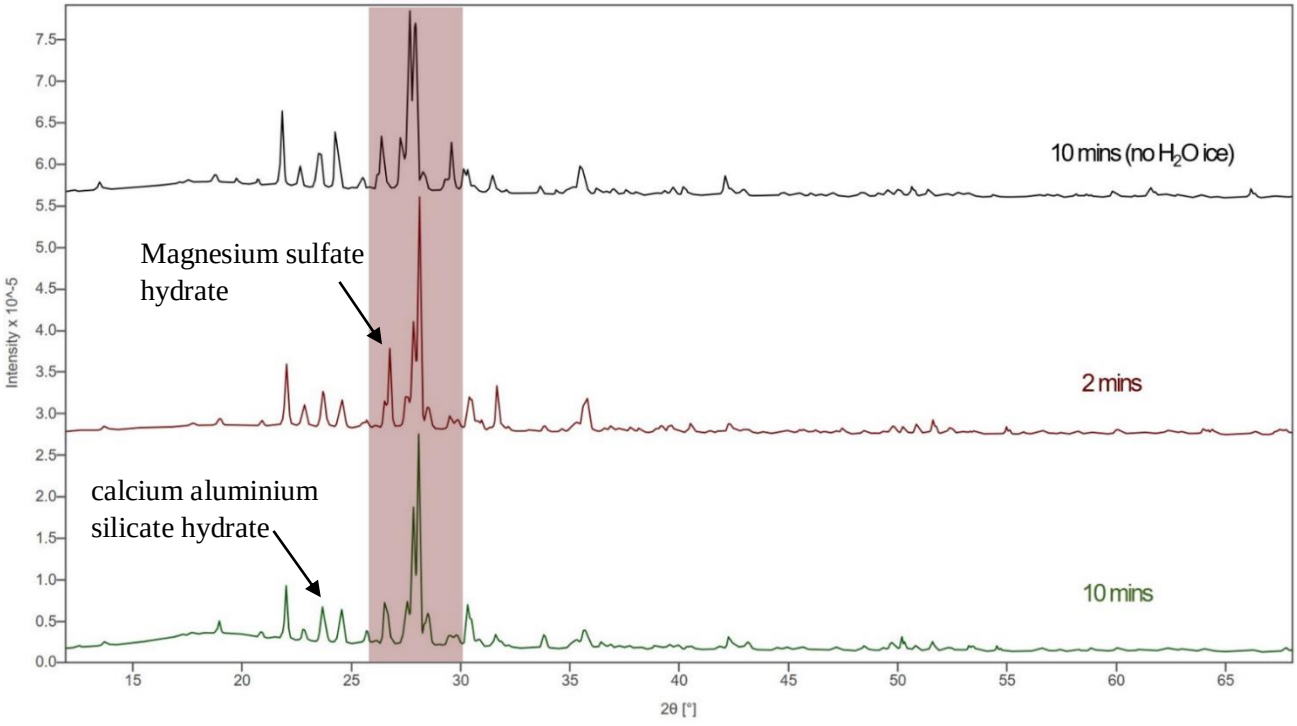

Figure 124. XRD diffractogram demonstrating the effect of milling the LHS-1 simulant with 25 % deionised H_2O ice on mineralogy. Scan taken between 15°-65° and a run time of 3 hours. Highlighted regions illustrate noticeable variations in relative peak intensities between samples.

Similarly, to the JSC-Lunar simulant, the incorporation of 25 % deionised water ice displayed little effect on the LHS-1 simulant's mineralogical structure upon milling for 2 and 10 minutes. Hydrated minerals such as magnesium sulfate hydrate and calcium aluminium silicate hydrate were potentially observed, as indicated by peak angle values of ~ 26.8° and 23.7° for both 2 and 10 minutes respectively. However, hydrated minerals were also observed in milling experiments without water ice, therefore it cannot be concluded that this potential production was water-driven.

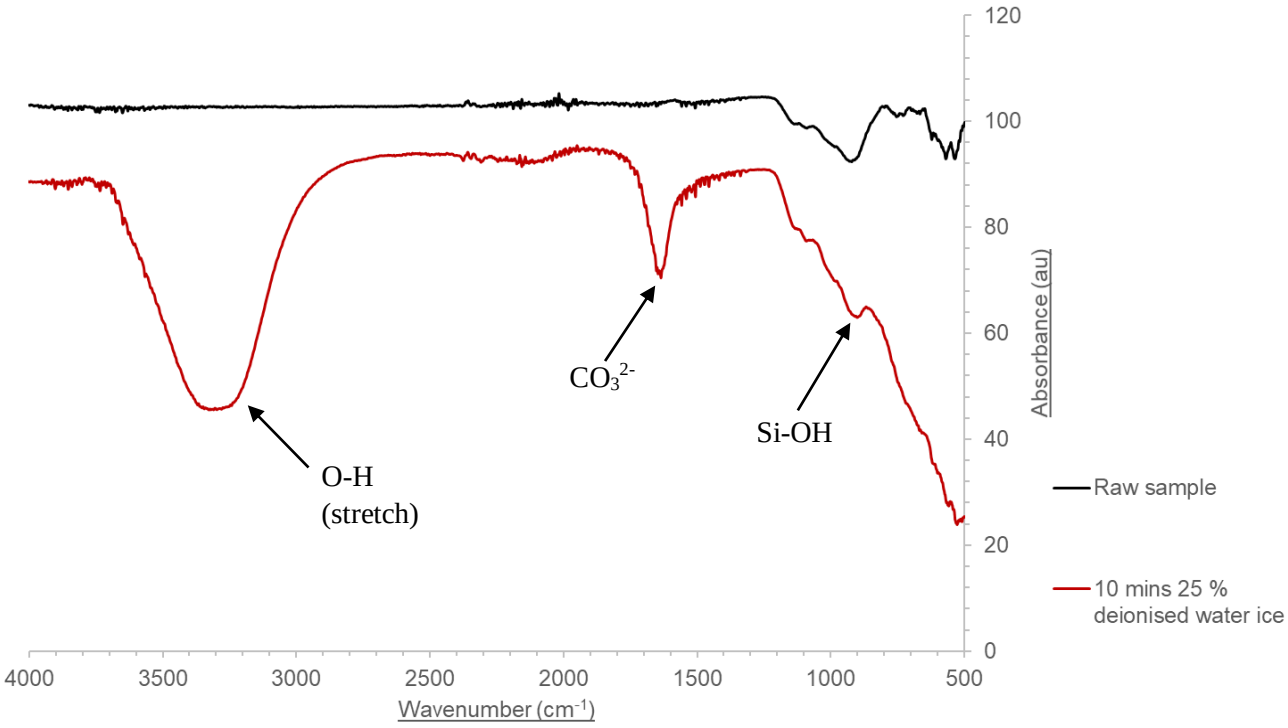

Figure 125. Infrared spectra (wavenumber range of 4000 cm^{-1}-500 cm^{-1}) assessing the effect of milling the LHS-1 simulant with 25 % deionised H_2O ice for 10 minutes on chemical composition. The incorporation of water is illustrated by the Si-OH absorbance band at ~ 950 cm^{-1}.

Infrared spectroscopy illustrated the effect of the incorporation of deionised water ice, as shown in Figure 125 above. No significant/notable differences in water-driven chemistry were observed between the Earth-based JSC-Lunar simulant and the synthesised LHS-1 simulant, apart from the broader Si-OH band.

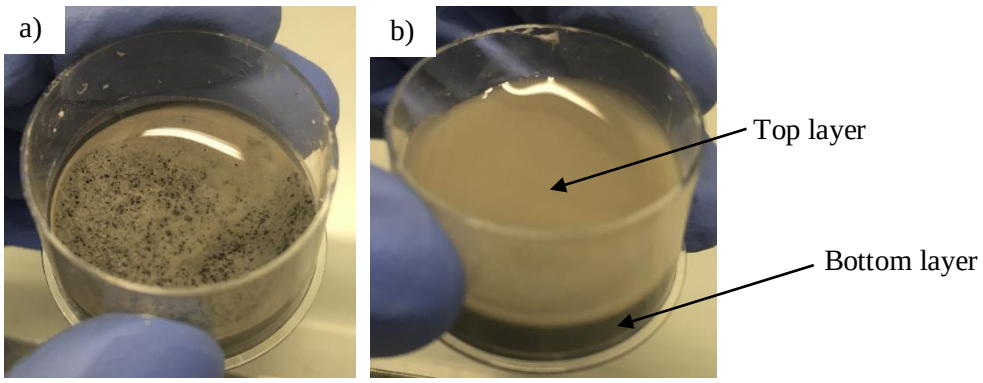

Figure 126. Photographs taken of the synthesised LHS-1 simulant milled (Retsch MM301 at a frequency of 10 Hz) with 25 % tap H_2O ice for a) 2 minutes; b) 10 minutes.

As seen in Figure 126, the physical appearance of the 25 % tap water ice 75 % LHS-1 regolith simulant mixture between a) 2 and b) 10 minutes was very different, with 2 minutes of milling displaying a noticeable grain-like texture perhaps due to larger grains not incorporating as much water into their crystalline structures in comparison to 10 minutes of milling, whereby the top layer of liquid is more prominent.

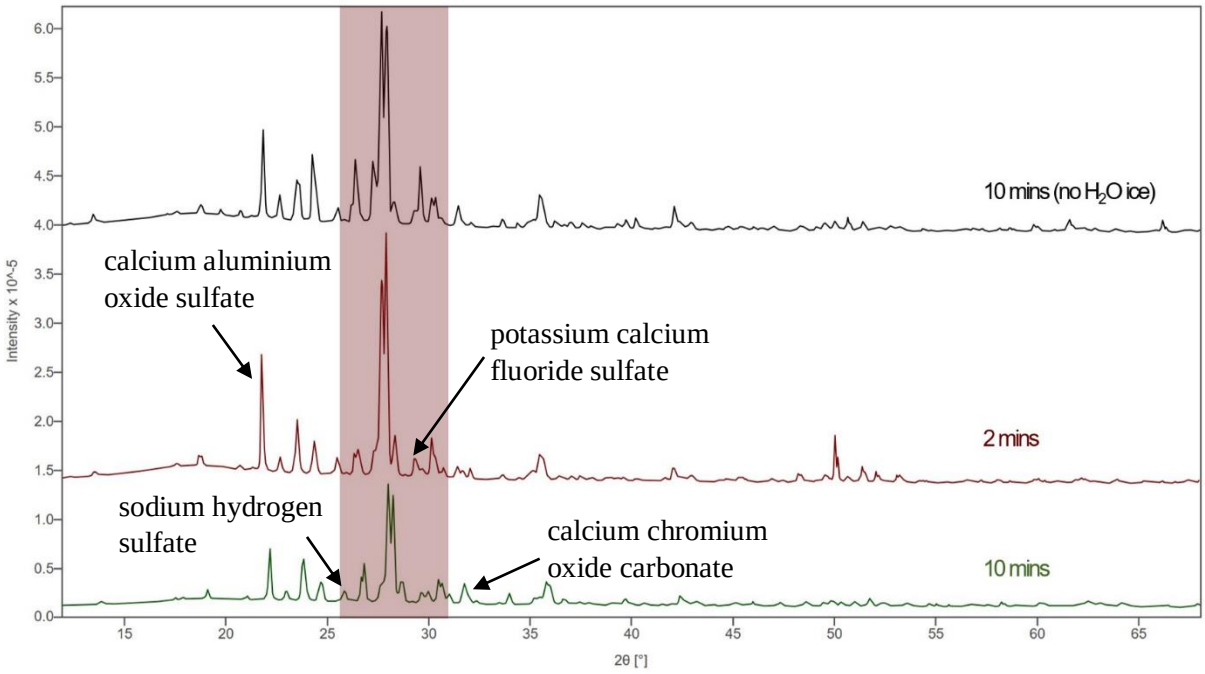

Figure 127. XRD diffractogram demonstrating the effect of milling the LHS-1 simulant with 25 % tap H_2O ice on mineralogy. Scan taken between 15°-65° and a run time of 3 hours. Highlighted regions illustrate noticeable variations in relative peak intensities between samples.

The incorporation of 25 % tap water ice appeared to have the most noticeable effect on mineralogical composition of the LHS-1 simulant, as illustrated above in Figure 127. Most notably, 10 minutes of milling potentially produced calcium chromium oxide carbonate, as indicated by the peak at ~ 30.5°.

Sulfates such as calcium aluminium oxide sulfate, sodium hydrogen sulfate, and potassium calcium fluoride sulfate were suggested by diffraction peaks at angles of ~ 23.8°, 26.8° and 28.0° respectively. A relatively high abundance of zinc-based mineral contributions were also potentially observed, including calcium zinc silicate, lithium zinc oxide, and zinc oxide sulfate, characterised by peaks angles of ~ 29.8°, 23.9° and 35.8° respectively.

All of the Lunar simulant samples formed two distinct layers upon milling the regolith-ice mixtures for and 2 and 10 minutes. The top and bottom layers of the LHS-1 extractions were sampled and examined by ATR-FTIR to examine any potential differences in chemistry, as shown in Figure 128 below. Only subtle differences were identified in the spectral region between 850 to 1200 cm^{-1}, potentially indicating a slightly lower abundance of non-hydrated silicates within the bottom layer. This suggests whilst this separation of layers is not primarily chemistry-driven, it may be caused by differences in grain size distribution (i.e. a physical property), with smaller grains present as a suspension at the top, and larger, coarser grains and particulates settling at the bottom as a precipitate.

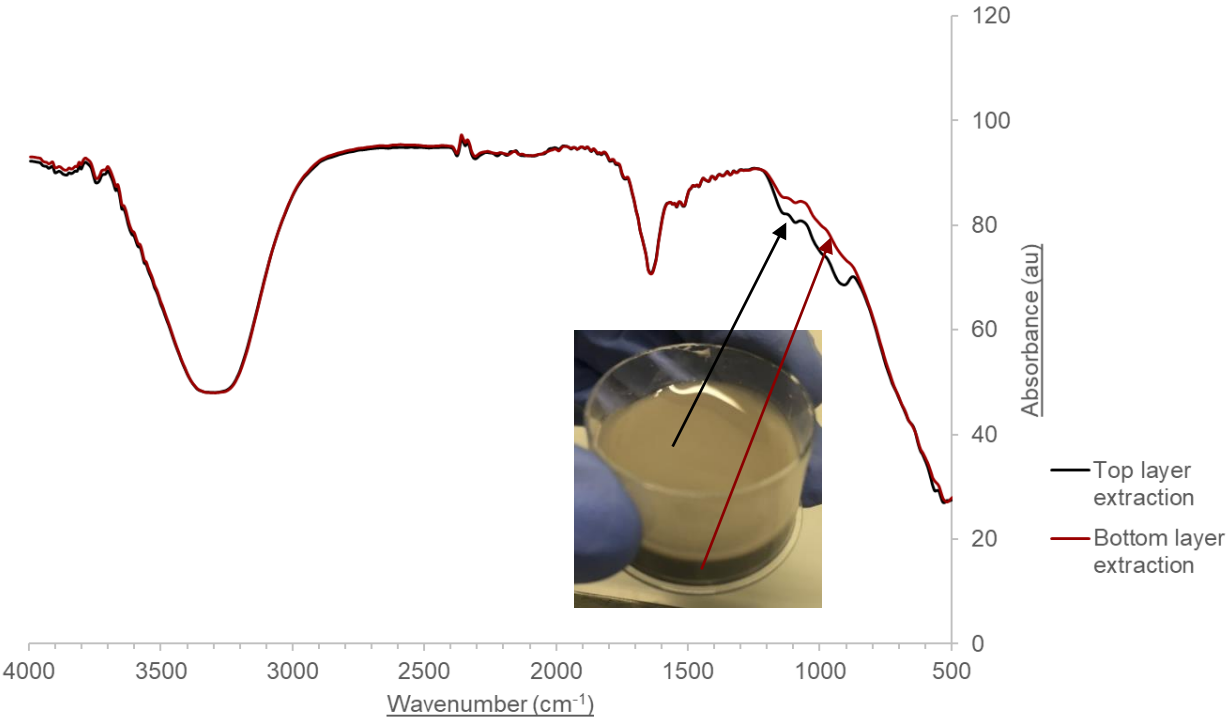

Figure 128. Infrared spectra of the 25 % tap H_2O ice 75 % LHS-1 simulant mixture upon milling for 10 minutes at a frequency of 10 Hz (Retsch MM301 mixer mill) comparing the chemical composition of the top and bottom layer extractions. Insignificant variations in induced chemistry can be observed.

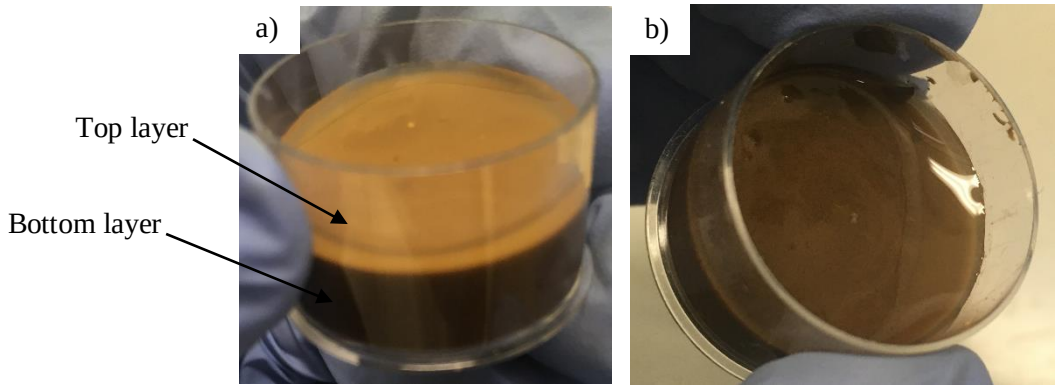

Figure 129. Photographs taken of the Earth-based JSC-Martian simulant milled (Retsch MM301 at a frequency of 10 Hz) with 25 % deionised H_2O ice for a) 2 minutes; b) 10 minutes.

As seen in Figure 129, the physical appearance of the 25 % deionised water ice 75 % JSC-Martian regolith simulant mixture between a) 2 and b) 10 minutes was notably different, with 2 minutes of milling more obviously demonstrating two distinct layers. However, in contrast to previously discussed physical properties, milling for 10 minutes displayed a less watery-texture, potentially suggesting greater retention of water due to smaller grain sizes and thus greater specific surface area. Previous analysis showed the hygroscopic nature of the Earth-based JSC-Martian simulant (as discussed in chapter 3), therefore suggesting greater incorporation of water due to environmental laboratory conditions.

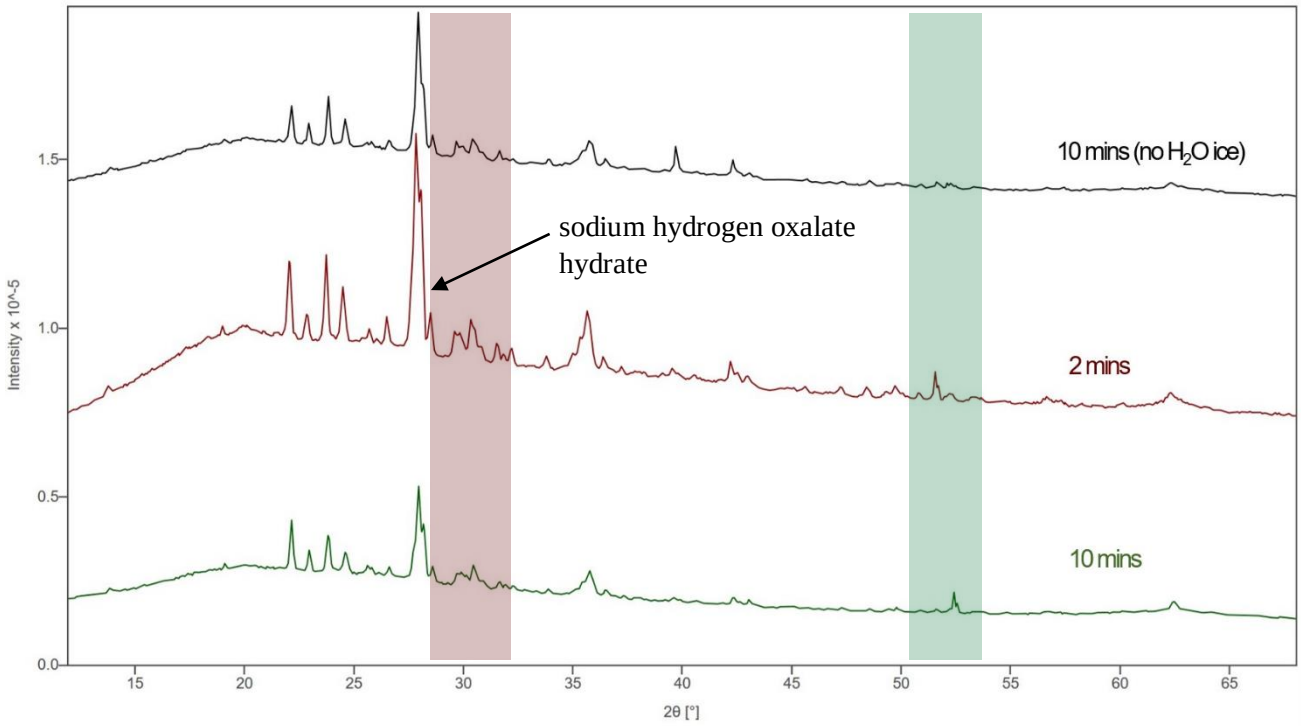

Figure 130. XRD diffractogram demonstrating the effect of milling the JSC-Martian simulant with 25 % deionised H_2O ice on mineralogy. Scan taken between 15°-65° and a run time of 3 hours. Highlighted regions illustrate noticeable variations in relative peak intensities between samples.

As illustrated in Figure 130 above, the incorporation of deionised H_2O ice seemed to have little effect on the mineralogical structure of the Earth-based JSC-Martian simulant. It is important to note the slight shift in diffractogram angle for the regolith-ice sample milled for 2 minutes, perhaps due to instrument or experimental error. Hydrated minerals such as sodium hydrogen oxalate hydrate indicated by the peak angle of ~ 29.7° were likely present, as also observed prior to milling with water ice.

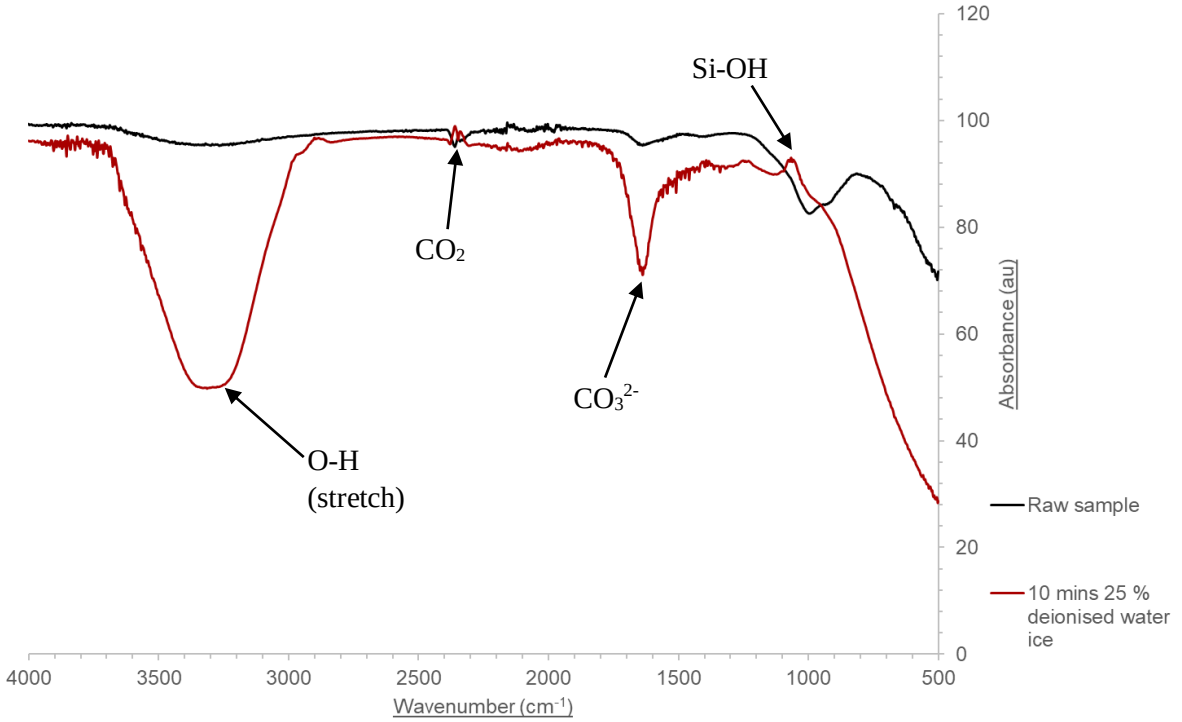

Figure 131. Infrared spectra (wavenumber range of 4000 cm^{-1}-500 cm^{-1}) assessing the effect of milling the JSC-Martian simulant with 25 % deionised H_2O ice for 10 minutes on chemical composition. Carbonate contributions can be seen due to the CO_3^{2-} absorbance band at ~ 1500 cm^{-1}.

Infrared spectroscopy illustrated a similar effect of the incorporation of deionised H_2O ice as discussed previously, as shown in Figure 131 above by the characteristic O-H (stretch) peak at ~ 3250 cm^{-1}. However, the addition of water ice caused a noticeable change in the state of the Si-OH bond vibration. The characteristic CO_2 peak was observed at ~ 2400 cm^{-1}, however again a change in state was observed.

Figure 132. Photograph taken of the Earth-based JSC-Martian simulant milled (Retsch MM301 at a frequency of 10 Hz) with 25 % tap H_2O ice for 10 minutes.

Figure 132 shown above illustrates the thick, paste-like texture and appearance of the JSC-Martian simulant after milling for 10 minutes with 25 % tap water ice. There was no separating and subsequent settling of layers observed unlike previously discussed regolith-ice mixtures, perhaps suggesting a more even distribution of regolith from mineral-water interactions.

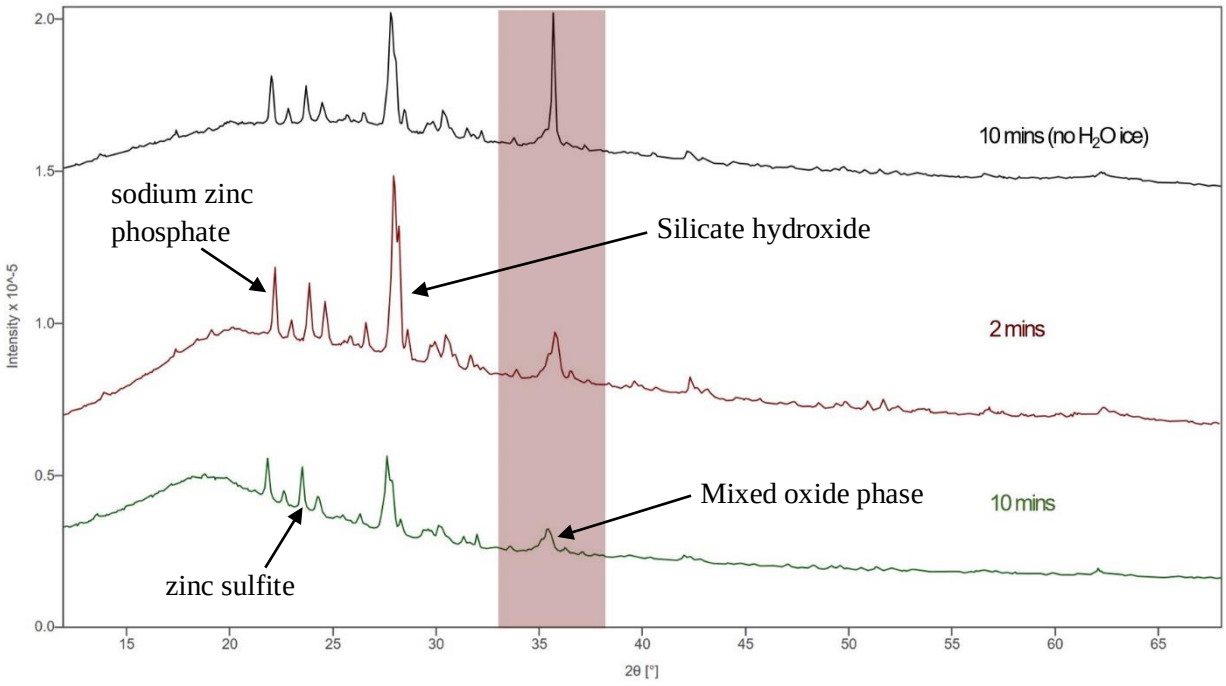

Figure 133. XRD diffractogram demonstrating the effect of milling the JSC-Martian simulant with 25 % tap H_2O ice on mineralogy. Scan taken between 15°-65° and a run time of 3 hours. Highlighted regions illustrate noticeable variations in relative peak intensities between samples.

The insertion of fluorides and zinc based minerals was suggested by XRD analysis of the 75 % JSC-Martian simulant – 25 % tap ice mixture, as presented in Figure 133 above. The sharp decline in peak intensity at ~ 35.8° as shown highlighted in Figure 133 was characterised by the potential contribution of a mixed oxide phase comprising of zinc titanium oxide, zinc manganese iron oxide, manganese chromium oxide, sodium zinc phosphate, calcium zinc sulfate, calcium iron oxide and iron titanium oxide. This peak analysis demonstrates the possible incorporation of minerals such as fluorides, and how they react with pre-existing primary and secondary minerals within the regolith material. Silicate hydroxide was suggested by the main feldspar-characteristic peak at ~ 27.9°, indicating hydroxylation of SiO_2 and Si-based minerals. Other zinc composing minerals, namely sodium zinc phosphate and zinc sulfite were perhaps indicated by diffraction angle values of ~ 22.2° and 24.7°.

Another example of the separation of layers upon milling with ice is shown in Figure 134, however, the Earth-based JSC-Martian simulant displayed a less noticeable difference in its physical appearance subsequent to milling, perhaps due to a smaller grain size distribution and thus a more even uptake of water. Two different water ice treatments (tap and deionised) have been shown to provide a variety of examples. This physical property is essential in order to understand the existence of water ice on the Lunar and Martian surface, and the potential difference in grain densities and regolith distribution within soil-ice mixtures and seasonal sublimation and deposition of water ices. Despite showing a lack in distinct chemistry, with more precise XRD analysis, there could be a different in crystalline phases and mineralogical structure depending on the area of extraction of the sample.

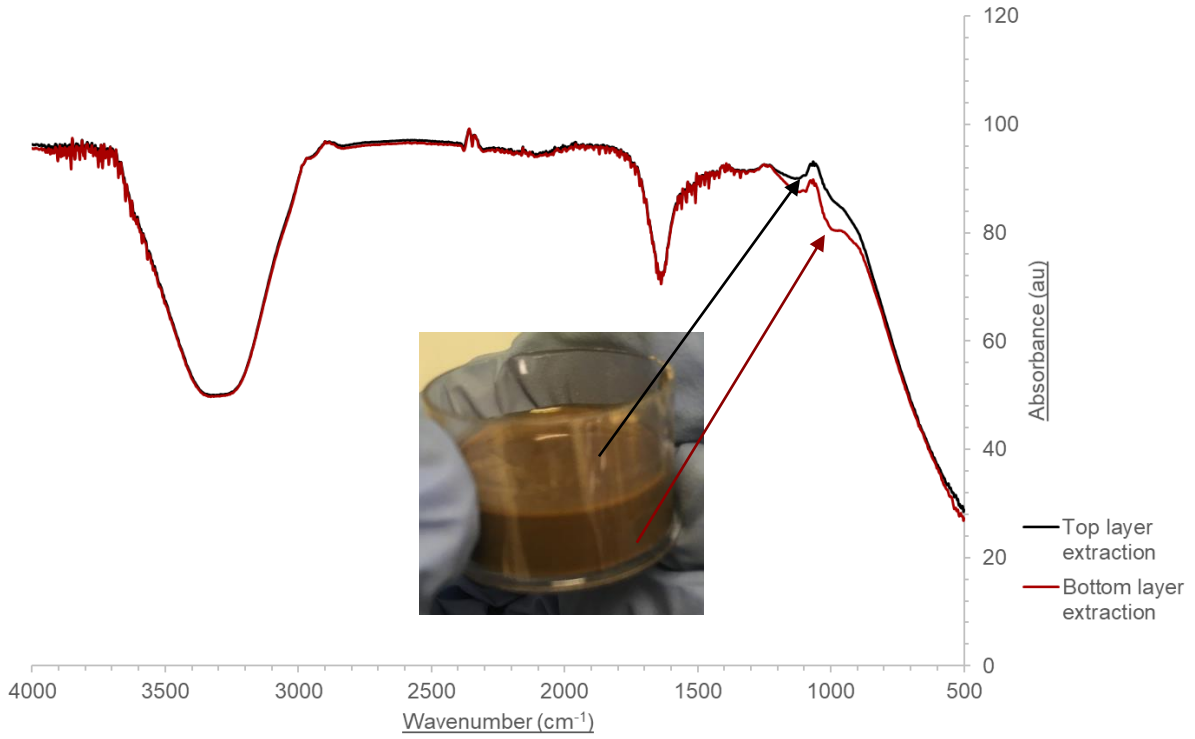

Figure 134. Infrared spectrum of the 25 % deionised H_2O ice 75 % JSC-Martian simulant mixture upon milling for 10 minutes at a frequency of 10 Hz (Retsch MM301 mixer mill) comparing the chemical composition of the top and bottom layer extractions. Insignificant variations in induced chemistry can be observed.

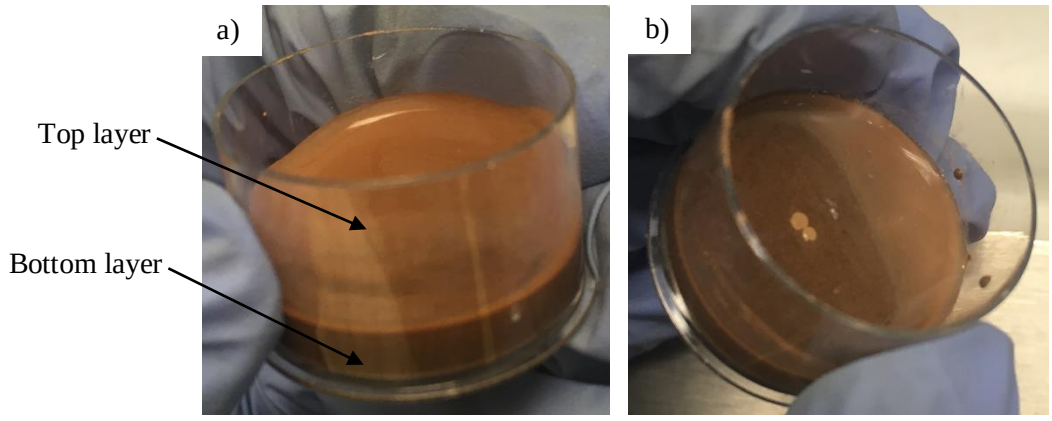

Figure 135. Photographs taken of the synthesised MGS-1 simulant milled (Retsch MM301 at a frequency of 10 Hz) with 25 % deionised H_2O ice for a) 2 minutes; b) 10 minutes.

As seen in Figure 135 above, the physical appearance of the 25 % deionised H_2O ice 75 % MGS-1 regolith simulant mixture between a) 2 and b) 10 minutes was not significantly different, with 2 minutes of milling only showing a slightly more watery top surface layer, and is lighter in colour and orange hued. Upon milling MGS-1 for 10 minutes, it's clumpy, cement-like appearance and texture (as discussed in chapter 3) may increase retention of water.

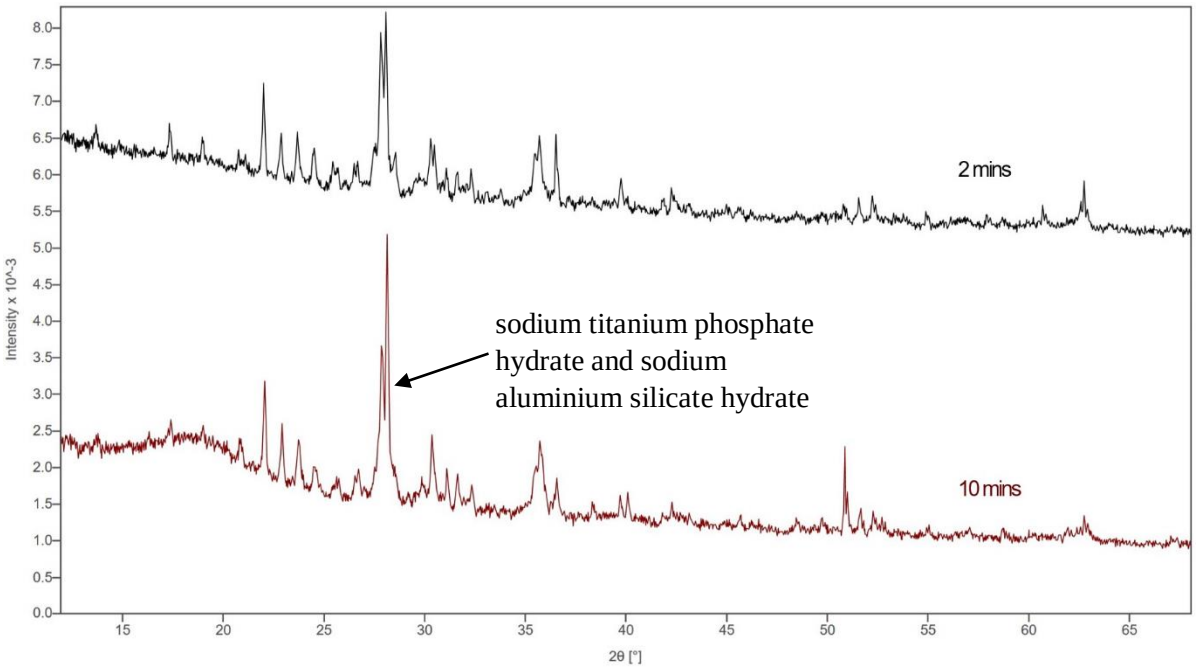

Figure 136. XRD diffractogram demonstrating the effect of milling the MGS-1 simulant with 25 % deionised H_2O ice on mineralogy. Scan taken between 15°-65° and a run time of 3 hours.

Deionised H_2O ice seemed to have little effect on the mineralogical structure and composition of the synthesised MGS-1 simulant, as observed in Figure 136 above. However, and in contrast to the other three simulants discussed previously, the main characteristic peak for feldspar contributions at ~ 28.1° seemed to alter slightly between 2 and 10 minutes of milling. Hydrated minerals, for instance sodium titanium phosphate hydrate and sodium aluminium silicate hydrate were indicated by this diffraction angle value, however, were possibly minerals present prior to milling with deionised water ice.

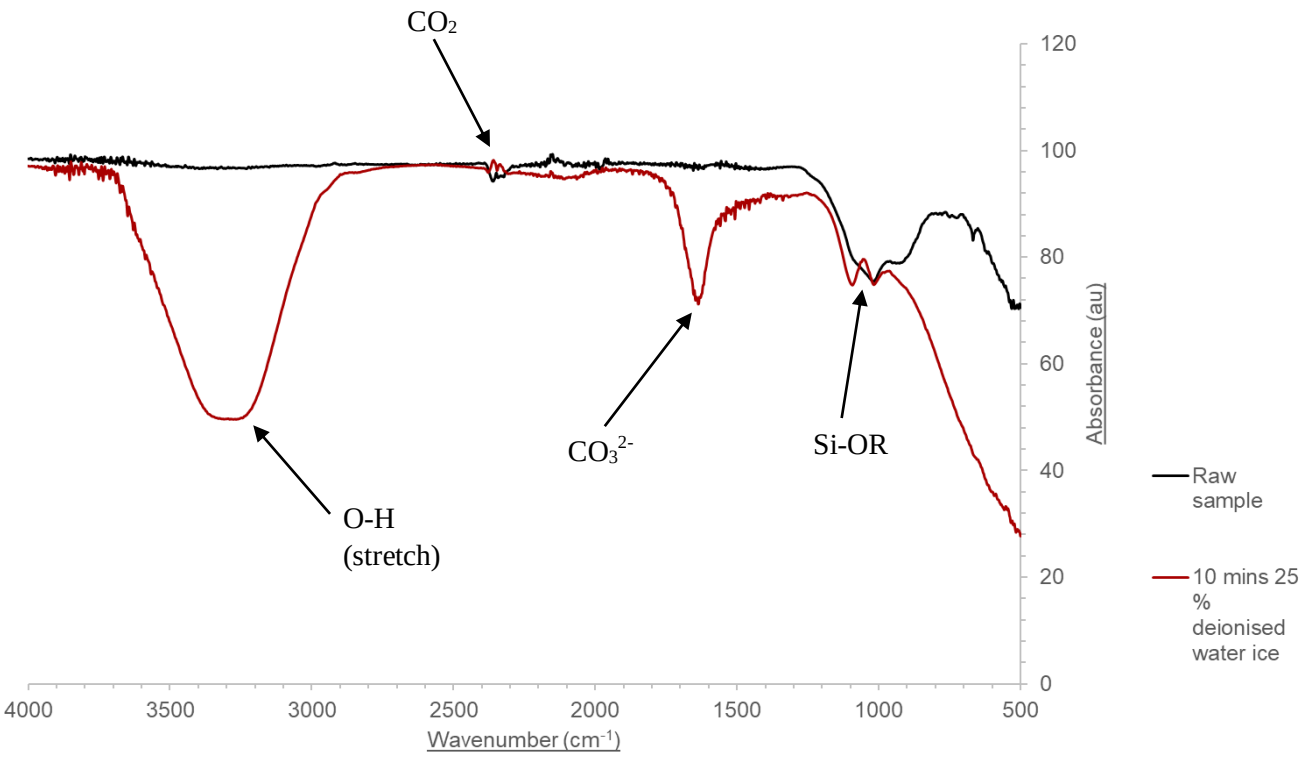

Figure 137. Infrared spectrum (wavenumber range of 4000 cm^{-1}-500 cm^{-1}) assessing the effect of milling the MGS-1 simulant with 25 % deionised H_2O ice for 10 minutes on chemical composition. Si-OR contributions are suggested by the doublet absorbance peak at ~ 950 cm^{-1}.

Infrared spectroscopy analysis illustrated the effect of the incorporation of deionised H_2O ice, as shown in Figure 137 above by the characteristic O-H (stretch) peak at ~ 3250 cm^{-1}. The effect of deionised H_2O ice on the silicate minerals found within the MGS-1 simulant is demonstrated by the doublet peak observed at ~ 950 cm^{-1} indicating the presence of Si-OR [46] bonds. The sharper, higher absorbance peak displayed at ~ 1600 cm^{-1} suggests the contribution of carbonate minerals (CO_3^{2-}). In a similar manner to the Earth-based JSC-Martian simulant, the presence of CO_2 was indicated by the characteristic doublet peak at ~ 2400 cm^{-1}, however was present as an altered state again.

Figure 138. Photograph taken of the synthesised MGS-1 simulant milled (Retsch MM301 at a frequency of 10 Hz) with 25 % tap H_2O ice for 10 minutes.

Figure 138 shown above illustrates the slightly paste-like and grainy texture and appearance of the MGS-1 simulant after milling for 10 minutes with 25 % tap H_2O ice. Similarly, to the LHS-1 simulant, this grainy texture may be due to a less homogenous sample in comparison to the Earth-based simulants, and thus an uneven distribution of regolith within the mixture.

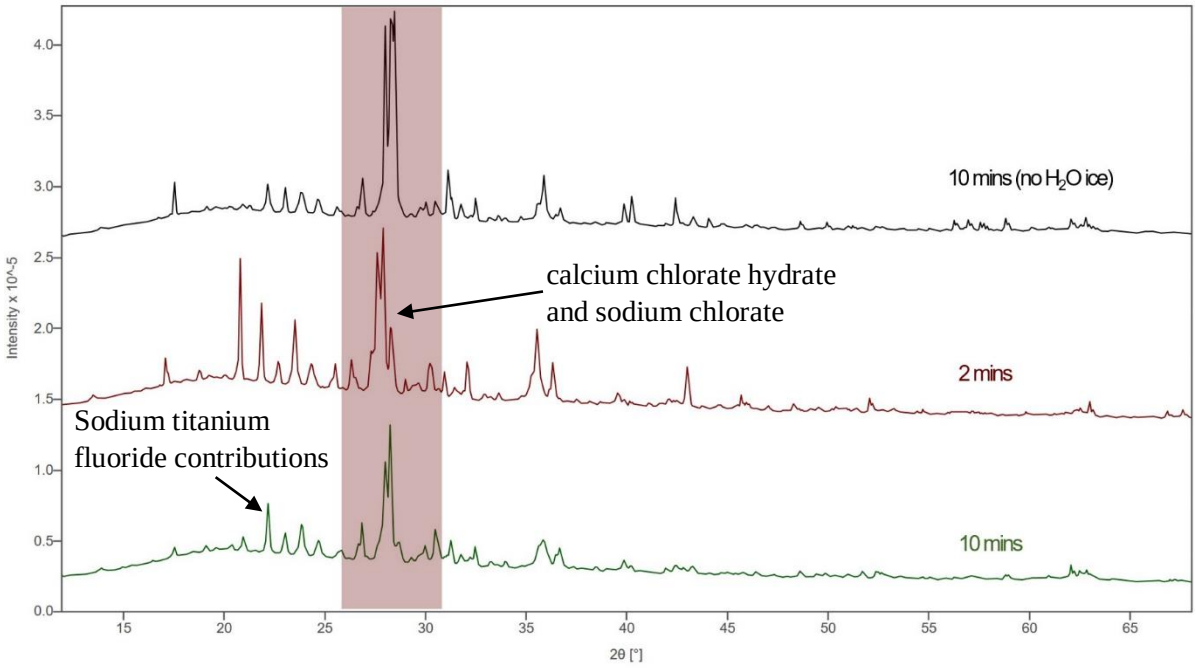

Figure 139. XRD diffractogram demonstrating the effect of milling the MGS-1 simulant with 25 % tap H_2O ice on mineralogy. Scan taken between 15°-65° and a run time of 3 hours. Highlighted regions illustrate noticeable variations in relative peak intensities between samples.

The effect of milling the synthesised MGS-1 simulant with 25 % tap H_2O ice was indicated by XRD analysis. As illustrated in Figure 139 above, in addition to fluoride and zinc-based minerals, the incorporation of chloride-based minerals was also suggested. This is particularly timely considering current research investigating the presence of chlorides on the Martian surface, for instance deposits of chloride salts when analysing the historic hydrological cycle on Mars. These salts would have dissolved rapidly, therefore providing a latest record for the presence of water in Martian history [70]. As the MGS-1 simulant represents an average composition of the surface, this could be very representative upon extended and more thorough analysis. The characteristic feldspar peak at ~ 27.9° suggested the presence of calcium chlorate hydrate and sodium chlorate, within the same phase as zinc magnesium sulfate and numerous other oxides present prior to regolith-ice milling experiments. Sodium titanium fluoride contributions were potentially indicated by the peak value of ~ 22.7°.

6.3 Summary and Conclusions

The incorporation of water ice has shown the introduction of hydrated minerals, for instance sodium aluminium silicate hydrates within the planetary analogues utilised during experiments. The manner of integration is required to be studied further, however, to assess where the water molecules are situated and whether this is in between the crystalline layers or elsewhere within the lattice structure. Additionally, the ability to sustain the water ice being incorporated must be implemented in future experiments to ensure chemistry is ice-driven, and not by water in its liquid state. Despite little variation in results depending on water treatment, the invaluable findings within this chapter include the clear observed water-driven alterations in mineralogy and induced chemistry, in particular the hydroxylation of silicate minerals and formation of carbonates shown by infrared spectroscopy analysis. As discussed in chapter 3, mechanical activation by means of milling causes the generation of surface radicals and charged grains, which is speculated to enable easier diffusion of CO_2 into lattice interstitial areas due to a lower activation energy (E_a) required for chemical adsorption. This integration of CO_2 weakens ionic bonds within the lattice, causing the leaching of ions such as Ca^{2+} into solution, subsequently leading to their hydration and thus the formation of hydrated minerals [29].

This is of significant relevance when interpreting the Lunar and Martian plains consisting of water ice deposits, and the existence of water on the Martian surface ~ 4 billion years ago. Through simulating potential induced chemical changes due to the presence of water ice, results can assist in the interpretation of regolith and its chemical properties during space exploration when comparing samples recovered from planetary plains such as Gale Crater compared to the polar ice caps on the Martian surface, or cold traps in comparison to the higher latitudinal areas on the Moon. Not just solely the presence and effects of water ice, but its transport alongside regolith from one plain to another and the induced chemical changes are invaluable environmental conditions to simulate on Earth in order to understand seasonal effects on the Lunar and Martian surface.

Chapter 6: Conclusions and Future Research

6.1 Primary Research Objectives

Despite ongoing examinations of planetary analogues and PFAs [1], the research presented in this thesis concerns the use of ball-milling techniques to examine mechanochemical-driven modifications in the chemistry and mineralogy of the Lunar and Martian surface due to regolith transport (including regolith ice mixtures) and thus environmental collisional impact processes within a relatively unexplored field. It has demonstrated the importance of experimental research comparing planetary analogues and illustrated how simulating small-scale regolith abrasion through mechanochemical techniques can be used to examine modification of planetary analogues and assist interpretations from current and upcoming space missions that retrieve and/or analyse Lunar and Martian regolith. Whilst it should be noted that ball milling for specific times may achieve smaller, finer grain sizes in comparison to environmental processes such as weathering, due to the mode of action and its associated energy, it still presents a viable laboratory technique for preliminary characterisation and analysing alterations at the macro and microscale. Assessing mechanochemical-induced alterations of these analogues and their physical, chemical and mineralogical properties has proved invaluable by allowing a direct comparison between Earth-based and synthetic simulants.

Space missions provide invaluable insight into the composition and environment of the Lunar and Martian surfaces, for instance the detection of chlorobenzene and dichloroalkanes in the Sheepbed Mudstone in Gale Crater on the surface of Mars through the employment of the Sample Analysis at Mars (SAM) instrument onboard Curiosity [70] and the recent discovery of hydrated minerals on the sunlit regions of the Moon through sample return from the Chang'e-5 mission [19]. Laboratory experiments allow more in depth investigations into the underlying processes that may have led to the production of these compounds, providing essential complementary information that informs future analyses and missions. It is therefore curious that despite the oxidising nature of both the Lunar and Martian surfaces due to aqueous alteration between water and mechanically activated mineral surfaces, being well known for some time [6], the effects of regolith transport and subsequent collisional processing on its chemistry and mineralogical composition have only very recently been experimentally investigated.

Assessing the effects of abrasion through regolith transport is immensely timely, as the investigation of extraterrestrial bodies continues to enhance understanding of not only environmental processes on planetary surfaces (and how they differ from Earth), but also their potential capability for habitability. Furthermore, an awareness of their environmental hazards, such as toxicity, when preparing for space missions is critical. Novel comparisons between Earth-based and synthetic analogues, like those carried

out within this work, are therefore essential for the development of accurate planetary analogues for terrestrial experimentation. The work shown in this thesis illustrates how milling processes were employed to not only simulate abrasion occurring on planetary surfaces on a small scale, but in addition to assessing the difference in behaviour between Earth-based and synthetic analogues when subjected to identical milling conditions, thus assisting in the development of planetary analogues for terrestrial utilisation.

6.2 Earth-Based and Synthetic Planetary Analogues

The results presented in this work demonstrated clear and significant observational variations between the Earth-based (JSC-Lunar and JSC-Martian) and synthetic (LHS-1 and MGS-1) simulants. In particular, several physical alterations were observed, including the mechanochemical-induced agglomeration of grains within the LHS-1 and MGS-1 analogues in comparison to the finer grains of the Earth-based materials. Such observations may provide a basis for direct, simple comparisons between analogue materials and regolith acquired through sample return missions. Considering the chemistry and mineralogy of the simulants, the production of secondary minerals has been speculated due to XRD analysis suggesting the contribution of phases such as potassium hydrogen carbonates and Si-O-M^+ bands within FTIR spectra. It is important to note that Earth-based analogues were naturally weathered and affected by a plethora of potential environmental conditions such as thermal radiation prior to these experiments, whereas synthetic analogues were produced by the blending of individual minerals. Therefore, analogues such as JSC-Lunar will have already been subjected to abrasion-induced chemical alterations. This may be considered advantageous, however, as samples recovered from planetary surfaces will not be in their raw, unaltered form. Despite the apparent effect of ball-milling on the chemical and mineralogical properties of the synthetic simulants, it is possible the Earth-based simulants are more representative of the Lunar and Martian surfaces, due to their natural incorporation of relevant minerals and oxide phases. On the other hand, synthesised analogues could be considered more functional, as directed synthesis allows incorporation of the exact compounds known to be present on the Moon and Mars through data interpretation from space missions.

Differences in behaviour upon identical experimental milling conditions have been reported in this study between the Earth-based and synthetic analogues, with more noticeable modifications in chemistry displayed for the LHS-1 and MGS-1 simulants due to mechanochemical activation. Regarding physical properties, clearer effects on texture and morphology were additionally observed, as seen previously reported with grains adhering to one another and cement-like appearances. This may suggest that the synthetic simulants are indeed more suitable for future experimental work, as their raw, un-weathered form indicates more concise observations and could be used to simulate abrasion and its subsequent effects on regolith composition with greater confidence. Sustainability of Earth-based and

synthetic planetary analogues must also be considered, however it is not clear as to which is more environmentally friendly, as the sourcing of both materials requires a great input of energy and apparatus.

Despite preliminary characterisation of the regolith analogues' constituent minerals, a necessary element of future work should be additional milling experiments involving the individual minerals, and a subsequent grain size analysis via sieving. Assessing the effects of abrasion on the constituent components of the simulants will thus enable more tailored and accurate analyses to be drawn when observing the effects of milling, through the understanding of individual mineral behaviour and mechanochemically-induced activation of specific reaction pathways.

This thesis also provided a preliminary analysis comparing potential differences in induced chemical changes when employing different ball mill apparatus. Due to little/insignificant differences seen when utilising the Retsch MM301 mixer mill, Fritsch P23 mini mixer and P7 planetary micromill, it is extremely important that future work incorporates longer milling times, (perhaps up to an hour) rather than a maximum of 10 minutes. Shorter milling times were appropriate for preliminary characterisations, however, in order to simulate abrasion occurring on the Lunar and Martian surface, longer running times are required to examine the extremities of abrasion potentially occurring on these bodies. Weathering through regolith transport will occur constantly and repeatedly, and for an extended period of time. Weathered material will be impacted numerous times through wind-driven processes and meteoritic impacts, indicating the additional importance of experimenting with pre-milled samples to analyse secondary abrasion processes. Future work could also include utilisation of the University of Kent's light gas gun (LGG) in conjunction with ball milling to assess the combinational effects of impact shock alongside periodical weathering. Previous research conducted by Tandy *et al.* at the University of Kent has investigated the regolith compositional alterations due to impacts, and the chemical composition of impact ejecta [71]. Aside from milling times, experimental variables such as milling frequency, apparatus material (e.g. use of agate milling vials and ball-bearings), size and number of ball bearings would be intriguing and invaluable factors to adopt in order to explore optimal grinding efficiency. As clear modifications in grain size, and thus mineral specific surface area, have been illustrated, a microscale examination of these modifications should now be explored to improve clarity and understanding of the relevance of these findings. This could perhaps be achieved through SEM-EDS mapping, however this experimental technique would not be time efficient due to the predicted large variability between different grain surfaces, depending on the area of observation.

6.3.2 CO_2 Sequestration

Through the combination of the mechanochemical and thermal activation of mineral surfaces, the capture and storage of $CO_{2\,(g)}$ has been speculated to occur by oxocarbon compound contributions

observed in XRD analysis, but most noticeably emphasised by FTIR spectroscopy (as seen by the characteristic CO_2 peak at ~ 2400 cm^{-1}) and TGA results which demonstrated a reduction in % mass. These findings are invaluable, as even though previous literature has shown the ability of minerals (in particular silicates) to capture $CO_{2\,(g)}$ (as discussed in previous chapters) [29], the ability for planetary analogue materials to do so, has not been previously reported (relating to literature on polymineralic materials [29]). Tumbling experiments have illustrated the potential for quartz sand to remove $CO_{2\,(g)}$ from the atmosphere due to triboelectrification induced by mechanochemical activation [15], however novel experimental work conducted within this thesis has demonstrated the analogous sequestration using materials containing a variety of mineral blends. However, future research is necessary to ascertain whether the induced CO_2 sequestration due to ball milling is an accelerated and analogous mechanism to the gaseous uptake observed by the aforementioned tumbling experiments. This finding is extremely relevant for the Martian surface which is composed of ~ 96 % $CO_{2\,(g)}$ [72] and therefore for the understanding of how minerals present within the surface soil may uptake atmospheric gases, and by which processes this occurs. Ball milling experiments under an appropriate atmosphere depending on the planetary environment being investigated is therefore essential to validate such observations.

6.4 Simulating Environmental Conditions

The harsh climatic conditions experienced on the Lunar and Martian surface are challenging to simulate within the laboratory, even on a small scale. However, other than the incorporation of water ice, invaluable future research should include mixing of regolith with CO_2 ice due to its known presence within the Lunar cold traps, and at the Martian polar caps [18, 20]. The extreme fluctuations in temperature and immensely low atmospheric pressure experienced on Mars [3,9,10] have not yet been considered in combination with effects of weathering, and in conjunction with the seasonal CO_2 deposition and its' subsequent sublimation. Simulating such climatic conditions driven by cyclic solar thermal radiation and subsequent cooling would allow simultaneous alterations driven by thermal and collisional processes to be analysed. Additional analyses may include irradiating the Lunar and Martian analogue samples UV light pre- and post-milling to assess if this may induce different chemical changes, simulating conditions experienced on the Lunar surface (due to the lack of an atmosphere) and on Mars. The potential chemistry induced during this experiments may differ from current ongoing UV irradiation studies of planetary analogues due to mechanochemical activation thus more reactive mineral grain surfaces.

6.4.2 Icy Environmental Conditions

Whilst the incorporation of water ice induced noticeable effects in the chemistry of the Lunar and Martian analogues, potential alterations in mineralogy were not as significant. These findings were extremely informative, as the exploration of regolith-ice mixtures and the mechanochemical-induced changes in chemistry had not yet been reported. Despite careful extraction, this could possibly be due to samples not being fully dried prior to ATR-FTIR analysis, and therefore the presence of water within the sample may have obscured the results. To further investigate this, samples should be thoroughly dried using a desiccator and subsequently analysed to assess the incorporation of water ice with greater confidence. For the scope of this thesis, heating of the analogue samples to aid drying was deliberately avoided to prevent further induced-chemical changes not attributable to the milling process. The minimal differences observed when comparing the deionised, distilled and tap water samples was also an important result of this thesis. This potentially implies that abrasive interactions between regolith and historic flowing water on the Martian surface may not have been influenced by the relative concentration of dissolved minerals or salts. As previously noted, rapid melting was observed when milling with water ice, which was not ideal for the accurate simulation of potential planetary abrasion processes, although adequate for the preliminary investigations within this thesis. The ancient hydrological system on Mars suggests that liquid water may have been present through studies of older terrains. For instance, the 'Dorsa Argentea' landscape formations which have been categorised as esker deposits formed by gravel or sediment deposits from glacial meltwater, suggesting temporary water underneath ice sheets [73]. This implies that the melting of water ice during milling experiments may be extremely useful to ascertain alterations in regolith composition under Martian glaciers. To prevent premature melting of water ice in future experiments, apparatus such as a cryogenic ball mill can be employed [26], although these introduce an additional expense. More economical methods such as pre-crushed ice that is refrozen at colder temperatures may be more appropriate, however, may also pose to be less realistic due to the requirement of such cold conditions.

To summarise, a detailed preliminary analysis of four Lunar and Martian simulants has been executed, demonstrating the potential for mechanochemical-induced alterations of their chemical and mineralogical composition. This novel research and the grounding it provides for future analyses will complement space missions and subsequent data interpretation, as the assessment of induced-chemical changes due to regolith (and regolith-ice mixture) transport simulated by ball-milling has not been explored prior to this study. It has demonstrated the use of ball-milling and complementary analytical techniques to enable analyses of not only the regolith's physical, chemical and mineralogical properties, but also how it has and will continue to evolve over time with varying climates.

References

[1] Foucher F., Hickman-Lewis K., Hutzler A., Joy K.H., Folco L., Bridges J.C., Wozniakiewicz P., Martínez-Frías J., Debaille V., Zolensky M., Yano H., Bost N., Ferrière L., Lee M., Michalski J., Schroeven-Deceuninck., Kminek G., Viso M., Russell S., Smith C., Zipfel J., Westall F. 2021. Definition and use of functional analogues in planetary exploration. *Planetary and Space Science* 197:105162.

[2] Cannon K.M., Britt D.T., Smith T.M., Fritsche R.F., and Batcheldor D. 2019. Mars global simulant MGS-1: A Rocknest-based open standard for basaltic martian regolith simulants. *Icarus* 317: 470-478.

[3] Cassaro A., Pacelli C., Aureli L., Catanzaro I., Leo P., and Onofri S. 2021. Antarctica as a reservoir of planetary analogue environments. *Extremophiles* 25: 437-458.

[4] ExoLith Lab. *ExoLith Lab*. Available from: Exolith Lab - Regolith Simulants (exolithsimulants.com) [Accessed 30/09/2022].

[5] Bazilevskaya E., Lebedeva Ma., Pavich M., Rother G., Parkinson D.Y., Cole D., and Brantley S.L. 2013. Where fast weathering creates thin regolith and slow weathering creates thick regolith. *Earth Surf. Process. Landforms* 38: 847-858.

[6] Hurowitz J.A., Tosca N.J., McLennan S.M., and Schoonen M.A.A. 2007. Production of hydrogen peroxide in Martian and Lunar soils. *Earth and Planetary Science Letters* 255:41-52.

[7] Papike J.J., Simon S.B., and Laul J.C. 1982. The Lunar Regolith: Chemistry, Mineralogy and Petrology. *Reviews of Geophysics and Space Physics* 20:761-826.

[8] Liu J., Liu B., Langevin Y., and Arnold R.J. 1977. The Evolution of the Lunar Regolith. *Earth Planet.Sci* 5:449-89.

[9] Zent A.P and McKay C.P. 1994. The Chemical Reactivity of the Martian Soil and Implications for Future Missions. *Icarus* 108: 146-157.

[10] Inge L.T.K., James R.C.G, Zan P., Bernard F., and Pascale E. 2006. The effects of Martian near surface conditions on the photochemistry of amino acids. *Planetary and Space Science* 54: 296-302.

[11] McKay D.S., Carter J.L., Boles W.W., Allen C.C., and Allton J.H. 1994. JSC-1: A new Lunar regolith simulant. *Engineering, Construction and Operations in Space IV,* American Society of Civil Engineers, pp. 857-866.

[12] Isachenkov M., Chugunov S., Landsman Z., Akhatov., Metke A., Tikhonov A., and Shishkovsky I. 2022. Characterisation of novel lunar highland and mare simulants for ISRU research applications. *Icarus* 376: 114873.

[13] Forward K.M., Lacks D.J., and Sankaran R.M. 2009. Triboelectric charging of lunar regolith simulant. *Journal of Geophysical Research* 114: 1-3.

[14] Merrison, J.P. 2012. Sand transport, erosion and granular electrification. *Aeolian Research* 4:1-16.

[15] Bregnhøj M., Knack Jensen S.J., Strunge K., Nielsen A.B., Thøgersen J., Nørnberg P., Skibsted J., and Finster K. 2023. Carbon Dioxide Sequestration by Triboelectric Charging of Tumbling Quartz Sand. *J. Phys. Chem. C* 25: 12008-12015.

[16] Melosh H.J. Regoliths, weathering, and surface texture. Planetary Surface Processes. United Kingdom: Cambridge University Press; 2011. p. 276-318.

[17] NASA. *NASA Orbiter Finds New Evidence of Frost on Moon's Surface.* Available from: NASA Orbiter Finds New Evidence of Frost on Moon's Surface – Moon: NASA Science [Accessed 05/10/2023].

[18] Li S., Lucey P.G., Milliken R.E., Hayne P.O., Fisher E., Williams J., Hurley D.M., and Elphic R.C. 2018. Direct evidence of surface exposed water ice in the lunar polar regions. *PNAS* 115: 8907-8912.

[19] Shifeng J., Munan H., Zhongnan G., Bohao Y., Yuxin M., Lijun D., Xu C., Yanpeng S., Cheng C., Congcong C., Yunqi M., Jiangang G., and Xiaolong C. 2023. Discovery of a new lunar mineral rich in water and ammonium in lunar soils returned by Chang'e-5 mission. *Earth and Planetary Astrophysics.* (no volume number provided) 1-17 doi: https://doi.org/10.48550/arXiv.2305.05263.

[20] Chevrier V. and Mathé P.E. 2007. Mineralogy and evolution of the surface of Mars: A review. *Planetary and Space Science* 55:289-314.

[21] Ben-Dor E., Levin N., Singer A., Karnieli A., Braun O., and Kidron G.J. 2006. Quantitative mapping of the soil rubification process on sand dunes using an airborne hyperspectral sensor. *Geoderma* 131:1-21.

[22] Edgar J.O., Gilmour K., White M.L., Abbott G.D., and Telling J. 2022. Aeolian driven oxidant and hydrogen generation in Martian regolith: The role of mineralogy and abrasion temperature. *Earth and Planetary Science Letters* 579: 1-10.

[23] NASA. *Jet Propulsion Laboratory - California Institute of Technology.* Available from: Catalog Page for PIA13163 (nasa.gov) [Accessed 03/04/2023].

[24] Grotzinger J.P., Crisp J.A., Vasavada A.R., and the MSL Science Team. 2015. Curiosity's Mission of Exploration at Gale Crater, Mars. *Elements* 11: 19-26.

[25] Schon S.C., Head J.W., and Fassett C.I. 2012. An overfilled lacustrine system and progradational delta in Jezero crater; Mars: Implications for Noachian climate. *Planetary and Space Science* 67: 28-45.

[26] Retsch®. *CRYOMILL*. Available from: Cryomill - the perfect mill for cryogenic grinding - RETSCH [Accessed 04/04/2023].

[27] Fakoya M.F and Shah S.N. 2017. Emergence of nanotechnology in the oil and gas industry: Emphasis on the application of silica nanoparticles. *Petroleum* 3: 391-405.

[28] Takacs L. 2002. Self-sustaining reactions induced by ball milling. *Progress in Materials Science* 47: 355-414.

[29] Stillings M., Shipton Z.K., and Lunn R.J. 2023. Mechanochemical processing of silicate rocks to trap CO_2. *Nature Sustainability* 6: 780-788.

[30] Chang R. *Physical Chemistry for the Chemical and Biological Sciences*. 2nd ed. United States of America: University Science Books; 2000.

[31] Grdadolnik J. 2002. ATR-FTIR Spectroscopy: Its Advantages and Limitations. *Acta Chimica Slovenica* 49: 631-642.

[32] LibreTexts™ Chemistry. *Raman and Surface-Enhanced Raman Spectroscopy. A*vailable from: 4.3: Raman Spectroscopy - Chemistry LibreTexts [Accessed 21/09/2023].

[33] Azotopics. *IR Versus Raman – The Advantages and Disadvantages.* Available from: IR Versus Raman - The Advantages and Disadvantages (azooptics.com) [Accessed 21/09/2023].

[34] Dunlap M. and Adaskaveg J.E. 1997. Introduction to the Scanning Electron Microscope – Theory, Practice & Procedures. Facility for Advanced Instrumentation, U.C. Davis.

[35] Stanford University. *School of Sustainability Scanning Electron Microscope Facility.* Available from: EDS Mapping | Scanning Electron Microscope Facility (stanford.edu) [Accessed 04/10/2023].

[36] Saadatkhah N., Garcia A.C., Ackermann S., Leclerc P., Latifi M., Samih S., Patience G., and Chaouki J. 2020. Experimental methods in chemical engineering: Thermogravimetric analysis – TGA. *Can J Chem Eng.* 98: 34-43.

[37] Menczel J.D. and Prime R.B. *Thermal Analysis of Polymers.* New Jersey, United States of Amerca: John Wiley & Sons; 2009.

[38] Roux S., Bensakhria A., and Antonini G. 2006. Study and Improvement of the Regeneration of Metallic Oxides Used as Oxygen Carriers for a New Combustion Process. *International Journal of Chemical Reactor Engineering* 4: 2.

[39] Devarajan R., Mohanesen K., Maria R., Mahendran S., Kadirgama K., Rahman M. 2020. Analysis of Alumina Particle Size and Shape Formation from Developed Planetary Ball Mill. *IOP Conference Series Materials Science and Engineering* 736: 2.

[40] MERCK. *Particle Size Conversion Table.* Available from: Particle Size Conversion Table (sigmaaldrich.com) [Accessed 20/07/2023].

[41] Degen T., Sadki M., Bron E., König U., Nénert G. 2014. The HighScore suite. *Powder Diffraction* 29: S13-S18.

[42] Simmons W.B., Tilley C.E., and The Editors of Encyclopaedia Britannica. *Olivine.* Available from: Olivine | Mineral, Rock & Magma | Britannica [Accessed 01/05/2023].

[43] Kleiv R.A. and Thornhill M. 2006. Mechanical activation of olivine. *Minerals Engineering* 19: 340-347.

[44] Mineralogy Database. *Olivine Mineral Data.* Available from: Olivine Mineral Data (webmineral.com) [Accessed 01/05/2023].

[45] NIST Chemistry WebBook. *Olivine-group minerals.* Available from: Olivine-group minerals (nist.gov) [Accessed 01/05/2023].

[46] Launer P.J. and Arkles B. *Infrared Analysis of Organosilicon Compounds: Spectra-Structure Correlations.* Morrisville, PA: Gelest, Inc. 2013.

[47] Simmons W.B. and The Editors of Encyclopaedia Britannica. *Pyroxene.* Available from: Pyroxene | Mineral Composition, Structure & Uses | Britannica [Accessed: 01/05/2023].

[48] Britannica. *Crystal structure.* Available from: Pyroxene - Crystal Structure, Minerals, Silicates | Britannica [Accessed 01/05/2023].

[49] Lekgoathi M.D.S. and le Roux J.P. 2011. Attenuated total reflectance powder cell for infrared analysis of hygroscopic samples. Spectrochimica Acta Part A: Molecular and Biomolecular Spectroscopy 82: 529-531.

[50] Britannica. *Anorthosite.* Available from: Anorthosite | Igneous, Plutonic, Mafic | Britannica [Accessed 01/05/2023].

[51] Database of ATR-FT-IR spectra of various materials. *Plagioclase.* Available from: Plagioclase – Database of ATR-FT-IR spectra of various materials (ut.ee) [Accessed 01/05/2023].

[52] Waseem M., Mustafa S., Naeem A., Shah K.H., Shah I., and Haque I.U. 2009. Synthesis and Characterisation of Silica by Sol-Gel Method. *J Pak Mater Soc* 3: 21.

[53] King H.M. *Ilmenite.* Available from: Ilmenite Mineral Data (webmineral.com) [Accessed 01/05/2023].

[54] Hipólito E.L., Fabela-Cedillo M.G., Torres-Martínez L.M., and Zarazúa-Morín M.E. 2023. Solar-driven CO_2 reduction using modified earth-abundant ilmenite catalysts. *Heliyon* 9: 1-11.

[55] Zahir Md H., Rahman M.M., Irshad K., and Rahman M.M. 2019. Shape-Stabilised Phase Change Materials for Solar Energy Storage: MgO and Mg $(OH)_2$ Mixed with Polyethylene Glycol. *Nanomaterials* 9: 7.

[56] Britannica. *Basalt.* Available from: Basalt | Definition, Properties, & Facts | Britannica [Accessed 01/05/2023].

[57] King H.M. *Basalt.* Available from: Basalt: Igneous Rock - Pictures, Definition, Uses & More (geology.com) [Accessed 01/05/2023].

[58] Luciani N., Van der Lubbe J.H.L., Verdegaal-Warmerdam S.J.A., Postma O., Nikogosian I.K., Davies G.R., and Koornneef J.M. 2022. Carbon and oxygen isotope analysis of CO_2 trapped in silicate minerals. *Chemical Geology* 602: 120872.

[59] Stroncik N.A. and Schmincke H-U. 2002. Palagonite – a review. *International Journal of Earth Sciences* 91: 680-697.

[60] Mindat. *Palagonite.* Available from: Palagonite: Mineral information, data and localities. (mindat.org) [Accessed 09/03/2023].

[61] Carrier B.L. and Kounaves S.P. 2015. The origins of perchlorate in the Martian soil. *Geophys. Res. Lett.* 42: 3739-3745.

[62] Database of ATR-FT-IR spectra of various materials. *Iron (III) oxide.* Available from: Iron(III) oxide – Database of ATR-FT-IR spectra of various materials (ut.ee) [Accessed 01/02/2023].

[63] Caster K.C. 1996. Arsoles, Stiboles, and Bismoles. Comprehensive Heterocyclic Chemistry II 2:857-902.

[64] LibreTexts™ Chemistry. *X-ray diffraction (XRD) basics and application. A*vailable from: X-ray diffraction (XRD) basics and application - Chemistry LibreTexts [Accessed 15/04/2023].

[65] Hara J. and Tsuchiya N. 2004. Coupled T (Thermal) – H (Hydrological) – C (Chemical) Process of Geothermal Alteration, Based on Experimental and Kinetic Considerations. Geo-Engineering Book Series 2: 655-660.

[66] Hernández Ma.de L.L., Álvarez-Gallegos A., Hernández J.A., and Silva-Martínez S. 2015. Cadmium removal from dilute aqueous solutions under galvanostatic mode in a flow-through cell.

[68] Zhou M., Zhang L., Lu H., Shao L., and Chen M. 2002. Reaction of silicon dioxide with water: a matrix isolation infrared and density functional theoretical study. *Journal of Molecular Structure* 605: 249-254.

[69] LibreTexts™ Chemistry. *Reactions of Main Group Elements with Water*. Available from: Reactions of Main Group Elements with Water - Chemistry LibreTexts [Accessed 21/09/2023].

[70] Freissinet C., Glavin D.P., Mahaffy P.R., et al. 2015.Organic molecules in the Sheepbed Mudstone, Gale Crater, Mars. *J. Geophys. Res. Planets* 120: 495-514.

[71] Tandy J.D., Price M.C., Wozniakiewicz P.J., Cole M.J., Alesbrook L.S., and Avdellidou C. 2020. Impact flash evolution of CO_2 ice, water ice, and frozen Martian and Lunar regolith simulant targets. *Meteoritics & Planetary Science* 55: 2301-23.

[72] Lin B. and Liu Z. 2021. Martian Atmospheric CO_2 and Pressure Profiling with Differential Adsorption Lidar: System Consideration and Simulation Results. *Earth and Space Science* 8: 1-14.

[73] Butcher F.E.G., Conway S.J., and Arnold N.S. 2016. Are the Dorsa Argentea on Mars eskers? *Icarus* 275: 65-84.

Appendices

Appendix 1

Figure 140. Photograph taken of 5 mm stainless steel ball bearings with iron rust residue.

Figure 140 is illustrated above to emphasise the rusting of apparatus post-milling on the Retsch MM301 mixer mill.

Appendix 2

Figure 141. Photograph taken of the JSC-Martian simulant milled for 10 minutes at a frequency of 30 Hz utilising the Fritsch P23 mini mixer mill.

Figure 141 shown above is presented as an example of the resulting material from employing the Fritsch P23 mini mixer mill. A higher degree of abrasion was observed in comparison to milling for 10 minutes on the Retsch MM301, perhaps due to more efficient grinding and more frequent, successful collisional impacts between ball bearings (their smaller diameter and greater volume) and the material.

Appendix 3

Figure 142. Photographs taken of the simulants milled for 10 minutes at a frequency of 400 rpm utilising the P7 planetary micromill a) JSC-Lunar; b) LHS-1; c) JSC-Martian; d) MGS-1.

Figure 142 illustrates the paste-like appearance of the synthesised LHS-1 and MGS-1 simulants after milling for 10 minutes on the P7 planetary micromill, in comparison to the fine grain texture of the JSC-Lunar and JSC-Martian Earth-based simulants.

Appendix 4 -

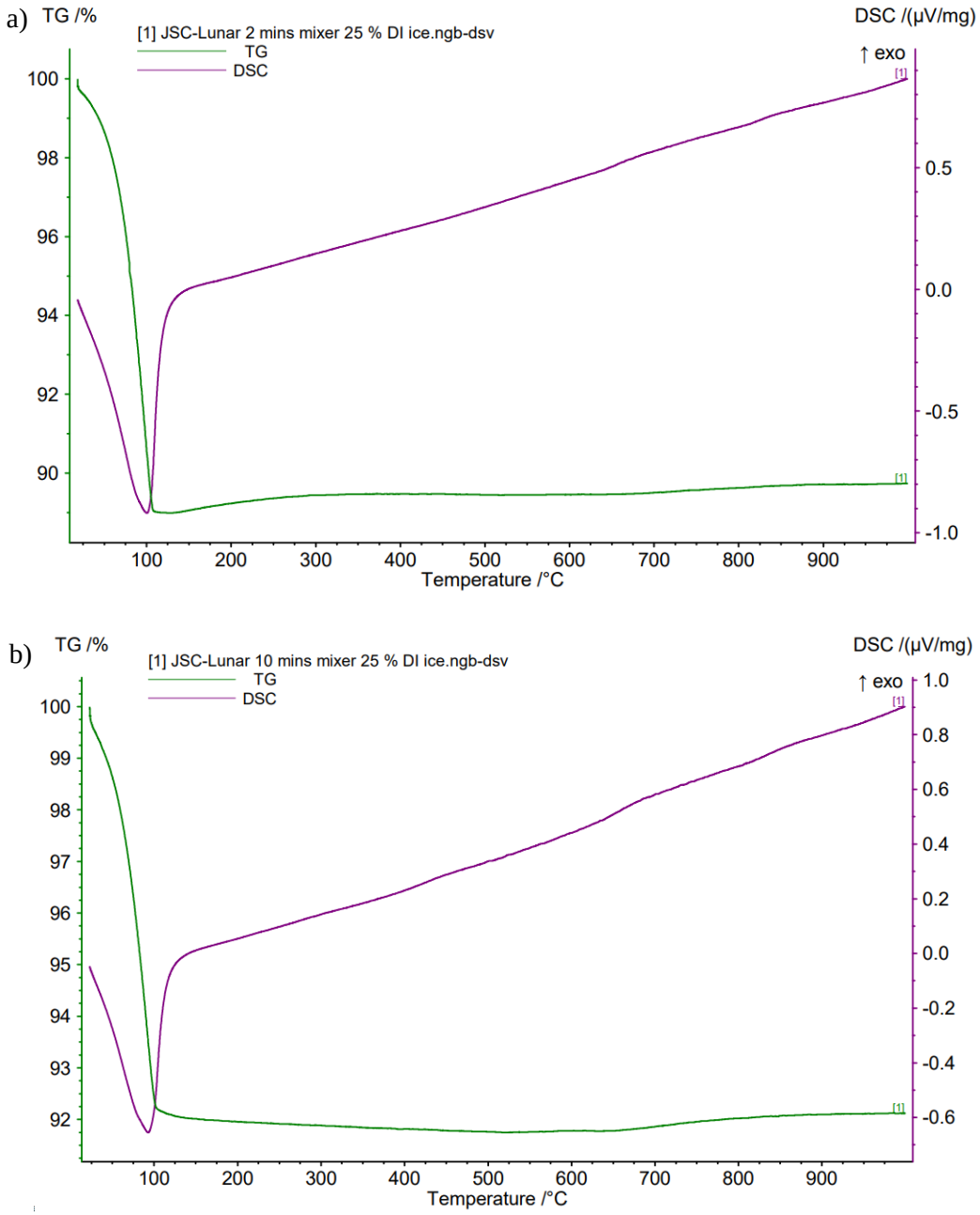

Figure 143. TGA-DSC results illustrating the effect of heating the milled 75 % JSC-Lunar 25 % deionised water ice sample for a) 2 minutes; b) 10 minutes.

Figure 143 above demonstrates the significant loss of water upon heating the JSC-Lunar and deionised water ice mixture for a) 2 and b) 10 minutes, illustrated by the sharp decline in % mass at 100 °C. Samples were ran on the TGA apparatus after being dried in a Na_2CO_3 desiccator for > 24 hours, however thermal effects simply showed the clear contribution and subsequent loss of water, and not any potential water ice-driven alterations in chemistry or hydrated minerals.

Appendix 5 -

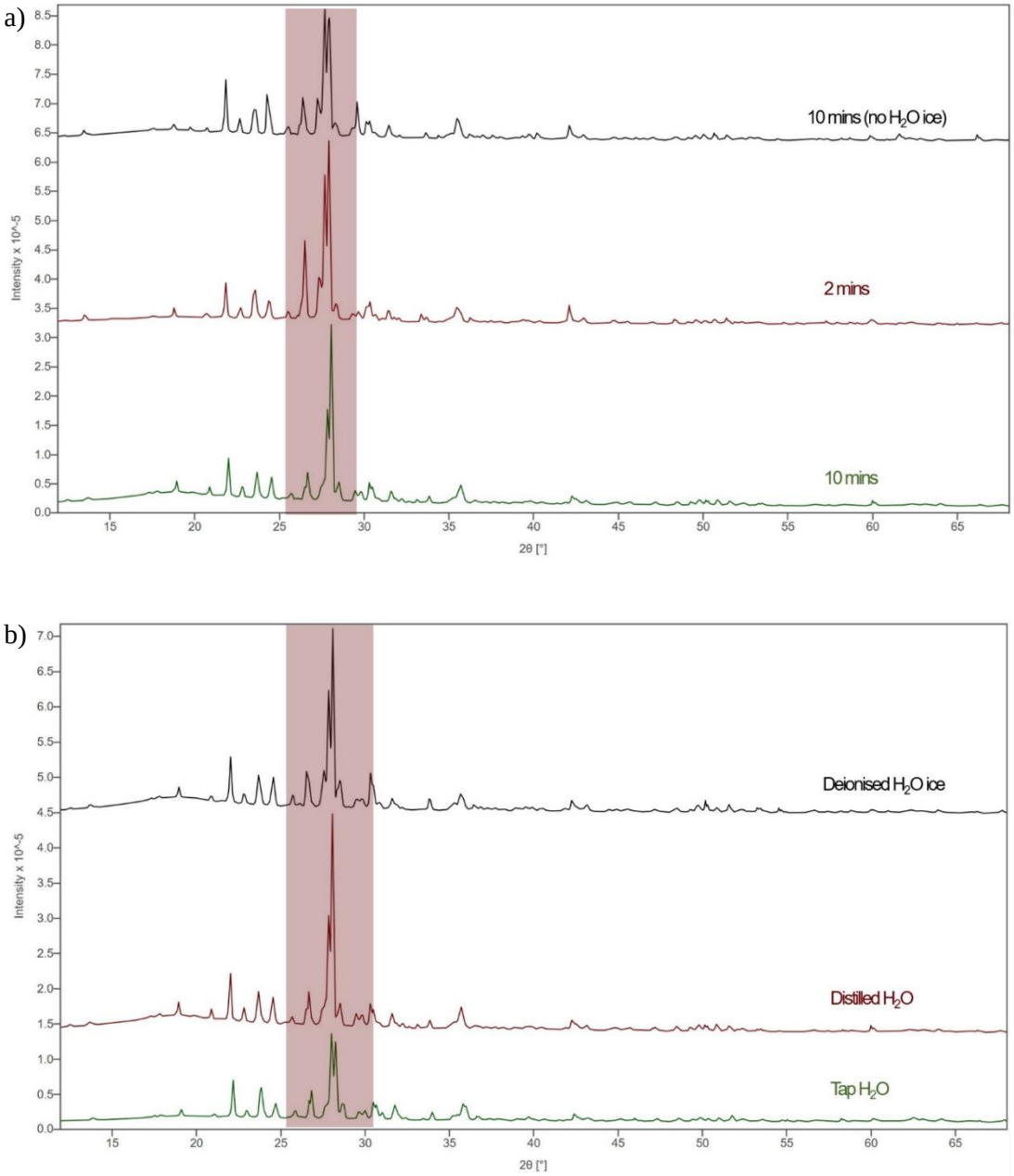

Figure 144. X-ray diffractogram results assessing the effect of water ice on the mineralogy of the LHS-1 simulant (where highlighted regions indicate noticeable changes in relative peak intensity) by illustrating a) Effect of milling with 25 % distilled water ice; b) Comparison of all three water ice treatments upon milling for 10 minutes.

Figure 144 above suggests that there are no notable alterations in mineralogical structure depending on the water treatment. This is of great relevance to planetary bodies, for instance the Martian surface when assessing the effect of different potential salts on regolith composition due to soil-ice mixtures, or when assessing the historical hydrological cycle of the Martian atmosphere and the effect of the transport of water downriver, transporting and incorporating different minerals into regolith.